MINISTÉRIO DA CIÊNCIA, TECNOLOGIA E INOVAÇÕES
INSTITUTO NACIONAL DE PESQUISAS ESPACIAIS

sid.inpe.br/mtc-m12e/2025/04.11.04.08-TDI

INVESTIGATING THE PHYSICAL PROPERTIES OF LOW IONIZATION GAS IN THE BROAD LINE REGION OF AGNS

Denimara Dias dos Santos

Doctorate Thesis of the Graduate Course in Astrophysics, guided by Dr. Alberto Rodríguez Ardila, approved in February 26, 2025.

URL of the original document:
<http://urlib.net/8JMKD2USNRW34T/4DAB495>

INPE
São José dos Campos
2025

PUBLISHED BY:

Instituto Nacional de Pesquisas Espaciais - INPE
Coordenação de Ensino, Pesquisa e Extensão (COEPE)
Divisão de Biblioteca (DIBIB)
CEP 12.227-010
São José dos Campos - SP - Brasil
Tel.:(012) 3208-6923/7348
E-mail: pubtc@inpe.br

MINISTÉRIO DA CIÊNCIA, TECNOLOGIA E INOVAÇÕES
INSTITUTO NACIONAL DE PESQUISAS ESPACIAIS

sid.inpe.br/mtc-m12e/2025/04.11.04.08-TDI

INVESTIGATING THE PHYSICAL PROPERTIES OF LOW IONIZATION GAS IN THE BROAD LINE REGION OF AGNS

Denimara Dias dos Santos

Doctorate Thesis of the Graduate Course in Astrophysics, guided by Dr. Alberto Rodríguez Ardila, approved in February 26, 2025.

URL of the original document:
<http://urlib.net/8JMKD2USNRW34T/4DAB495>

INPE
São José dos Campos
2025

Cataloging in Publication Data

Santos, Denimara Dias dos.

Sa59i Investigating the physical properties of low ionization gas in the broad line region of AGNs / Denimara Dias dos Santos. – São José dos Campos : INPE, 2025.

xxii + 146 p. ; (sid.inpe.br/mtc-m12e/2025/04.11.04.08-TDI)

Thesis (Doctorate in Astrophysics) – Instituto Nacional de Pesquisas Espaciais, São José dos Campos, 2025.

Guiding : Dr.Alberto Rodríguez Ardila.

1. Active galatic nuclei. 2. Photoionization mododelling. 3. Broad-line region. 4. Low-ionization lines. 5. Double-peaked emission. I.Title.

CDU 524.64

MINISTÉRIO DA CIÊNCIA, TECNOLOGIA E INOVAÇÃO

INSTITUTO NACIONAL DE PESQUISAS ESPACIAIS

DEFESA FINAL DE TESE DE DENIMARA DIAS DOS SANTOS
REG.58706/2021, BANCA N°018/2025

No dia 26 de fevereiro de 2025, de forma Presencial/Híbrido, o(a) aluno(a) mencionado(a) acima defendeu seu trabalho final (apresentação oral seguida de arguição) perante uma Banca Examinadora, cujos membros estão listados abaixo. O(A) aluno(a) foi **APROVADO(A)** pela Banca Examinadora, por unanimidade, em cumprimento ao requisito exigido para obtenção do Título de Doutora em Astrofísica, com a exigência de que o trabalho final a ser publicado deverá incorporar as correções sugeridas pela Banca Examinadora, com revisão final pelo orientador Dr. Alberto Rodriguez Ardila.

Título: "Investigating the Physical Properties of Low Ionization Gas in the Broad Line Region of AGNs."

Observações da banca: O aluno deverá incorporar as sugestões da banca e a revisão final do texto será feita pelo orientador

Membros da banca:

Dr. Carlos Alexandre Wuensche de Souza - Presidente - Membro Interno (DIAST/INPE & Docente PGAST)

Dr. Alberto Rodríguez Ardila - Orientador - Membro Interno (LNA & Docente PGAST)

Dr. Luis Gabriel Dahmer Hahn - Membro Externo (Shanghai Astronomical Observatory)

Dra. Marina Trevisan - Membro Externo (Universidade Federal do Rio Grande do Sul)

Dra. Thaisa Storchi Bergmann - Membro Externo (Universidade Federal do Rio Grande do Sul)

Dra. Zulema Abraham - Membro Externo (Universidade de São Paulo)

Documento assinado eletronicamente por **Carlos Alexandre Wuensche de Souza**, **Pesquisador**, em 07/03/2025, às 13:06 (horário oficial de Brasília), com fundamento no § 3º do art. 4º do Decreto nº 10.543, de 13 de novembro de 2020.

Documento assinado eletronicamente por **Alberto Rodriguez Ardila**, **Pesquisador Titular**, em 07/03/2025, às 13:39 (horário oficial de Brasília), com fundamento no § 3º do art. 4º do Decreto nº 10.543, de 13 de novembro de 2020.

Documento assinado eletronicamente por **Marina Trevisan**, **Usuário Externo**, em 07/03/2025, às 13:53 (horário oficial de Brasília), com fundamento no § 3º do art. 4º do Decreto nº 10.543, de 13 de novembro de 2020.

Documento assinado eletronicamente por **Zulema abraham (E)**, **Usuário Externo**, em 08/03/2025, às 15:29 (horário oficial de Brasília), com fundamento no § 3º do art. 4º do Decreto nº 10.543, de 13 de novembro de 2020.

Documento assinado eletronicamente por **Luis Gabriel Dahmer Hahn**, **Usuário Externo**, em 09/03/2025, às 23:26 (horário oficial de Brasília), com fundamento no § 3º do art. 4º do Decreto nº 10.543, de 13 de novembro de 2020.

A autenticidade deste documento pode ser conferida no site https://sei.mcti.gov.br/verifica.html, informando o código verificador **12651011** e o código CRC **4EE28522**.

Referência: Processo nº 01340.001334/2025-79 SEI nº 12651011

"Deus dos antigos, cuja forte mão
Rege e sustem os astros da amplidão
Do cintilante céu inspirador
Com gratidão cantamos Teu louvor".

Cantado por Euza de Aguiar Santos

A meus pais ***Ademar*** *e* ***Regina***

ACKNOWLEDGEMENTS

Inicialmente, gostaria de dizer que esta Tese é um ato político, porque, de onde venho, não é esperado (e nem incentivado) que as pessoas se tornem doutoras, ou que façam parte da "elite intelectual" do país. Portanto, o que por muitos anos da minha vida foi apenas um sonho de menina — ser astrofísica — se tornou um símbolo de persistência e resistência. Se tornou uma oportunidade de "furar" uma camada social, que, apesar de eu ainda não ter certeza de que meus esforços me garantirão isso, sigo sonhando por mim e pela minha família. Agora, sim, vamos aos agradecimentos. Primeiro, gostaria de agradecer Aquele que é meu amigo, que me sustenta e me ensina a ser melhor, a pessoa/ser mais incrível e legal que existe, Jesus. Aos meus pais amados, que, essencialmente, me deram forças para suportar essa jornada de 11 anos de estudos árduos, dolorosos e cansativos. Ao meu pai Ademar, que, como ama relembrar, deu muitas "alavancadas" para que eu pudesse aprender inglês e fazer a graduação, mesmo sem ter nenhuma condição financeira aos nossos olhos, mas sempre aos de Deus, tínhamos. Pai, obrigada por, desde que eu disse querer fazer Física, você, mesmo sem se quer compreender as leis da natureza, disse que ia me dar todo suporte que eu precisasse e, em nenhum momento, me desanimou. Você é uma rocha inabalável e meu exemplo. Mãe, minha "frôzinha", sei que para você, todo sacrifício de viver longe foi muito penoso em meio à dificuldade, e eu te entendo e te agradeço. Obrigada por ser uma das pessoas que mais me motiva e me dá forças. Obrigada pelo seu carinho, seu amor, pelas inúmeras discussões sobre "leva comida, filha", mesmo eu dizendo que não tinha como porque não cabia na mala. Eu te amo infinitamente. Agora, agradeço à pessoa que, praticamente, acompanhou toda minha jornada acadêmica de 11 anos, porém, por azar ou caos do cone de luz, apenas entrou nela como amor da minha vida no fim da graduação. Agradeço ao meu amor, Diego, que antes era colega da "fila da PROAES" e agora é o amor da minha vida. Ego, obrigada por todos os abraços, pelos milhares de horas em ligações que sempre começam gentilmente com "como foi seu dia, amor?". Obrigada por me fazer sentir priorizada por você em todos os detalhes, por cuidar de mim todos os dias e regar nosso amor como uma "pratinha" ou uma "denimalis". Obrigada por todo frango frito que tivemos que comer para aguentar nossas pós-graduações, por insistir que eu ia gostar um dia de açaí, por todas as viagens, discussões de resultados e perrengues. Obrigada pelo Dengoso (e obrigada Dengoso). Obrigada por tornar minha vida leve, descontraída e, ao mesmo tempo, sólida como a base que estamos construindo juntos. Obrigada por todo suporte em muitos momentos difíceis e por compartilhar os melhores também. Eu te amo, Dr. Santos, D.C. dos raios cósmicos, e tenho muito orgulho de você. Agradeço também à minha irmã,

Regiane, meu sobrinho David, minhas pessoas querida que estão com Jesus, Célia, Euza e Valdmiro. Esses últimos, apesar de infelizmente não terem a oportunidade de me ver completar a jornada, sempre me apoiaram. Agradeço agora a todas as minhas amigas do fundo do meu coração pelo apoio. Mami (Barbara), amiga dos AGNs e da vida. Me iluminou e me abraçou em incontáveis momentos. Obrigada por todos os cafés superfaturados que salvaram nossa saúde mental, por não me julgar, me ouvir e dar a mão sempre. Obrigada por dividir o choro e memes de galinha. Te amo, minha galinha preferida. À minha amiga mestre dos raios Taji (Tagianne, sim, sei como se escreve seu nome). Taji, obrigada pelos cafés, pelo seu carinho em forma de bolinho de canela, por me ouvir, pelo nosso passeio mensal no Centervale, pelos lanches, por me incentivar a me exercitar, por tudo que nem cabe aqui desde que chegou na minha vida. Amo você, amiga. Agradeço também à minha amiga, Xuxu, por todo apoio e amor. Juzínea, pelos longos anos de caminhada e cuidado. Às minhas amigas: Ana Luíza, Gabriela(s), Marinas (Meimei, Guria, Mariana), e meu amigo Bruno. Agora, agradeço à pessoa que, sem me conhecer, apostou em mim e também é o autor desta tese: meu orientador Alberto. Obrigada pela confiança, pelo suporte, paciência, por falar "ai Denimara, porque você pensa isso de você?" quanto estou insegura, e por dividir foto dos seus lindos gatinhos, deixando meu dia mais feliz. Por me ensinar tudo o que sei sobre observações, dados e tudo o mais que me auxiliou a me tornar a profissional que sou. Estou animada para trabalharmos juntos em nossos futuros projetos. Agradeço também a todos do meu grupo de pesquisa, em especial a Murilo, Panda, Marcos e Fernando. Murilo, você foi essencial para eu saber observar no Tspec-4, saber lidar com os fits do FeII. Marcos e Fernando, obrigada pelas dúvidas sanadas e pela paciência comigo aprendendo Python. Panda, good friend and collaborator, all your patience in teaching me about CLOUDY, theory, answering me basic questions, Indian Gods, food, English, and always encouraging everything. Também agradeço a meu orientador da graduação, e amigo, Ladário. Por sempre estar por perto, me acompanhando e assistindo meu progresso como física e pessoa. A todos os meus professores e instituições em que estudei, especialmente ao INPE pelos últimos 6 anos. Agradeço a CAPES e CNPq, que, em meio ao caos que vivemos, mantiveram-se de pé, mesmo que muitos os desejavam ver cair. Agradeço a todas as pessoas que cruzaram meu caminho e que torcem pela ciência do Brasil. E sim, agradeço ao meu país, que tem um sistema público de ensino que me permitiu me tornar Astrofísica. Espero um dia retornar à sociedade o dinheiro público investido em mim. Desejo vida longa à ciência brasileira, que resistamos em meio ao caos e jamais perder as esperanças na nossa sociedade.

ABSTRACT

This thesis investigates the physical properties, geometry, and kinematics of the low-ionization gas in the broad-line region (BLR) of active galactic nuclei (AGNs). It focuses specifically on FeII emission in the optical and near-infrared (NIR) spectral regions, as well as the low-ionization line (LIL) O I λ8446, λ11297. We are presenting the first simultaneous FeII modeling in optical and NIR regions using the CLOUDY photoionization code, covering the wavelength range, 4000−12,000 Å. Our analysis indicates that the optical and NIR FeII emissions can be reproduced under consistent physical conditions, with hydrogen densities between $10^{11} - 10^{12}$ cm^{-3} and near-solar metallicity. Additionally, we investigate the influence of Lyman-α fluorescence, which is found to play a role in the NIR, while collisional processes are more significant in optical FeII emission. This dual modeling approach allows for the understanding of the physical conditions that drive the FeII emission across different spectral regions. Moreover, we investigate the geometry of the low-ionization gas in the BLR through the detection of double-peaked (DP) emission profiles of O I and Paα. This analysis is conducted in the local Seyfert 1 galaxy III Zw 002, marking the first unambiguous detection of a double-peaked broad emission line in the NIR. This simultaneous DP detection of multiple emission supports the interpretation of a disk-like geometry for the BLR, extending up to its outer edge. Still, with disk modeling we obtained an important parameter, the disk inclination, which further contributed to a better understanding of the BLR geometry and black hole mass estimation. Furthermore, we extend the study of the low-ionization gas by analyzing its kinematics, focusing on the detection of outflows in FeII emission lines in the Seyfert 1 galaxy 1H 0707-495. By using NIR spectroscopy, we detect broad components in H I, Fe II, and O I, with FWHM values around 500 km s^{-1}, and observe a blue-asymmetric profile, interpreted as outflowing gas. This feature, previously observed in X-ray and high-ionization lines (HILs) in 1H 0707-495, has not been observed before in LILs. It provides evidence that the wind extends into the outer BLR, possibly affecting the kinematics of the gas, which is conventionally considered well-virialized. Thus, this thesis provides a comprehensive study of the low-ionization gas in AGNs, highlighting its complexity. Despite being an extremely compact region, its observational and geometric characteristics vary from object to object. This is reflected in the physical, geometric, and kinematic conditions, based on the observed and simulated properties of the BLR. The results presented here improve our understanding of the intricate environment of AGNs and open perspectives for future studies on the interactions between the BLR, the accretion disk, and the outflows.

Palavras-chave: Active Galatic Nuclei. Photoionization mododelling. Broad-line region. Low-ionization lines. Double-peaked emission.

INVESTIGANDO AS PROPRIEDADES FÍSICAS DO GÁS DE BAIXA IONIZAÇÃO NA REGIÃO DE LINHAS LARGAS DOS AGNS

RESUMO

Esta tese investiga as propriedades físicas, a geometria e a cinemática do gás de baixa ionização na região de linhas largas (*Broad line Region*, BLR) dos núcleos ativos de galáxias (*Active Galactic Nuclei*, AGNs). O foco específico está na emissão de FeII nas regiões espectrais óptica e no infravermelho próximo (*Near Infrared*, NIR), assim como na linha de baixa ionização (*Low Ionization Line*, LIL) O I λ8446, λ11297. Apresentamos a primeira modelagem simultânea de FeII nas regiões óptica e NIR usando o código de fotoionização CLOUDY, cobrindo o intervalo de comprimento de onda de 4000−12,000 Å. Nossa análise indica que as emissões de FeII ópticas e NIR podem ser reproduzidas sob condições físicas consistentes, com densidades de hidrogênio entre $10^{11} - 10^{12}$ cm^{-3} e metalicidade próxima à solar. Além disso, investigamos a influência da fluorescência de Lyman-α, que desempenha um papel no NIR, enquanto os processos colisionais são mais significativos na emissão óptica de FeII. Essa abordagem de modelagem simultânea permite entender as condições físicas que impulsionam a emissão de FeII em diferentes regiões espectrais. Além disso, investigamos a geometria do gás de baixa ionização na BLR por meio da detecção de perfis de emissão de pico duplo (DP) de O I e Paα. Essa análise foi realizada na galáxia Seyfert 1 III Zw 002, marcando a primeira detecção inequívoca de uma linha de emissão larga com pico duplo no NIR. A detecção simultânea de DP em múltiplas emissões apoia a interpretação de uma geometria tipo disco para a BLR, estendendo-se até sua borda externa. Através da modelagem do disco, obtivemos um parâmetro importante, a inclinação do disco, que contribuiu para um melhor entendimento da geometria da BLR e da estimativa da massa do buraco negro. Ainda, expandimos o estudo do gás de baixa ionização analisando sua cinemática, com foco na detecção de *outflow* nas linhas de emissão de FeII na galáxia Seyfert 1 1H 0707-495. Usando espectroscopia no NIR, detectamos componentes largas em H I, Fe II e O I, com valores de FWHM em torno de 500 km s^{-1}, e observamos um perfil azul-assimétrico, interpretado como um gás em *outflow*. Essa característica, observada anteriormente nas linhas de emissão de raios-X e de alta ionização em 1H 0707-495, não havia sido observada antes em LILs. Ela fornece evidências de que o vento se estende até a BLR externa, afetando possivelmente a cinemática do gás, a qual é convencionalmente considerado bem virializado. Assim, esta tese fornece um estudo abrangente do gás de baixa ionização em AGNs mostrando sua complexidade. Apesar de se tratar de uma emissão extremamente compacta, suas características observacionais e geométricas diferem de objeto para objeto. Isso se reflete nas condições físicas, geométricas e cinemáticas, com base nas propriedades observadas e simuladas da BLR. Os resultados apresentados aqui aprimoram nossa compreensão do intrincado ambiente dos AGNs e abrem perspectivas para futuros estudos sobre as interações entre a BLR, o disco de acreção e os *outflows*.

Palavras-chave: Núcleos Ativos de Galáxias (AGNs). Modelagem de fotoionização. Região de linhas largas. Linhas de baixa ionização. Emissão de pico duplo.

LIST OF FIGURES

Page

LIST OF TABLES

Page

CONTENTS

Page

1 INTRODUCTION

1.1 A historical overview

A century ago, the size of our galaxy, the Milky Way, was unknown. Hence, the size of the Universe was also a big question. During this time, there were constant discussions and debates about the distance scale of the Universe. The most famous debate promoted was named "the great debate" by Shapley and Curtis (1921), in which no winning idea existed. A decade later, Hubble (1934) used the Cepheid variables stars to measure the distances from Earth to a sample of galaxies. The study presents a plot that shows a direct correlation between the receding velocity of the galaxy with respect to Earth and the galaxy's distance. The slope of such a plot measures the expansion rate of the Universe, a quantity well known as the Hubble constant. The discovery made by Edwin Hubble was the result of previous efforts of Henrietta Swan Leavitt (LEAVITT; PICKERING, 1913) an astronomer who has not been mentioned for a long time in the literature. However, this was the birth of extragalactic astronomy, which reveals to us how complex our Universe is: we live in one of a hundred billion galaxies, with many shapes and sizes.

As a result of advancing knowledge in extragalactic astronomy, many objects initially classified as nebulae were later reclassified as galaxies. Later, Carl Seyfert observed a subsample of these objects characterized by strong emission lines in their optical spectra from various elements, such as hydrogen, oxygen, sulfur, nitrogen, iron and broad permitted lines. These objects were later known as Seyfert Galaxies (SEYFERT, 1943). In Burbidge et al. (1963), the authors identify and summarize many features about the Seyfert galaxies, that they are compact and have very bright nuclei, and demonstrate emission line features that are usually not seen in the spectrum of a normal galaxy. In some galaxies, the emission lines exhibit a broad width, which is interpreted as Doppler motion corresponding to gas velocities of hundreds to thousands of kilometers per second. Based on these several observational arguments, they suggested that the Seyfert galaxies should have violent events occurring in their nuclei. However, their nature was still unknown.

Schmidt (1963) discovered the cosmological nature of the quasi-stellar-radio sources (quasars), re-examining the spectrum named 3C 273. The quasars with a stellar-like appearance, i.e., point-like sources, present bright "blue" nuclei (because they showed up in the blue filters), and very similar emission lines species to Seyfert galaxies, but more intense. The quasars and Seyfert were immediately suspected to have some kind of relationship. After 20 years, the first images of the host galaxies of

quasars were obtained, proving their similarities with Seyfert galaxies (BOROSON; OKE, 1982).

Over the years, several works (ZEL'DOVICH; NOVIKOV, 1965; SALPETER, 1964; LYNDEN-BELL, 1969) recognized that the phenomenon of describing a large amount of energy coming from the very center of these galaxies is the accretion of matter onto a supermassive black hole (SMBH). Galaxies in which that process is at work are known to host an Active Galactic Nucleus (AGN). The AGN consists of the central SMBH of the host galaxy in an active phase that is accreting matter. In this scenario, the surrounding matter, heated by its viscosity, emits radiation, which explains the observed luminosity in the nuclei of the AGN.

The AGN phenomenon is nowadays believed to be part of the evolution of a galaxy, and the nuclear active phase can be intermittent in their life. The first direct observational evidence for an AGN was provided by recent observations of the SMBH shadow in the M87 galaxy (THE EVENT HORIZON TELESCOPE COLLABORATION, 2019). Moreover, another observation proved that a supermassive black hole inhabits even regular galaxies such as our galaxy, the Milky Way. In the latter case, the black hole has very low activity, making our Galaxy not display AGN activity (EVENT HORIZON TELESCOPE COLLABORATION et al., 2022; YUSEF-ZADEH et al., 2025).

1.2 AGN phenomenology

An active nucleus contains an accretion disk that can be geometrically thin and optically thick with a temperature range of $10^4 - 10^6$ K. Matter accreting onto the black hole loses angular momentum and, due to the gravitational attraction of the supermassive black hole, is drawn towards it. During this process, the energy of the infalling matter is converted into kinetic energy. As the material accelerates, it experiences intense shear between fluid elements, which increases the temperature of the accreting gas. This increased thermal energy is subsequently converted into radiative energy, under the Eddington limit[1]. In the inner part of the disk, turbulence is driven by magnetic instabilities, likely channeling matter in a wind or even in a relativistic jet along the dominant "rotation axis". (BARGER, 2004).

The accretion disk exhibits a temperature gradient, which can be categorized into

[1]The Eddington Limit is the maximum luminosity that a massive object can have in order to remain in hydrostatic equilibrium. If the system goes beyond this limit, the radiation pressure will become greater than the gravitational force, resulting in the loss of mass from the object.

two distinct regions: external and internal. The continuum emission is the integrated energy output in frequency space and is typically modeled as a modified blackbody due to the sum of individual contributions from rings at different temperatures (SHAKURA; SUNYAEV, 1973; CZERNY; ELVIS, 1987). This emission, represented as the Spectral Energy Distribution (SED) shown in Figure 1.1, spans a wide wavelength range, from X-rays to the near-infrared (NIR), with the accretion disk emission dominating throughout (KORATKAR; BLAES, 1999).

Near the accretion disk is located the free-electron corona. This is an ionized region, where free electrons are accelerated by strong magnetic fields and gravitational forces, with high-temperature $T \sim 10^9$ K (NAKAMURA; OSAKI, 1993). In AGN, the hot corona is optically thin and strongly coupled to the disk through magnetic fields, with both structures accreted onto the central black hole. The region is time-dependent, where the spatial distribution of relativistic electrons and their emitted radiation changes in response to variations in the accretion process (NAKAMURA; OSAKI, 1993). The corona plays a key role in X-ray emission by upscattering low-energy photons from the disk through inverse Compton scattering, producing high-energy X-rays (HAARDT; MARASCHI, 1991). A fraction of the disk's radiation is reprocessed by the corona, with the reprocessed photons either returning to the disk or being emitted freely (FABIAN; ROSS, 2010). The emission from the hot-electron corona is represented in Figure 1.1 in cyan. The green dotted line in Figure 1.1 shows the reflected radiation, which is caused by corona emission that is reflected by the material around the nucleus (NETZER, 2011). The soft X-ray excess component (ARNAUD et al., 1985) is shown in Figure 1.1 in purple. This component is modeled as a warm corona (1 keV) and can affect the line production in the BLR (FABIAN et al., 1986). It is present in AGN spectra and is particularly strong in narrow-line Seyfert 1 galaxies (discussed in the Section 1.8) (FABIAN et al., 2004). This set of features describes the central source, which is known as the Standard Model of AGN (NETZER, 2015).

Figure 1.1 - Spectral Energy Distribution of an AGN.

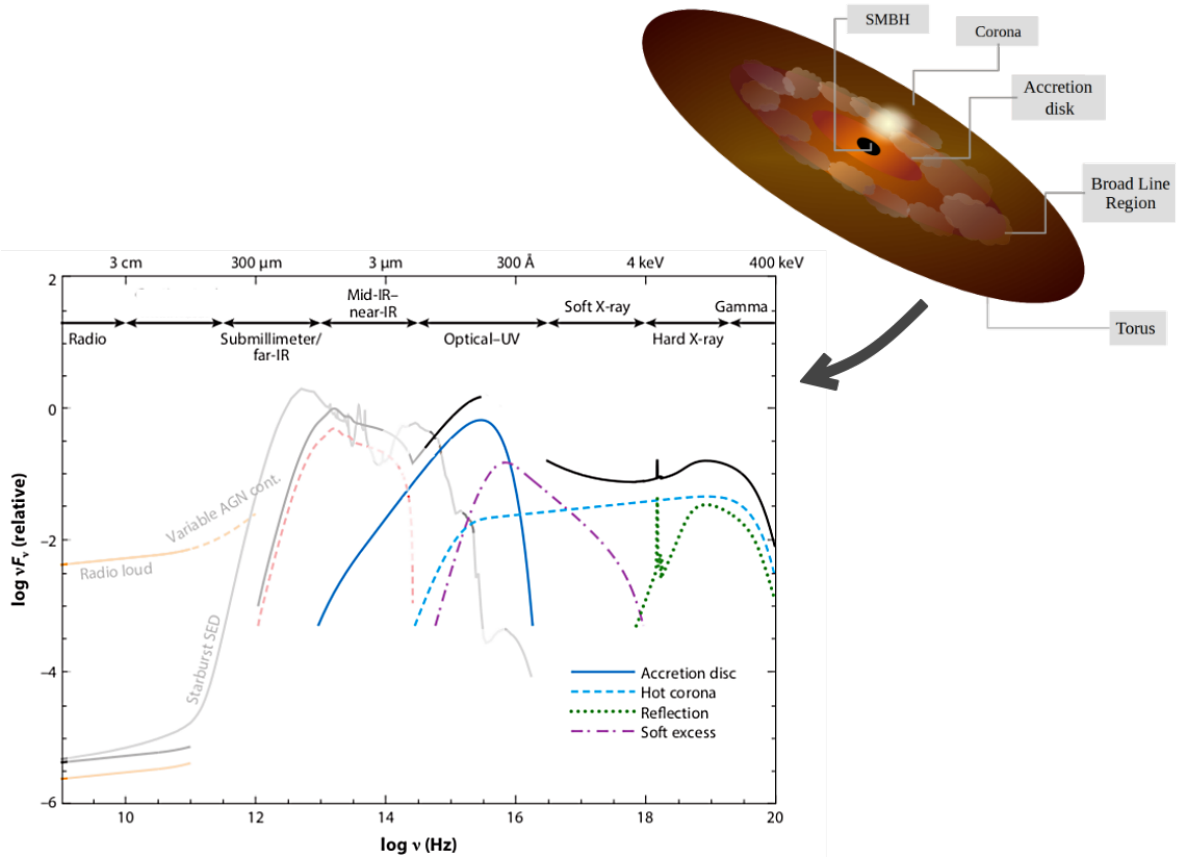

Upper right: An 2D artistic impression of the scenario for the central source is given by the SMBH in the center, with the accretion an accretion disk surrounding it. Near the surface of the disk is the broad line region. Bottom left: SED of the previously explained scenario. The accretion disk emission is represented with a blue solid line, and the scatter emission from circumnuclear material due to the Compton reflection is in a dot green curve. The hot corona emission is in a blue dashed line and the soft X-ray excess component due to the warm corona is represented with purple. The sum of all emissions is represented by a black solid line.

SOURCE: Modified from Hickox and Alexander (2018).

1.3 Type I AGN and the unified model

AGN emission covers a wide range of energies of the electromagnetic spectrum, from gamma-ray to radio (YANG et al., 2020). From the optical spectrum, we can distinguish between AGN of Type I and Type II (HICKOX; ALEXANDER, 2018). Type I

systems exhibit a strong optical continuum from the accretion disk as well as emission lines (broad permitted and semi-permitted, and narrow forbidden lines). The broad and forbidden emission lines have different widths because they originate from different regions. Meanwhile, Type II AGN show an optical continuum that includes the contribution of the host galaxy and spectra dominated by narrow emission lines (CAPETTI et al., 1996). An example of both spectra is shown in Figure 1.2.

The difference between Type I and Type II AGN is explained by the Unified Model, which proposes that these two classes are essentially the same but viewed from different angles. Many of the characteristics typically associated with Type I AGN, such as broad emission lines and a strong UV-optical continuum, can also be observed in polarized light in Type II AGN (ANTONUCCI, 1993). The polarization is caused by dust grains scattering the emission from the central engine into the observer's line of sight. A key structure in this model is the torus, a doughnut-shaped region of gas and dust that surrounds the central engine. The torus obscures the central engine from the observer at certain viewing angles. Thus, the relative orientation of the observer with respect to the central source and its torus determines whether the AGN is classified as Type I or Type II in the optical spectrum.

The Unified Model scenario is illustrated in Figure 1.2, showing the inner parsecs of the central engine composed of the SMBH, hot corona, and accretion disk. Still, on a sub-parsec scale, there is the Broad Line Region (BLR), which is ionized from the AGN radiation, producing permitted and semi-permitted emission lines. The BLR and its emission are central to this thesis and will be discussed in detail in the next section. The dusty torus is located next to BLR and has an opening angle that contributes to collimating the radiation in an "ionization cone". An external region of the AGN is located in the Narrow Line Region (NLR), with lower density $\sim 10^2 - 10^5\,\mathrm{cm}^{-3}$ responsible for emitting narrow forbidden lines characterized by the Full-Width-at-Half Maximum (FWHM) of $300 - 800\,\mathrm{km\ s}^{-1}$ (HICKOX; ALEXANDER, 2018). The gas is photoionized from the central source producing emission lines such as [OIII]λ5007, [NII]λ6585, [SII]λ6731. Furthermore, forbidden, high ionization emission lines are observed (χ >100 eV), named coronal lines (CLs), e.g, [FeVII]λ6087 and [SiVI]λ19630 (PRIETO et al., 2021).

Figure 1.2 - Scheme of the AGN unification model.

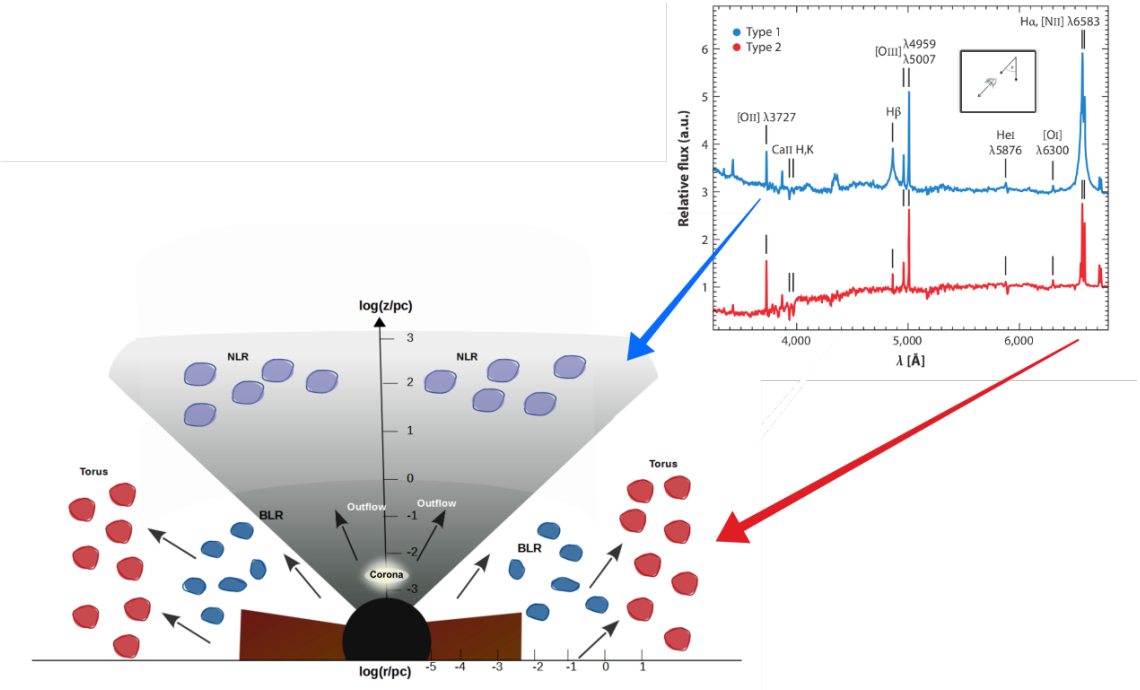

Examples of a Type I (unobscured nucleus) and a Type II (obscured nucleus), respectively in blue and red. shows broad permitted lines and narrow permitted and forbidden lines on top of a blue continuum emission, while in Type II only narrow components are observed. In these sources, the continuum emission is dominated by the stellar component of the host galaxy.

SOURCE: Modified from DiPompeo et al. (2018) and Hickox and Alexander (2018).

1.4 The Broad Line Region

The broad emission line width in active galaxies is primarily explained by the dynamical motion of the emitting material around the black hole. This led to the formulation of the BLR cloud concept in the 1970s (NETZER, 1977)). Initially, the cloud distribution was assumed to be spherical due to the unknown cloud geometry. Currently, it is widely accepted that BLR clouds are part of continuous or clumpy winds related to the equatorial plane of the accretion disk (D'ONOFRIO et al., 2012). The exact geometry remains uncertain, but long-term observation campaigns employing reverberation mapping techniques, particularly on the Hβ line, have enabled to unveil of very important parameters related to this emission region (PETERSON, 1993; KASPI et al., 2000; LIRA et al., 2018; JIANG et al., 2016).

Based on estimations of reverberation mapping (RM), the radius of the BLR is found to be located between light-days and light-weeks (10^{16}–10^{17} cm) from the SMBH (KASPI et al., 2000). The Emission Clouds (EC) within the BLR are ionized by radiation from the surface of the accretion disk (CZERNY et al., 2014). Due to its proximity to the central source, the gravitational potential of the SMBH hole directly affects the gas movement, as seen in the width and shift of the emission lines (POPOVIĆ, 2020), represented in Figure 1.3. The EC has different distances from the black hole, resulting in different orbital velocities. In Figure 1.3, the green color shows a non-virialized region where clouds with higher velocities are located closer to the SMBH. The light green and red colors show a virilized region where clouds with lower velocities are farther away from the SMBH. The high-velocity gas component contributes to the wings, while the external gas contributes to the central part of the line profile. The distance from the black hole ($R_{\rm BLR}$) influences the FWHM of the line, showing how the random and rotational gas movement depends on the SMBHs gravitational potential. Once emitted near the SMBH, the line profile is subject to strong gravitational redshift, which causes a red asymmetry in the observed emission. This effect, illustrated in the figure, shows how the gravitational redshift alters the profile of the line, particularly near the SMBH region, leading to the observed red asymmetry (POPOVIC et al., 1995).

The BLR emission lines can be divided into two distinct types: Low Ionization Lines (LILs) and High Ionization Lines (HILs). The first group includes ions with an ionization potential (IP) up to 50 eV, such as He II, He I, and C IV, which are emitted from the inner, higher-density region, where the cloud movement is not virialized and is closer to the disk. For this reason, HILs exhibit strong inflow/outflow signatures, as indicated by the asymmetry in their line profiles. In contrast, the LILs, which have an IP < 20 eV, such as Hβ, MgII, FeII, O I, and Ca II, are emitted in an external, lower-density, and virialized region. Because their emission location is far from the black hole than the HILs, in general, LILs do not exhibit features of asymmetries in their emission line profiles. Several works (KASPI et al., 2000; KUEHN et al., 2008; BARTH et al., 2013) using RM have found different time delays for HIL and LIL, suggesting that they are emitted at different distances from the SMBH. These BLR distance estimations, in combination with the width of the broad spectral lines, allow us to derive the SMBH mass. Given that in the vicinity of the SMBH, the BLR motion is described as a virialized system, the rotational gas velocity v_{gas} is

Figure 1.3 - Gravitational influence of SMBH on the BLR line profile.

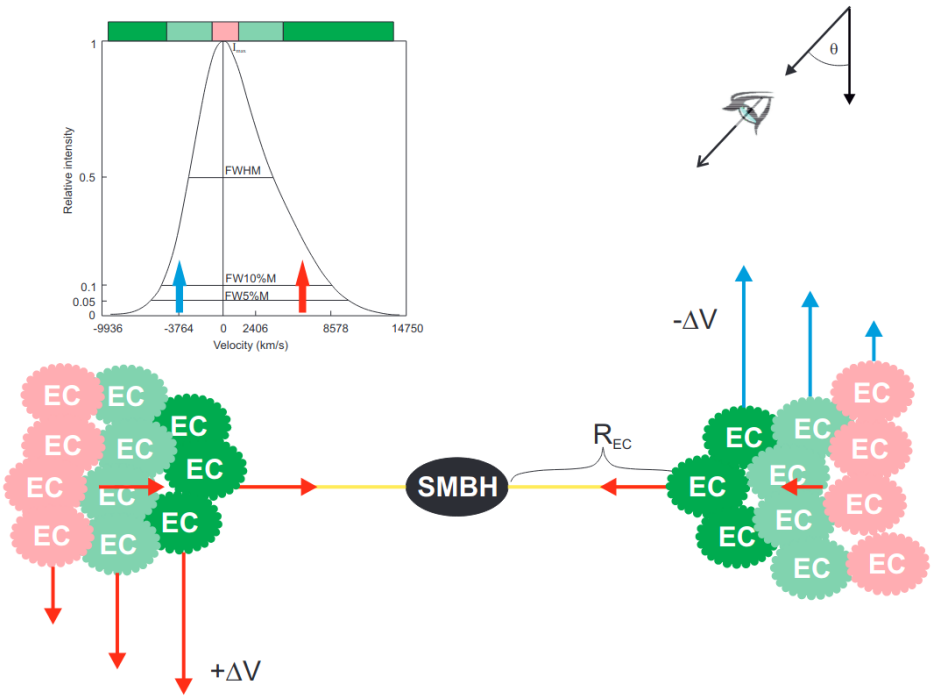

Cartoon depicting the BLR gas motion around the SMBH and the expected effects in the broad-line profile (upper left panel) are shown. In red, regression, and blue approximation, the rotation movement is represented by arrows. The top panel shows a red asymmetrical profile when the line is emitted from a very close region to the BH. The horizontal red arrows represent the direction of gas movement toward the central SMBH.

SOURCE: Popović (2020).

connected to the SMBH mass M• through the relation 1.1:

$$v_{gas}^2 = \frac{\mathrm{G}\, M\bullet}{R_{\mathrm{BLR}}}, \tag{1.1}$$

where R_{BLR} is the BLR radius and G is the gravitational constant. It is important to mention that R_{BLR} is measured concerning one specific emission line, i.e., it is the distance from the central source to a particular line-emitting region in the BLR. This is different from the total size of the BLR. Assuming a virial factor f, which includes all unknown information of the BLR such as geometry and inclination, we can obtain the virial relation of the black hole mass, and the BLR is expressed by the Equation 1.2 (COLLIN et al., 2006),

$$M\bullet \propto \frac{f\, v_{gas}^2\, R_{\mathrm{BLR}}}{\mathrm{G}}. \tag{1.2}$$

The relation between the gas velocity ($v_{\rm gas}$) and the observed velocity along the Line-Of-Sight (LOS) ($v_{\rm obs}$) is expressed by:

$$FWHM \sim v_{\rm obs} \sim v_{\rm gas} \cos\theta, \tag{1.3}$$

where θ is the angle between the rotation axis of the gas and the observer's line of sight (LOS). The observed velocity is the component of the gas's velocity projected along the LOS, which depends on the inclination angle θ of the gas's motion relative to the observer. As the angle θ increases (meaning the motion becomes less aligned with the line of sight), the observed velocity decreases. This projection leads to the observed broadening of emission lines, which is connected to the gas's true motion.

In a virialized system, we can assume that the FWHM is equivalent to v_{obs} because it corresponds to the rotational velocity of the gas surrounding the SMBH. Replacing the Equation 1.3 to 1.2 the BH mass is finally estimated as 1.4,

$$M\bullet = \frac{f\, FWHM^2\, R_{\rm BLR}}{\rm G}. \tag{1.4}$$

From the virial Equation 1.4, we can determine $M\bullet$, once we have the FWHM and the $R_{\rm BLR}$, assuming a value for the f-factor. These last two parameters can be determined by RM (BLANDFORD; MCKEE, 1982; BOCHKAREV; GASKELL, 2009; PETERSON, 2004; BENTZ et al., 2009), and the radius-luminosity relation ($R_{\rm BLR}$−L) (KORATKAR; GASKELL, 1991; LAOR, 1998; KASPI et al., 2005; GRIER et al., 2017; DU; WANG, 2019).

The compact nature of the BLR does not allow it to be spatially resolved (STURM et al., 2018). Consequently, the study of the region relies mainly on spectral analysis: single-epoch spectra and variability studies such as RM campaigns. Reverberation studies have suggested that the BLR has a Keplerian cloud motion component, a complex component associated with spiral arms structures in the Keplerian BLR disk, and turbulent movements such as inflow, and outflow (SHAPOVALOVA et al., 2008; SHAPOVALOVA et al., 2010; GRIER et al., 2013).

The single-epoch spectrum technique is simpler and less costly in telescope time than RM, and by measuring the emission line properties, it is possible to obtain information about the gas emitting location, kinematics, and SMBH mass. From a theoretical perspective, photoionization simulations are used to study BLR physical conditions such as intensity of the ionizing radiation, gas density, and metallicity (PANDA et al., 2018; PANDA et al., 2020). In addition, simulations are a useful

approach to analyze the predictions of the BLR formation and dynamics (CZERNY; HRYNIEWICZ, 2011; NADDAF et al., 2021). In this work, we use the single-epoch technique and the theoretical approach to infer about the low ionization gas in the BLR.

The broad emission line profiles can be represented by single or multiple profiles, for example, the Gaussian profile represents very well broad components with widths above 4000 km s^{-1}, as well as outflow or inflow components. AGN with broad lines with FWHM below 2000 km s^{-1}, such as the Narrow Lines Seyferts-1 (see 1.8 Section) usually have their line profiles better modeled by Lorentzian profiles than Gaussian profiles (SULENTIC et al., 2011). In addition, a small fraction of AGN present double-peak profiles, which are generally associated with a Keplerian gas disk. From the properties of the emission lines, we can also infer the internal and external BLR radius. The external radius is delimited by the dust sublimation temperature (1500 K for graphite, 2000 K for carbonates) (BARVAINIS, 1987; SALPETER, 1977; NENKOVA et al., 2008), where an efficient delimiter of the BLR external region are the LILs, in special the FeII (PANDA et al., 2019; CZERNY et al., 2019).

1.5 An introduction to photoionization modeling used to BLR studies

In an AGN, the central continuum source is responsible for photoionizing the BLR gas. The photon with an energy equal to or larger than the ionization potential of an atom or an ion is absorbed by it, producing a free electron. For example, ionized hydrogen requires 13.6 eV (RYBICKI; LIGHTMAN, 2024). Then, a free electron recombines with an ion, producing a downward cascade to lower energy levels of the atom or ion. This process produces emission lines when the electron descends to lower energy levels. The excitation process occurs when an electron bound to an ion or atom is excited to a higher energy level. This excitation can occur via the absorption of a photon or by a collision with a free electron. If the electron in the excited state cascade down spontaneously, an emission line is produced after every jump downwards (PRADHAN; NAHAR, 2011). Under thermodynamic equilibrium conditions, the ionization balance (or equilibrium) equation implies that the number of photoionization is the same as the recombination (RYBICKI; LIGHTMAN, 2024). Considering a hydrogen cloud surrounding an isotropic emitter, energy (hv), and a cross-section of the medium being ionized (σ_v), the number of photoionizations per unit volume and per unit time is given by 1.5:

$$4\,\pi\,n_{\mathrm{H}^0}\int_{v_0}^{\infty}\frac{\sigma_v\,J_v}{\mathrm{h}\,v}\;=\;n_e\,n_p\,\sigma_v(H^0\,T)\;[cm^{-3}\,s^{-1}] \tag{1.5}$$

where n_{H^0} [cm^{-3}] is the number of the total particle density − number per volume of neutral atoms, and J_v is the mean intensity of the incident radiation field per unit solid angle. The quantity $n_e n_p \sigma_v(H^0 T)$ is the recombination coefficient, which depends on an $\mathrm{n}\,L$ [2] state and the Maxwell-Boltzmann distribution function for electrons. Ionizing photons eject electrons from hydrogen and other elements, while radiative recombination returns the atoms to lower stages of ionization, leading to a photoionization equilibrium. The photoionization equilibrium is governed by the intensity and the spectral energy distribution of the ionizing radiation and the density of the gas.

The electrons add thermal energy to the gas, while many processes convert this energy to line and continuum emissions that carry out the energy and cool the gas. These processes include radiative recombination, bremsstrahlung, and collisional excitation of bound levels by electron impact. The balance of heating and cooling leads to an equilibrium temperature, typically around 10,000 K (OSTERBROCK; FERLAND, 2006). Still, considering a pure hydrogen cloud with no radiation losses, the thermal equilibrium assumes that the input energy by photoionization (G) is equal to the energy lost by recombination (L_{R}),

$$G(H) \;=\; L_R(H). \tag{1.6}$$

$G(H)$ and $L_{\mathrm{R}}(H)$, depend on recombination coefficients for the intensity of the radiation field and kinetically averaged recombination. Thermal equilibrium assumes that the atomic/ionic populations are given by Boltzmann's distribution, the radiation field is of a blackbody, and that all collisional processes occur at the same temperature. From the eq. 1.5, the radiative transfer equation $v \to v_0$ can be written as,

$$\frac{dI_v}{ds} \;=\; -\,n_{\mathrm{H}^0}\,\sigma_v\,I_v + j_v \tag{1.7}$$

where I_v is the specific intensity and J_v is the local emission coefficient [$\mathrm{erg\,cm^{-3}\,s^{-1}\,str^{-1}}$] for ionizing radiation.

The BLR sizes could only be estimated from photoionization arguments (DIBAI et al., 1967). The luminosity in a line depends on the volume of the emitting region and the emissivity. The integrated luminosity emitted by the central source for $4\,\pi$ sr, in a specific flux F_v is given by,

$$L \;=\; 4\,\pi\,R^2_{BLR} \int_{v1}^{v2} \pi\,F_v\,d_v\,[\,\mathrm{erg\,s^{-1}}]. \tag{1.8}$$

[2] here $\mathrm{n} = 2$, principal quantum number and L, angular momentum quantum number

The ionization equilibrium is driven by the intensity and ionizing incident radiation field and the density of the gas. An important quantity is the ionization parameter U, which expresses the ratio of the hydrogen ionizing photon density to the total hydrogen density. Thus, higher U gives a higher degree of ionization (D'ONOFRIO et al., 2012). The dimensionless parameter U is denoted by,

$$U = \frac{\Phi(H)}{n_{\rm H}\, c} = \frac{Q_{\rm H}}{4\,\pi\, r^2\, n_{\rm H}\, c} \tag{1.9}$$

where r [cm] is the separation between the center of the source of ionizing radiation and the illuminated face of the cloud, $n_{\rm H}$ is the hydrogen density, c is the speed of light, $Q_{\rm H}$ is the number of hydrogen-ionizing photons emitted by the central object, and $\Phi\,({\rm H})\,[{\rm cm^{-2}\,s^{-1}}]$ is the surface flux of ionizing photons.

Then, the primary information to constrain the emitting region of these lines is given by their distance from the ionizing source, the radius of the BLR ($R_{\rm BLR}$) in this case. The BLR radius can be inferred using the photoionization theory (PANDA, 2021a),

$$R_{BLR} = \sqrt{\frac{Q(H)}{4\,\pi\, h\upsilon\, n_{\rm H}\, c}} = \sqrt{\frac{L_{bol}}{4\,\pi\, {\rm h}\upsilon\, n_{\rm H}\, c}}\ \ [cm], \tag{1.10}$$

where $L_{\rm bol}$ is the bolometric luminosity. It is important to note that ${\rm h}\upsilon = 1$ Rydberg here − for photoionization of hydrogen and hydrogen-like species. The transition probability is computed from a transition matrix element that, in turn, depends on the wave functions of the initial and final states, and an operator corresponding to the appropriate moment of the radiation field. In addition, radiative transitions are governed by the symmetries of the atomic states involved, as specified by the quantized angular and spin momenta of the initial and final states. The main equations thermal equilibrium 1.6, equation of transfer for radiation 1.7, ionization parameter 1.9, and ionization equilibrium Equation 1.5, summarize the photoionization modeling.

Photoionization modeling allows us to evaluate the physical conditions required to produce a given emission line spectrum (JOLY, 1991; FERLAND et al., 1998; FERLAND et al., 2017; PANDA; SANTOS, 2021). The output of the modelling is obtained after specifying the external radiation field striking a cloud (with a shape and intensity), the chemical composition and grain content of the gas, and the geometry of the gas. These points are essential to the understanding of the physical conditions of the gas that is responsible for the emission of the spectral lines. In our case, the BLR.

1.6 FeII emission: optical and NIR

The first identification of the FeII lines was made by Wampler et al. (1967). Over the years, observational and theoretical aspects concerning the FeII emission were addressed in the literature (COLLIN-SOUFFRIN et al., 1986; JOLY, 1987; JOLY, 1991; NETZER; WILLS, 1983). The FeII emission is ubiquitous because it has more than 10,000 energy levels and approximately one million radiative transitions (D'ONOFRIO et al., 2012). Due to the blending of hundreds of thousands of multiplets, the entire range from UV to NIR appears as a continuum in the spectrum. These numerous emissions from the FeII ion are responsible for carrying out 25% of the total BLR energy output. This makes FeII an important coolant of BLR gas (WILL et al., 1985).

Historically, most studies on FeII are concentrated in the optical region between $4400-5200$Å, where a series of blended multiplets are located. In particular, the emission from the same transition (m37 and m38) compose the so-called 4570 Å FeII bump, which is used to classify an AGN in terms of FeII strength (OSTERBROCK, 1977; BOROSON; GREEN, 1992). It is defined as $R_{4570} \approx \mathrm{F(FeII}\ \lambda 4570\,\text{Å})/\mathrm{F\,(H}\beta)$ and is gauged by computing the ratio of the integrated FeII intensity/flux between $4434-4684$Å to the flux of the broad component of the Hβ[3] defined as $R_{4570} \approx \mathrm{F(FeII}\ \lambda 4570\,\text{Å})/\mathrm{F\,(H}\beta)$. It is estimated that 5% of the AGN have $R_{4570} > 1$, and only 0.5% present extreme FeII emission ($R_{4570} > 2$), which implies that majority of AGN have low FeII emission ($R_{4570} < 1$) (BERGERON; KUNTH, 1984; LAWRENCE; SAUNDERS, 1988; RAKSHIT et al., 2017).

Several studies have explored the photoionization modeling framework to compute the FeII spectrum across the UV-NIR range. These studies have explored excitation processes such as self-fluorescence, collisional fluorescence, and continuum fluorescence, into optical models to explain the observed FeII emission features in AGN (WILL et al., 1985; JOLY, 1993). Self-fluorescence occurs when FeII atoms are excited by radiation from nearby atoms, and they return to a lower energy state by emitting radiation at the same wavelength. Collisional fluorescence occurs when energetic particles, such as electrons, collide with FeII atoms, exciting them to higher energy states. The atoms then emit radiation as they return to a lower energy state (COLLIN-SOUFFRIN et al., 1980). Continuum fluorescence is driven by ionizing radiation from the accretion disk or corona, exciting FeII atoms, and causing them to emit radiation as they return to lower energy levels (WILL et al., 1985; JOLY,

[3]The FeII intensity also can be determined through the EW ratio as $\mathrm{EW(FeII}\ \lambda 4570\,\text{Å})/\mathrm{EW\,(H}\beta)$

1991; JOLY, 1993).

Figure 1.4 - Highly simplified Grotrian diagram for FeII.

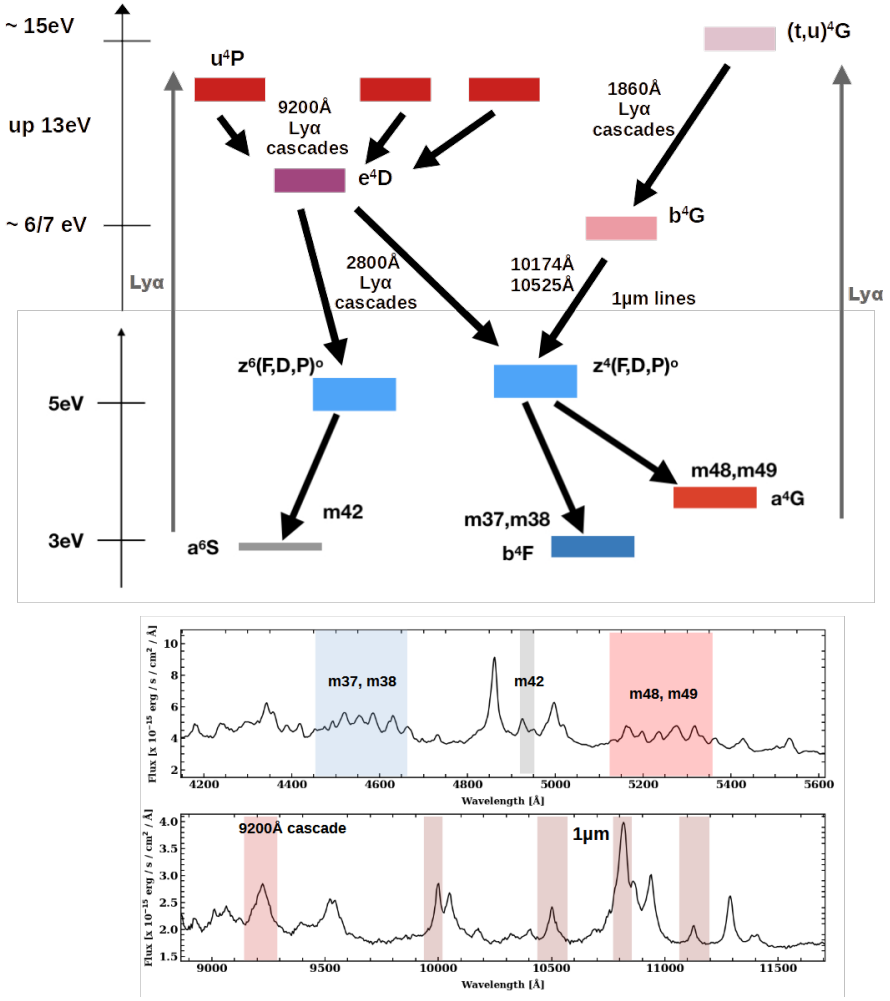

Upper panel: Highly simplified Grotrian diagram representation for the transitions of Fe II in NIR and UV. Lower panel: 1 Zw I Optical and NIR spectrum, with the emissions illustrating the emissions of the diagram. Where highlight colors are the important emissions in the optical and NIR context. Optical shows the blue FeII bump of 4570Å and the red is the 5200Å bump and the FeII satellite emission to [OIII]λ5007. The NIR spectrum shows the 9200Å bump and the four 1-micron lines.

SOURCE: Modified from Marinello et al. (2020a), Rodríguez-Ardila et al. (2002), and Marziani et al. (2021).

In the NIR advances were made (SIGUT; PRADHAN, 1998; SIGUT; PRADHAN, 2003) including the Lyα fluorescence (see Grotrian diagram 1.4) to explain the FeII emission at 8500−9500Å. Only this mechanism could excite energy levels up to

13 eV, and it was proved observationally by Rodríguez-Ardila et al. (2002).

Due to the complexity of the FeII ion, Figure 1.4 presents a simplified Grotrian diagram showing only transitions of interest in this thesis. The Lyman-α fluorescence process promotes the emission of FeII lines at 1 μ m, and is exclusively responsible for the 9200Å bump (SIGUT; PRADHAN, 1998; SIGUT; PRADHAN, 2003; RODRÍGUEZ-ARDILA et al., 2002). The Lyα fluorescence promotes energy levels populations up to $\sim$ 15 eV as the (t, u)^{4}G, where the first decay to b^{4}G level ($\sim$ 6 eV) is responsible to emit UV photons corresponding to transitions around 1860Å. After this, a second decay occurs from the (t, u)^{4}G level, which emits 1 μ m FeII lines (see Figure 1.4). These lines are the strongest NIR lines λ9997, λ10502, λ10863 and λ11127, collectively known as the Fe II 1μm lines (RUDY et al., 2000). Their strength is measured by the ratio of the integrated fluxes of 1μm lines summed, by Paβ broad component ($R_{1\mu\,\mathrm{m}}$) (MARINELLO et al., 2016b). After decay and consequently emission of 1-micron lines, the z^4(D, F) level is populated. This level is responsible for the optical emission of the 4570Å bump. However, the diagram in Figure 1.4 (on the left) shows how the emission occurs at 9200Å. Absorption of a Lyα photon by an FeII ion can excite it to energy levels up to 13 eV, where, in time, occurs the primary cascade – (u^4(P, D)$\rightarrow$e^{4}D and v^{4}F $\rightarrow$ e^{4}D) – emitting the 9200Å bump. Eventually, a second cascade occurs – e^{4}D $\rightarrow$ z^4(D, F) – emitting 2800Å lines, populating the energy level of z^4(D, F), responsible for optical FeII.

Moreover, the FeII emission is strongly connected to the quasars' phenomenology, where Boroson and Green (1992) showed that the emission is related to intrinsic AGN properties by relating the FeII strength to other emission line properties. They calculated the FeII content in an AGN through an empirical template and by applying a mathematical technique called Principal Component Analysis (PCA), they found that the FeII is anti-correlated with the [OIII]λ5007 intensity and the FWHM of Hβ. Another important aspect of FeII emission is its connection to a subclass of AGN known as Narrow Line Seyfert-1 (NLSy1) galaxies (see Section 1.8). These objects often exhibit stronger FeII emission compared to the majority of AGN, although the physical mechanisms behind this enhanced emission are still not fully understood. (ZHOU; WANG, 2004; MAO et al., 2010; PANDA et al., 2019) Above all, there are still other basic questions about FeII gas, such as its nature, the precise location in the BLR where it is emitted, and its kinematics, which are yet to be solved in its entirety.

1.6.1 Proxies for low ionization gas studies in AGN: correlation between FeII, CaT, and O I emissions

The study of low-ionization gas in AGN is essential for understanding the physical conditions within the BLR. Emissions from FeII, Ca II at $\lambda\lambda\lambda$8498, 8542, and 8662 and O I λ8446 offer valuable insights into the properties of this gas, with each emission line arising from regions with specific ionization states and densities (PANDA, 2021d; MARTÍNEZ-ALDAMA et al., 2021a). Although these lines originate from different ionization conditions, their correlation and interplay can reveal a more unified picture of the low-ionization gas in AGN (MARTÍNEZ-ALDAMA et al., 2015).

The O I atoms are not exposed to the ionization radiation directly. Because of that the primary mechanism to produce the O I emission is Lyβ fluorescence. For the Lyβ fluorescence mechanism to operate efficiently, a sufficient amount of neutral hydrogen must be present within the emitting region. This availability directly influences the strength of the O I emission observed in the spectrum. In addition, a high optical depth of the emitting region for the O I line (t$\sim$$10^3$$-$$10^4$), enables Ly$\beta$ photons to be recycled multiple times within the gas, further enhancing their absorption by O I atoms and boosting the fluorescence emission (PERSSON; MCGREGOR, 1985).

Similarly, the FeII emission lines are produced in dense, partially ionized regions, while the CaT lines, typically observed in the infrared, are associated with even more neutral and denser regions (PERSSON; MCGREGOR, 1985). The differences in ionization between these lines provide valuable clues about the physical conditions within the low ionization gas in the BLR (PANDA et al., 2019; PANDA, 2021d; PANDA, 2021b). FeII emissions are linked to regions where the material is dense but not fully neutral, while CaT lines arise from regions that are even more shielded from radiation, making it harder for photons to escape (PERSSON; MCGREGOR, 1985). This makes CaT lines a crucial indicator of extremely dense and neutral material, which is harder to ionize compared to the regions emitting FeII and O I lines (JOLY, 1981; JOLY, 1989).

The relationship between FeII, CaT, and O I emissions can be understood through their shared characteristics and their distinct ionization conditions. Persson and McGregor (1985) observed a correlation between the linewidths of CaT and O I, suggesting that the regions emitting these lines share similar kinematics. This observation was later extended by Persson (1988), who showed a correlation between the emission lines of CaT and O I in AGN with strong FeII emissions. These AGN exhibited prominent CaT and OI features in their spectra, which led to further in-

vestigations into the potential of using these simpler ions as proxies for studying FeII gas (RODRÍGUEZ-ARDILA et al., 2002; MARTÍNEZ-ALDAMA et al., 2015; PANDA, 2021d; MARTÍNEZ-ALDAMA et al., 2021b). This approach may simplify spectral analysis and theoretical modeling.

Observational studies of FeII, CaT, and O I emissions have revealed that these ions exhibit similar FWHM values (JOLY, 1991; RODRÍGUEZ-ARDILA et al., 2002; MARINELLO et al., 2016b; MARTÍNEZ-ALDAMA et al., 2021b), suggesting that they share comparable kinematics and probably originate from the same spatial region. Recent works have reinforced the correlation between NIR FeII emission and CaT (MARINELLO et al., 2016b; MARINELLO et al., 2020a), reinforcing the idea of using these less complex ions as proxies for exploring the nature and location of FeII emission gas in the NIR.

Theoretical photoionization models (JOLY, 1987; MARTÍNEZ-ALDAMA et al., 2015; PANDA et al., 2020) indicate that FeII, O I, and CaT ions are indeed emitted from regions with similar physical conditions, including hydrogen density ($n_{\rm H}$), ionization parameter (U), and column density ($N_{\rm H}$). Although earlier modeling studies have focused on physical properties inferred from UV−optical FeII emissions, emissions, in this work we offer a new perspective by incorporating a simultaneous optical and NIR approach, providing an underexplored analysis of the physical environment of these LILs.

Understanding the physical properties required to explain the observed CaT and O I spectrum can help explain the FeII puzzle and if the kinematics of these species are interrelated. All these issues are strongly connected, and their solution may hold the key to understanding the geometry and evolution of the BLR clouds.

1.7 Emission from the accretion disk and its relationship with the Broad-Line Region (BLR)

The emission lines observed in AGN are primarily powered by the accretion disk surrounding the SMBH. The accretion disk, formed by material falling towards the black hole, generates high temperatures and radiation due to intense gravitational and frictional forces, previous described in Section 1.2. Assuming the disk is Keplerian and optically thick, as is commonly assumed in the standard disk model, its emission closely resembles the Big Blue Bump (BBB) feature observed in AGN spectra (COLLIN; HURÉ, 2001). In this model, radiation primarily originates from the region known as the "laminar flow" or "skin" of the disk, located within the inner

radius up to $10\,R_{\rm G}$, where $R_{\rm G} = {\rm G}M/c^2$ is the gravitational radius of the BH with mass M (BLANDFORD et al., 1992), where it emits its highest energies in the form of X-rays and UV radiation (MALKAN; SARGENT, 1982). The optical emission is produced by regions located at a few $100\,R_{\rm G}$ (COLLIN-SOUFFRIN, 1991; COLLIN; HURÉ, 2001).

Once the disk starts to irradiate, strong winds rise from the surface (MURRAY; CHIANG, 1997; PROGA; KALLMAN, 2004). These winds may be optically thick in the radial direction, shielding the disk at larger radii from further irradiation (GALLAGHER; EVERETT, 2007). The extension of the irradiated disk is difficult to determine observationally, as it depends on the local wind outflow rate. The accretion disk becomes gravitationally unstable about a radius of $1000\,R_{\rm G}$, where the disk's local gravity dominates, and radiation pressure no longer dominates (MURRAY; CHIANG, 1997). At this point, the flaring disk is directly irradiated (LOSKA et al., 2004) and has Keplerian velocities. At this point, the standard disk model of Shakura and Sunyaev (1973) is not valid in the case of instability (COLLIN-SOUFFRIN, 1991; COLLIN-SOUFFRIN; DUMONT, 1990; HURÉ et al., 1994). Owing to the gravitational instability, the disk breaks into fragments, which, if they do not collapse (GOODMAN; TAN, 2004), could form the clouds responsible for the BLR, as they interact with the central UV-X continuum (LOSKA et al., 2004)

For broad-line clouds to capture sufficient ionizing radiation, the coverage factor of the continuum source must be greater than 0.1 (COLLIN, 2006). The most natural structure to explain this configuration is an accretion disk, which could be considered either warped or flaring (COLLIN-SOUFFRIN; LASOTA, 1988), where the photoionized broad-line clouds, particularly those emitting the Balmer lines, cannot lie directly along the line of sight to the central source, unless some degree of absorption occurs in the lines (HAMANN et al., 1997; LOSKA et al., 2004). These clouds are thought to be confined to a relatively flattened structure, with the observer viewing the system from a direction close to perpendicular to the cloud plane. It is believed that the gas is located near the equatorial plane of the system, close to the disk surface or even connected to it (MURRAY; CHIANG, 1997).

1.7.1 Double-Peaked profiles and accretion disk Line emission

One of the most intriguing features of some AGN is the presence of double-peaked emission lines, the most prominent examples are found in AGN such as Arp 102B, 3C 390.3, and 3C 332, all of which exhibit broad double-peaked Balmer lines (CHEN et al., 1989; CHEN; HALPERN, 1989). These emissions probably originate from

the photoionized surface of the accretion disk that surrounds the central black hole, between a few hundred and a few thousand gravitational radii from the SMBH (CHEN; HALPERN, 1989). These double peaks are thought to arise from the motion of gas in the accretion disk, where the gas is moving both toward and away from the observer. The profile is most pronounced when the disk inclination is between $\sim 20°$ and $\sim 37°$. This orientation enables the observer to distinguish the emission from the gas moving toward and away from the black hole (STORCHI-BERGMANN et al., 2017).

Models for the line profiles based on this scenario were developed by Chen et al. (1989) and later extended by other authors (ERACLEOUS et al., 1995). These models can fit the majority of observed profiles very well (ERACLEOUS; HALPERN, 1994). The remaining profiles can be fitted with more sophisticated models that invoke a perturbed accretion disk (STRATEVA et al., 2003; SCHIMOIA et al., 2012a; SCHIMOIA et al., 2017). The disk interpretation comes not only from the fact that it provides good fits to the line profiles, but also because it has a complete physical model (STORCHI-BERGMANN et al., 1995; LEWIS et al., 2010; DUMONT; COLLIN-SOUFFRIN, 1990a; DUMONT; COLLIN-SOUFFRIN, 1990b; ROKAKI et al., 1992) associated with it that explains all properties, and disfavors all alternatives involving black hole binary (BEGELMAN et al., 1980), bi-conical outflows (ZHENG et al., 1990; GOAD; WANDERS, 1996; MARZIANI et al., 1993), and reinforces the disk interpretation of double-peaked emitters (ERACLEOUS; HALPERN, 2003; ERACLEOUS et al., 2006; ERACLEOUS et al., 2009).

The emission is not common in all AGN because several conditions are needed to observe double-peaked lines, such as the viewing angle, disk geometry, and thickness of the emission ring (COLLIN-SOUFFRIN; DUMONT, 1990). Thus, it is important to note that a flat Keplerian disk will not necessarily give rise to double-peaked line profiles. In addition to these conditions, the ratio of the outer to inner radius of the line-emitting portion of the disk must be small, $\xi 2/\xi 1 < 100$ (COLLIN-SOUFFRIN; DUMONT, 1990). For larger values of this ratio, the two peaks get so close together that they blend, and the line profile appears single-peaked (JACKSON et al., 1991) (see illustration in Figure 1.5). The same effect can also be produced if the line of sight of the observer is close to the axis of the disk (MURRAY; CHIANG, 1997).

The other important aspect is the transfer of photons within the disk, because it can influence the amount of light emitted from different regions, resulting in changes in the emission line profiles (CHIANG; MURRAY, 1995; PROGA; KALLMAN, 2004).

Figure 1.5 - Example for disk with larger values of radius.

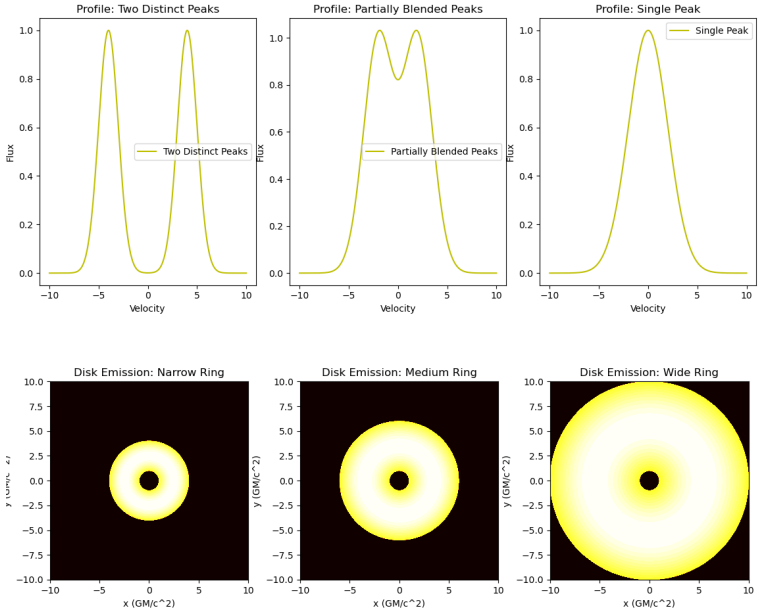

For larger values of radius, the two peaks get so close together that they blend, and the line profile appears single-peaked (JACKSON et al., 1991).

Chiang and Murray (1995) and Murray and Chiang (1997) studied how photons escape from a disk with outflowing atmosphere, and they found that the opacity of the disk depends on the speed of the gas in the atmosphere, which is seen differently depending on the observer's line of sight. This causes the disk emission to be uneven, with the regions where the gas is moving faster emitting less light. As a result, the outer parts of the line profile become weaker while the central part becomes stronger, turning a double-peaked line into a single-peaked one.

To account for double-peaked variability, it was necessary to develop sophisticated models to reproduce the line profiles, which were inspired by dynamical models for non-asymmetric and time-dependent disks (ERACLEOUS et al., 1995; STORCHI-BERGMANN et al., 1997). Some models include an elliptical disk, and others are not necessarily elliptical, but the model must have non-asymmetric perturbations, such as spiral arms (LEWIS et al., 2010; STRATEVA et al., 2003).

The study of double-peaked emitters provides valuable insights into the unification of AGN classes. These objects are often found in radio-loud AGN, even in LINERs (STORCHI-BERGMANN et al., 1997), but recent studies have shown that double-peaked lines can also occur in radio-quiet AGN (STRATEVA et al., 2003). This

suggests that the phenomenon of double-peaked emission lines is not restricted to one subclass of AGN, but may be a more general feature of the AGN population. Studying these objects is important for understanding the role of accretion disks, outflows, and the interaction between the black hole and the surrounding gas in shaping the observed spectra of AGN.

1.8 Narrow Line Seyfert 1 (NLSy1)

Narrow-line Seyfert 1 galaxies (NLSy1s) are AGN whose broad emission line components are narrower than usual for a classic Seyfert 1. They are defined through the optical spectrum: the broad permitted line Hβ hows FWHM $<$ 2000 km s^{-1}, and the ratio between the emission of [OIII]λ5007/Hβ $<$3 (OSTERBROCK; POGGE, 1985; KOMOSSA, 2007; OIO et al., 2019). Even some NLSy1 lines can exhibit broad Hβ components with widths similar to the values found for the NLR lines. However, the emission lines are truly associated with the BLR emission. (GOODRICH, 1989).

In a Quasars Main Sequence (QMS) context (MARZIANI et al., 2003; MARZIANI et al., 2018), the NLSy1s are distinguished by a low FWHM (Hβ) regime in Population A (SULENTIC et al., 2011). When we divide the QMS into bins based on R_{4570}, the FeII emission strength is spread across the bins, ranging from 0 to 2 (MARZIANI et al., 2018). However, within Population A, the majority of sources located in the bin where $R_{4570} > 1$ (corresponding to strong FeII emitters) are classified as NLSy1s (DONG et al., 2010a). This distribution explains the usual relationship between FeII emission strength and NLSy1s. In addition, NLSy1s super-strong FeII emitters (R_{4570} $>$2), such as PHL 1092 with R_{4570} = 2.58 (MARINELLO et al., 2016b), show extreme Eddington ratios and low BH masses $\sim 10^{6-8}$ M$\bullet$ (MATHUR et al., 2001; LAKIĆEVIĆ et al., 2018), and it seems that the lower FWHM increases with luminosity. Contrary to these extreme sources with a well-defined relationship between FeII emission and $L_{\rm bol}/L_{\rm Edd}$, for low FeII emitters the relationship becomes uncertain due to the difficulty in accurately measuring R_{4570} (D'ONOFRIO et al., 2012).

In general, NLSy1s have been studied in the optical and NIR, with a wide range of questions, such as the location of FeII emission using reverberation mapping (HU et al., 2015), black hole mass estimation (DURRÉ; MOULD, 2021), deviations from the radius luminosity relation (DU; WANG, 2019) and super-Eddington accreting massive black holes in AGN (DU et al., 2015). Besides recent studies suggest that NLSy1s may represent AGN in an early phase of evolution when the black hole is still growing (MATHUR, 2000; NEGRETE et al., 2018), many questions about

NLSy1s are open, such as: Is NLSy1s a progenitor to Pop A sources? Are these extreme conditions the reason we observe a strong FeII? What differs between extreme NLSy1s and low FeII NLSy1s? All approaches are needed to understand the phenomenology of these sources, including emission line properties measured from a wide spectral range (including the NIR for example), SED studies, and theoretical models. In particular, the FeII emission could help estimate the physics of the LIL emitting BLR, such as metal content and density.

Figure 1.6 - The optical plane of the Quasars Main Sequence.

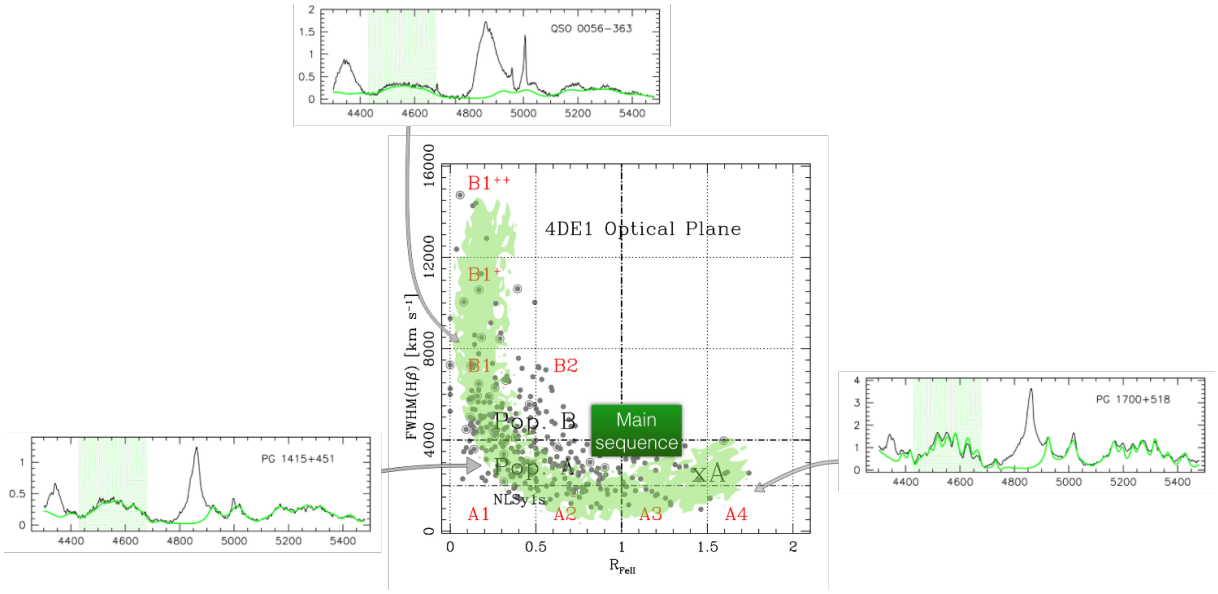

The distribution of data points in the optical plane of the Eigenvector 1 FWHM(Hβ) vs R_{Feii} (in our work named R_{4570}) traces the QMS. The thick horizontal dot-dashed line separates populations A and B, and the thin identifies the limit of NLSy1s. The vertical dot-dashed line marks the limit for extreme Population A (xA) sources of FeII emission. Dotted lines separate spectral types, subdividing into a grid of bins of FWHM(Hβ) and FeII emission strength. Bins A1, A2, A3, and A4 are defined in terms of increasing R_{FeII} with a bin size of $R_{FeII} = 0.5$, while bins B1, B1+, B1++, etc. are defined in terms of increasing FWHM(Hβ) = 4000 km s^{-1}. The three quasars spectra are exemplary of general trends involving LILs observed along the quasar main sequence, where the green line represents the FeII template.

SOURCE: Modified from Marziani et al. (2018).

1.8.1 Extreme NLSy1s

AGN located at the extreme of the optical plane (see Figure 1.6) are named "Extreme NLSy1s". Their spectra show widths of the broad component of Hβ below 1500 km s^{-1} or even smaller than 1000 km s^{-1}. They also present strong FeII emission ($R_{4570} > 1.5$). These extreme NLSy1s are involved in many subjects of study: (i) FeII emission (HU et al., 2015; MARINELLO et al., 2020a); (ii) extreme Pop A sources in the QMS (ŚNIEGOWSKA et al., 2018; MARINELLO et al., 2020a); (iii) low mass of BH and super-Eddington ratio (WANG et al., 2014; DU et al., 2015; JIN et al., 2017), (iv) study of the BLR gas kinematic in this extreme conditions through the analysis of parameters determined from fitting the line profiles as relative strength, width, and asymmetry (mainly related to outflows) (OIO et al., 2019); (v) x-ray variability (FABIAN et al., 2004), and SED (PANDA et al., 2019). Regarding spectral analysis, most studies published in the literature are focused on optical properties (PAUL et al., 2021). In the last years, Marinello et al. (2020a) added the NIR spectral region to study the extreme NLSy1s PHL 1092, with a focus on FeII emission. They acquired important information about the spectral properties and physical conditions of the BLR and analyzed it in the EV1 context.

Extreme NLSy1s that show exceptionally prominent FeII emission in their spectra are termed Zwicky 1-like objects (PAUL et al., 2021). Among the most notable extreme NLSy1s, in addition to I Zw 1, are 1H 0707-495, Mrk 1044, IRAS 03450+0055, PHL 1092, SDSSJ224028.85-010649.9, PG 1244+026, IRAS 07598+6508 and QSO RX J0439.6-5311 (RODRÍGUEZ-ARDILA; MAZZALAY, 2006; RIFFEL et al., 2006; MARINELLO et al., 2016b; MARINELLO et al., 2020a; PAUL et al., 2021; JIN et al., 2017).

In addition to the similarities between these I Zw 1-like sources, they are divided into "complex" and "simple" NLSy1s (GALLO, 2006a). The two NLS1 subtypes have a similar intrinsic optical/UV AGN continuum but are distinguished between "simple" and "complex" in the X-ray emission. The "complex" NLS1s show much weaker x-ray emissions between 2−10k eV. In addition, in the optical spectra, they may show intrinsically weak forbidden lines of [OIII]λ5007. Jin et al. (2017) suggests that "simple" NLS1s have low inclination angles, with a clear line of sight to the central source. However, the "complex" has a larger inclination angle and, so the disc wind material can block the line of sight of the observer to the central engine. As a result, there is an X-ray absorption in the continuum.

1.9 Ultra-fast Outflows (UFOs) and NLSy1s

Ultra-fast outflows (UFOs) in AGN have garnered significant attention due to their extreme speeds, which can exceed 10,000 km s^{-1}, and their high-energy characteristics. These outflows, which are believed to originate in relativistic disk winds a few hundred gravitational radii from the central supermassive black hole (SMBH), play an essential role in the feedback processes that influence galaxy evolution (MATTEO et al., 2005). In particular, the large amount of kinetic energy ($> \sim 0.05 L_{\rm bol}$) of UFOs is substantial enough to potentially clear the surrounding gas and contribute to the regulation of SMBH growth (FABIAN et al., 2002; MATTEO et al., 2005; MATTEO et al., 2019).

UFOs are commonly detected in the X-ray band, with absorption features that can vary significantly depending on the time scales of AGN variability (CAPPI, 2006; TOMBESI et al., 2010; LONGINOTTI et al., 2018). However, recent studies have revealed that UFO absorption signatures are not confined to X-rays but are also present in other wavelengths, including the UV band (KRISS et al., 2018; MEHDIPOUR et al., 2022). For example, in the case of PG 1211+143, a broad, relativistically blueshifted Lyα absorption feature was detected in the HST/COS spectrum, which matched the velocity of one of the X-ray UFO absorption components (KRISS et al., 2018). This discovery suggests that UFOs may exhibit multi-ionization outflows across different wavelengths, indicating their complex structure and varying energy states (KOSEC et al., 2018a).

NLSy1 galaxies are ideal for studying UFOs, as they are characterized by low-mass SMBHs and high accretion rates, often exceeding their Eddington limits (KOMOSSA, 2007). These extreme accretion rates provide the conditions necessary for the formation and acceleration of UFOs, which are now observed in many NLSy1 sources, including IRAS 132243809 (PARKER et al., 2017), WKK 4438 (JIANG et al., 2018), and 1H 0707495 (KOSEC et al., 2018a). The detection of blueshifted Fe absorption lines in these sources observed above 7 keV, supports the idea of relativistic winds originating in the accretion disk (CHARTAS et al., 2002; CAPPI, 2006).

The UV signatures of UFOs in NLSy1s, such as the detection of low-ionization X-ray UFOs in IRAS 17020+4544, further demonstrate that these outflows can entrain and shock the ambient medium, producing secondary UFO components detectable in the UV band (KOSEC et al., 2018a; MEHDIPOUR et al., 2022). These findings are particularly valuable, as they help building a complete understanding of the con-

nection between small-scale outflows near the accretion disk and large-scale galactic outflows (TOMBESI et al., 2010; LONGINOTTI et al., 2018).

These recent works show how multiwavelength findings are important, since they can indicate that UFOs may be multi-ionization outflows in AGN.

1.10 Main goals

The main goal of this thesis is to investigate the properties of the Broad Line Region by focusing on the low ionization gas. To achieve this, we will use Low-Ionization Lines, such as FeII, O I, and CaT, to study the physical conditions, geometry, and kinematics of the gas. This will be accomplished through three distinct studies: photoionization modeling the simultaneous optical and near-infrared (NIR) emission of FeII, as a probe for analyzing the gas conditions in the LIL gas; by the detection and modelling of the O I double-peaked; and trough outflow detection in the Fe II emission line. To achieve these goals, the specific objectives of this work are as follows:

- Modelling simultaneously optical and NIR FeII emissions using CLOUDY photoionization simulations, providing constraints on the physical conditions, such as hydrogen density, metallicity, and column density, that reproduce the observed FeII emission in AGN like I Zw 1.
- Study the BLR geometry through the analysis of double-peaked emission lines, particularly O I and Paα, in the Seyfert 1 galaxy III Zw 002. This analysis will provide clues about the inclination of the accretion disk and the spatial extension of the BLR region.
- To inquire about the kinematics in the low-ionization gas in the BLR, we use the NIR spectroscopy Narrow-line Seyfert 1 1H 0707-495. We study the kinematics of the LIL gas by investigating the broad emission lines of HI, FeII, and OI. A blueshift associated with FeII, reveals outflow signatures in the LIL gas of the 1H 0707-495. This is important to help determine the role of radiation pressure in the dynamics of the LIL gas and its effect on the BLR's structure.

Combining these approaches, this thesis aims to contribute to a key understanding of the physical properties, geometry, and dynamics of the low-ionization gas in the BLR, and to provide an overview picture of the LIL gas in AGN. This thesis is

structured as Chapter 2 describes the sample, reduction, telescopes, and their instruments employed to observe, and methodology to analyze the spectra. Chapter 3 presents results on the modeling of FeII emission. Chapter 4 presents the double-peaked detection and the respective find, and the last Chapter 5 shows our results regarding the BLR kinematics. Finally, Chapter 6 shows the main conclusions of this work and future perspectives.

2 OBSERVATIONAL DATA AND ANALYSIS METHODS

Previous works have shown that the NIR has advantages compared to the optical (GARCIA-RISSMANN et al., 2012; MARINELLO et al., 2016a; MARINELLO et al., 2020a) such as (i) the FeII lines are not as heavily blended as in the optical region; (ii) critical diagnostics of the excitation mechanisms of FeII are located in that spectral region; (iii) other ions emitted by the BLR and that can be used as proxies of the FeII emission (i.e., Ca II and O I) have their strongest lines in the NIR. Because of this, we focus on NIR spectroscopy in this work. A full description of the selection criteria for each source, observation, data reduction, and analysis methods used can be found in the following sections.

2.1 Sample selection

This section will discuss the sample, the motivation behind the selection of the objects, and the unique characteristics of each, highlighting their potential to address the objectives outlined earlier in Section 1.10 of this thesis.

2.1.1 Selection of sample based on the Quasar Main Sequence (QMS)

In this study, the selected objects were chosen based on their position in the Quasar Main Sequence (QMS) (see Figure 2.1), a well-established framework that classifies AGN into two distinct populations: Population A (Pop. A) and Population B (Pop. B) (SULENTIC et al., 2000; MARZIANI et al., 2003; MARZIANI et al., 2018). This classification is based on observable parameters such as the FWHM of the Hβ line, the strength of FeII emission, the X-ray properties, and the C IV λ1549 line profile asymmetry. The average value of $L_{\rm bol}/L_{\rm Edd} \sim 0.2$ corresponds to the limit between the two populations (MARZIANI; SULENTIC, 2014).

Population A sources are characterized by narrow FWHM(Hβ) values (FWHM<4000), broad Lorentzian line profiles, strong FeII emission, and blue-shifted C IV λ1549 Å lines, with typical low mass, and high accretion rate SMBHs (SULENTIC et al., 2011). These objects include a significant fraction of NLSy1 galaxies (SULENTIC et al., 2000; MARZIANI et al., 2018). A special subset of this class, known as extreme NLS1s or xA sources within the QMS classification, (MARZIANI et al., 2018; ŚNIEGOWSKA et al., 2018; MARINELLO et al., 2020b) shows highly super-Eddington accretion sources (JIN et al., 2017; PANDA; MARZIANI, 2023). These xA objects exhibit spectral features such as extremely prominent FeII (i.e., $R_{4570} > 1.5$) (WANG et al., 2014; DU et al., 2015; MARINELLO et al., 2020b), very

rapid X-rays, and UV flux variability (GALLO, 2006b). In some cases, they also harbor UFOs signatures (TOMBESI et al., 2010; PARKER et al., 2017).

Population B sources show broad-line profiles with FWHM(Hβ) $> 4000\,\mathrm{km\ s^{-1}}$, best represented by a Gaussian function. Generally, they present weak FeII emission, no excess in soft X-rays, and redshift asymmetry (MARZIANI; SULENTIC, 2014) in the Balmer lines. In this group, most AGN have low accretion rates. Shen and Ho (2014) speculated the influence of orientation effects in the spread of $\mathrm{FWHM_{H\beta}}$ values along the QMS. The confirmation was made from observation by Sun and Shen (2015) and Panda et al. (2019) by modeling. Since Pop A has the tendency of showing a more face-on orientation than Pop B, where the orientation tend to be more edge-on, the orientation effect is relevant in sources with weak FeII emission. In some way, it influences the different line profiles observed between populations. At least, persistently, $\mathrm{R_{4570}}$ increases with the Eddington rate and decreases with increasing black hole mass (PANDA et al., 2017; ŚNIEGOWSKA et al., 2018).

The three AGN selected for this study, III Zw 002, I Zw 1, and 1H 0707495, were chosen due to their distinct positions along the QMS, as shown in Figure 2.1. I Zw 1, as the prototype FeII emitter, is a Pop. A source known for its strong FeII emission and narrow FWHM(Hβ) values. This makes I Zw 1 ideal for studying the FeII emission and its relationship with other spectral features. In contrast, III Zw 002 is classified as a Pop. B source, with a broad Hβ component, low FeII emission, and a typical red asymmetry of this population. Finally, 1H 0707-495, another Pop. A source, was selected due to its extreme spectral variability and the presence of UFOs, providing an opportunity to investigate the relationship between FeII emission and ultra-fast outflows.

Using the QMS as a selection criterion, the objects chosen for this work are expected to cover a wide range of physical conditions and provide valuable information on subjects such as the FeII emission and BLR emission properties including the geometry and kinematics of the emission gas. The next sections will discuss each object in detail, focusing on their characteristics and their role in addressing the objectives of this thesis.

Figure 2.1 - Position of the selected AGN on the Quasar Main Sequence (QMS) plane.

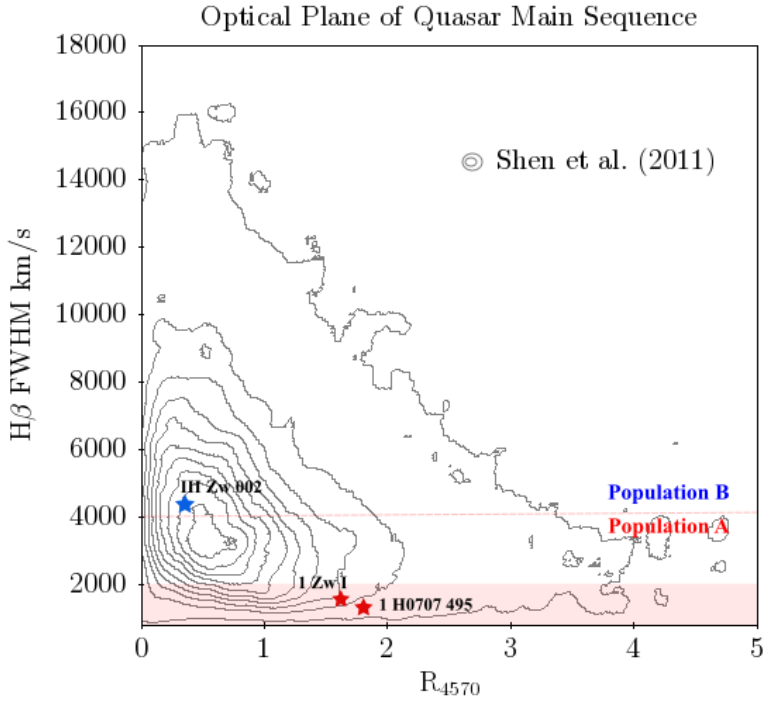

The objects III Zw 002, I Zw 1, and 1H 0707495 are plotted on the QMS, represented by stars. They are distinct within respective colored stars, where red for Population A (Pop. A) and blue for Population B (Pop. B). The contour represents the quasar properties catalog from Shen et al. (2011), which includes 105,783 quasars with emission line measurements relevant to the optical plane QMS. The red line represents the distinction of the NLS1 sub-class in Pop. A. I Zw 1 is positioned in Pop. A is a prototypical FeII emitter, while III Zw 002 belongs to Pop. B with broad Hβ and low FeII emission. 1H 0707495, another Pop. A source, is notable for its extreme FeII, and narrow Hβ than 1 Zw I.

2.2 III Zw 002

III Zw 002, also named Mrk 1501 and PG 0007+106, is a Seyfert 1 AGN classified as a radio-intermediate source at z = 0.089. Studies over the years have reported strong variability in III Zw 002 from high energies (γ-ray and X-ray) to radio (BRUNTHALER et al., 2000; BRUNTHALER et al., 2005; LIAO et al., 2016; GONZALEZ et al., 2017). These works have provided information regarding the central engine and jet activities on the sub-parsec scale for this source.

In optical, the first evidence of variability and the presence of an asymmetric profile in the Hβ line in III Zw 002 was noticed by Popović et al. (2003). They constructed a mean and an RMS spectrum using 41 spectra gathered at different epochs spanning between 1972−1998 in the wavelength region from 4740 Å to 5900 Å. They saw a

persistent feature/bump in the blue and red shoulders of the full profile of Hβ, fitted using a disk model plus a Gaussian component.

Grier et al. (2012) showed from a dense reverberation mapping campaign with about 80 spectra taken between January 2010 and July 2011, a similar result to that of Popović et al. (2003). They found a persistent feature ∼30-40 Å redward of the line center of Hβ, both in their mean and rms spectrum. However, the blueward feature, ∼35 Å of the line center, showed up only in their mean spectrum, unlike the result from Popović et al. (2003). Grier et al. (2012) also showed the velocity-resolved maps around the Hβ region that demonstrate an extended shoulder redward of the central wavelength that corresponds to a time lag of ∼2-10 days whereas the line center corresponds to a time lag of $15.5^{+2.2}_{-1.9}$ days, resulting in a virial black hole mass of $M_{\rm BH} = 3.34\pm0.49\times10^7 M_\odot$. The black hole mass estimated for this source using the $M_{\rm BH}$ - $\sigma_\star$ relation is about 5.5 times more massive, i.e., $(1.84\pm0.27)\times10^8 M_\odot$ reported in the same work (GRIER et al., 2012).

In this work, we carry out a spectroscopic analysis in the NIR of the Seyfert 1 galaxy III Zw 002 aimed at confirming the double-peaked nature of this source. The large wavelength coverage of the spectrum ($0.9 - 2.4$ μm) will allow us to study simultaneously several broad line features emitted by the BLR (O I, H I, and He I). We highlight that this is the first time that such an analysis is made on this source covering the JHK-bands, allowing us to explore a new wavelength interval in a yet very interesting source.

2.3 I Zw1

The Seyfert 1 galaxy, I Zwicky 1 (I Zw1) at z=0.061, has been considered a prototypical FeII emitter and for that reason has been widely studied in the literature (JOLY, 1991; VESTERGAARD; WILKES, 2001; VÉRON-CETTY et al., 2004; HUANG et al., 2019; PARK et al., 2022). The object is classified as NLSy1 (OSTERBROCK, 1977), and the spectrum in the optical region shows strong FeII emission, which due to the blending of thousands of such lines form a pseudo-continuum (RUDY et al., 2000). The emission of FeII in I Zw 1 has been the subject of extensive research, as it spans from the UV to the NIR regions.(OSTERBROCK; POGGE, 1985; WILL et al., 1985; LAOR et al., 1997; RUDY et al., 2000; MARZIANI et al., 2022).

The optical and UV spectral regions of the I Zw 1 historically have been the focus of FeII study. Boroson and Green (1992) made the first template of the FeII based on the observed spectrum by isolating and excluding all emission lines except those of

FeII. Since then, other studies have also successfully utilized templates to quantify the optical FeII emission in large AGN samples (SULENTIC et al., 2000; DONG et al., 2010b; KOVAČEVIĆ et al., 2010; MARINELLO et al., 2016b). Kovačević et al. (2010) create an innovative optical FeII template derived via a semi-empirical approach, combining the observed FeII emission with theoretical predictions based on allowed transitions between energy levels for the ion. By meticulously measuring individual FeII multiplet groups, the study (KOVAČEVIĆ et al., 2010) achieved a better overall agreement and was successful in obtaining an improved estimate for the R_{4570}. Reproducing the FeII emission in sources similar to I Zw 1 has been challenging, as empirical templates struggle to replicate specific features in observed spectra. In a recent development, Park et al. (2022) introduced a new optical template based on the Mrk 493 AGN spectrum to improve the modeling of FeII emission in I Zw 1-like sources.

Advances made by Vestergaard and Wilkes (2001) in the UV region extended the I Zw 1 template to that regime, allowing its application to quasar spectra. They employ the same template methodology of Boroson and Green (1992)using a high-quality HST/FOS (Hubble Space Telescope/Faint Object Spectrograph) spectrum of I Zw 1. Subsequent efforts have created since then several templates, effectively characterizing UV-optical FeII emission across large samples of AGN (TSUZUKI et al., 2006; KOVACEVIĆ-DOJCINOVIĆ; POPOVIĆ, 2015; DONG et al., 2010b; KOVAČEVIĆ et al., 2010).

Significant progress in predicting NIR FeII spectra were accomplished through the utilization of the Lyα fluorescence excitation mechanism to elucidate FeII emissions within the wavelength range of, $8500 - 9500$ Å (SIGUT; PRADHAN, 1998; SIGUT; PRADHAN, 2003). The Lyα process exclusively governs the stimulation of energy levels reaching up to 13.6 eV, giving rise to the emission lines observed in that spectral region. Observations by Rodríguez-Ardila et al. (2002) supported that prediction. The first semi-empirical template of FeII in the NIR (and unique so far) was derived by Garcia-Rissmann et al. (2012) (hereafter GR) using the observed spectrum of I Zw 1 and the theoretical models of Sigut and Pradhan (1998), Sigut and Pradhan (2003), Sigut et al. (2004). They successfully modeled the FeII emission in I Zw 1 and in another strong FeII-emitting galaxy, Ark 564. Afterward, this semi-empirical template was successfully applied in the NIR FeII modeling in several AGN spectra (MARINELLO et al., 2016b; MARINELLO et al., 2020a).

Based on the information mentioned above, the FeII spectrum of I Zw 1 is ideal for

studying the physical properties of the emitting gas. Especially because recently, it was the subject of a reverberation campaign by Huang et al. (2019). This is particularly interesting because the I Zw 1 BLR radius determined by them is an interesting variable for diminishing the number of free parameters required for photoionization modeling, allowing an increase in the precision of the simulation results.

In this work, we will carry out photoionization simulations and compare the output to the I Zw 1 optical and NIR spectra. We aim at investigating the physical conditions in AGN with strong FeII emission. Additionally, we will study how the Lyman-α fluorescence contributes to the optical and NIR FeII emissions and estimate the Lyman$-\alpha$ effect to the gas physical conditions. Our approach also allows us to explore the CaT and O I gas as analogs of the FeII gas. For this purpose, we compare CLOUDY models (FERLAND et al., 2020) exploring three new FeII atomic models—those of Bautista et al. (2015), Tayal and Zatsarinny (2018), and Smyth et al. (2018). We will cover the wavelength intervals $4434 - 4684$ Å and $8000 - 11600$ Å.

2.4 1H 0707-495

1H 0707−495 is a low-redshift ($z = 0.04$) NLS1 galaxy, well known for its extreme variability and spectral shape (TURNER et al., 1999; LEIGHLY, 1999; BOLLER et al., 2002). Moreover, it displays a very strong soft X-ray excess, and relativistic broad iron line, believed to arise from emission reprocessed by the accretion disk (FABIAN et al., 2009). 1H 0707−495 was also the first AGN where an X-ray reverberation lag was detected (FABIAN et al., 2009; ZOGHBI et al., 2010). One characteristic that makes this AGN interesting is the presence of blueshifted absorption features from an UFO, detected by Dauser et al. (2012) and Hagino et al. (2016) using XMM-Newton spectra. Moreover, in its X-ray spectra emission lines from O VIII and N VII are observed (KOSEC et al., 2018b), in particular, when the continuum flux is low. Various authors have at times invoked low ionization partial-covering absorption in 1H 0707−495, either as a way of producing the spectral structure at 7 keV at the Fe K edge Mizumoto et al. (2014) or as a way of producing soft X-ray variability Boller et al. (2021).

In the ultraviolet (UV), Hubble Space Telescope (HST) STIS (Space Telescope Imaging Spectrograph) observations of 1H 0707−495 reported by Leighly and Moore (2004) shows that at least part of the outflows detected in the X-rays is also observed in the UV emission lines. Overall, the STIS spectrum is characterized by a very blue continuum; broad, strongly blueshifted high-ionization lines (including C IV and N V); narrow, symmetric intermediate (including C III], Si III], and Al III)

and low-ionization (e.g., Mg II) lines. These latter features are centered at the rest wavelength. The study of their emission line profiles reveals that the high-ionization lines are associated with a wind, while the intermediate- and low-ionization lines arise from low-velocity gas. Therefore, the latter component is likely associated with the accretion disk or with the base of the wind.

Despite the wealth of information about 1H 0707−495 in the X-ray, UV, and optical, very little is known about the NIR properties of this source. Indeed, to the best of our knowledge, only Durré and Mould (2022) employed this AGN as part of a southern sample of NLS1 to study the kinematics of the broad line region (BLR) using the Paα line. The NIR wavelength range, though, is highly valuable because (i) the FeII emission lines, notably the FeII lines around the 1-μm region, are isolated or semi-isolated, unlike in the UV-optical region, allowing a better and more accurate determination of the line properties (RUDY et al., 2000; RODRÍGUEZ-ARDILA et al., 2002; RIFFEL et al., 2006); (ii) the H I lines, particularly, Paα and Paβ are isolated, allowing the characterization of their emission line profiles; (iii) continuum emission due to hot dust starts to show up in this spectral region.

2.5 Observation and data reduction

In this thesis, three telescopes were employed. The SOuthernn Astrophysical Research (SOAR), Gemini North, and the NASA Infrared Telescope Facility (IRTF). In all cases, the spectrographs in the cross-dispersed (XD) mode were employed. For all observation, the minimum signal-to-noise (S/N) required was S/N $\sim$ 70 in order to have secure detection of all the lines of interest to this work (λ9997, λ10502, λ10863 and λ11127) as well as other BLR features (Paschen lines, O I λ8446, Ca II $\lambda\lambda\lambda$8498, 8546, 8662). This value is based on previous spectra collected for our research group in a similar analysis using the same instruments. Because of the point-like nature of the objects, nodding along the slit using the ABBA pattern is suitable for our science. The targets were selected for each telescope based on their K magnitude, which varies from 10 to 14, and their telluric standard has typical magnitudes of K = 6-11. They were observed immediately before or after each science target for optimal telluric bands removal and flux calibration.

NIR spectra of III Zw 002 were collected on the night of July 28, 2021, at the Gemini North 8.1 m telescope using the GNIRS spectrograph in the cross-dispersed mode. This configuration covers simultaneously the $0.8 - 2.5$ μm spectral range. A slit width of 0.675" $\times$ 7" and a 32 l/mm grating were employed, providing an approximately constant spectral resolution of 1700. Data were acquired by nodding along

the slit using the ABBA pattern. Eight Individual exposures of 150 s each were collected. The telluric star A0V HIP186 (V = 6.3 mag) was observed right after the target at an airmass of 1.052. It is also important to note that the air mass during the observation of III Zw 002 varied very little (1.011−1.143). In addition, the difference in airmass between the telluric standard and the galaxy was merely 0.009. The goodness of the telluric correction can be clearly appreciated in Figure 2.2, as the residuals at the regions of bad atmospheric transmission (in light gray in Figure 2.2) are very close to the RMS of the continuum at the locations free of telluric features. Moreover, it can be seen that O I is located in a region free of telluric features. Thus, from the O I point of view, we can unambiguously state that the double-peak detection is real.

In Paα, the red wing of that line falls very close to a strong H_2O absorption. However, the blue peak as well as the start of the red peak of the line are safe from these effects. Furthermore, the reduction process was done by 3 different collaborators, in an independent way, to cross-check the final spectrum. In all cases, the double-peaked profiles were very clear, with an excellent match in shape and flux, showing differences of less than 5%.

The observations were reduced using the non-official pipeline XDGNIRS (v 2.0), with the basic scripting set up by (GONZÁLEZ-MARTÍN et al., 2009) and fully tested and documented by (MASON et al., 2015). XDGNIRS delivers a fully reduced, wavelength and flux calibrated 1D spectrum with all orders combined (MASON et al., 2015). Briefly, it cleans the 2D images from radiative events and prepares a master flat to remove pixel-to-pixel variations. Thereafter, the s-distortion solution is obtained from daytime pinhole flats and applied to the science and telluric images to rectify them. Arc frames were used to find the wavelength dispersion solution, followed by the extraction of 1D spectra from the combined individual exposures. The telluric features of the science spectrum were removed using the telluric standard spectrum. Thereafter, the flux calibration is achieved assuming a black body shape for the standard star (PECAUT; MAMAJEK, 2013) scaled to its K-band magnitude (SKRUTSKIE et al., 2006). Finally, the different orders were combined in a single 1D spectrum. The final spectrum in rest-frame wavelength is shown in Figure 2.2 except the part corresponding to the $H-$band because it has no spectral features of interest to this work.

Figure 2.2 - NIR spectrum of III Zw 002 in rest wavelength, observed with GEMINI-N/GNIRS on 2021-07-28.

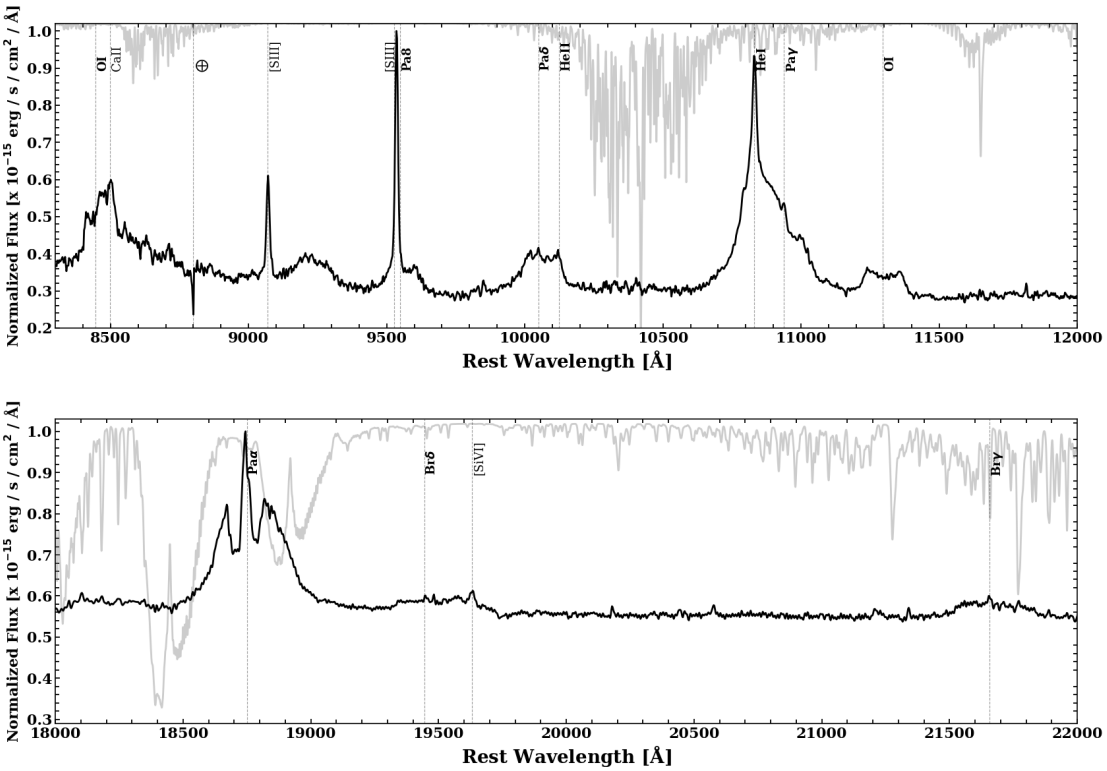

Here we show the spectral region of J and K bands, respectively covering 0.7μm-1.3μm (upper panel), and 1.7μm-2.3μm (down panel). We also mark the most notable emission lines, and in bold-face the emission lines exhibiting double-peaked feature. The background atmospheric transmission filter is represented in gray.

SOURCE: Santos et al. (2023).

NIR spectroscopy of 1H 0707-495 was obtained using the Triplespec-4 spectrograph (SCHLAWIN et al., 2014) attached to the 4.1 m Southern Astrophysical Research Telescope (SOAR) on the night of 23 February 2022. The science detector used is a 2048 × 2048 Hawaii-2RG Hg-Cd-Te array with a sampling of 0.41 arcsec/pixel. The slit assembly is 1.1 arcsec wide and 28 arcsec long. The delivered spectral resolution R is approximately 2850 across the different dispersion orders. Observations were performed by nodding in two positions along the slit. Right before the science target, the A1V star HIP 32913 (V=7.57), which is close in airmass to the former (airmass = 1.06), was observed to remove telluric features and to perform flux calibration.

Wavelength calibration was carried out using skylines present across the NIR spec-

tra. The spectral reduction, extraction, and wavelength calibration procedures were performed using SpeXTool v4.1, an IDL-based software developed and provided by the SpeX team (CUSHING et al., 2004) with some modifications specifically designed for the data format and characteristics of ARCoIRIS, written by Dr. Katelyn Allers (private communication).

Telluric feature removal and flux calibration were conducted using xtellcor (VACCA et al., 2003)). The different orders, extracted using an aperture window of 2" centered at the peak of the source light profile, were merged into a single 1D spectrum from 0.94 to 2.4 μm using the xmergeorders routine. The final reduced spectrum includes an error vector, which appears as a third extension in the data file. This error vector measures the uncertainty in flux calibration at every wavelength and takes into account errors propagated through the extraction process.

The final, merged spectrum was corrected for redshift, determined from the brightest lines detected. We employed Paα, Paβ, O I 1.128 μm, Fe II 1.0501 μm and [S III] 0.953 μm to this purpose. The average value obtained was $z = 0.04126$, in excellent agreement with the values reported in the literature (LEIGHLY et al., 1997; LEIGHLY; MOORE, 2004) and in the NASA/IPAC Extragalactic Database. Afterward, we corrected the spectrum for Galactic extinction using the Cardelli et al. (1989) law and the extinction maps of Schlafly and Finkbeiner (2011). A value of E(B-V)= 0.084 was adopted.

Finally, the I Zw 1 NIR spectrum was observed using the 3.2 m IRTF telescope (NASA, U.S. National Aeronautics and Space Administration, Infrared Telescope Facility) at Mauna Kea, Hawaii-USA in 2003. It was used the SpeX spectrograph in cross dispersion mode (SXD) covering the wavelength interval $0.8 - 2.4\,\mu$m, and photometric near-infrared bands zJHK, with a spectral resolution, R = 2000 corresponding to the $0.8'' \times 15''$ slit. Details of the observations and data reduction can be found in Garcia-Rissmann et al. (2012). It is important to notice that the reduction process is essentially similar to that of 1H 0707-495, as the SpeXTool v4.1 pipeline was originally developed for the SpeX spectrograph and later modified for use with the TSPEC-4. The optical counterpart region was obtained from Rodríguez-Ardila et al. (2002). The optical spectrum was obtained at the CASLEO Observatory (Complejo Astronómico el Leoncito, San Juán, Argentina), employing the *REOSC* spectrograph in long slit mode covering the range $3500 - 6800$ Åwith a resolution of 0.10 Å pixel^{-1}.

All the sample basic information are listed in Table 2.1. Moreover, it is important

Table 2.1 - Sample information.

Name	AR	DEC	z	K-mag	V-mag	Telescope/instrument
III Zw 002	00h10m31.0s	+10d58m30s	0.089	11.7	15.4	Gemini North/GNIRS
1H 0707-495	07h08m41.5s	-49d33m06s	0.041	12.7	15.7	SOAR/Triplespec-4
I Zw 1	00h53m34.9s	+12d41m36s	0.061	10.1	14.0	IRTF/SpeX

Summarized basic informations for the three sources.

to point out that for all galaxies, we applied telluric correction, flux, and wavelength calibration to the NIR spectra. They were observed with seeing conditions $\sim 0.8 - \sim 1$. In addition, these spectra were corrected for redshift and Galactic extinction using the Cardelli et al. (1989) and the extinction maps of Schlafly and Finkbeiner (2011), with an adopted value of E(B-V) = 0.084.

2.6 Analysis methods: continuum and emission line measurements

We developed scripts to fit the continuum emission and measure the optical and NIR emission line fluxes. This procedure allows us to derive various properties, including those of the central source, hot dust, and emission lines. Using the optical and NIR FeII templates, we calculate the strength of FeII emission through the ratios R_{4570} and $R_{1\mu m}$. These scripts were tested and applied to a sample of 67 objects from the work of DIAS DOS SANTOS, D. (2021). The same methodology for continuum and emission line measurements was applied in Chapter 3 and Chapter 4, where the scripts were used for data analysis. It is worth noting that, for the last part of this thesis, while the general approach remained unchanged, the scripts were further developed by another collaborator from our team. The code employs a non-linear least squares method, utilizing `scipy.optimize.curve_fit`, and further details regarding the implementation can be found in Chapter 5.

2.6.1 Continuum emission

The continuum in the optical to the NIR spectral range can usually be described by a combination of two components: a power law and a blackbody. The first component is attributed to the low-energy emission of the accretion disk and dominates the accretion disk, and it dominates up to $\sim 1.2\,\mu$m. For longer wavelengths, the disk emission becomes less relevant, and the emission from hot dust takes over, represented by a blackbody with a peak in the K-band.

In this work, the continuum fitting was carried out using a Python script, which is provided in Appendix A.1. The points for the fit were selected by the script and

extracted from continuum regions in the NIR as proposed by Riffel et al. (2006). For each spectrum, a blackbody function and a power law were fitted through nonlinear least squares minimization, using the LMFIT library in Python (NEWVILLE et al., 2014). This is a python library, where for default we use the Levenberg-Marquardt (leastsq) method to select the best fit. The leastsq minimizes the difference between the model and the input data, i.e., the residual, choosing the best parameters to fit (NEWVILLE et al., 2014).

The power law describes the low energy tail of the continuum emitted by the central source, and its relevance in the NIR is determined by the temperature of the disk. It strongly influences the continuum emission up to 1.2 μm and is analytically represented by:

$$F_{\rm PL} = f\left(\frac{\Delta\lambda}{\lambda_{\rm ref}}\right)^{\alpha}, \tag{2.1}$$

where f is the scaling factor, $\Delta\lambda$ is the wavelength range to be fitted, $\lambda_{\rm ref}$ is the reference wavelength, and α is the spectral index. The spectral index α is determined by the fitting process within the range from -3 to 0. When α is close to zero, the spectral index corresponds to a flatter continuum emission, typically associated with the outer regions of the accretion disk. On the other hand, when α approaches -3, it indicates a steeper spectrum, which is characteristic of a strong emission from the inner parts of the accretion disk, producing a sharp power-law in the continuum.

Additionally, a second component becomes dominant in the continuum at wavelengths longer than 1.2 μm, peaking near 2.2 μm. This component is attributed to the emission from hot dust, likely located within the gas and dust torus (RODRÍGUEZ-ARDILA; MAZZALAY, 2006). It is modeled as blackbody radiation, and the fitting model for this component is represented by:

$$F_{\rm BB} = f\left(\frac{\lambda_{\rm ref}^5 \exp\left(\frac{c}{T\Delta\lambda} - 1\right)}{\Delta\lambda^5 \exp\left(\frac{c}{T\Delta\lambda}\right) - 1}\right), \tag{2.2}$$

where the parameters of the equation are, T, the temperature of the blackbody, f, the scaling factor, and $\lambda_{\rm ref}$, the reference wavelength. Additionally, the wavelength range to be fitted ($\Delta\lambda$) is passed to the modeling functions 2.1 and 2.2.

We adopted a temperature range for the hot dust between 500 K and 2000 K, with 500 K as the lower limit and 2000 K as the upper limit. These values represent the temperature range of the dust that contributes to the observed NIR continuum. The 2000 K value corresponds to the sublimation temperature of hot dust, based on

the assumption that the sublimation of most astrophysical grains occurs within the range of 1500 K to 2000 K (BARVAINIS, 1987; SALPETER, 1977).

The LMFIT is a standard method used to find the best-fitting parameters for the free variables of the input functions (FBB and FPL). The resulting parameters of the fit include the spectral index (α), the blackbody temperature (T), and the integrated flux of both components, individually and in total. The power-law index provides information about the central source, whereas the blackbody temperature characterizes the emission from the hot dust. It is crucial to provide consistent initial values for the free parameters, as this ensures the script avoids being trapped in local minima. Figure 2.3 shows an example of continuum fitting for III Zw 002, where the AGN and hot dust are shown respectively using the colors blue and orange.

Figure 2.3 - Continuum decomposition carried out in III Zw 002.

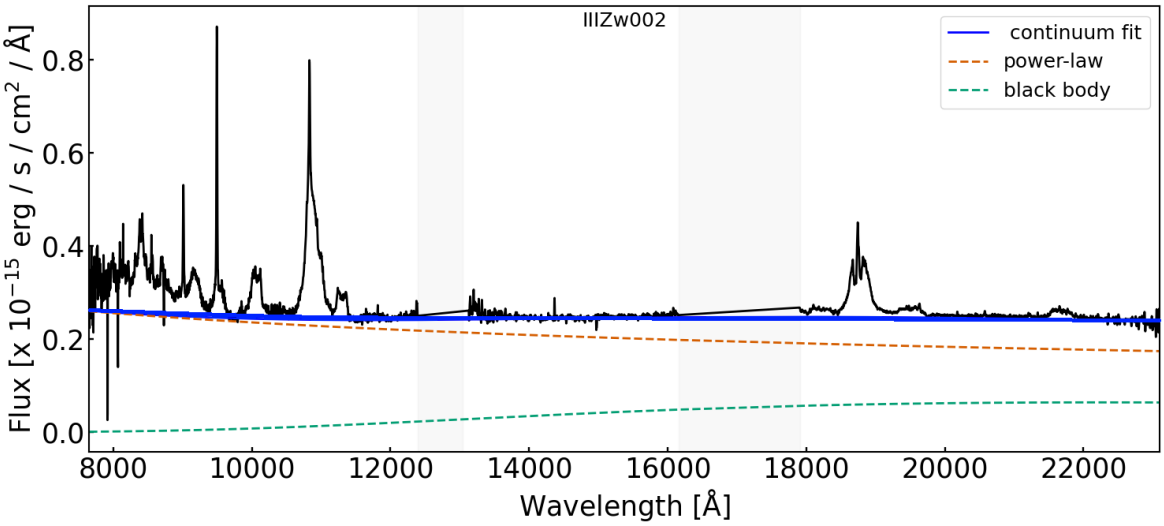

The continuum components are in dashed-green and orange, respectively, for the host dust and accretion disk contributions. The sum of the components is represented by a blue solid line.

2.6.2 Optical and NIR FeII template

Historically, optical and UV templates have been created based on the FeII emission of the I Zw 1 spectra, which contributed to examining the broad emission lines and quantifying the optical FeII emission in Type I AGN (VESTERGAARD; WILKES, 2001; TSUZUKI et al., 2006; DONG et al., 2010a; KOVAČEVIĆ et al., 2010). Ad-

vancements in the NIR FeII modeling were made by Garcia-Rissmann et al. (2012) with a semi-empirical template using both observations of I Zw 1 and theoretical models (SIGUT; PRADHAN, 2003; SIGUT et al., 2004). This template is particularly important for studying the four FeII lines in the 1 μm region (RICHARDSON et al., 2014), which are of key interest to our work.

In the optical region, we used the empirical FeII template developed by Boroson and Green (1992), derived from the spectrum of I Zw 1. To generate this template, it is necessary to isolate all lines except those of FeII. The next step is to convolve the I Zw 1 template with a Gaussian profile, which broadens the lines. The width of the lines (in velocity space) is chosen to match that of the isolated FeII line at, 10502 Å in the NIR. This convolution ensures that the template used for the optical spectrum is consistent with the width found in the NIR region. It is important to note that this step in our procedure is not required for all spectra modelling. In the case of the I Zw 1 spectrum itself, which is the basis of the template, no convolution is required. Therefore, its line widths are used without any further broadening. Also, for objects with narrower line widths than those of I Zw 1, no convolution is applied, because the line widths in the template can not be made narrower than that of I Zw 1. In such case, the template is used as it is. However, for objects with broader lines, the convolution step is necessary to fit the template and match the observed line widths. In this case, the optical FeII template is optimized by minimizing the chi-square value over the region between 4100 Å and 4700 Å, where the model that best fits the data is chosen.

In order to model the FeII emission in the NIR, we apply the semi-empirical template of Garcia-Rissmann et al. (2012), which includes approximately 1915 FeII lines in the wavelength range of $8000 - 11600$ Å. This template is constructed using a combination of observed spectra and photoionization models, providing the positions and relative intensities of the emission lines. Since the template is based on theoretical models, it initially lacks of any broadening. Therefore, to adapt the template to any AGN spectra, we apply a broadening procedure using a grid of FWHM values, with the broadening parameter derived from the isolated FeII line at 10502 Å. Then, the final broadened template is scaled to the observed spectrum using the line flux at 10502 Å. The best-fitting NIR template is selected by minimizing the chi-square value in the region around the 10502 Å line.

All procedures described in this section are exemplified in the Appendix A.2 and A.3. Figure 2.4 shows an example of the optical FeII template fit in panel (a) and the

NIR template fit in red in panel (b). By employing both optical and NIR templates, we can study the FeII emission across a broad wavelength range, improving our understanding of the physical properties of the emitting gas.

Figure 2.4 - Spectra of galaxy I Zw 1.

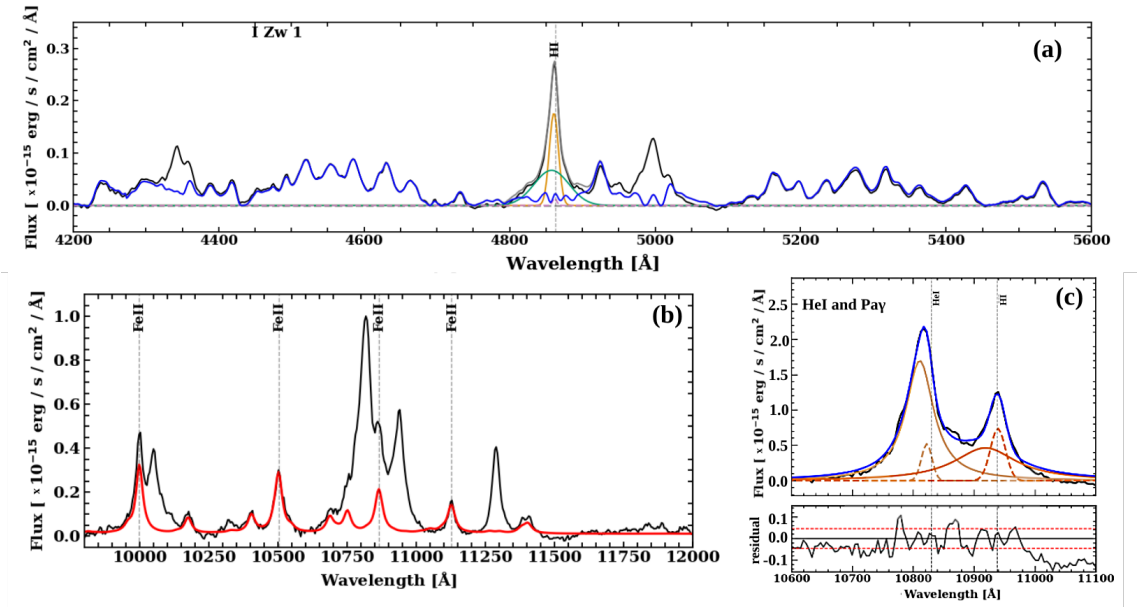

(a) The observed optical spectrum (in black) along with those with Hβ emission line fits the outflow (green), BLR (yellow), and faint narrow (dashed orange) components. The blue curve represents the optical FeII template. (b) The measured near-infrared spectrum (in black) along with the fit to the semi-empirical (GARCIA-RISSMANN et al., 2012) template (red), highlighting four main NIR FeII lines used to estimate the 1-micron intensity. (c) The Paγ-HeI line blended with HeI for the observed spectrum (in black) and the fits to the BLR (solid orange) and NLR components. See subection 2.6.2 for details.

SOURCE: Santos et al. (2024).

2.6.3 Emission line fit

After the continuum and FeII emission subtraction from the spectrum, we measure the flux, FWHM, and centroid position of the most important lines. To this purpose, we created Phyton scripts using LMFIT to fit the emission lines. These scripts used Gaussian or Lorentzian profiles to represent the BLR components. The choice between these two functions was always done following the χ^2 that minimizes the residual left after subtraction of the fit profile. Overall, BLR profiles of NLS1 were best represented using Lorentzian, while those of Type I AGN with broader lines followed Gaussian shapes (MARINELLO et al., 2016b). For lines emitted by the

NLR, we used only Gaussian components. In the NIR, the AGN spectra are dominated by strong emission features from the Paschen line series, HeI λ10830, OI λ8446 and λ11297, CaT λ8498, and FeII λ10502, as shown in the (a) and (c) panels of Figure 2.4. Of particular interest to this work are the low ionization lines of OI, CaT, FeII (see Figure 2.5), and the Balmer and Paschen series of hydrogen.

Figure 2.5 - Emission lines of main interest in this thesis.

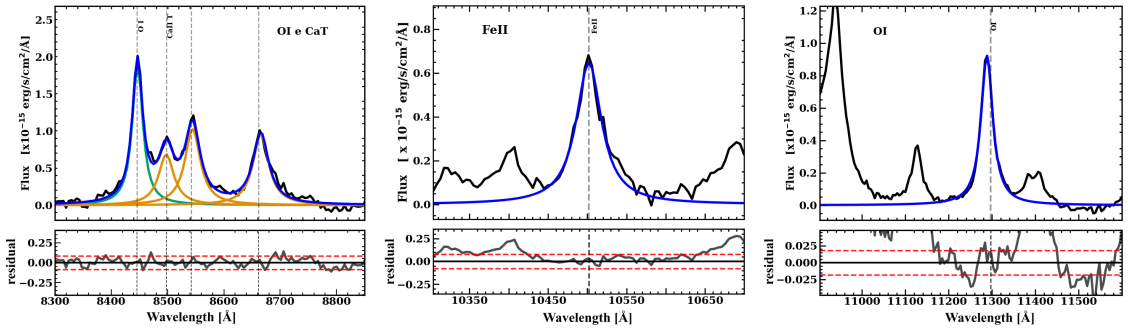

Fits of the low ionization lines OI λ8446 and λ11297, CaT λ8498, and FeII λ10502.

2.7 CLOUDY photoionization code

To create as realistic models as possible for reproducing the FeII emission, we employ CLOUDY (FERLAND et al., 2017; FERLAND et al., 2020) photoionization code. We used CLOUDY to model the physical conditions of a gas so that its emitted spectrum matches the observed one.

The code predicts both the emitting and the absorbed spectra from a gas ionized by an incident radiation field. CLOUDY solves the photoionization equilibrium equations for each ion and from this result, it calculates the emitted spectrum by the cloud considering the metallicity, the gas density (column density (N_H), local hydrogen density (n_H)), and the distance from the cloud to the radiation source.

Furthermore, it uses radiative transfer equations to calculate the diffuse field of radiation and to be able to couple to the different emitting regions within the cloud. Also, atomic/molecular data are needed to compute the overall spectral features. Then, CLOUDY calculates the number of interactions by computing the transition probabilities, collision rates, and photoionization cross-sections for each ion present in the cloud. The main points of how CLOUDY works are described below.

The incident radiation field is specified as intensity, energy per unit area, or lumi-

nosity, and power emitted by the central source into $4\,\pi$ sr. The distinction between them is important because when the input is in luminosity, the inner radius of the cloud should also be specified. Another fundamental input is the incident radiation field shape or SED. It is essential that the radiation field represents the real observed radiation field or is as similar as possible to reproduce the observed condition because the simulated emission lines will be promoted by the incident radiation. Furthermore, CLOUDY generates an output continuum from the SED.

Another critical input parameter is the chemical composition of the cloud. Abundances are relative to the total hydrogen density and can be specified as absolute or scale factors relative to it. CLOUDY has extensive stored abundance sets for elements in the gas phase. However, the material as dust (grains) is not included in our modeling setup. When it is necessary to investigate the effects of global enrichment or depletion of the elements, it is useful to use the metal content option, which is not our case. The abundance of the entire mixture of metals can be increased by a scale factor in the code.

In addition, hydrogen density (cm^{-3}) is a fundamental parameter, and other commands that specify how the hydrogen density is set and how it changes with radius or depth can also be included. CLOUDY include models of the energy levels of atoms, ions, and molecules, which are used to predict line spectra. These models are collectively referred to as "species". Databases with the highest number of levels give the best spectroscopic accuracy but can take quite some time to compute because they can include hundreds to thousands of levels. Furthermore, CLOUDY includes the option of selecting collisional processes and fluorescent continuum options. In special to the FeII study, the fluorescent continuum is important for the excitation of the many FeII lines. In the Section 2.7.1 is presented all datasets employed in this work.

All radiative transfer effects, such as line thermalization, destruction by background opacities, pumping by the incident continuum, and escape from the cloud, are included in the treatment of line formation.

Since the total optical depths are not known in the first iteration, it is necessary to iterate again, but by default, a single iteration is used. This approach is often sufficient for low-density nebulae such as planetary nebulae or H II regions. For some resonance transitions, a second iteration is enough to establish a fairly accurate line optical depth scale. Nevertheless, the iteration to convergence command will continue to iterate until the optical-depth scale is well-defined.

Finally, there is also a stop criterion for converting the simulation to the cloud at some depth. For example, in the case of the BLR, the gas is optically thin to energetic radiation, and the outer radius of the cloud could be specified by a column density, physical thickness in cm, or optical depth. Multiple stopping criteria can be specified, and the calculation will stop when the first one is met.

2.7.1 Overview of the FeII datasets used in this work

The default model for the FeII ion in CLOUDY is the one defined by Verner et al. (1999). It comprises 371 energy levels (up to ∼11.6 eV) able to predict the intensities of 68,635 lines. Beyond the Verner et al. (1999) data set, we applied to our spectral synthesis models three recent FeII data sets, Bautista et al. (2015), Tayal and Zatsarinny (2018) and Smyth et al. (2018). Figure 2.6 shows the FeII energy level diagram for each dataset, and we detailed them below.

Figure 2.6 - The diagram shows the energy levels of various models.

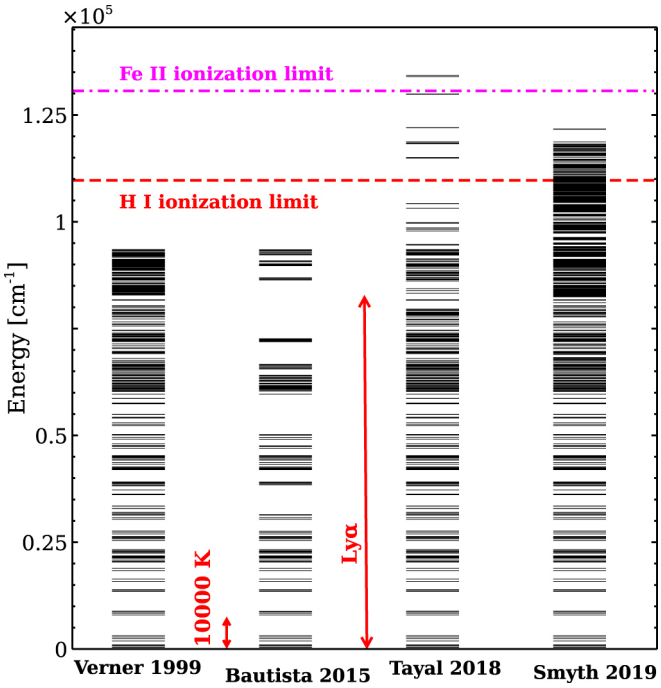

The diagram shows the energy levels of various models. From left to right: data sets derived by Verner et al. (1999), Bautista et al. (2015), Tayal and Zatsarinny (2018), and Smyth et al. (2018). The horizontal dashed lines indicate the limits of HI and FeII ionization. The energy of the Lyα transition, an important source of photo-excitation of FeII, is also shown.

SOURCE: Sarkar et al. (2021).

Bautista et al. (2015) present an ion with 159 levels up to $\sim 11.56\,\mathrm{eV}$, producing 628 emission lines. In particular, the FeII ion comprises 52 lowest metastable levels, which accounts for essentially forbidden lines in the optical and IR spectral regions. This allows the atomic model to be used to explore mainly [FeII] live diagnostics in these spectral ranges. Although we are only interested in $4000 - 12000$ Å, it is important to point out that Bautista et al. (2015) reports no transition between $2000 - 3000$ Å.

Tayal and Zatsarinny (2018) FeII model contains 340 energy levels, with energy up to $\sim 16.6\,\mathrm{eV}$, producing 57,635 emission lines. This dataset allows a more detailed treatment of the measured FeII spectra from astrophysical sources, which in particular is interesting for our study. We point out that the Tayal and Zatsarinny (2018) model does not necessarily include the Bautista et al. (2015) energy levels, i.e., the emission lines predicted from Tayal and Zatsarinny (2018) are different from the previous models.

Smyth et al. (2018) report new 20 configurations, 6,069 atomic structure model, including 716 energy levels leading to produce 255,974 emission lines with the highest energy level of $\sim 26{,}4\,\mathrm{eV}$. The dataset compared with Tayal and Zatsarinny (2018) includes more relevant forbidden and allowed transitions. One of the benefits of Smyth et al. (2018) is that the ion can achieve higher energy levels (up $13\,\mathrm{eV}$), which is important for FeII NIR emission.

The Garcia-Rissmann et al. (2012) (GR hereafter) developed a semi-empirical template from the prototypical FeII emitter I Zw 1. This template is used to model the FeII emission in several AGN FeII emitters. In particular, it is suitable to compute the NIR FeII strength in an AGN. We compared the simulated spectra (after normalizing them) with the GR template, which provides the wavelengths and intensities of the FeII lines (see Figure 2.7). Figure 2.7 displays the comparison between the different FeII datasets. An interesting feature is that Verner et al. (1999) predicts an additional strong FeII line that is not present in the Garcia-Rissmann et al. (2012) spectra, highlighting a key difference between the two models. Regarding the Bautista et al. (2015) dataset, it does not reproduce the permitted emissions we are particularly interested in. This discrepancy can likely be explained by the fact that the model is primarily designed to predict forbidden transitions. On the other hand, the spectra from Smyth et al. (2018) and Tayal and Zatsarinny (2018) show a better agreement with the Garcia-Rissmann et al. (2012) template. In subsection 2.7.2 we detailed the results from Verner et al. (1999), Tayal and Zatsarinny (2018), and

Figure 2.7 - A comparison of resulted spectra from each FeII atomic data (VERNER et al., 1999; SMYTH et al., 2018; TAYAL; ZATSARINNY, 2018; BAUTISTA et al., 2015), with the GR template.

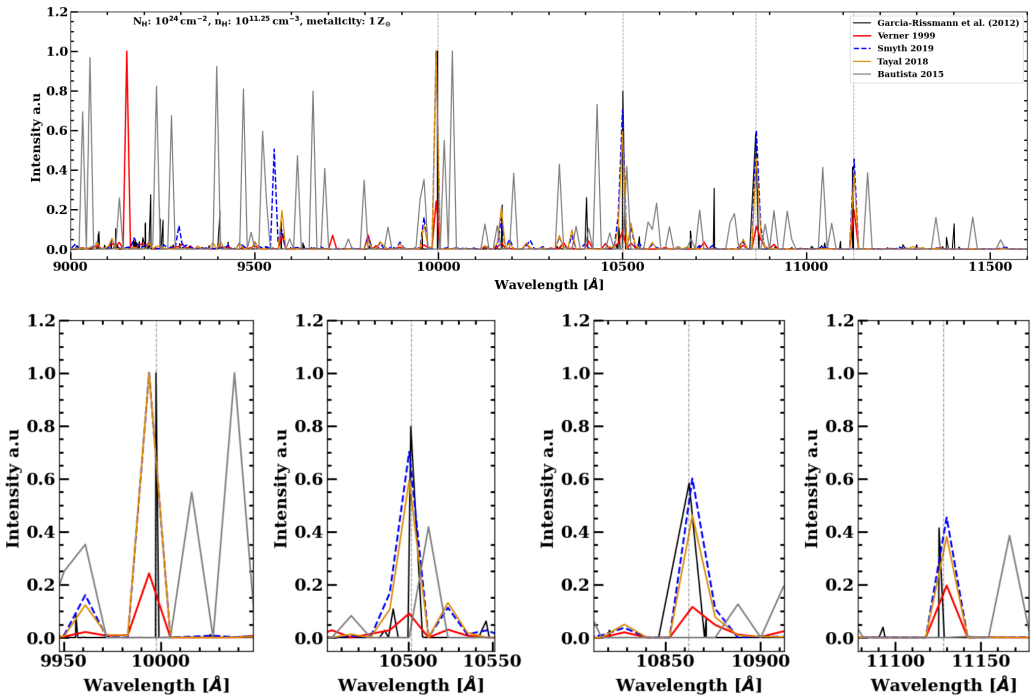

Upper Panel: Predicted pseudo-continuum for FeII emission for n_H=$10^{11.25}$ cm^{-3} using solar abundances for column density case 10^{24} cm^{-2}. The atomic databases Verner et al. (1999), Bautista et al. (2015), Tayal and Zatsarinny (2018), and Smyth et al. (2018), respectively, are in colors red, gray, orange, and dashed-blue. The Garcia-Rissmann et al. (2012) template is in black. Down Panel: Zooming in the 1-mícron line region. All spectra are normalized by their respective maximum values between 9000 Å – 1200 Å.

Smyth et al. (2018).

2.7.2 Photoionization modeling setup

We performed numerical simulations using CLOUDY v17.03 (FERLAND et al., 2017) to investigate the physical conditions in the BLR of the AGN I Zw 1. To minimize the number of free parameters in our simulations, we adopted several fixed values based on previous studies. Specifically, we constrained the AGN ionizing continuum using a constant shape derived directly from the continuum data, as described in Panda et al. (2020). We use the BLR luminosity at 5100 Å of I Zw 1 from Kaspi et al. (2000), whose observation period closely matches that of the optical and NIR spectra used in this work. The luminosity at 5100 Å value used is $L_{5100} = 3.19 \times 10^{44}$ erg s^{-1} Kaspi

et al. (2000).To minimize the number of free parameters in our modeling approach and increase the confidence of our results, we used the BLR radius' based on the Hβ emission line, where the value is $R_{\rm BLR} = 37.2$ light-days Huang et al. (2019).

To further constrain our model, we fixed the cloud column density to $N_{\rm H} = 10^{24}$ cm^{-2}, as concluded from earlier studies involving the recovery of the optical FeII emission in this source (PANDA et al., 2020; PANDA; SANTOS, 2021). Also, we adopted the spectral energy distribution (SED) for I Zw 1 from Panda et al. (2020) as the input radiation field in our simulations (see Figure 2.8). Consequently, the remaining free parameters include: (i) the cloud mean hydrogen density, $n_{\rm H}$, which varies between 10^9 and 10^{14} cm^{-3}, and (ii) the metal content (Z) in the cloud, which ranges from 0.1 to 10 in solar units, estimated using the GASS10 module (GREVESSE et al., 2011).

We incorporated two scenarios for the internal random motions within the BLR clouds, specifically micro-turbulence, with velocities ($V_{\rm turb}$) of 10 and 100 km s^{-1}. The micro-turbulence is attributed to random motions of photons within the ionized gas, likely triggered by magnetic fields in the confined clouds (BOTTORFF; FERLAND, 2000; REES, 1987), and serves as a secondary contributor to the overall line width, as demonstrated in previous studies (e.g., Kollatschny and Zetzl (2013)). The micro-turbulent velocity values were previously derived by Bruhweiler and Verner (2008), who successfully modeled the FeII emission in the UV region of I Zw 1. These authors found that a micro-turbulence in the range of approximately $10 - 30$ km s^{-1} enhances the accuracy of the model results (BRUHWEILER; VERNER, 2008). Moreover, references (PANDA et al., 2018; PANDA; SANTOS, 2021) found that a micro-turbulence velocity between 10 and 100 km s^{-1} can accurately reproduce the FeII emission in the optical region.

In addition to scenarios that involve microturbulence, we performed simulations without microturbulence ($V_{\rm turb} = 0$). This comprehensive modeling effort results in a total of 609 model combinations, calculated as $N(N_{\rm H}) \times N(n_{\rm H}) \times N(Z) = 3 \times 29 \times 7$. We analyze the results of these models to assess potential inconsistencies with observational quantities measured in the optical and NIR, specifically in terms of the relative FeII strengths, namely R_{4570} and $R_{1\mu m}$. Finally, we derived solutions from the models that align with the aforementioned observational properties.

Figure 2.8 - The SED of the I Zw 1.

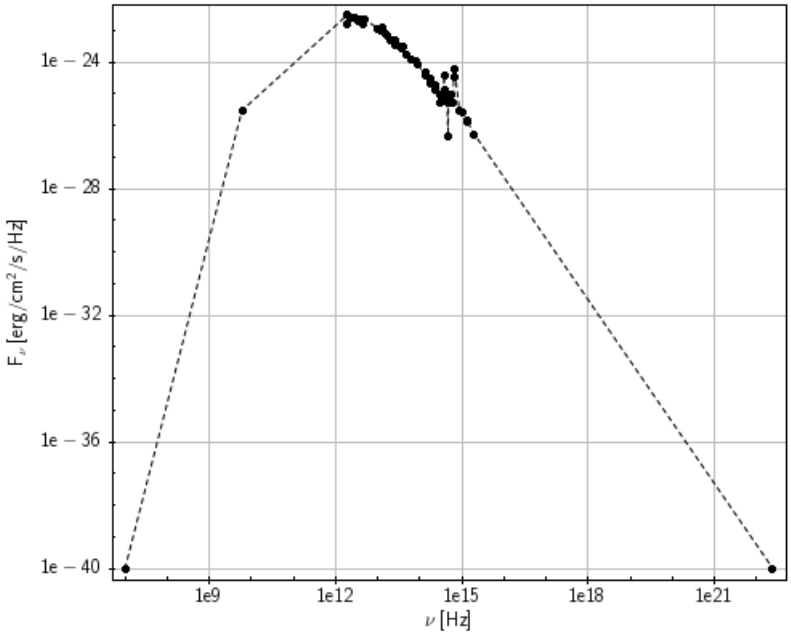

The I Zw 1 is considered a prototypical FeII emitter.
SOURCE: Panda et al. (2020).

2.8 Double-peaked emission spectral fitting

In order to explain the nature of the double-peaked profiles in III Zw 002, we assume that at least part of the emission originates from different portions of a circular Keplerian disk. In the next subsection, we will describe the disk model employed to this purpose.

2.8.1 The Keplerian disk model

To model the double-peaked profile, we use the prescription of Chen et al. (1989) and Chen and Halpern (1989), where the model assumes that the broad double-peaked emission line originates from different portions of a circular Keplerian disk, between the inner (ξ_1) and external (ξ_2) radii. In addition, the disk has an inclination angle i relative to the plane of the sky and has spiral arms. The total line flux of the emission line is given by the integration of the specific intensity from each location in the disk, in the frame of an emitting particle,

$$F = \int_{\nu_o}^{\nu_f} \int_{\xi_1}^{\xi_2} \int_{0}^{2\pi} I(\xi, \Phi, \nu_e)\, d\nu\, d\xi\, d\phi, \tag{2.3}$$

and the specific intensity is given by,

$$I(\xi,\phi,\nu_e) \;=\; \frac{\epsilon(\xi,\theta)}{4\,\pi}\,\frac{e^{-(\nu_e-\nu_0)^2/2\,\sigma^2}}{(2\,\pi)^{1/2}\sigma}, \tag{2.4}$$

where ν_e is the emission frequency, ν_0 is the rest frequency, and σ is the local "broadening parameter" (CHEN; HALPERN, 1989). It is well known that the double-peaked profile in AGN shows variability in the red and blue peaks of the profile (STRATEVA et al., 2003; SCHIMOIA et al., 2012b; SCHIMOIA et al., 2015), alternating the intensities with time. This asymmetry is suggested to be associated with spiral arms, or "lumps" in the disk. In addition, several works using dedicated monitoring campaigns have proposed that the BLR structure could have effective spiral arms (SHAPOVALOVA et al., 2008; SHAPOVALOVA et al., 2010; SHAPOVALOVA et al., 2012; GRIER et al., 2012; GRIER et al., 2013; GRIER et al., 2017; WANG et al., 2022). The model in this paper assumes asymmetric emissivity of the disk due to perturbations in the spiral arms, with an emissivity law given by

$$\begin{aligned}\epsilon(\xi,\theta) \;=&\epsilon(\xi)\Bigg\{1+\frac{A}{2}\,exp\left[-\frac{4l\,n\,2}{\delta^2}(\phi-\Psi)^2\right]\\ &+\;\frac{A}{2}exp\left[-\frac{4\,ln\,2}{\delta^2}(2\,\pi\;-\;\phi+\Psi)^2\right]\Bigg\},\end{aligned} \tag{2.5}$$

and the asymmetric emissivity is given by,

$$\epsilon(\xi) \;=\; \begin{cases} \epsilon_0\xi^{-q_1}, & \xi_1 \;<\; \xi \;<\; \xi_q,\\ \epsilon_0\xi_q^{-(q_1-q_2)\xi^{-q_2}}, & \xi_q \;<\; \xi \;<\; \xi_2 \end{cases} \tag{2.6}$$

where ξ_q is the saturation radius (maximum emissivity). After hitting the maximum at the saturation ξ_q radius, the emissivity behavior changes. The q_1 is the index before the saturation, and thereafter changes to q_2. A is the brightness contrast between the spiral arm and the underlying disk. The expression between square brackets describes how the arm's emissivity changes with the azimuthal distance $\phi-\Psi_0$. It is assumed that the arm's emissivity behaves like a Gaussian function with an FWHM $=\delta$ (azimuthal width).

The relation between the azimuthal angle ϕ_0 and the angular position Ψ_0 at the top

of emissivity of the spiral arm is given by:

$$\Psi_0 = \phi_0 + \frac{ln(\xi/\xi_{sp})}{tan\, p}, \tag{2.7}$$

where ϕ_0 is the azimuthal angle, p is the pitch angle, and ξ_{sp} is the innermost radius of the spiral arm.

After making the necessary substitutions, we get the spectral profile of the line F_χ. From Chen and Halpern (1989), F_χ is calculated as:

$$F_\chi = F_0 \int_{\xi_1}^{\xi_2} \int_0^{2\pi} \exp\left[-\frac{(1+\chi-D)^2\nu_0^2}{2\sigma^2 D^2}\right] \left[1+\xi^{-1}\left(\frac{1-\sin i\cos\phi}{1+\sin i\cos\phi}\right)\right] D^3\, \epsilon(\xi,\phi)\, \xi\, d\xi\, d\phi, \tag{2.8}$$

where F_0 is a normalization constant between the observation and the modeled profile, and D is the Doppler factor:

$$D = \left(1-\frac{3}{\xi}\right)^{1/2} \left(1+\frac{\sin i\sin\phi}{\xi^{1/2}}\right)^{-1}. \tag{2.9}$$

In summary, the model has 11 free parameters that together define it, as illustrated in Figure 2.9.

Figure 2.9 - Illustration of the disk model.

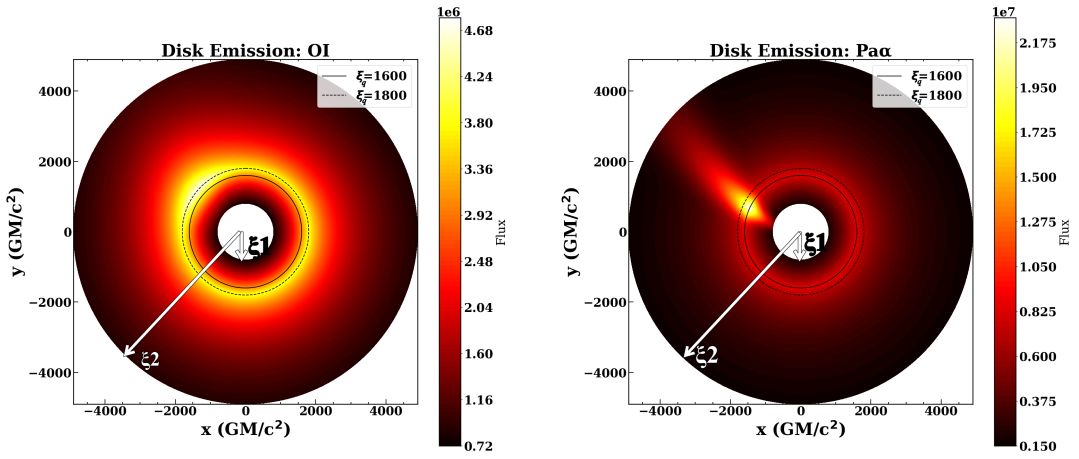

ξ_1 and ξ_2 are, respectively, the inner and outer radii of the line emission region. ξ_q is the break radius of the radial emissivity, where each emission line has its maximum emissivity radius. This illustration was drawn based on the emission lines of interest for this work, after applying the disk model.

2.8.2 An additional broad component

In most cases, it is necessary to add a Gaussian component that is connected to non-disk clouds, which are located above and below the disk plane. The Gaussian component contributes to the central hump in the line profile, showing typical values for FWHMs of a BLR (up to 1000). This component can be a determining factor in III Zw 002 to explain the "box" profile observed in O I. The profile of O I is unusual when compared to the majority of double-peaked sources reported in the literature. However, it is very similar to the one reported by Hung et al. (2020) in the Hα line. In order to determine the profiles for Paα and O I, we fit the best three parameters that describe the Gaussian: amplitude, center, and width. This additional broad component was represented by the following equation,

$$F_G(\lambda) = A \exp - \frac{(\nu - \nu_o)^2}{2\,\sigma^2}, \tag{2.10}$$

where A is the emission line amplitude, σ is the width, ν the frequency and ν_o the center of the line.

Once we have the best parameters of the disk model, we combine it with expression 2.8 and apply a scale factor to the disk model to find the best contribution of both components to the total profile. In this process we use the LMFIT to obtain the best fit parameters (NEWVILLE et al., 2014), as described in Section 2.6.3 about emission line fitting process.

3 MODELING THE FeII EMISSION IN THE NIR

Despite its importance, modeling the FeII emission in the NIR has not been thoroughly explored, especially for reproducing observed spectra. While many studies have modeled the FeII spectrum in the optical and UV regions, to the best of our knowledge, simultaneous analysis of the optical and NIR spectral regions in the context of photoionization modeling, has not been conducted so far. Recent advances (PANDEY et al., 2024) focused on optical-UV modeling, but NIR emission remains largely unexplored. Given that NIR FeII lines are less blended than optical lines, they provide a unique opportunity to study the BLR with greater precision, especially regarding the physical conditions in the emitting gas.

By comparing the output of photoionization models such as CLOUDY (FERLAND et al., 2020) with the observed spectra of I Zw 1, we aim to provide key parameters to constrain the gas physical conditions in AGN with strong FeII emission. This work combines the first simultaneous optical-NIR approach to study the FeII and related ions to provide a comprehensive view of the BLR's physical environment.

This chapter begins with Section 3.1, where we discuss the estimation of FeII intensity from optical and NIR spectra of I Zw 1. In Section 3.2, we present the first results based on spectral synthesis using the Verner et al. (1999) FeII dataset. Section 3.3 follows with results from state-of-the-art FeII datasets. Finally, the results are summarized with a discussion and conclusions[1].

3.1 Optical and NIR FeII intensity estimation

Our model constraints are based on the optical and NIR spectra of I Zw 1. From these data, we derived key FeII properties, such as intensity, FWHM, and luminosity, which are referenced in Chapter 2.6. Using the spectra and template fits, we obtained the optical FeII and NIR intensities and their ratios to the nearest hydrogen line.

For optical FeII, we found $R_{4570} = 1.62 \pm 0.06$, which is aligned with previous studies, with values around 1.47 (SULENTIC et al., 2000) (see emission lines fitted described in Section 2.6.3).

[1]This chapter is partially based on the article titled "Joint Analysis of the Iron Emission in the Optical and Near-Infrared Spectrum of I Zw 1" by Santos et al. (2024), published in the MPDI Physics, in a Special Issue Spectral Line Shapes in Astrophysical and Laboratory Plasma (2023) - (see https://doi.org/10.3390/physics6010013).

Table 3.1 - Characteristics measured from the near-infrared and optical spectra of I Zw 1, where the fluxes are given in 10^{-14} erg s^{-1} cm^{-2} Å^{-1} units. See text for details.

FeIIλ10502	FeIIλ9998	FeIIλ10863	FeIIλ11127	Paγ	$R_{1\mu m}$	Hβ	FeIIλ4570	R_{4570}
2.70±1.38	4.13±1.06	0.150±0.17	2.32±1.29	5.96±0.83	0.46±0.47 to 1.48±0.15	10.30±1.84	16.70±2.80	1.62±0.06

The $R_{1\mu\,\mathrm{m}}$ is calculated as the ratio of the combined fluxes of the four brightest NIR isolated FeII lines at the wavelengths λ9997, λ10502, λ10863, and λ11127 to the flux of Paβ broad component (RODRÍGUEZ-ARDILA et al., 2002). In the literature, $R_{1\mu\,\mathrm{m}}$ for 1 Zw I was reported by Marinello et al. (2016b) with the value of 1.81 ± 0.08. Because the Paβ line was affect by strong telluric residuals, they estimated that ratio using the Paα line and rescaled it to Paβ intensity using the theoretical line ratio Paα/Paβ from Garcia-Rissmann et al. (2012).

Here we estimated $R_{1\mu\,\mathrm{m}}$ by measuring the flux of Paγ and re-scaled it to the flux of Paβ. However, our approach does not rely on the theoretical value for the Paβ/Paγ ratio (i.e., 0.8531) (MARINELLO et al., 2020a). Instead, we investigated how that ratio changes under varying gas physical conditions using our CLOUDY simulations. To do this, we assumed a fixed column density of 10^{24} cm^{-2} for each dataset described in the Section 2.7.1 and their corresponding micro-turbulence cases. We found that the ratio depends on the cloud density, which is influenced by the range of metal content assumed in this study, as described below.

In Figure 3.1, we present the dependence of the Paβ/Paγ ratio with cloud density, as influenced by the metal content range assumed in this work, using the dataset from Verner et al. (1999). The ratio of Paβ/Paγ varies between 1.05 and 3.38 in the simulations.

Using these simulated ratios, we derived the corresponding $R_{1\mu\,\mathrm{m}}$. First, "the observed" flux of Paγ was rescaled by applying the simulated ratio to obtain the flux of Paβ for both the minimum and maximum values of the ratio. Then, we calculated the corresponding minimum and maximum $R_{1\mu\,\mathrm{m}}$. As a result, $R_{1\mu\,\mathrm{m}}$, varied between 0.46 ± 0.47 and 1.48 ± 0.15 for the Verner et al. (1999) dataset.

Furthermore, the Paγ/Paβ ratio was also evaluated using the datasets from Smyth et al. (2018) and Tayal and Zatsarinny (2018), as shown in Figure 3.2. The ratios obtained from these datasets are very similar to each other and, like the results from

Figure 3.1 - The luminosity ratio for Paβ to Paγ.

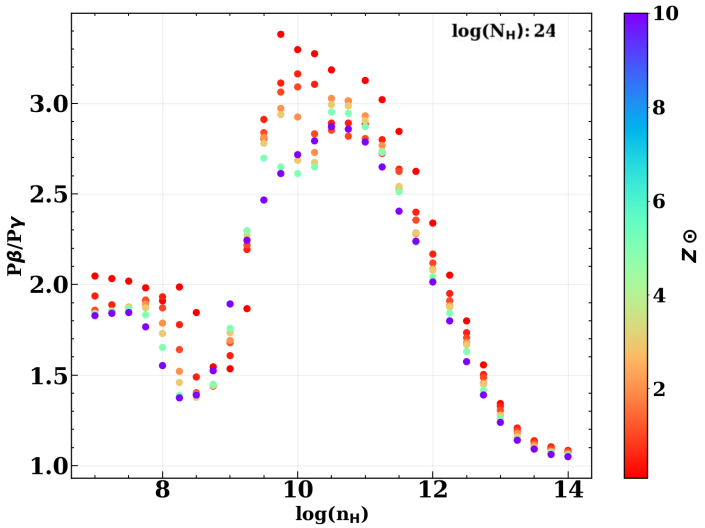

The luminosity ratio for Paβ to Paγ obtained from simulations used here for a range of local hydrogen densities (n_H), Verner et al. (1999) dataset, and no micro-turbulence. The colors correspond to the different metal content. The cloud column density is 10^{24} cm^{-2} at zero micro-turbulence.

SOURCE: Santos et al. (2024).

Verner et al. (1999), they also depend on cloud density and metal content.

The values of the ratio vary between 0.99 and 2.43 without micro-turbulence. It is important to note that adding micro-turbulence to the models the interval for that ratio remains unchanged.

3.2 Joint analysis of the iron emission in the optical and near-infrared spectrum of I Zw 1

We derived the optical FeII and the NIR FeII ratios from the CLOUDY simulations, denoted as R_{4570} and $R_{1\mu m}$, respectively. Rodríguez-Ardila et al. (2002), Marinello et al. (2016b) demonstrate that the optical and NIR intensities are correlated, indicating that both emissions should have origin and excitation mechanisms in common.

Micro-turbulence refers to small-scale, random gas motions within the emitting regions of the BLR, which are not resolved in the macroscopic flow of the gas. These turbulent motions increase the interaction between gas particles, including FeII ions, leading to more efficient absorption of ionizing photons. As a result, micro-turbulence enhances the FeII emission, as shown in previous studies for UV and optical regimes

Figure 3.2 - The luminosity ratio for Paβ to Paγ obtained from simulations used here for a range of local hydrogen densities, n_H.

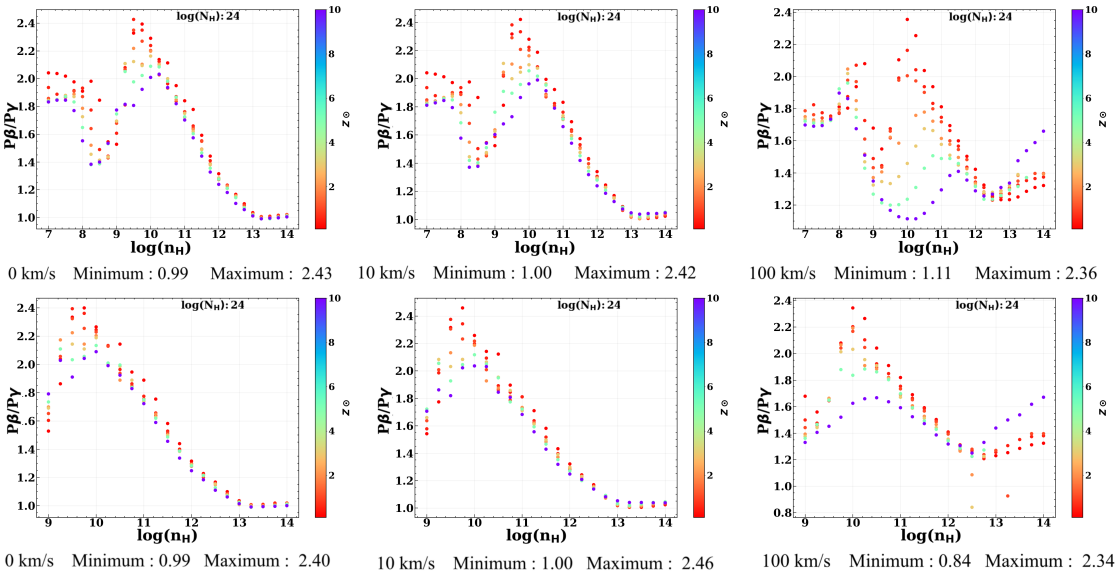

The colors correspond to different metal content. The cloud column density is 10^{24} cm^{-2}. The ratios from (a) to (c) are shown using, Smyth et al. (2018) and from (d) to (f) are shown using Tayal and Zatsarinny (2018). The first figure represents the case without micro-turbulence (zero km s^{-1}), the second with 10 km s^{-1}, and the third with 100 km s^{-1}, respectively for up and down panels.

(VÉRON-CETTY et al., 2004; BRUHWEILER; VERNER, 2008; PANDA, 2021d). Moreover, introducing micro-turbulence into the gas can enhance the R_{4570} ratio similarly to increase the metal content in the gas, acting as a metallicity controller (PANDA, 2021d).

The micro-turbulence effect has been extensively studied in the optical FeII emission (BRUHWEILER; VERNER, 2008; PANDA, 2021d) but, it has been out of focus in the NIR. In this paper, we study the micro-turbulence effect applied to the NIR FeII region for the first time. The results are shown in Figure 3.3 for the column density scenario of 10^{24} cm^{-2} for the optical (Figure 3.3a-c) and NIR (Figure 3.3d-f) spectral regions. The diagnostic diagrams in Figure 3.3 show the outcomes for $V_{\rm turb}$ values of 0, 10, and 100 km s^{-1}, for R_{4570} and $R_{1\mu\,\rm m}$ ratios as a function of the local cloud density. Figure 3.3 demonstrates how the intensities vary with different metal content levels in the BLR clouds depicted by the color gradient We further highlight the observed ratios, R_{4570} and $R_{1\mu\,\rm m}$, and their associated uncertainties, obtained by fitting the observed spectra within the gray and blue shaded regions, respectively.

Figure 3.3 - Diagnostic diagrams from simulations for R_{4570} and $R_{1\mu m}$.

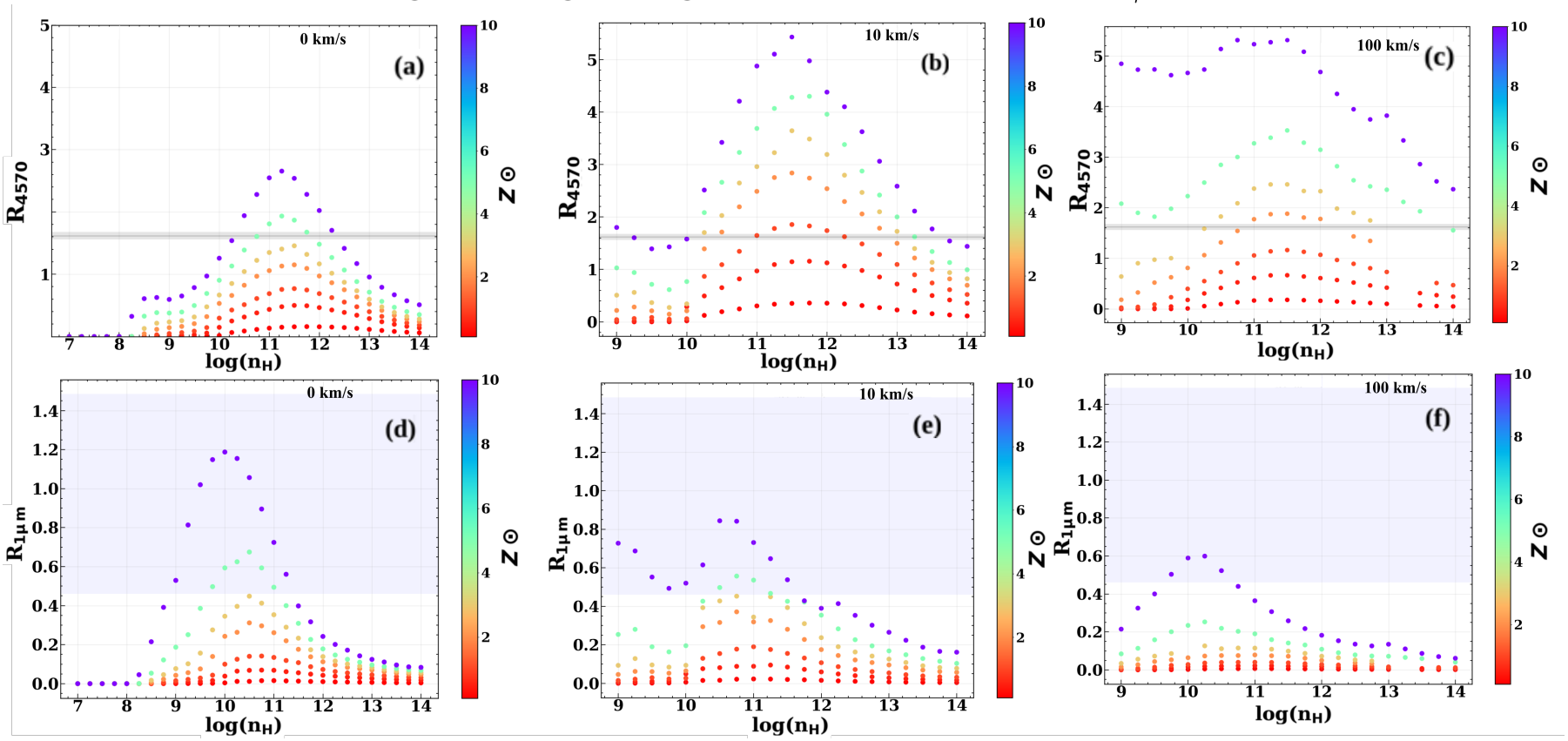

Diagnostic diagrams from simulations for R_{4570} (a)–(c) and $R_{1\mu m}$ (d)–(f) intensities versus log n_H for the column density $N_H = 10^{24}$ cm^{-2} with the micro-turbulent velocities, V_{turb} = 0 km s^{-1} (a, d), 10 km s^{-1}(b, e), and 100 km s^{-1} (c, f). The color bars represent metallicities ranging from 0.1 $Z_\odot$ to 10 $Z_\odot$. The dark gray line represents the observed value of R_{4570}, and the light gray bar shows the associated error margin. The blue shaded region denotes the estimated values for $R_{1\mu m}$ derived from the minimum and maximum Paβ/Paγ ratios obtained using CLOUDY simulations. Check the text for details.

SOURCE: Santos et al. (2024).

3.2.1 No micro-turbulence

Our result without micro-turbulence (i.e., at $V_{\rm turb}$ = 0 km s^{-1}) is shown in Figure 3.3(a, d), where the simulated results from CLOUDY are compared with the observed values for optical and NIR, R_{4570} = 1.62 ± 0.06 and $R_{1\mu\,\rm m}$ = 0.46–1.48, represented by the gray and blue bands, respectively (the symmetric errors for 1-micron values are 0.15 and 0.47, respectively, also shown in Table 3.1). Here, the widths of the gray bands account for the uncertainties associated with the ratios. The results show that R_{4570} can be reproduced with a metal content above 3 $Z_{\odot}$ and with a local hydrogen density between $10^{10.75}$ and $10^{12.50}$ cm^{-3}. Moreover, from the NIR results, to reproduce $R_{1\mu\,\rm m}$, one needs local hydrogen densities varying from $10^{9.00}$ to $10^{11.50}$ cm^{-3}, and a metal content above 3 $Z_{\odot}$. These results demonstrate a suitable physical parameters range to be able to reproduce the FeII strengths for I Zw 1 in the optical and NIR regimes within the setup considered here.

3.2.2 Applying micro-turbulence

Previous studies (BRUHWEILER; VERNER, 2008; PANDA et al., 2020) demonstrated that the value obtained for R_{4570} simulations can also be achieved by decreasing the metallicity but increasing the micro-turbulence velocity. To investigate how changing metallicity and micro-turbulence can increase both optical and NIR emissions simultaneously, we included two cases of micro-turbulent velocity at 10 and 100 km s^{-1} and compared them with the default case (i.e., with no micro-turbulence).

One would expect that the micro-turbulence in the gas would increase the Brownian motion within the cloud and allow for the FeII ions to receive preferentially more ionizing photons, consequently leading to an increase in the intensity of the FeII lines.

The results using micro-turbulence of 10 and 100 km s^{-1} are shown in Figure 3.3 (b, e) and Figure 3.3 (c, f), respectively. Our results for the optical region reveal that the strength of the FeII at 4570Å increases with the increase of micro-turbulence, as expected from previous investigations (PANDA et al., 2020; PANDA, 2021d).

On the other hand, the results in the NIR show a different behavior compared to the ones in the optical, as presented in Figure 3.3. Considering a single case with $n_{\rm H} = 10^{12}$ cm^{-3}, solar metallicity, and $V_{\rm turb}$ = 10 km s^{-1} (see Figure 3.3 e), $R_{1\mu\,\rm m}$ is approximately 0.2, whereas at 100 km s^{-1}, it dropped to about 0.05 (see Figure 3.3f).

In contrast, the case with no micro-turbulence produces the $R_{1\mu\,\mathrm{m}}$ value of about 0.1 (see Figure 3.3 d). Notably, the absence of micro-turbulence results in lower $R_{1\mu\,\mathrm{m}}$ values compared to the scenario with $V_{\mathrm{turb}} = 10$ km s^{-1}, as expected, based on the results obtained in the optical regime.

For metallicities above solar, $R_{1\mu\,\mathrm{m}}$ values overall decrease when compared to scenarios without micro-turbulence. The $R_{1\mu\,\mathrm{m}}$ appears to be suppressed and fails to increase as expected from the optical results. For example, when the highest metallicity value of $10Z_{\odot}$ are considered (see Figure 3.3), $V_{\mathrm{turb}} = 10$ km s^{-1}, and 100 km s^{-1}, the maximum FeII ratio in the NIR is, respectively, about 0.8 and 0.6, whereas in the no-micro-turbulence case, this ratio approximately to 1.2.

It is worth emphasizing that the intensity of the NIR FeII is characterized by the ratio of four isolated emissions to the Paβ line, whereas the ratio in the optical is composed of blended FeII multiplets (m37, m38) normalized by the Hβ (KOVAČEVIĆ et al., 2010; MARZIANI et al., 2021). Hence, to understand the variations in $R_{1\mu\,\mathrm{m}}$, one needs to study the behavior of the Paβ line across the parameter space, especially under the influence of micro-turbulence. We notice that the luminosity of the Paβ emission significantly exceeds that of the NIR FeII lines. In contrast, in the optical range, both the Hβ and the optical FeII lines exhibit a similar increase in luminosity according to density, as shown in Figures 3.4 and 3.5.

Furthermore, the 1-micron lines exhibit two significant excitation mechanisms, collisional and Lyman-α fluorescence, whereas the FeII bump at 9200 Å is exclusively influenced by the Lyman-α fluorescence mechanism (RODRÍGUEZ-ARDILA et al., 2002; MARINELLO et al., 2016b). This distinction is an important indicator of the Lyman-α fluorescence mechanism.

We note that the 9200 Å region, as studied here, remains unaffected by the enhancement of micro-turbulence in the models. This last information will be discussed in detail in the next work.

Figure 3.4 - Micro-turbulence case of 10 km s^{-1}.

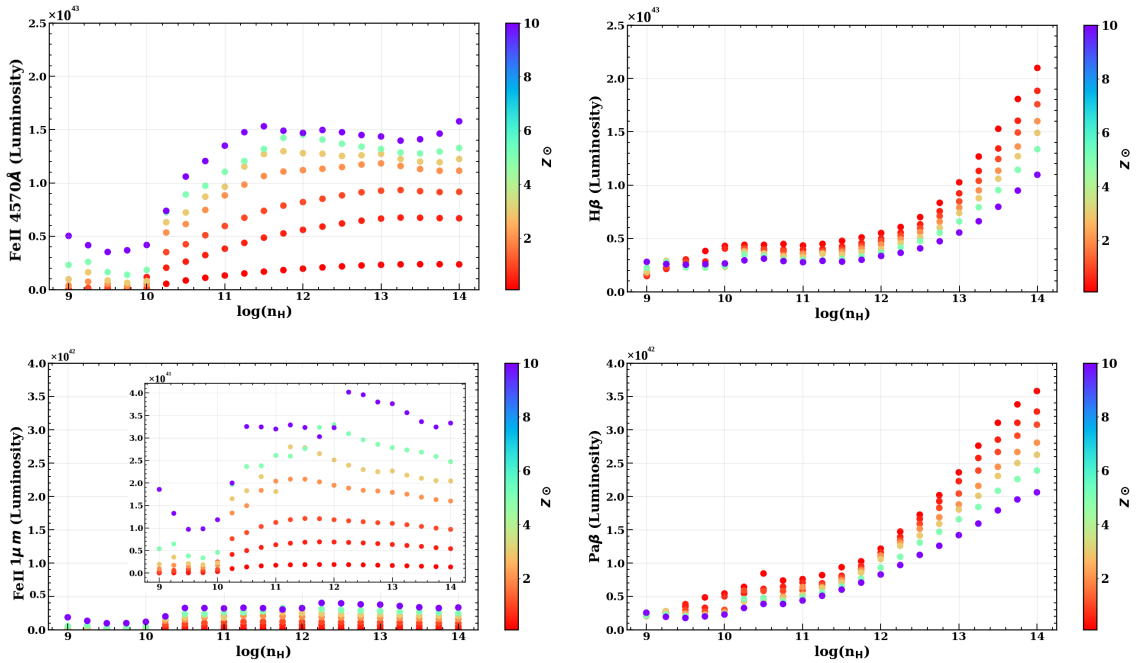

The luminosity of the 4570 Å bump (top left), the luminosity of Hβ line (top right), the sum of the luminosity of the 4 FeII 1-micron lines (bottom left), and Paβ luminosity (bottom right) versus local hydrogen density. The colors correspond to the metal content, $Z_{\odot}$, as indicated.

SOURCE: Santos et al. (2024).

Figure 3.5 - Micro-turbulence case of 100 km s^{-1}.

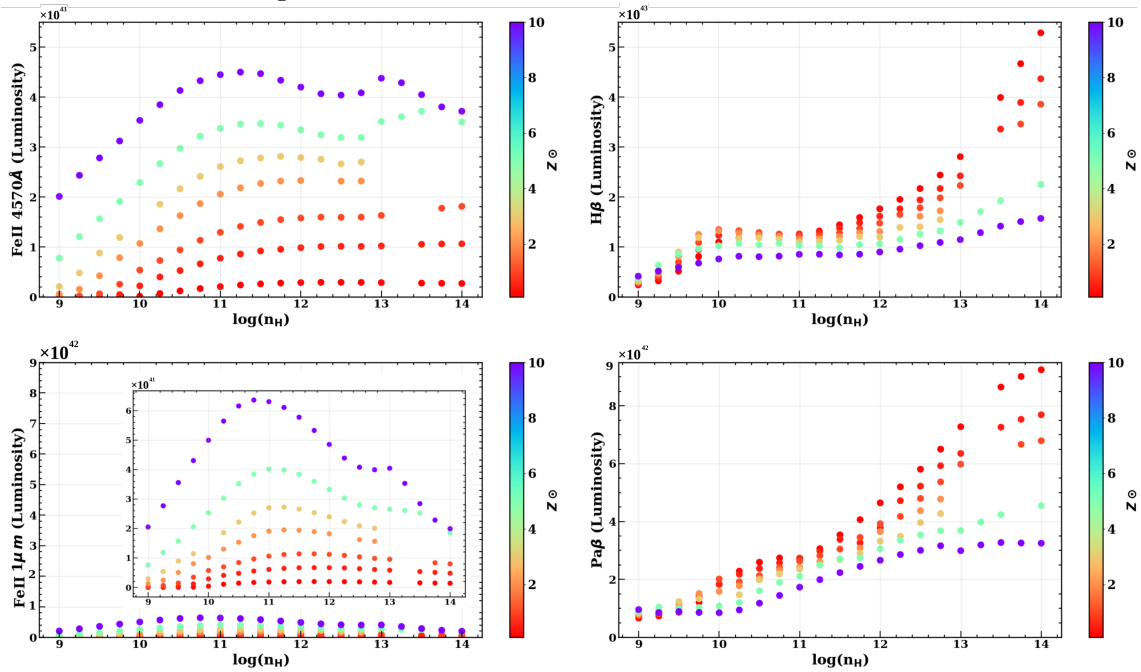

Same as Figure 3.4, but for the micro-turbulence case of 100 km s^{-1}.

SOURCE: Santos et al. (2024).

3.2.3 Discussion

The specific influence of micro-turbulence on the NIR emission of FeII is particularly intriguing in comparison to its well-documented impact in the optical region. The optical models suggest that when micro-turbulence is introduced in the gas, it enhances the intensity of the FeII lines. Surprisingly, our simulations indicate an opposite trend in the NIR region, where the $R_{1\mu\,\mathrm{m}}$ displays lower values when micro-turbulence is on and increases. The discrepancy between the measurements and CLOUDY predictions may pose a question about the true impact of micro-turbulence in the NIR.

However, here we attribute the unexpected effects observed in the 1-micron lines to a limitation in our simulation approach, where we fixed the column density as a stopping criterion. Allowing this parameter to vary freely could introduce a complex interaction between the column density and the metal content in the ionized gas. This is similar to the findings of Panda (2021d), who observed such an interplay in the case of optical FeII emission. When the column density exceeds or approaches $10^{24.5}$ cm^{-2}, the cloud reaches an optical depth about or higher than 1 and the area of scattering effect becomes significant; see Panda (2021d) for more details. The limit at 10^{24} cm^{-2} serves to constrain the cloud's physical condition, drawing inspiration from prior investigations (BRUHWEILER; VERNER, 2008; PANDA, 2021d) wherein the radiative calculations are made under the optically thin regime. Thus, the non-monotonic behavior in the NIR may be ascribed to the collective influence of the micro-turbulence and cloud column density. In light of these intricate findings, further dedicated investigations are necessary to unravel the exact mechanisms at play, which also includes advances in the available FeII atomic datasets.

Despite the limitations discussed, our models are still valid for the $\mathrm{R}_{1\mu\mathrm{m}} \sim 1.81$ value found by Marinello et al. (2016b), even though this value is relatively high within the physical conditions proposed in this study. However, to reproduce such a high value, it is required a metal content that exceeds $10\,Z_{\odot}$. That might mean that the optical and NIR FeII emissions require quite different metal compositions, even though they are formed in clouds that should be spatially located very close to each other or still in the same cloud. This latter aspect is confirmed by the correlation observed for the FWHMs for FeII in the optical and NIR (MARINELLO et al., 2016b). Nevertheless, exploring scenarios with significantly elevated metal content may be a possibility in future research on the NIR FeII emission, especially for high-accreting sources.

Furthermore, it is worth emphasizing the importance of investigating how the hydro-

gen line ratios within the BLR of an AGN vary under different physical conditions. This inquiry will significantly improve the precision of measuring the FeII ratio in the NIR for quasars with a non-reliable Paβ line (see Marinello et al. (2016b) and Marinello et al. (2020a) for other examples). A future study should be considered, as it has the potential to further refine our understanding of AGN environments and enhance the accuracy of key astrophysical measurements.

In summary, this first joint analysis of the iron emission in the optical and NIR spectra of I Zw 1 was devoted to understanding the physical conditions that leads to the FeII emission in this source. We investigated how changes in micro-turbulence and metal content impact both the optical and NIR emissions of FeII. To this purpose we introduce micro-turbulent velocities of 10 and 100 km s^{-1}, a range of 10^{9}–10^{14} cm^{-3} in the cloud density and metal content from sub-solar to 10 times solar. Notably, this research is the first one to examine the impact of micro-turbulence in the NIR regime. While the findings here align with prior results in the optical region, when micro-turbulence is introduced in the NIR, we notice conflicting results.

Nonetheless, there is an overall agreement within the parameter ranges studied in the two wavelength regimes. The set of physical conditions that simultaneously reproduce optical and NIR FeII intensities are $n_{\rm H} = 10^{10.75}$–$10^{11.50}$ cm^{-3} and a metal content within the range 5 $Z_{\odot} \lesssim Z \lesssim 10\ Z_{\odot}$. In conclusion, this result is significant not only for this source but is also applicable for I Zw 1-like AGN.

3.3 Modelling the FeII Emission using new atomic models

In this section, we conduct a simultaneous analysis of optical and NIR FeII emission to understand the physical conditions in AGN using new atomic models of Tayal and Zatsarinny (2018), and Smyth et al. (2018). We also examine the contribution of Lyman-α fluorescence to the FeII spectrum and estimates its impact on the gas physical conditions. Additionally, our simultaneous approach allows us to explore the CaT and OI emission as an analogs of the FeII gas.

Building upon our previous work using the FeII dataset from Verner et al. (1999), we examine the influence of different micro-turbulence velocities (0, 10, and 100 km s^{-1}). These velocities impact the physical conditions necessary to simulate the R_{4570} and $R_{1\mu\,\rm m}$ ratios. A detailed discussion of the results from these simulations is presented in the following sections.

3.3.1 Analysis without Micro-turbulence

Figures 3.6 and 3.7 show the parameter space of metallicity versus local hydrogen density. The color bar represents the R_{4570} and $R_{1\mu\,\mathrm{m}}$ ratios. The top panels show models without micro-turbulence, while subsequent panels illustrate results with increasing micro-turbulence, i.e., $v = 10\,\mathrm{km\ s^{-1}}$ (middle row) and $v = 100\,\mathrm{km\ s^{-1}}$ (bottom row), which we will analyze in the next subsection. We also include key observational constraints. The solid black line represents the observed value of R_{4570}, with dashed black lines marking the associated uncertainties. The white dot-dashed lines show the range of $R_{1\mu\,\mathrm{m}}$ values estimated in Section 3.1.

The results using the Smyth et al. (2018) FeII atomic model (Figure 3.6) show that both $R_{1\mu\,\mathrm{m}}$ and R_{4570} can be reproduced simultaneously when the local hydrogen density ranges from $10^{11.50}\,\mathrm{cm^{-3}}$ to $10^{12.50}\,\mathrm{cm^{-3}}$ and the metallicity is greater than $2\,Z_{\odot}$. We note, though, that the ratios can be reproduced individually in a wider range of conditions. For instance, the observed $R_{1\mu\,\mathrm{m}}$ ratio can be reproduced from subsolar metallicity, $0.5\,Z_{\odot}$, and a density range of $10^{10.0}\,\mathrm{cm^{-3}}$ to $10^{11.0}\,\mathrm{cm^{-3}}$, while all solutions for R_{4570} requires a higher metallicity condition, from $2\,Z_{\odot}$, and a different N_{H} range, from $10^{11.00}\,\mathrm{cm^{-3}}$ to $10^{12.00}\,\mathrm{cm^{-3}}$. Such metallicities were not obtained when using the Verner et al. (1999) dataset (see previous section) where the minimum metallicity requirement was $\mathrm{Z}_{\odot}$ larger than 3. Without micro-turbulence, Panda (2021d) obtained a metallicity $\sim 10{-}20\ Z_{\odot}$. This represents a significant improvement provided by the application of the updated dataset utilized in the current study.

The results obtained using the Tayal and Zatsarinny (2018) dataset are present in Figure 3.7. We reproduce R_{4570} and $R_{1\mu\,\mathrm{m}}$ under overlapping physical conditions, with local hydrogen densities spanning from $10^{11.25}\,\mathrm{cm^{-3}}$ to $10^{11.50}\,\mathrm{cm^{-3}}$ and metallicity greater than $3\,Z_{\odot}$. It is noteworthy that the $R_{1\mu\,\mathrm{m}}$ is reproduced within a density range of $10^{10.50}\,\mathrm{cm^{-3}}$ to $10^{12.50}\,\mathrm{cm^{-3}}$, and exhibits metallicity above $2\,Z_{\odot}$. In a similar N_{H} range, we obtained R_{4570} from $10^{11.25}$, $\mathrm{cm^{-3}}$ to $10^{11.75}\,\mathrm{cm^{-3}}$, however it is required a higher metallicity condition than $3\,Z_{\odot}$.

From Smyth et al. (2018) and Tayal and Zatsarinny (2018) results, we note that despite FeII datasets advancements, the optical results remain very comparable across different models, likely because the number of transitions remains the same. Nevertheless, a clear improvement is observed in the NIR counterpart with the newer models, particularly using Smyth et al. (2018). This discrepancy may be due to differences in their respective energy levels, as NIR FeII emissions require energies above

Figure 3.6 - Parameter space, showing hydrogen density ($\log N_{\rm H}$) versus metallicity ($Z_{\odot}$) for models using the Smyth FeII dataset.

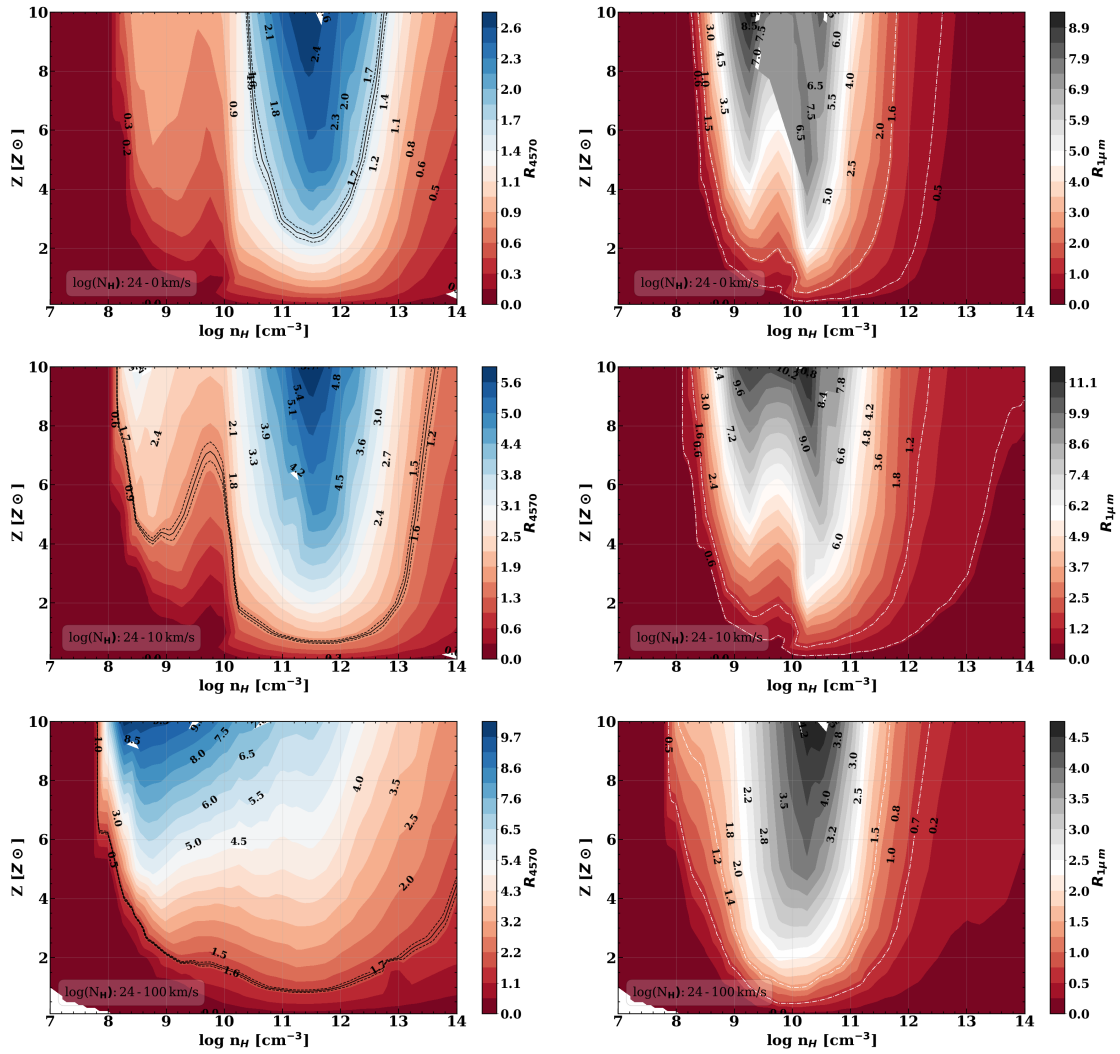

The colors indicate the $\rm R_{4570}$ or $\rm R_{1\mu m}$ ratios. From top to bottom, the panels represent differences in micro-turbulence velocities: $v = 0\,\rm km\ s^{-1}$, $v = 10\,\rm km\ s^{-1}$, and $v = 100\,\rm km\ s^{-1}$. The white dot-dashed lines represent the range of values for Paβ flux and FeII 1 μm line intensities based on our approach (see Section 3.1). The solid line and the dashed black lines, respectively, are the observed value of R_{4570} and associated error bars.

$\sim 7\,$eV, and in some cases up to $\sim 13\,$eV. While Tayal and Zatsarinny (2018) extends up to approximately $\sim 16.6\,$eV, Smyth et al. (2018) reaches the highest energy levels, up to $\sim 26.4\,$eV. These energy levels are critical for NIR emission lines, whereas the default dataset Verner et al. (1999) only reaches up to 11.6 eV. In contrast to NIR FeII transitions, the bulk of the optical FeII emission requires energies of $\sim 5\,$eV (RODRÍGUEZ-ARDILA et al., 2002; MARINELLO et al., 2016b; MARINELLO et al., 2020a), which is effectively accounted for in all datasets.

Figure 3.7 - Same as Figure 3.6 but for Tayal FeII atomic dataset.

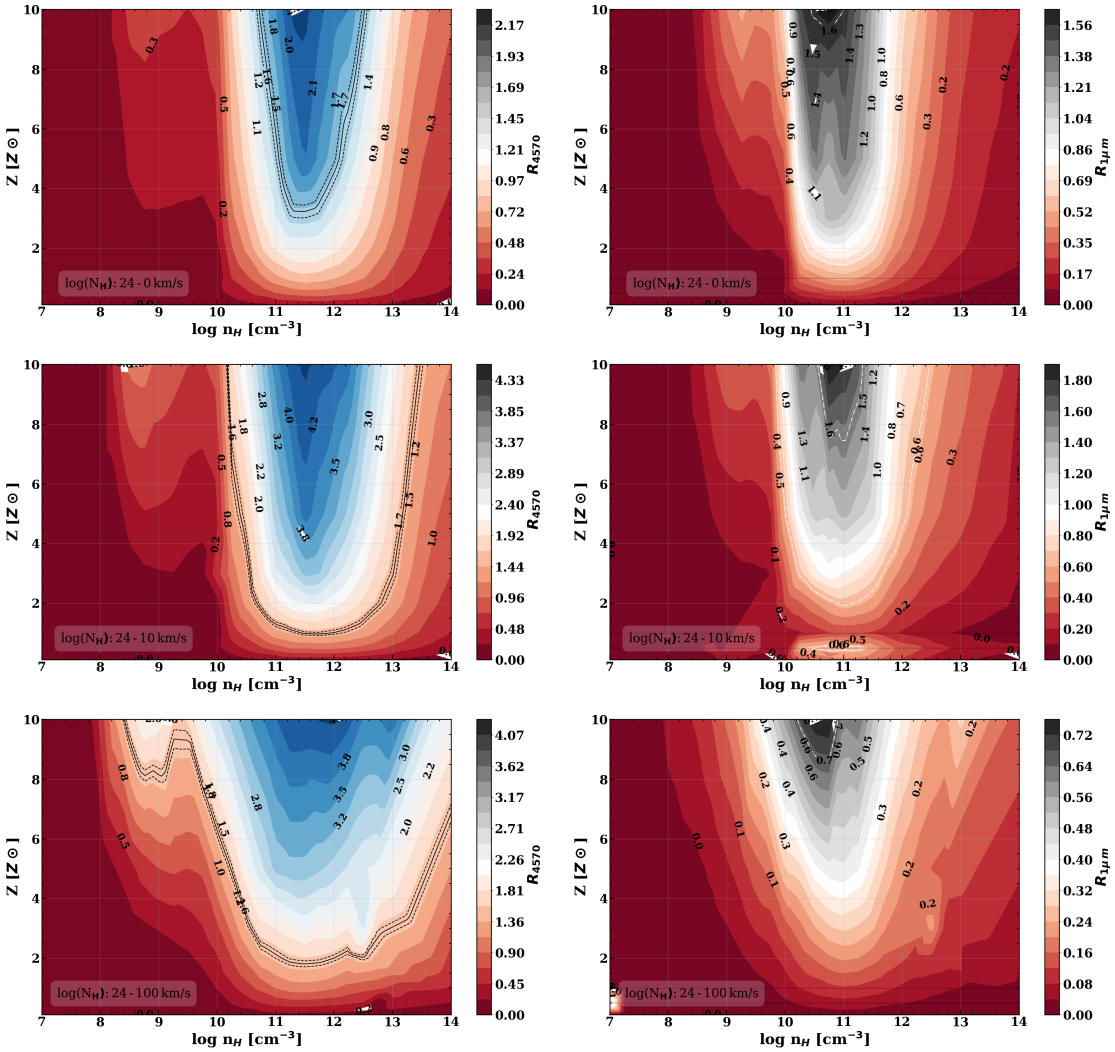

3.3.2 Impact of micro-turbulence on FeII emission

Here, we use micro-turbulences of $v = 10\,\mathrm{km\ s^{-1}}$, and $100\,\mathrm{km\ s^{-1}}$ in our models, as shown in figuras 3.6 and 3.7 as representative cases. We observed an improvement in the FeII ratios for both datasets. Considering $v = 10\,\mathrm{km\ s^{-1}}$ (see middle panels in Figure 3.6 and 3.7), R_{4570} and $R_{1\mu\,\mathrm{m}}$ ratios can be simultaneously reproduced under overlapping physical conditions, with local hydrogen densities from $10^{11.00}\,\mathrm{cm^{-3}}$ to $10^{12.00}\,\mathrm{cm^{-3}}$ at solar metallicity. Compared to Verner et al. (1999) results, the set of physical conditions that can simultaneously reproduce both ratios is $n_{\mathrm{H}} = 10^{10.75}$–$10^{11.50}$ $\mathrm{cm^{-3}}$, and a metal content within the range $5\ Z_{\odot} \lesssim Z \lesssim 10\ Z_{\odot}$. The main advantage of the Smyth et al. (2018) and Tayal and Zatsarinny (2018) datasets is their ability to reproduce the FeII ratios under metallicity conditions that are three times lower than those required by the Verner et al. (1999) model.

Figure 3.7 in middle panel show our models for micro-turbulence of $10\,\mathrm{km\ s^{-1}}$ using Tayal and Zatsarinny (2018) FeII dataset. In general, the results are positive for reproducing FeII ratios simultaneously, and they are comparable to those without micro-turbulence, much like the results obtained for the Smyth et al. (2018) dataset. In addition to that, we observe a small local hydrogen density subset of solutions, $10^{10.50}\,\mathrm{cm^{-3}} < n_{\mathrm{H}} < 10^{11.50}\,\mathrm{cm^{-3}}$, where the ratios exhibit different metal conditions, solar metallicity for optical and $0.5\ Z_{\odot}$ for NIR, approximately. The R_{4570} and $R_{1\mu\,\mathrm{m}}$ are simultaneously reproduced around $10^{10.75}\,\mathrm{cm^{-3}} < n_{\mathrm{H}}$ with $2Z_{\odot}$ metallicities. Also, we note that the optical models shown in Figure 3.7 provide a broader n_{H} range of solutions, which can be reproduced under solar conditions.

For completeness, we also ran models with micro-turbulence at 100 $\mathrm{km\ s^{-1}}$ for Smyth et al. (2018) and Tayal and Zatsarinny (2018) atomic data, as shown in the bottom panels in figuras 3.6 and 3.7. We discarded these results from our analysis because the NIR physical conditions are very different from the optical conditions.

Despite the inclusion of micro-turbulence, the range of n_{H} values remains consistent with the models without micro-turbulence. For optical FeII emission, we found $10^{10.75}\,\mathrm{cm^{-3}}$ to $10^{12.25}\,\mathrm{cm^{-3}}$, while for NIR emission $10^{9.75}\,\mathrm{cm^{-3}}$ to $10^{11.75}\,\mathrm{cm^{-3}}$. In general, our results show that R_{4570} and $R_{1\mu\,\mathrm{m}}$ can be reproduced in more consistent physical conditions than models without micro-turbulence.

We also identified solutions where R_{4570} and $R_{1\mu\,\mathrm{m}}$ were obtained individually at densities below $n_{\mathrm{H}} = 10^{10}\,\mathrm{cm^{-3}}$ using Smyth et al. (2018) and Tayal and Zatsarinny (2018). Considering the spatial proximity of the optical and NIR emission clouds

(MARINELLO et al., 2016b), we discarded these solutions due to the significantly different metallicity requirements: solar for NIR and $4\,Z_{\odot}$ for optical. On the other hand, we just consider solutions above $10^{10}\,\mathrm{cm}^{-3}$, because they were considered reliable once is possible simultaneously reproduce R_{4570} and $R_{1\mu\,\mathrm{m}}$ ratios. Moreover, even in the case which are possible obtained individual intensities ratios, in general the metallicity conditions are very similar, $1\,Z_{\odot}$ for R_{4570}, and $0.5\,Z_{\odot}$ for $R_{1\mu\,\mathrm{m}}$.

Our results indicate that, independently of the FeII data used, increasing the micro-turbulence to the gas allows the ratios to share similar physical conditions, such as lower metal content. This finding is important because it confirms previous optical studies and demonstrates that the effect remains consistent (PANDA, 2021d). The use of micro-turbulence reduces the problem of a higher metal content of BLR, such as $10\,Z_{\odot}$, which is not simple to understand physically.

Finally, when we analyze the $R_{1\mu\,\mathrm{m}}$ and R_{4570} ratios individually, we note a trend independent of the dataset: NIR FeII reaches its maximum ratio at hydrogen densities of $10^{10.0} - 10^{11.0}\,\mathrm{cm}^{-3}$, whereas optical FeII peaks at higher densities of $10^{11.0} - 10^{12.0}\,\mathrm{cm}^{-3}$ and tends to require higher metallicity compared to the NIR. This result suggests that the NIR FeII emission is produced farther away from the central source than the optical counterpart. It also supports the scenario where the optical (MARINELLO et al., 2016b) FeII might be preferentially more affected due to the accelerated mass ejected material, while the NIR is more shielded.

3.4 Discussions

3.4.1 Reinforcing the paradigm of optical−NIR FeII correlation via modeling

Unlike UV-optical lines, the NIR FeII emission lines have the significant advantage of being isolated or semi-isolated (see Figure 3.8), allowing for easier modeling and accurate determination of individual line properties. In the NIR spectrum, the most intense FeII emission lines are collectively known as the $1\,\mu$m lines, which originate from the same energy level $(\mathrm{t},\,\mathrm{u})^4\,\mathrm{G} \rightarrow \mathrm{z}^4\,(\mathrm{D},\,\mathrm{F})$ (RODRÍGUEZ-ARDILA et al., 2002; MARINELLO et al., 2016b; MARINELLO et al., 2020a). The decay and consequent emission of the $1\,\mu$m lines populate the $\mathrm{z}^4\,(\mathrm{D},\,\mathrm{F})$ level responsible for the optical emission centered at 4570 Å bump.

From an observational point of view, the R_{4570} and $R_{1\mu\,\mathrm{m}}$ ratios are intrinsically correlated, suggesting a common excitation mechanism responsible for both emissions,

likely dominated by Lyman-α fluorescence (MARINELLO et al., 2016b). This correlation can play a key role in allowing comparative studies of FeII emissions across different wavelength ranges.

Figure 3.8 - The UV-optical-NIR FeII emission spectrum from a constant density ($n_{\rm H}$=$10^{10.75}$ cm^{-3}) single cloud with a column density of 10^{24} cm^{-2}, assuming solar abundances.

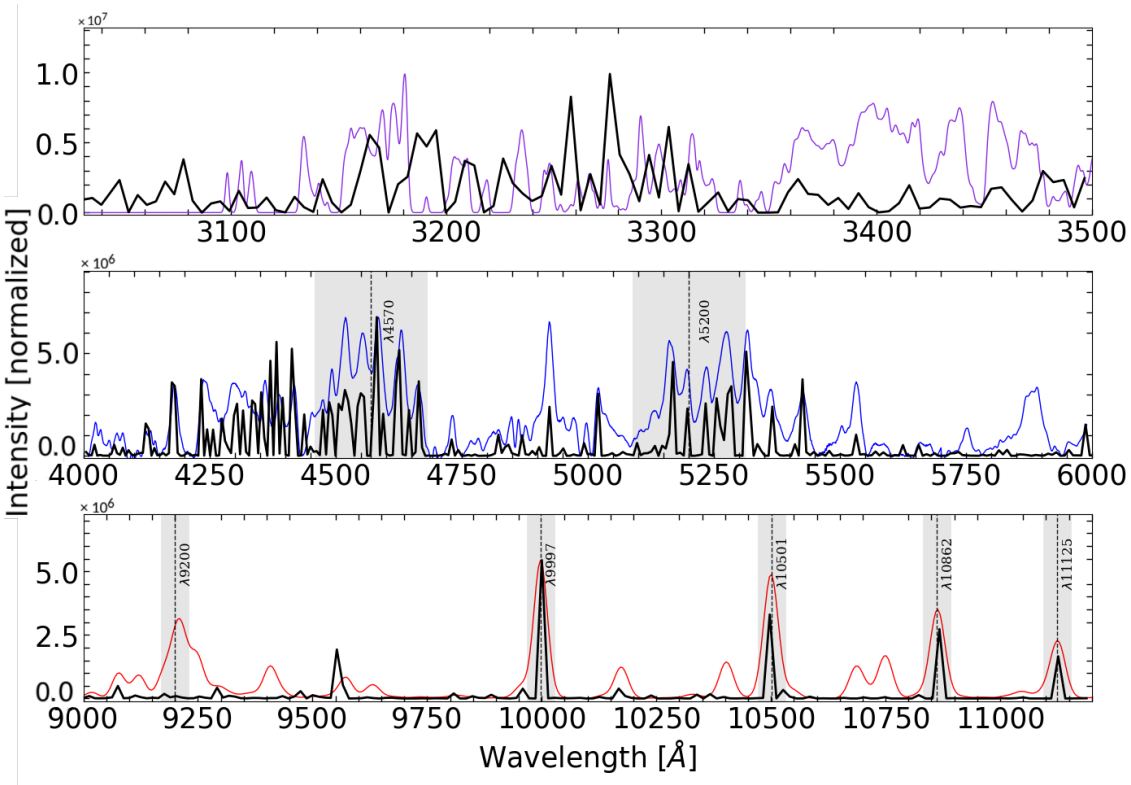

In purple, blue, and red, respectively, UV (VÉRON-CETTY et al., 2004), optical (BOROSON; GREEN, 1992) and NIR FeII (GARCIA-RISSMANN et al., 2012). The optical and UV are naturally broadened because they are empirical templates. The NIR was broadened by 1107 ± 507 km s^{-1} based on λ 10502 FWHM. The FeII optical blue and red bumps, centered at λ4570 and λ5200, are highlighted in gray, as well the 1 μm lines (λ9997, λ10502, λ10863, λ11127) and the 9200 Å bump. The grey shadows emphasize the area corresponding to our lines of interest. The pseudo-continuum was constructed using the FeII dataset from (SMYTH et al., 2018).

In this context, our results from photoionization modeling (constant density, single cloud approximation) corroborate these observational findings by demonstrating that optical and NIR FeII emissions can indeed be reproduced under overlapping physical conditions. We find that both emissions can be simultaneously reproduced using a narrow range of local hydrogen density from $10^{11.0}$ cm^{-3} to $10^{12.0}$ cm^{-3},

with nearly solar metallicity assuming a small micro-turbulence velocity of 10 km s^{-1}. This agreement between models and observations strengthens the hypothesis that the physical conditions driving both optical and NIR FeII emissions are closely related. Our work links theoretical and observational results, providing physical evidence of the common environment responsible for these emissions.

In addition, we note that regardless of the FeII dataset used, NIR FeII reaches its maximum strength at local hydrogen densities of $10^{10.0} - 10^{11.0}$ cm^{-3} under sub-solar metallicity conditions. In contrast, optical FeII peaks at densities in the interval $10^{11.0} - 10^{12.0}$ cm^{-3} and requires at least solar metal content. This variation may indicate an alternative scenario that needs to be explored, that optical and NIR FeII emissions originate from slightly different locations within the BLR's vertical structure. Previous findings using the FeII dataset from Verner et al. (1999) also indicate that emissions reach their maximum ratios at different intervals of N_H (SANTOS et al., 2024). This behavior is also observed even under low column density conditions, such as $10^{23.0}$ cm^{-2} (SANTOS et al., 2023). Further modeling across other strong FeII-emitting AGN is necessary to confirm the persistence of these results.

3.4.2 Impact of Lyman-α excitation on optical and NIR FeII emissions

It has been more than two decades since Lyman-α fluorescence was proposed as the only mechanism responsible for the FeII emission at 9200 Å (SIGUT; PRADHAN, 1998), and a major contributor to the NIR FeII spectral features, later confirmed observationally (RODRÍGUEZ-ARDILA et al., 2002; MARINELLO et al., 2016b). Lyman-α can excite energy levels up to 13 eV, and through the decay process contributes to populate lower energy levels (around 5 eV) that are responsible for optical FeII emission. However, several key questions remain: Does Lyman-α affect the optical and NIR FeII emissions differently? Does its contribution vary with different physical conditions? And to what extent does this mechanism contribute to the overall emission in these wavelength ranges?

To evaluate the influence of Lyman-α fluorescence in 1 μm and 4570 Å emissions, we consider two sets of simulations within our CLOUDY setup: enabled (which is activated by default in CLOUDY) and another without it. For these models, we considered hydrogen densities ranging from $10^{8.0}$ to $10^{13.0}$ cm^{-3}, metallicities from 0.1 to 5 times the solar value, and a micro-turbulence velocity of 10 km s^{-1} for a column density, $N_H = 10^{24.0}$ cm^{-2}. By comparing the luminosity ratios from the two cases (with and without Lyman-α) as a function of hydrogen density and metallicity, we obtain insights into the impact on the 1 μm and 4570 Å emissions. Our result,

shown in Figure 3.9, reveals how Lyman-α excitation affects the optical and NIR spectra.

Overall, we observe that the presence of Lyman-α excitation leads to an increase in the FeII intensities in both the optical and NIR regimes, particularly notable at lower hydrogen densities and metallicities. The ratio close to 1, at $n_{\rm H} = 10^{10.75}$ cm^{-3} and solar metallicity (see Figure 3.9), indicates that the effects with and without Lyman-α are relatively indistinguishable under these physical conditions for optical FeII. We observe similar behavior for 1 μm lines, in densities exceeding $10^{11.0}$ cm^{-3} and in high metallicities ($> 2\,Z\odot$). This indicates that the presence of other excitation mechanisms, such as collisional excitation mechanisms, is significant in these dense environments. Consequently, Lyman-α may not be the primary excitation mechanism under these conditions, leading to a possible decrease in FeII intensity observed at 1 μm.

In the absence of Lyman-α excitation (see Figure 3.10), we observe a decrement in the luminosity of FeII emission. Despite the absence of Lyman-α pumping, we still recover the 1 μm lines, indicating that collisional excitation and other mechanisms (e.g., FeII pumping) still contribute to the excitation processes. However, these mechanisms contribute much less significantly than Lyman-α (MARINELLO et al., 2016b). From these results, we infer that when Lyman-α photons are abundant, they become the dominant excitation source, leading to enhancement of the emissions, as illustrated in Figure 3.6 (middle panel).

Although the optical and NIR results are aligned, the effect of Lyman-α on the 4570 Å line does not enhance the emission as significantly as it does in the NIR, as shown by the comparison of Figures 3.6 (Lyman$-\alpha$ on) and Figure 3.10 (Lyman$-\alpha$ off). This indicates that the presence of Lyman$-\alpha$ does not primarily contribute to increasing the 4570 Å emissions. This can be attributed to several factors, such as, efficiency of energy transfer, energy redistribution during the transitions, and non-radiative de-excitation processes, in addition to preferentially denser regions producing the optical FeII lines.

The energy redistribution in the decay process consists of probabilities that depend on the Einstein coefficients (A_{ki}), based on the values available from the NIST Atomic Spectra Database (NIST)[2] (KRAMIDA et al., 2024). For the transitions of interest present in the Grotrian diagram (see Figure 1.4), we can see that the

[2]National Institute of Standards and Technology https://physics.nist.gov/asd

Figure 3.9 - The contour plots show the impact of Lyman-α mechanism on optical and NIR FeII emission.

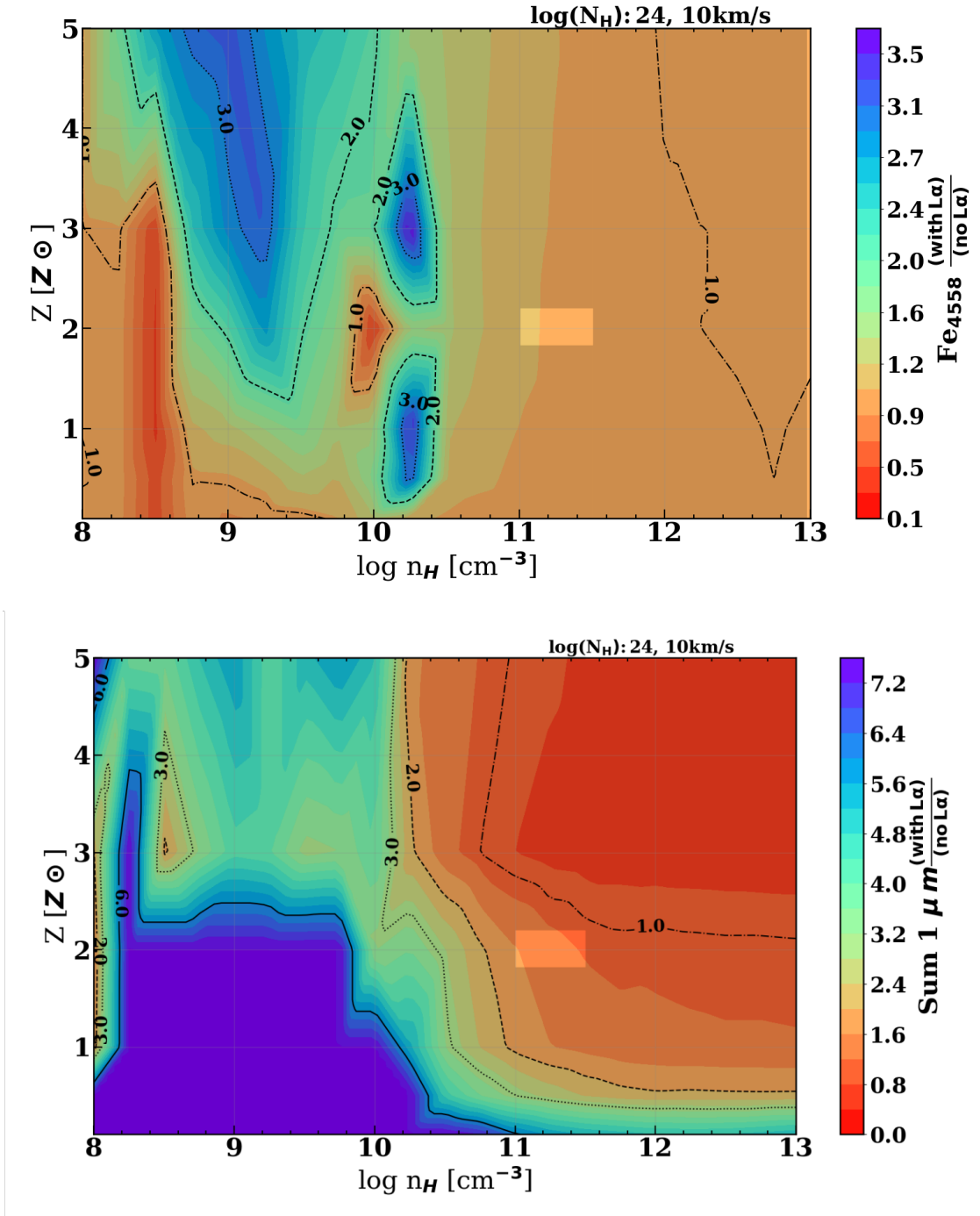

The ratio of FeII emission with and without Lyman-α excitation for the 4570 Å(left) and 1 μm (right) lines are represented in color scales. The plots are a function of hydrogen density ($\log n_H$) and metallicity ($Z_\odot$) for a turbulence velocity of 10 km s^{-1} and a column density of 10^{24} cm^{-2}. The shaded region represents the simultaneous solutions found for the reproduction of FeII emission in both NIR and optical.

different coefficients for optical and NIR emissions indicate distinct probabilities of radiative decay for the various energy levels. For example, the A_{ki} coefficients for UV−NIR transitions are significantly higher than those for optical transitions. This suggests that most of the energy after the initial excitation by Lyman−α is emitted as UV and NIR, where it is predominantly redistributed through these transitions before it can contribute to levels responsible for optical emissions. This may explain why Lyman−α does not maximize optical emissions as it does in the NIR.

It is also essential to highlight that the 9200 Å FeII emission provides crucial information to study the influence of Lyman−α, and can lead to more accurate recovery of the NIR FeII spectrum (SIGUT; PRADHAN, 1998; SIGUT; PRADHAN, 2003; RODRÍGUEZ-ARDILA et al., 2002; MARINELLO et al., 2016b). In this work, we note that none of the available atomic FeII dataset reproduce the 9200 Å emission. The improvement of energy levels, (t, u)^4 G, responsible for the 9200 Å is critical as it may have the potential to bias UV studies, particularly in the secondary Lyman−α cascades from the u^4 P group at 2800 Å (as shown in the Grotrian diagram), and primary transitions from the (t, u)^4 G group at 1800 Å. The improvement of the atomic datasets is crucial for improving the accuracy of recovering both NIR and UV spectroscopic measurements.

Figure 3.10 - FeII ratios using Lyman-α off.

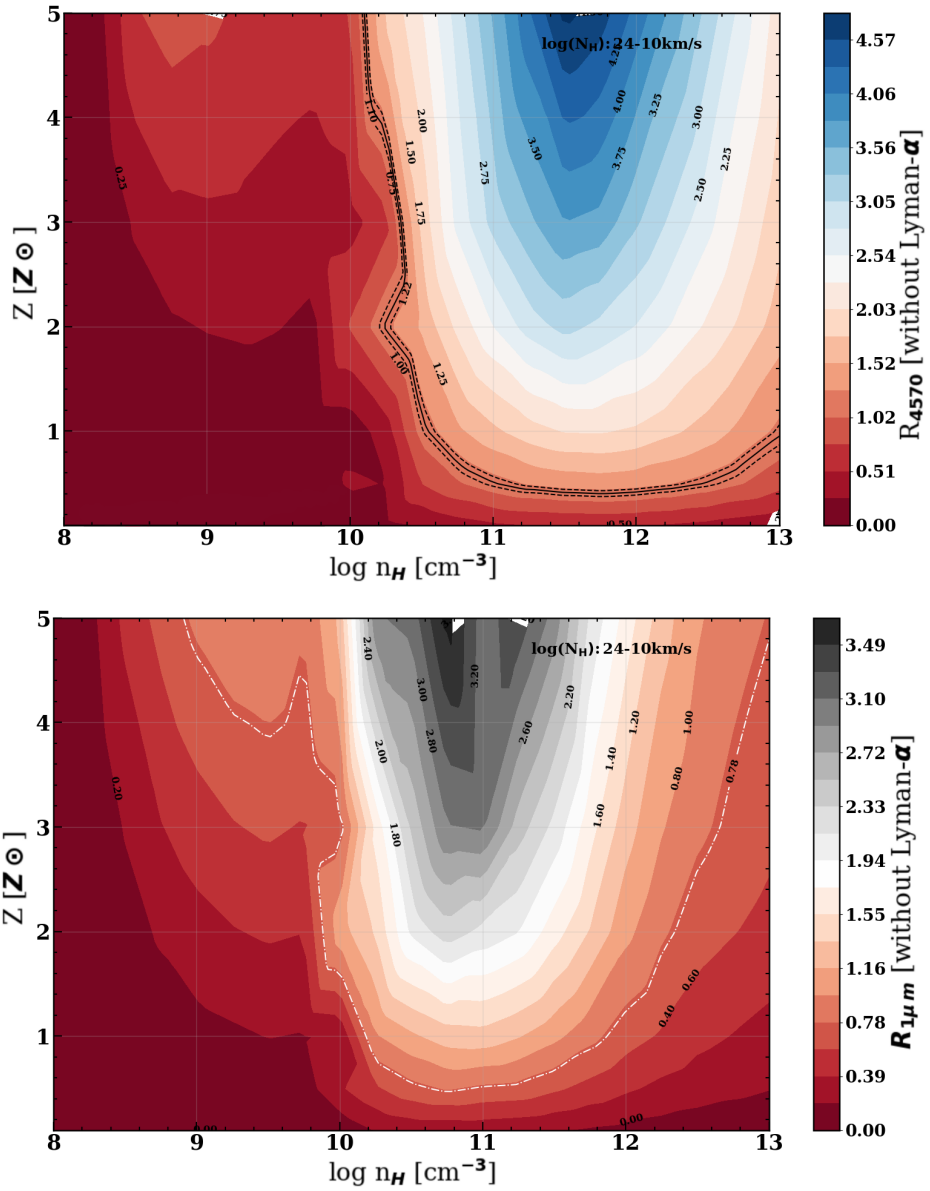

The figure shows the optical ratio R_{4570} (top panel), and the $R_{1\mu m}$ (bottom panel) with Lyman-α off. Both panels display the ratios for $10^{8.0}\,\mathrm{cm}^{-3} < \mathrm{n_H} < 10^{13.0}\,\mathrm{cm}^{-3}$. The colors correspond to different metal content. The cloud column density is $10^{24}\,\mathrm{cm}^{-2}$ and the turbulence velocity is $10\,\mathrm{km\ s}^{-1}$. The dataset employed is Smyth et al. (2018).

3.4.3 The FeII−CaT−OI connection

Persson (1988) was a pioneer in proposing a correlation between CaT and OI emissions in AGN with strong FeII emissions. In his work, he noted that these AGN also displayed prominent CaT and OI features in their spectra. Building on this start-

ing point, several observational and theoretical studies (JOLY, 1991; RODRÍGUEZ-ARDILA et al., 2002; MARINELLO et al., 2016b; PANDA et al., 2020; MARTÍNEZ-ALDAMA et al., 2021b) have investigated the idea of using these less complex ions as a proxy to study the FeII gas, to simplify the spectral analysis and theoretical modeling.

From observational results, FeII, CaT and O I emissions show similar FWHM values (JOLY, 1991; RODRÍGUEZ-ARDILA et al., 2002; MARINELLO et al., 2016b; MARTÍNEZ-ALDAMA et al., 2021b), indicating that these ions share similar kinematics, and likely originate from a co-spatial region. Moreover, theoretical photoionization models (JOLY, 1987; MARTÍNEZ-ALDAMA et al., 2015; PANDA et al., 2020) show that FeII, OI, and CaT ions are emitted in regions with similar physical conditions, such as local hydrogen density ($n_{\rm H}$), ionization parameter (U), and column density ($N_{\rm H}$). Those previous modeling studies have focused on physical properties derived from UV−optical FeII emissions. In contrast, our work uses a simultaneous − optical and NIR − approach, providing a distinct and rarely explored analysis of the environment for the FeII emitter gas.

Since the evidence suggests that O I and CaT could be used as alternatives for FeII study (PANDA, 2021d; MARTÍNEZ-ALDAMA et al., 2021b), we tested the observed OI/CaT ratio in our models to determine their agreement with the theoretical predictions. Figure 3.11 shows the OI/CaT ratio as a function of metallicity ($Z_{\odot}$) and local hydrogen density. The contour lines indicate different ratio values, with colors representing the intensity. Our observed OI/CaT ratio aligns with the black solid-line contour on the plot, corresponding to a range from sub-solar metallicity, and densities $n_{\rm H} = 10^{\,9.0} - 10^{\,11.75}\,{\rm cm}^{-3}$. This shows that the physical conditions under which that emission is formed are comparable to those where FeII is formed. The consistency between our observational data and theoretical models supports the idea that these ions can serve as proxies for investigating FeII emissions in AGN, as suggested by Panda et al. (2020), Panda (2021d), Martínez-Aldama et al. (2021b).

Figure 3.12 presents the luminosity of OI (panel a), CaT (panel b), the sum of FeII emissions at 1 μm (panel c), and luminosity of the 4570 Å bump (panel d), as functions of local hydrogen density ($n_{\rm H}$) and metallicity ($Z_{\odot}$). The observed line luminosity values are represented by the solid black line. Overall, the observed luminosities are well reproduced within the density range of $10^{10.0}$ to $10^{12.0}$ cm^{-3}. From Figure 3.12 we can see that the maximum luminosity emitted by the CaT gas does not coincide with the physical condition range for the maximum NIR FeII and

Figure 3.11 - Parameter space composed by local hydrogen density (log ($N_{\rm H}$) on the x-axis and metallicity in solar units on the y-axis.

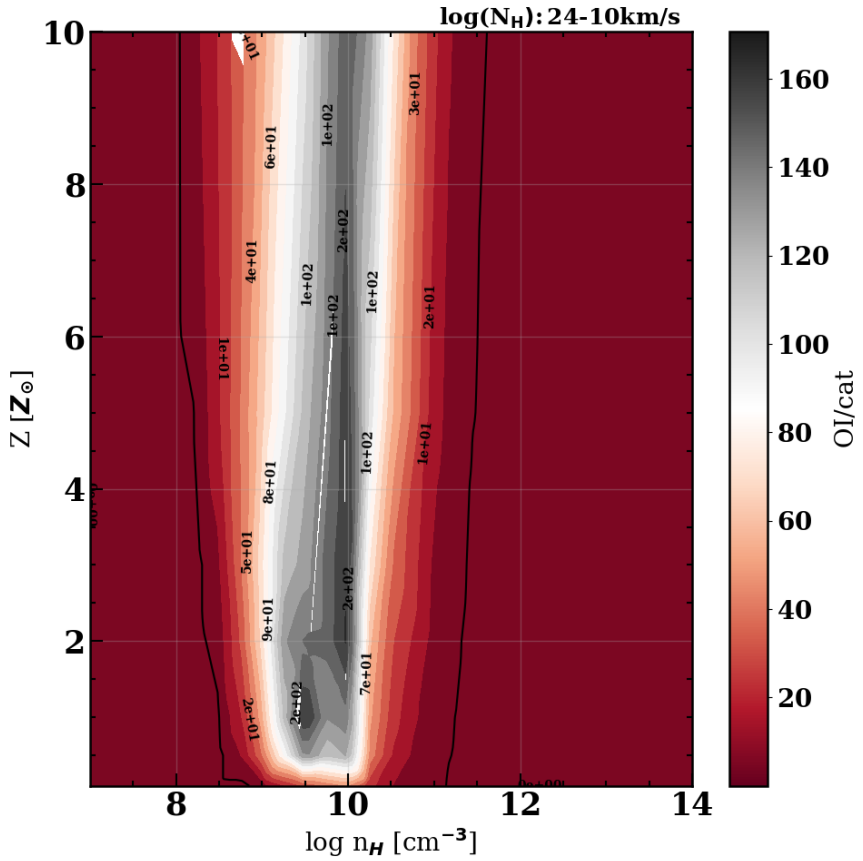

The color bars represent the O I/Ca II ratios from our models, and the black solid line is the observed ratio. We used Smyth et al. (2018) dataset, and parameter set of 10 km s^{-1} micro-turbulence and 10^{24} cm^{-2} column density.

OI emissions.

In Figure 3.12 panel (a), the maximum luminosity of OI occurs within the density range of $10^{10.0}$ to $10^{11.0}$ cm^{-3}, with observed values within the sub-solar to solar metallicity range. This indicates that our models can accurately reproduce these observations at their maximum emitted luminosity. The density range aligns with the region where FeII NIR emission is also maximized, suggesting that these emissions likely occur under the same physical conditions or even in co-spatial regions within the BLR.

While the observed CaT luminosity can be reproduced at densities similar to those of O I and NIR FeII emissions (around $10^{10.0}$ to $10^{11.0}$ cm^{-3}), the maximum CaT luminosity is achieved at higher densities, starting from $10^{11.0}$ cm^{-3}. Notably, the

Figure 3.12 - Parameter phase, composed by local hydrogen density (log ($N_{\rm H}$) on the x-axis and luminosity on the y-axis.

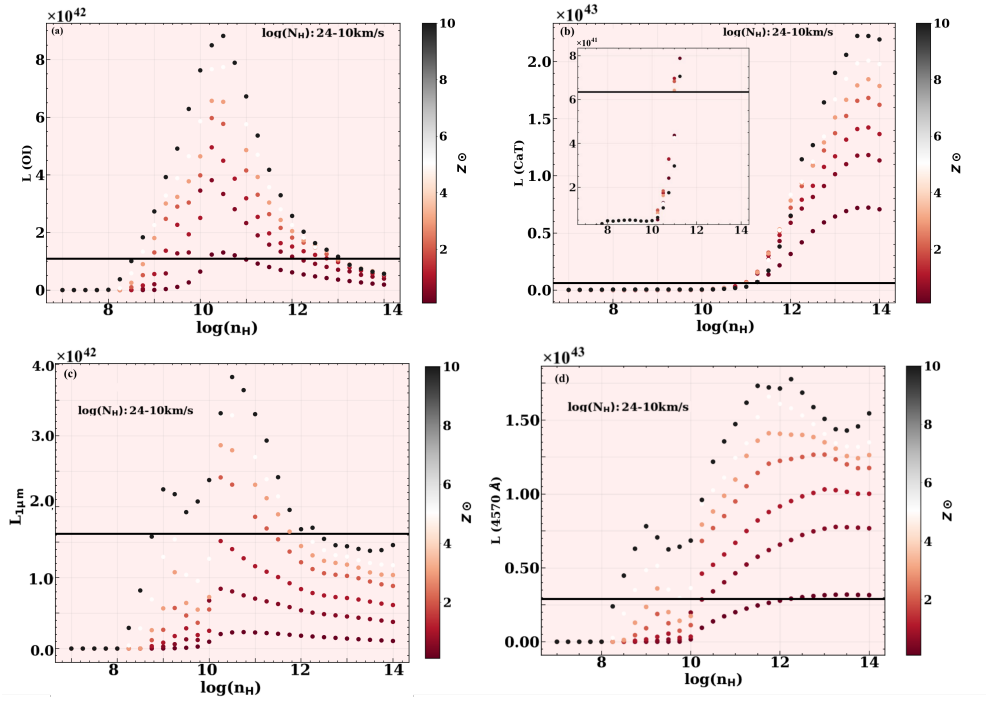

The color bars represent the metallicity in solar units and the black solid line is the luminosity observed value. From panel (a) to (d), show OI luminosity, Ca II luminosity, 1 μm luminosity, and optical luminosity of 4570 Å bump. For all panels, we use 10 km s^{-1} micro-turbulence and 10^{24} cm^{-2} column density, using Smyth et al. (2018) dataset. The luminosities are in erg cm^{-2}s^{-1}.

highest luminosities for optical FeII are also found at densities comparable to those where the peak CaT emission occurs (see Figure 3.12, panel (d)). These results suggest an alternative scenario in which the majority of CaT and FeII emission, originates from the denser and more internal regions of the BLR, corroborating previous findings (PANDA et al., 2020; PANDA, 2021d). In this possible scenario, CaT and FeII emissions could be produced at similar densities to those of OI, and NIR FeII, but their maximum emissions are expected to come from a denser and deeper region of the BLR.

3.5 Conclusions and summary

In this chapter, we have conducted a comprehensive study of FeII emission across the optical and NIR regimes. Our analysis employs state-of-the-art photoionization modeling and atomic FeII datasets to explore the physical conditions of the FeII gas within the BLR in the prototype NLS1 I Zw 1, specifically targeting the reproducibility of the R_{4570} and $R_{1\mu\,\rm m}$. In addition, we compare model predictions to

observations and the possibility that the gas emitting FeII shares similar physical properties to that emitting O I and CaT (MARINELLO et al., 2016b; PANDA et al., 2020).

Our findings confirm that the optical and NIR FeII emissions can be reproduced under overlapping physical physical conditions using the datasets from Smyth et al. (2019) and Tayal and Zatsarinny (2018). For the Smith dataset, the local hydrogen density ranges from $10^{11.0}$ - $10^{12.0}$ cm^{-3} and the metallicity is up to solar. The addition of micro-turbulence (10 km s^{-1}) in the models significantly improves the agreement between the observed and simulated spectra, acting as a metallicity controller and bringing the theoretical predictions closer to the observed (PANDA et al., 2020).

Furthermore, our work highlights the crucial role of Lyman-α fluorescence in enhancing the overall FeII NIR emission, particularly the 1 μm lines. This excitation mechanism also contributes significantly to the FeII emission in the UV. Lyman-α fluorescence indirectly influences the optical region as well, as the cascading process from the NIR emission levels extends to the optical, affecting in particular the emission around 4570 Å. Given that our results show a less pronounced influence of Lyman-α on optical emission, we suggest that other mechanisms, such as collisional excitation, may be responsible for the optical emission in these regions.

We observed that the O I/CaT ratio agrees with theoretical models, suggesting that the O I and CaT emissions can serve as proxies for the FeII emission, particularly under similar physical conditions. However, we also found that while the observed CaT luminosity can be reproduced at densities comparable to those of O I and NIR FeII emissions, the maximum CaT luminosity is observed at higher densities, similar to the maximum optical FeII.

These findings suggest that CaT and optical FeII emissions originate primarily from denser inner regions of the BLR, while O I and NIR FeII emissions likely arise from relatively less dense outer regions. This possible scenario implies a stratified structure within the BLR, where different ions peak their emission at different depths. This stratification hints at a complex layering of emission regions, with O I, CaT, and FeII emissions trace varying physical conditions within the BLR, potentially occurring at different heights above the accretion disk. This supports the idea that, while O I and CaT can act as proxies for FeII under certain conditions, the specific physical context must be taken into account to accurately interpret these emissions.

Our study provides a more detailed view of the physical conditions within the low ionization gas, emphasizing the importance of considering an appropriate atomic dataset for the spectral region of interest. Future work could further refine these models, exploring other FeII emitter AGN to verify if these findings can be generalized for I Zw 1-like sources.

4 FIRST OBSERVATION OF DOUBLE-PEAKED O I EMISSION IN THE NEAR-INFRARED SPECTRUM OF AN ACTIVE GALAXY

AGN spectra typically exhibit symmetric or asymmetric BLR emission line profiles, with the latter displaying blue or red asymmetries, most commonly attributed to outflows or inflows, respectively (DU et al., 2018; BAO et al., 2022). However, a fraction of AGN show complex features, departing from the signatures expected when the gas in the BLR is either in outflow or inflow. Among these interesting sources are the ones exhibiting double-peaked broad emission lines. They are associated with a flattened disk-like BLR structure, first proposed by Chen et al. (1989) and Chen and Halpern (1989) in the optical region after observing the Hα line in the Type-I AGN Arp 102B. Later, several works in the literature suggested that the double-peaked emission originates from the outer parts of a relativistic Keplerian disk of gas of about $\sim$1000 gravitational radii[1] surrounding the SMBH (STORCHI-BERGMANN et al., 1993; STORCHI-BERGMANN et al., 1995; ERACLEOUS et al., 1995; STORCHI-BERGMANN et al., 1997; ERACLEOUS; HALPERN, 2003; STRATEVA et al., 2003; SCHIMOIA et al., 2017; STORCHI-BERGMANN et al., 2017). Other works have suggested alternative explanations for the double-peaked emission, such as hybrid disk models, a binary black hole, or a BLR dominated by a radiatively accelerated wind (see Eracleous et al. (2009) for a complete review), but the disk-like geometry for the BLR still has the best-supporting evidence from theoretical and observational grounds (ERACLEOUS; HALPERN, 2003; SCHIMOIA et al., 2017; STORCHI-BERGMANN et al., 2017).

Double-peaked emission lines are most frequently observed in optical spectra, particularly in the Balmer lines. In the UV region, evidence of double-peak emission detection has been reported in the Mg II line (STRATEVA et al., 2003). However, in the NIR, reports of the observation of double-peak line profiles are very scarce. To the best of our knowledge, only one object, SDSSJ153636.22+044127.0 (ZHANG et al., 2019), presents evidence of double-peak BLR lines. Paβ and He I λ10830 were fitted using the disk model commonly used in optical. However, in general, other well-known double-peaked sources in the optical, such as NCG1097 (STORCHI-BERGMANN et al., 1993; STORCHI-BERGMANN et al., 1995; REUNANEN et al., 2002; STORCHI-BERGMANN et al., 2017), do not show double-peaked profiles in the NIR.

In this work, we carry out the first spectroscopic analysis in the NIR of the Seyfert 1

[1] $\xi = R_g = G\,M_{BH}/c^2$, where M_{BH} is the black hole mass.

galaxy III Zw 002 aimed at confirming the double-peaked nature of this source. The large wavelength coverage of the spectrum ($0.9 - 2.4$ μm) allow us to study simultaneously several broad line features emitted by the BLR (O I, H I, and He I)[2].

Figure 4.1 - Overlapping double peak profile for Paschen α, in solid black line, and O I in dotted gray line.

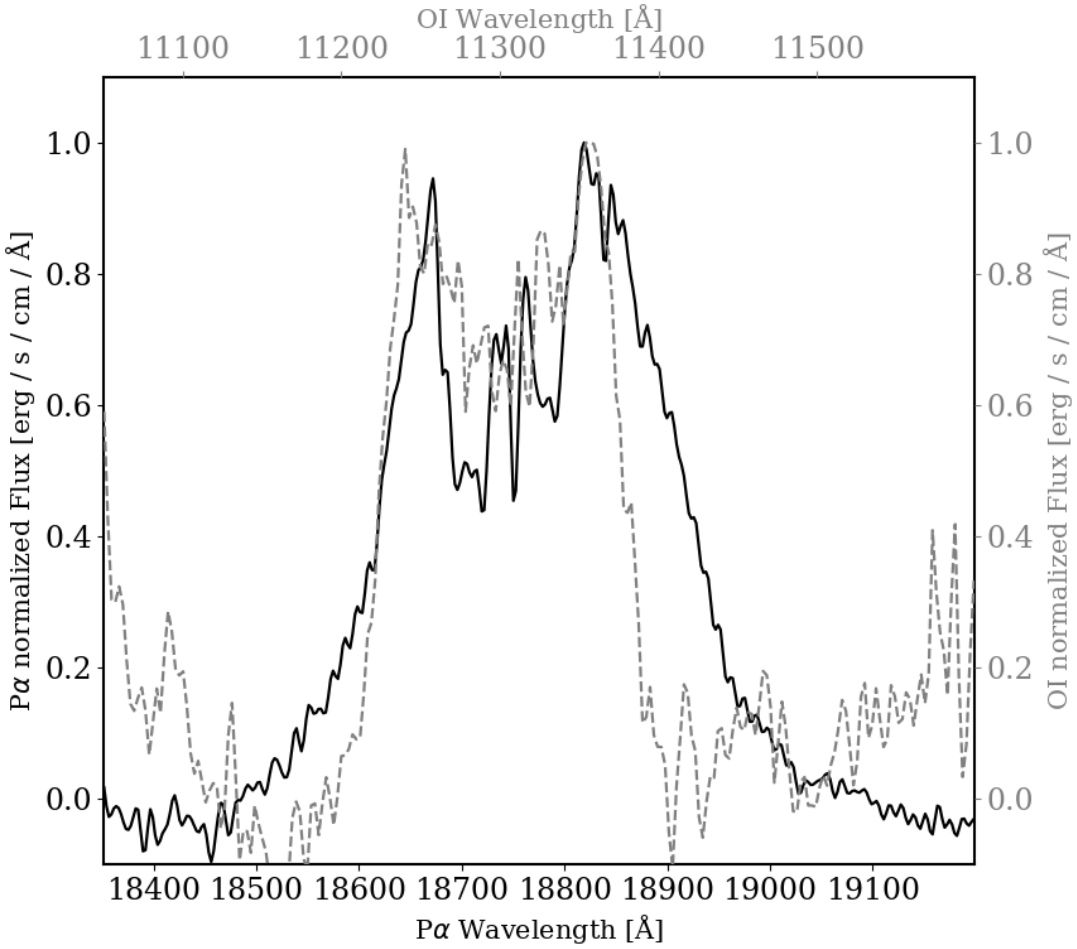

We subtract the narrow component of Paschen α to compare the profiles.

SOURCE: Santos et al. (2023).

[2]This chapter is based on the article titled "First Detection of a Double-peaked Profile in the O I and Paα Emission Lines in the Seyfert 1 Galaxy III Zw 002" by Santos et al. (2023), Published in The Astrophysical Journal Letters, August 2023 (see DOI 10.3847/2041-8205/952/2/L24).

4.1 Analysis and results

The NIR spectrum of III Zw 002 displays the typical features of a Type I AGN, including broad H I and He I lines. Paβ is not detected, as it falls in the gap between the $J-$ and the $H-$bands. The continuum emission in the NIR for III Zw 002 is characterized by two components: the emission from the accretion disk, which dominates up to 1.2 μm, and the hot dust emission, peaking around 2.2 μm (see Figure 2.3). The former was modeled using a power-law with a spectral index of -0.362, and the latter was modeled with a blackbody at a temperature of 1302 K, consistent with typical values for Type I AGN (RODRÍGUEZ-ARDILA; MAZZALAY, 2006; LANDT et al., 2011). This combination of disk and hot dust emission reflects the standard emission behavior observed in Type I AGN, with no distinctive characteristics in III Zw 002 when compared to other similar objects.

In terms of Fe II emission, III Zw 002 is a weak emitter in the optical regime, with a ratio of $R_{4570} \sim 0.3$ as reported in the literature (MARZIANI et al., 2003). No significant Fe II emission is observed in the NIR for III Zw 002, and measuring it proves challenging due to the negligible presence of Fe II lines. Additionally, the key Fe II 10502 Å line falls within a telluric absorption region, further complicating the measurement.

The most notable and distinguishing feature of the III Zw 002 spectrum is the presence of double-peaked profiles in different emission lines. Figure 2.2 shows clear double-peaked profiles in the lines of Paα and O I λ11287 (hereafter O I). The double-peaked profile observed in Paα exhibits the characteristic 'horn' signature, which contrasts with the optical region, where double-peaked profiles, particularly in the Balmer lines are not detected. These findings are further explored in the following Section 4.1.1, where we present our detailed results. Figure 4.1 compares the profiles of the latter two lines, normalized to unity. Although both profiles show conspicuous differences mostly in the degree of asymmetry and width, their double-peak structure is remarkable.

Finally, after a visual inspection and analysis of the NIR spectrum (see Figure 2.2), in addition to O I and Paα, we found compelling evidence of double-peaked profiles in the He I λ10831, Paδ, and Br δ lines. However, these lines are highly blended or have a smaller S/N than O I, and Paα making their modeling complex. For that reason, in this thesis, we focus on the well-isolated lines.

To model O I and Paα double-peaked profiles, we use the disk model described in

Table 4.1 - Fitting parameters for the Disk+BLR model for the O I and Paα Lines.

Parameter	O I	Paα
q_1	-1	-1
ϕ_0 (^{o})	151	165
i (^{o})	18	18
δ (^{o})	50	18
p (^{o})	176	176
A	0.5	3.5
q_2	2.5	2.5
ξ_1 (R_g)	800 (8.38 lt-day)	800 (8.38 lt-day)
ξ_q (R_g)	1800 (18.86 lt-day)	1600 (16.77 lt-day)
ξ_2 (R_g)	5000 (52.43 lt-day)	5000 (52.43 lt-day)
σ ()	1175	1175
Factor	0.72 ± 0.03	0.37 $\pm$ 0.01
Gaussian Component		
Peak * (BC)	0.17 ± 0.01	0.18 $\pm$ 0.011
Center (BC, in Å)	11303.92 ± 2.28	18787.53 $\pm$ 1.76
FWHM (BC, in)	2474.56 ± 387.25	5460.85 $\pm$ 150.49
Peak * (NC)	...	0.53 $\pm$ 0.02
Center (NC, in Å)	...	18745.17 $\pm$ 0.25
FWHM (NC, in)	...	410.91 $\pm$ 10.76
Normalized flux*	$\times 6.92 \times 10^{-17}$	$\times 2.03 \times 10^{-16}$

Rg = 0.010 lt-day, assuming the black hole mass of 1.84×10^8 M$\odot$ (GRIER et al., 2012).

* [erg s^{-1} cm^{-2} Å^{-1}]

Section 2.8. The results obtained will be discussed in the next section.

4.1.1 Results from the spectral fitting

Table 4.1.1 shows the parameters obtained for the disk model and Gaussian components. The Paα line presents well-separated peaks (see Figure 4.2). The A parameter, the contrast in the spiral arms, is responsible for reproducing the peak intensities. Here, we found a value of $A = 3.5$. The saturation radius (ξ_q) found from the fit for Paα is $\sim$1600 gravitational radii. This parameter is responsible for fitting the prominence of the profile wings and is an essential parameter related to the maximum emissivity of the disk spiral arms. The parameter "factor" in Table 4.1.1 is a scale factor applied to the disk model regarding the total line profile. From the fit we obtained the values of 0.72 ± 0.07 and 0.37 ± 0.01 for O I and Paα, respectively.

We note that O I exhibits peaks with similar intensities, resembling a "boxy" shape, unlike the Paα line profile, as we may see in Figure 4.2. The parameter A, obtained

from the fit result for O I, shows the value 0.5, which is responsible for reproducing the slight difference between the intensities of blue and red peaks. The parameters associated with the disk, such as internal and external radius, pitch angle, disk inclination, and emissivity power-law index are equal for both lines, confirming the reliability of our model. In contrast, we obtained different values in both lines for the parameters related to the spiral arms, such as the saturated radius, azimuthal position, and spiral arms distance. We found, for instance, a value for ξ_q of about 1800 gravitational radii, i.e., larger than that of Paα. This is in agreement with the literature, which suggests that the O I line is likely produced in the outer BLR (MARTÍNEZ-ALDAMA et al., 2015; MARINELLO et al., 2016b; PANDA et al., 2020; PANDA, 2021c).

Figure 4.2 - Paα and O I emission line fits.

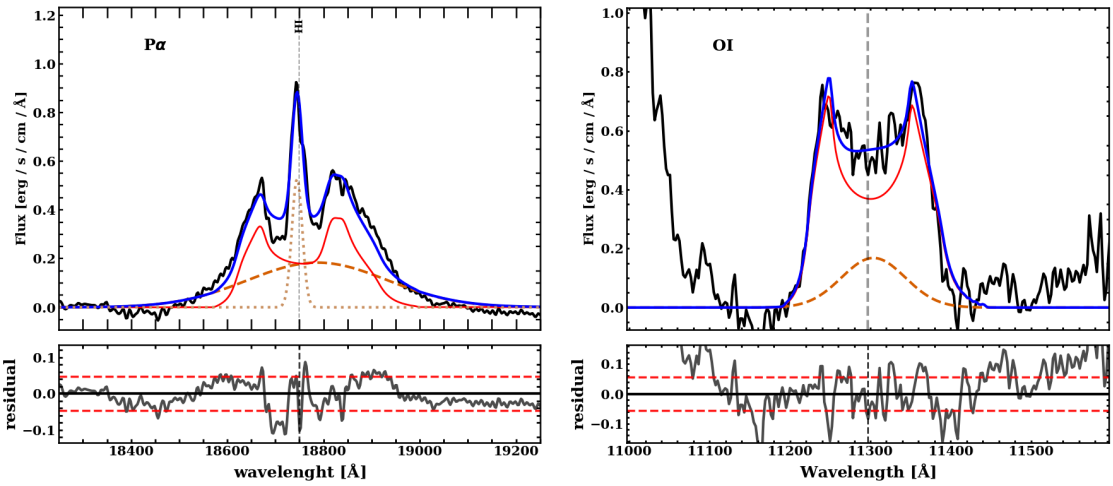

Left: observed profile for Paα (black solid line), fitted double-peaked component (red solid line), and residuals in gray line. The dotted and dashed red lines are narrow and broad Gaussian components, respectively. Right: fit of the O I, where the colors have the same meaning for the disk and broad Gaussian component.

SOURCE: Santos et al. (2023).

Regarding the Gaussian components, to fit the Paα profile, we added two components: a broad one (BC) associated with the nondisk BLR region contributing to fit profile wings and a narrow component (NC) associated with the emission produced in the narrow line region (NLR). O I does not display an NC, as the observed emission is produced in its entirety in the BLR (RODRÍGUEZ-ARDILA et al., 2000; MATSUOKA et al., 2008).

4.2 Discussion

We have successfully modeled in III Zw 002 the double-peaked profile detected in O I and Paα assuming a Keplerian disk model. The physical interpretation of this result points out that both emission lines originate in a BLR distribution of clouds dominated by a planar geometry, with orbits well described by those of a Keplerian disk. Interestingly, from the modeling, the disk is geometrically more extended in O I than in Paα. This result is consistent with several works that have demonstrated through kinematic and photoionization models that the O I line originates in the outer portion of the BLR (MARTÍNEZ-ALDAMA et al., 2015; MARINELLO et al., 2016b; MARINELLO et al., 2020a; PANDA et al., 2020; PANDA, 2021c).

Our results present solid evidence that the bulk of the BLR follows a planar geometry, similar to several other papers suggesting that other AGN also have a disk-like BLR (PANCOAST et al., 2014; STORCHI-BERGMANN et al., 2017; SERGEEV, 2020). The consistency between the model fits made to Paα and O I points out that both lines are emitted by the same disk, providing further support to our hypothesis.

In general, double-peaked emission lines have been observed in a single line in AGN spectra (ERACLEOUS; HALPERN, 2003; STRATEVA et al., 2003; SCHIMOIA et al., 2017; STORCHI-BERGMANN et al., 2017). Here, we simultaneously found double-peaked emission in two different BLR lines. Furthermore, from the disk parameters obtained in the fit, Paα and O I are emitted in different locations in the disk, i.e., different radii and azimuthal distances. That would explain the different shapes observed in both profiles, even though the same disk emits them. The Paα originates in a complex internal region, nearer to the AGN than O I. That makes the former line suitable to map the variability of the AGN continuum emission. In contrast, otherwise, O I likely would not change considerably with time because of its larger distance from the central ionizing source.

From the reverberation campaigns carried out on III Zw 002 (GRIER et al., 2012), Grier et al. (2013) constructed velocity-delay maps by means of the measured time delays in different velocity bins of the Hβ emission line. The authors gathered evidence of (i) an "extended BLR" (see Figure 4 (GRIER et al., 2013)); (ii) radial stratification of the gas ionization; and (iii) the geometry of BLR consistent with a thick inclined disk. Due to the employment of different spectral lines, i.e., Hβ by Grier et al. (2017), and Paα by our study, we expected a minor variation in the physical scale. Specifically, Grier et al. (2017) reported a maximum emissivity radius of around 15.5 ld-day for Hβ, while our findings for the Paα line indicate

16.77 ld-day. The findings of Grier et al. (2017) align with our conclusions regarding the BLR disk-like geometry of III Zw 002, providing further validation and support for the results presented in this thesis. To the best of our knowledge, this is the first time that two broad double-peaked NIR emission lines have been unambiguously detected simultaneously in an AGN. This remake open the possibility of studying the structure of the BLR using multiwavelength observations, via several broad double-peaked emission lines.

Here, it is important to remember that the disk model considers spiral arms, which may exhibit brightness contrast between the arms and change in emissivity according to the distance from the AGN (CHEN; HALPERN, 1989). These BLR spiral arms are composed of matter that is involved in the dragging process under the SMBH gravitational potential (SHAPOVALOVA et al., 2008; SHAPOVALOVA et al., 2010; GRIER et al., 2012; GRIER et al., 2013; GRIER et al., 2017; SHAPOVALOVA et al., 2012). That process may be responsible for the asymmetries in the line profile observed in O I and Paα.

The BH mass of III Zw 002 can be estimated by assuming that the gas motion within the BLR is dominated by the gravitational potential of the BH, and using the virial equation $M_{\rm BH} = f \times R_{\rm BLR} \times \Delta V^2/{\rm G}$, where G is the gravitational constant, ΔV is the velocity dispersion of the clouds, $R_{\rm BLR}$ is the BLR radius, and f is the virial factor (PETERSON, 2004). Commonly, the velocity dispersion can be approximated by the FWHM, typically of the broad Hβ component. Instead, we use the FWHM of the Paα, due to the NIR regime of our study. Despite the virial factor being a key element in estimating the black hole masses, it directly depends on the disk inclination i, which cannot be measured directly from observations (PETERSON, 2004; BENTZ et al., 2009; DU et al., 2015; GRIER et al., 2012; GRIER et al., 2013; GRIER et al., 2017; DU; WANG, 2019; PANDA et al., 2019; BONTÀ; PETERSON, 2022).

Thus, the virial factor carries an intrinsic bias into black hole masses estimation. By means of the disk fitting, the disk inclination is derived among the fitted parameters and the virial factor can be estimated by $f = 1/(\kappa^2 + sin^2 i)$, where, κ carries information on the disk geometry. Using the inclination we estimated (i=18$^{\rm o}$) and four different values for κ: 0.3, 0.2, 0.1, and 0.0 (where κ=0 refers to a flat disk geometry) (COLLIN et al., 2006; GRIER et al., 2013; STORCHI-BERGMANN et al., 2017; PANDA et al., 2019), we obtained virial factors 5.39, 7.38, 9.47, and 10.47, respectively. These results are consistent with the inclinations measured for

NGC 5273 (i=16°), NGC 3227 (i=17°), and NGC 5548 (i=19°), and with estimated virial factors of 12, 11.7, and 9.4, respectively (STORCHI-BERGMANN et al., 2017).

Moreover, the Paα FWHM value (5460.85±150.49) we measure in this work is close to the FWHM value obtained from the rms spectrum for Hβ (5054±145 km s^{-1}) from Grier et al. (2012). Thus, we employed the FHWM of Paα instead of that of Hβ to estimate the BH mass, since the measured FWHM of both lines are consistent. Furthermore, we used the same BLR radius obtained by the later authors. Using these parameters, we estimate BH masses of $4.86 \times 10^8 M_\odot$, $6.65 \times 10^8 M_\odot$, $8.55 \times 10^8 M_\odot$, and $9.44 \times 10^8 M_\odot$, which are in good agreement with BH mass estimated by RM, $1.84 \times 10^8 M_\odot$, using f=5.5 (GRIER et al., 2012).

The results above fall within the relation presented by Storchi-Bergmann et al. (2017) (see Figure 8 of their paper), which shows that low inclinations (implying larger virial factors) are associated with larger FWHM of broad lines. Our results allowed us to set an important constraint on the f factor and a more robust estimation of the BH mass. In this context, the disk modeling approach can be a powerful alternative to minimize the uncertainties related to the virial factor, which is an essential parameter to probe the BLR geometry and cloud distribution (COLLIN et al., 2006; STORCHI-BERGMANN et al., 2017; PANDA et al., 2019).

4.3 Final comments and future works

We report, for the first time, the simultaneous detection of a double-peaked profile in the O I λ11297 and Paα emission lines in the local Seyfert 1 galaxy III Zw 002. The analysis presented in this thesis employs the NIR of this source covering the JHK bands for the first time, allowing us to explore double-peaked profiles in a new wavelength interval.

The O I λ11297 emission line is located in a region free of atmospheric absorptions, making our detection quite solid and confirming the double-peaked nature of that source. As a result, the disk model applied successfully to the O I and Paα line allowed us to infer the geometry of the outer region of the BLR. From the fit of the model, we suggest that for III Zw 002 that the O I emission comes from a flattened region emitting low ionization lines.

Analysis of the model fitting parameters reveals that the disk has a low inclination angle, $i = 18°$. The disk model proves to be a robust method for reducing uncertainties associated with the f factor. This parameter is crucial to study the geometry

and cloud distribution of the BLR, and determine the SMBH mass.

5 FIRST DETECTION OF OUTFLOWING GAS IN THE OUTSKIRTS OF THE BROAD LINE REGION IN 1H-0707-495

This chapter investigates the BLR of the NLS1 galaxy 1H 0707-495[1], a source known for its extreme variability and spectral characteristics, including a strong soft X-ray excess and relativistic broad iron lines (TURNER et al., 1999; FABIAN et al., 2009). We are interested in this source because of its complex UFO signatures detected in previous X-ray and UV studies. Despite the wide information in the X-ray and UV bands, very little is known about the spectral properties of 1H 0707−495 in the NIR.

Several evidences suggested that this source to be a very interesting target in the NIR. First, it is known to have prominent FeII emission. Therefore, we expect to detect bright and isolated FeII lines in this spectral range. Second, very likely O I and the CaT are prominent because of the known relationship between FeII, O I and Cat. And third, we would like to confirm the presence of UFOs in the low-ionization gas in the BLR.

In the next sections we report our results from the NIR spectroscopy analysis carried out on 11H 0707−495. Observations and data reduction were already described in Chapter 2.6.

5.1 Results

Overall, the NIR spectrum of 1H 0707-495 displays similar characteristics to that observed in other NLS1 (RODRÍGUEZ-ARDILA et al., 2002; RIFFEL et al., 2006; MARINELLO et al., 2016a; MARINELLO et al., 2020c). The most important difference is the lack of bright emission features from the narrow-line region (NLR), such as the forbidden [S III] 0.953 μm, [Fe II] 1.257 μm, molecular lines from H_2, and coronal lines, which are rather faint or not detected in 1H 0707−495. This result is consistent with previous observations (PAUL et al., 2021). Moreover, the NLR component of the permitted H I lines seems absent, except likely in the Paschen lines.

The continuum emission is dominated by a strong featureless component, with the flux increasing steeply towards shorter wavelengths. No evidence of stellar absorption

[1]This chapter is based on the article titled "First Detection of Outflowing Gas in the Outskirts of the Broad-line Region in 1H 0707-495" by Alberto Rodríguez-Ardila, Marcos Antonio Fonseca-Faria, Denimara Dias dos Santos, Swayamtrupta Panda, and Murilo Marinello (RODRÍGUEZ-ARDILA et al., 2024), published in The Astronomical Journal on April 26, 2024 (see DOI 10.3847/1538-3881/ad36bf).

Figure 5.1 - Near-IR spectrum of 1H 0707-495 in rest wavelength already corrected for a Galactic extinction E(B-V)=0.084.

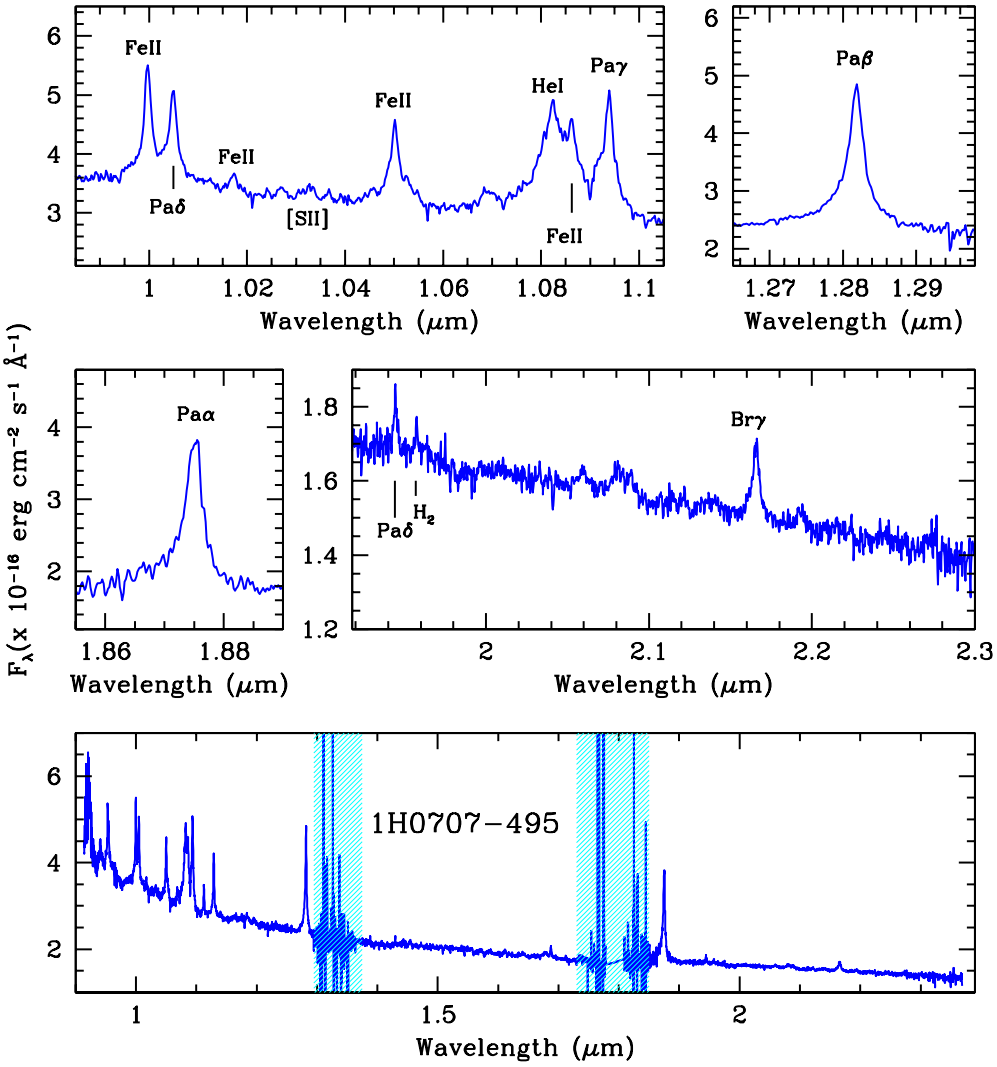

The bottom panel shows the spectrum in the wavelength interval 0.94−2.4 μm while the boxes in the upper and mid-rows are insets of the bottom spectrum at some spectral regions of interest to this work. The most important emission lines are identified. The shaded areas in blue are regions of bad atmospheric transmission.

SOURCE: Rodríguez-Ardila et al. (2024).

features were detected in the observed spectrum. Thus, we assume that the stellar contribution is below 10% of the observed continuum (RIFFEL et al., 2006).

To characterize the NIR continuum emission, we first fit a function described by a

power-law of the form $F_\lambda \propto \lambda^\alpha$, where λ is the wavelength and α the spectral index of the power-law. Special care was taken to exclude emission lines in the spectral windows that were used in the fit. We found unsatisfactory results with that function and concluded that it alone cannot reproduce the observed NIR continuum. We then employed a composite function, consisting of an underlying power-law plus a blackbody component. It has been employed successfully in the fitting of the NIR continuum in other AGN, including NLS1 (GLIKMAN et al., 2006; RIFFEL et al., 2009; LANDT et al., 2011). Our results show that a power-law with spectral index $\alpha = -1.95 \pm 0.25$ and a blackbody of temperature $T_{\rm BB} = 1299 \pm 100$ K reproduce satisfactorily the observed continuum. The errors quoted for the aforementioned parameters are within 2σ uncertainties. Figure 5.1 shows the fit (upper panel) and the nebular spectrum after subtraction of that component.

The value of α derived in this work in the NIR is, within errors, very close to that of -2.3 reported by Leighly and Moore (2004) for the UV/optical continuum. We note that the latter authors do not quote any uncertainty associated with the spectral index. Despite this, we conclude that the power law in the NIR likely represents the low-energy tail of the continuum produced by the central source. The blackbody component is associated with the hottest dust component, likely located in the inner face of the obscuring torus (GLIKMAN et al., 2006; LANDT et al., 2011).

After the continuum fitting, we subtracted the power-law and the blackbody components from the observed spectrum. This procedure is carried out to study the pure emission line spectrum of 1H 0707−495. However, the analysis that will be presented in Section 5.1.1 is not affected by this step (see below).

5.1.1 The emission line spectrum of 1H 0707-495

The emission line spectrum in 1H 0707-495 is dominated by permitted, broad features, most of them associated with the BLR. The only NLR lines detected are the [S III] 0.953 μm in the blue edge and the H_2 line at 1.957 μm in the $K-$band. Both features are intrinsically faint. It is important to notice that the forbidden emission line of [S III] is usually the strongest forbidden line in the NIR (RIFFEL et al., 2006). We characterized the observed emission lines in terms of the integrated flux, full-width at half maximum (FWHM), and centroid position of the line peaks. To this purpose, we fitted Gaussian or Lorentzian functions to individual lines or to sets of blended lines. This procedure was carried out using a set of custom scripts written in PYTHON by our team. The code uses non-linear least squares, with SCIPY.OPTIMIZE.CURVE_FIT. Open source software was employed,

Figure 5.2 - [Upper panel: Fit applied to the NIR continuum emission (black line) in 1H 0707-495.]

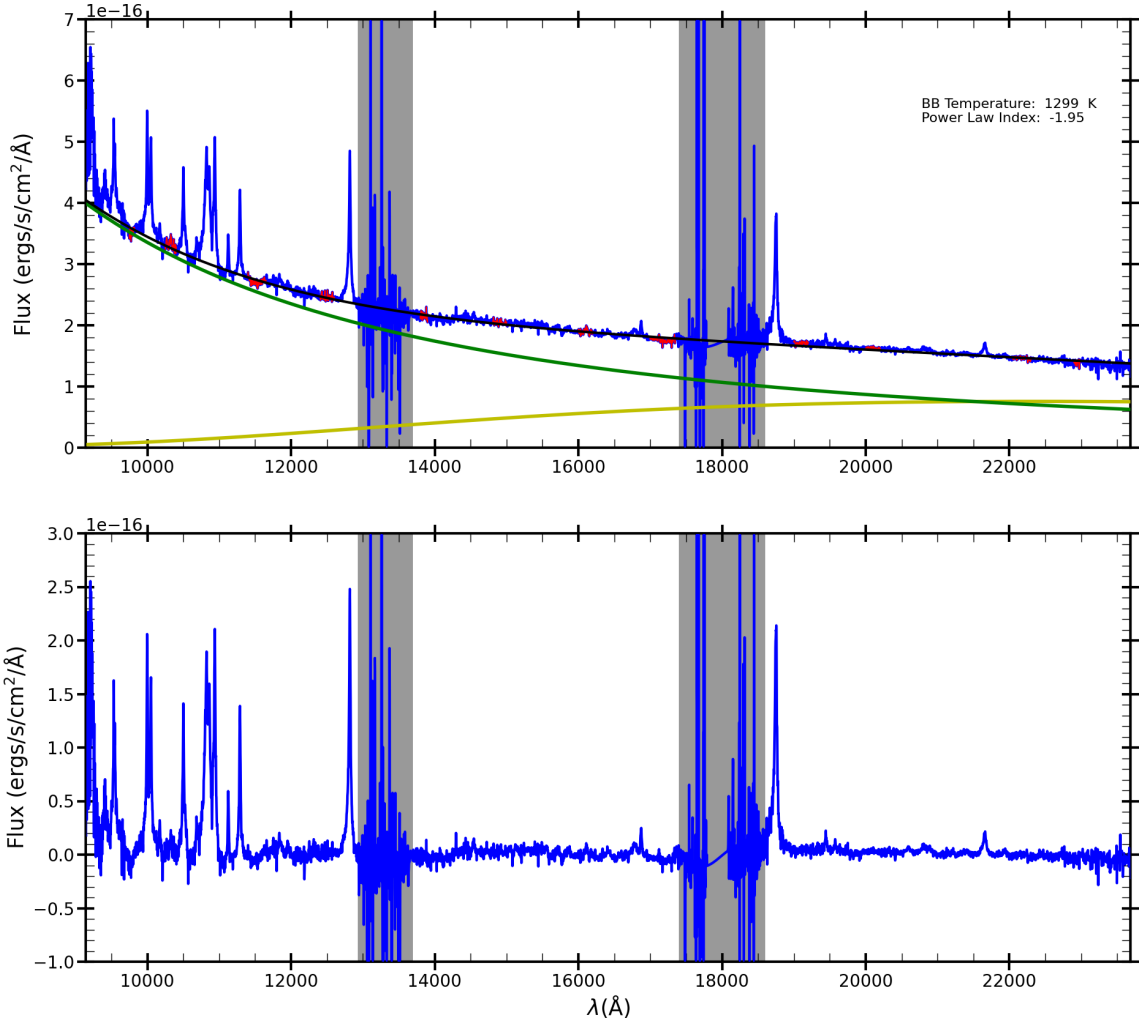

Upper panel: Fit applied to the NIR continuum emission (black line) in 1H 0707-495 with a composite function, consisting of a power-law (green line) of the form $F_\lambda \propto \lambda^\alpha$ with α=-1.95 and a blackbody (gold line) of temperature T_{BB}=1300 K. The spectral windows employed in the fitting are marked in red. The bottom panel shows the nebular spectrum after subtraction of the continuum emission. The grey stripes are regions of bad atmospheric transmission.

SOURCE: Rodríguez-Ardila et al. (2024).

such as MATPLOTLIB (HUNTER, 2007), NUMPY (WALT et al., 2011) and SCIPY (VIRTANEN et al., 2020). For each emission line, up to 3 Gaussian components or 2 Gaussian components and one Lorentzian are allowed. Constraints for the lines were also added such that lines belonging to the same ion should have the same FWHM (in velocity space) and obey the theoretical wavelength separation.

Figure 5.1.1 shows a zoom around the region where the Paβ line is located. It is the strongest BLR line detected in the NIR spectrum. We first fit the observed profile with two components − a narrow one, from the NLR and a broad profile, associated with the BLR. The results are presented in the upper two panels of Figure 5.1.1. In the left panel, the BLR is represented by a single Gaussian profile while in the right panel, it is assumed that the BLR contribution can be represented by a Lorentzian profile. A quick inspection to both fits evidences residuals as large as ∼10% of the peak intensity of the line. Moreover, the largest residuals are mostly concentrated towards the blue wing of the emission line profile.

We then tested a scenario of a BLR consisting of two components to account for the observed large residuals in the previous case. The results are shown in the bottom two panels of Figure 5.1.1. In both cases, we kept the former BLR component (Gaussian – left panel, and Lorentzian, right panel) and included an additional blueshifted broad Gaussian component. All the parameters associated to this extra component were left free in the fit. It can be seen that after the addition of the latter component the residuals were considerably reduced in both cases, being limited now to ∼3% of the line peak.

Although the addition of a second BLR component offers a better description of the observed Paβ profile, it is well-known that the root-mean-square (RMS) of the continuum residuals decreases with the increase of the number of components, regardless of their physical meaning. However, it is worth noticing at this point that previous works on 1H 0707−495 had already reported the detection of blue-asymmetric profiles in UV lines such as C IV, Si IV, and O IV (LEIGHLY; MOORE, 2004). Leighly and Moore (2004) also point out that low-ionization lines such as Mg II in the UV or Hβ in the optical were modeled using a Lorentzian profile, with no evidence for either blue or red asymmetries and centered at the systemic velocity. It is important to mention, though, that the latter two lines are located in regions that are strongly contaminated by broad humps of Fe II emission. This makes the full characterization of their line profiles very uncertain.

Even though our results on Paβ agree with previous observational findings using UV spectroscopy on this AGN, to have firm evidence of the need for a second component, we employed the Bayesian Information Criteria (BIC). It was first introduced by Schwarz (1978) to guide on model selection, which is the problem of distinguishing competing models, sometimes featuring different numbers of parameters. Here, we apply the BIC to test if a second Gaussian component is indeed necessary. To this

purpose, we apply Equation 5.1, which evaluates the BIC, to the line fits described above,

$$BIC = N * ln(RSS/N) + k * ln(N) \tag{5.1}$$

where N is the number of data points employed in the fit, RSS is the sum of the square of the residuals, and k is the number of free parameters of the model. Equation 5.1 is a simplification of a more general expression provided by Liddle (2007). The model giving the smallest BIC among the candidates is the one favoured. If the difference in BICs between two competing models is 0–2, this constitutes "weak" evidence in favor of the model with the smaller BIC; a difference in BICs between 2 and 6 constitutes "positive" evidence; a difference in BICs between 6 and 10 constitutes "strong" evidence; and a difference in BICs greater than 10 constitutes "very strong" evidence in favor of the model with smaller BIC.

It is important to mention that the BIC attempts to mitigate the risk of over-fitting by introducing the penalty term $k * ln(N)$, which grows with the number of parameters. This allows to filter out unnecessarily complicated models, which have too many parameters to be estimated accurately on a given data set of size N.

Using Equation 5.1 and the values of N and k listed in Table 5.1.1, we determine the BIC for the profile modelling applied to Paβ and depicted in Figure 5.1.1. The results are in Columns 5-6 and 11-12 of that same Table. It is possible to see that the smallest BICs (-6910 and -6938) are obtained when the BLR is modeled with two components: a broad profile (Gaussian or Lorentzian) with the line peak very close to the systemic velocity (the classical BLR) plus a blueshifted, broad Gaussian component. Moreover, the difference ΔBIC (Columns 7 and 13) between the BLR represented by one or two components is >10 regardless of the profile employed to represent the classical BLR. Therefore, we conclude that a broad, blueshifted, component is a requirement to properly model the observed Paβ profile. Here, we suggest that this extra component represents the outflow already detected in UV lines by Leighly and Moore (2004) in this object.

Table 5.1.1 lists the centroid position, flux, full-width at half maximum (FWHM), and the shift of the line peak relative to the laboratory position found for each component of both the Gaussian and the Lorentzian approach. The errors in the fluxes are representative at the 2σ level across all cases.

Table 5.1 - Parameters employed in the line fitting procedure and resulting BIC values.

Line	Gaussian BLR						Lorentzian BLR					
	N	K*	K**	BIC*	BIC**	Δ BIC	N	K*	K**	BIC*	BIC**	Δ BIC
Paβ	87	6	9	-6747	-6910	163	87	6	9	-6836	-6938	102
FeII λ10501	68	12	15	-5288	-5359	71	68	12	15	-5339	-5377	38
O I	72	3	6	-5649	-5733	84	72	3	6	-5769	-5721	-48
FeII+ Paδ+ He II+ FeII	138	15	21	-10690	-10938	248	138	15	21	-10848	-10931	83
[S III]+ Pa 8	53	15	21	-4104	-4170	66	53	15	21	-4090	-4161	71

Parameters employed in the line fitting procedure and resulting BIC values. N is the number of data points, K is the number of parameters modeled (three for every Gaussian or Lorentzian function) and BIC is the Bayesian information criterion determined by Equation 5.1. Columns 2-7 list the results when a classical Gaussian BLR is assumed and columns 8-13 show the results for a Lorentzian BLR. * values without a second Gaussian component; ** values when considering a second, blueshifted Gaussian component. Δ BIC is the difference of BIC for model i and the minimum BIC value, $\mathrm{BIC}_{\mathrm{min}}$.

The BIC values from the Paβ fit also allow us to test whether the classical BLR is best described by a Gaussian or a Lorentzian profile. We found that the smallest BIC is obtained with the latter function. The ΔBIC between these two models (Columns 7 and 13) is 28, that is, larger than 10. This agrees to previous results reported by (LEIGHLY; MOORE, 2004) to model the Hβ line.

When a Lorentzian profile is employed to represent the classical BLR, it has an FWHM of 602 km s^{-1} and is centered at the systemic velocity. The outflow component, modeled using a Gaussian component, is found to be blueshifted by -725 km s^{-1} and has an FWHM of 2545 km s^{-1}. We note that the maximum error associated with the peak position of the line is 30 km s^{-1} while that associated with the FWHM is 35 km s^{-1}. These values were extracted from the maximum value of the root mean square (RMS) of the wavelength calibration provided by the reduction pipeline, and from the measurement of the FWHM around the Paβ line, assuming different continuum levels, respectively. They can be considered as standard for the analysis presented in the remainder of this work.

We notice that the Paα line in the $K-$band is also detected in our data (see Fig-

Figure 5.3 - Line fit carried out to the Paβ line.

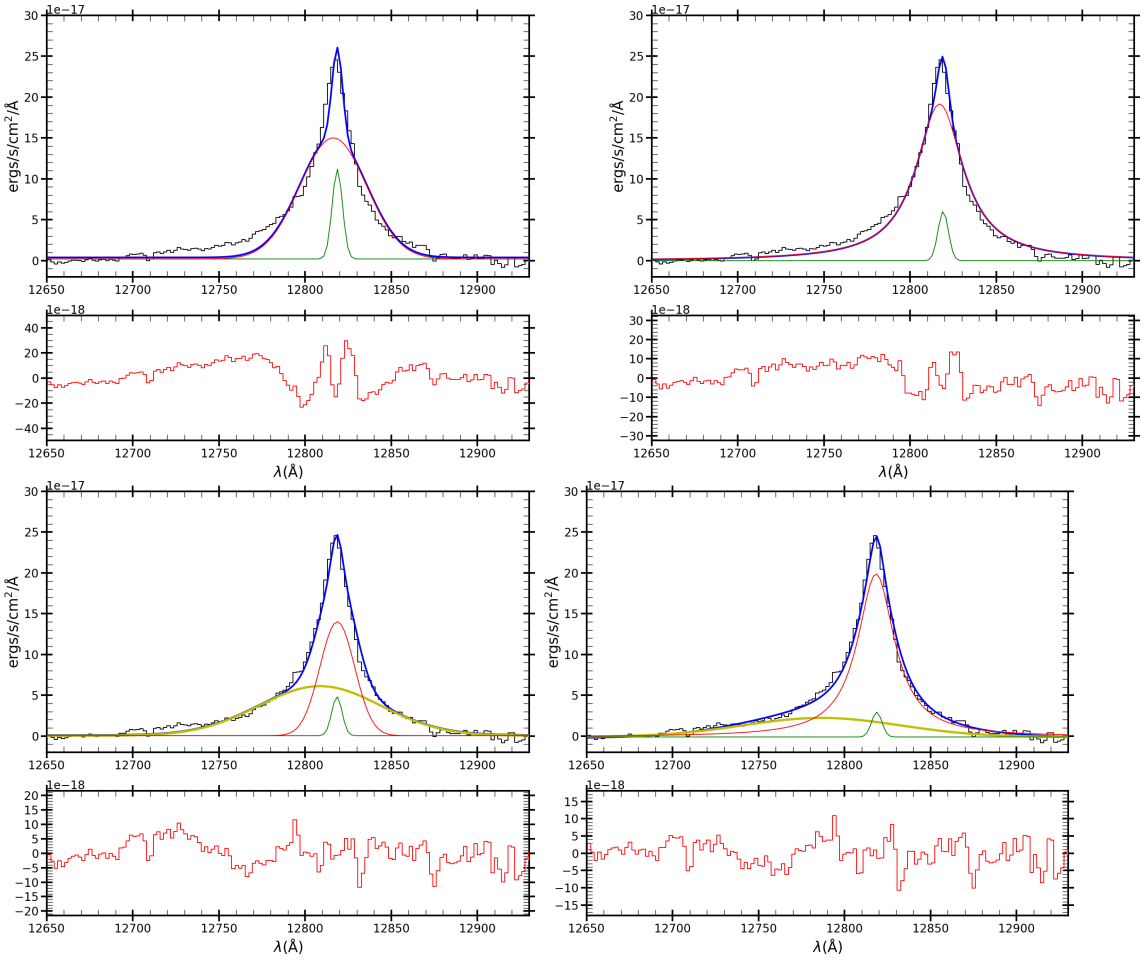

The upper two panels show the results after considering a BLR composed of a single Gaussian (left) or a Lorentzian component (right). The BIC found from this approach are in Table 5.1.1. The bottom two panels display the results after the addition of a blueshifted Gaussian component to the classical Gaussian BLR (left) and a Lorentzian BLR (right). The corresponding BIC values are also in Table 5.1.1. In all panels, the observed profile is the black histogram, the green curve is the NLR contribution, the red curve is the BLR contribution and the yellow curve is the additional blueshifted Gaussian component associated with the BLR. The blue line is the modeled profile. The bottom panel is the residual after subtracting the modeled emission line profile from the observations.

SOURCE: Rodríguez-Ardila et al. (2024).

ure 5.1). However, we refrain from using it in the analysis done here because the blue wing of the line is very close to the poor transmission region between the $H-$ and $K-$ bands. An inspection of Figure 5.1 allows us to confirm the presence of a strong blue-asymmetric profile in Paα, very similar to that of Paβ. However, because the former displays a lower S/N and is fainter than the latter (which contradicts the

Table 5.2 - Line parameters (center, flux, FWHM, and shift from the centroid position) for the Gaussian (columns 2-5) and the Lorentzian fits (columns 6-9).

Line	Gaussian BLR				Lorentzian BLR			
	Centre (Å)	Flux	FWHM (km s^{-1})	$\Delta\lambda$ (km s^{-1})	Centre (Å)	Flux	FWHM (km s^{-1})	$\Delta\lambda$ (km s^{-1})
[S III] $_{\rm NLR}$	9532	0.49±0.04	122	41	9532	0.47±0.04	119	41
[S III] $_{\rm out}$	9526	0.83±0.13	565	-170	9526	0.78±0.14	583	-164
Pa 8 $_{\rm NLR}$	9546	0.10±0.05	118	0	9546	0.08±0.04	118	0
Pa 8 $_{\rm BLR}$	9547	1.18±0.16	550	28	9547	2.33±0.15	597	16
Pa 8 $_{\rm out}$	9541	1.37±0.44	1934	-157	9525	0.83±0.64	2533	-669
FeII $_{\rm BLR}$	9997	2.11±0.13	408	9	9997	4.02±0.11	430	6
FeII $_{\rm out}$	9988	2.88±0.54	1834	-279	9972	1.02±0.53	1850	-765
Paδ $_{\rm NLR}$	10049	0.17±0.04	137	0	10049	0.10±0.03	137	0
Paδ $_{\rm BLR}$	10049	1.72±0.14	537	0	10049	4.08±0.14	598	0
Paδ $_{\rm out}$	10044	3.18±0.51	1954	-149	10026	1.87±0.69	2615	-686
He II $_{\rm BLR}$	10120	0.27±1.87	771	-118	10120	0.28±0.14	540	-118
FeII $_{\rm BLR}$	10172	0.39±0.13	523	29	10172	0.62±0.17	591	29
FeII $_{\rm BLR}$	10491	0.40±0.16	415	0	10491	0.50±0.14	427	0
FeII $_{\rm BLR}$	10503	1.63±0.16	414	57	10502	3.04±0.14	432	29
FeII $_{\rm out}$	10489	2.07±0.62	1840	-341	10472	1.20±0.55	1856	-826
O I $_{\rm BLR}$	11289	1.97±0.15	440	53	11288	4.60±0.47	546	27
O I $_{\rm out}$	11281	2.27±0.58	1802	-159	–	–	–	–
Paβ $_{\rm NLR}$	12818	0.36±0.06	127	0	12819	0.23±0.06	128	23
Paβ $_{\rm BLR}$	12819	3.52±0.20	543	23	12818	8.20±0.21	602	0
Paβ $_{\rm out}$	12809	5.38±0.75	1945	-210	12787	2.70±0.84	2545	-725

Line parameters (center, flux, FWHM, and shift from the centroid position) for the Gaussian (columns 2-5) and the Lorentzian fits (columns 6-9). Fluxes in units of 10^{-15} erg cm^{-2} s^{-1}. The subscripts "NLR", "BLR", and "out" refer to the component emitted by the narrow line region, the classical broad line region, and the outflow component, respectively.

Paschen decrement), we opted to leave Paα out.

5.1.2 The NIR Fe II emission

In addition to the permitted H I lines, the NIR spectrum of 1H 0707−495 also shows the presence of prominent FeII emission features, in particular, the ones at λ9997, λ10501, λ10863, and λ11127 (RUDY et al., 2000; RODRÍGUEZ-ARDILA et al., 2002; MARINELLO et al., 2020c). Because of their proximity in wavelength, they are termed as the 1 μm FeII lines and are emitted after the decay of the common upper term b^{4}G. Overall, FeII at λ9997 and λ10501 are very conspicuous and moderately isolated lines. For that reason, they will be employed here in the analysis of the FeII emission line profiles. The former is ∼50 Å apart from Paδ, the nearest strongest emission feature, while FeII λ10501 is indeed a blend of FeII at λ10493 and λ10501, rarely being resolved because of their proximity. Moreover, the expected flux ratio

λ10501/λ10493 is $\sim$8 (MARINELLO et al., 2016a). Thus, the flux of λ10501 dominates the blend. At the redshift of 1H 0707−495, the lines at λ10863 and λ11127 are located in regions of bad atmospheric transmission, preventing us from using them reliably.

In this section we will focus on the results obtained for the Fe II λ10501 blend. As with the Paβ line, We first tested the hypothesis of a line profile being represented solely by the classical BLR component. The results are shown in Figure 5.1.3. The BIC values are listed in the Table 5.1.1. It is possible to see the presence of residuals in the blue wing in λ10501. For this reason, we included an outflow component to the most prominent line, that is, the one centered at λ10501. The left panel of Figure 5.1.2 illustrates the result after the addition of that component plus a Gaussian profile to account for the classical BLR contribution. In the right panel, a Lorentzian profile for that component is assumed. The lines at λ10493, λ10526, and λ10546 are also emitted by FeII but are considerably fainter features than that at λ10501. For this reason, only the classical BLR component was used to fit them. The outflow component, if present, is at the S/N level. The BIC found from these fits are in Table 5.1.1. Table 5.1.1 lists the best-fit parameters found for FeII blend centered at λ10501.

Figure 5.4 - Deblending procedure applied to the FeII λ10501 line.

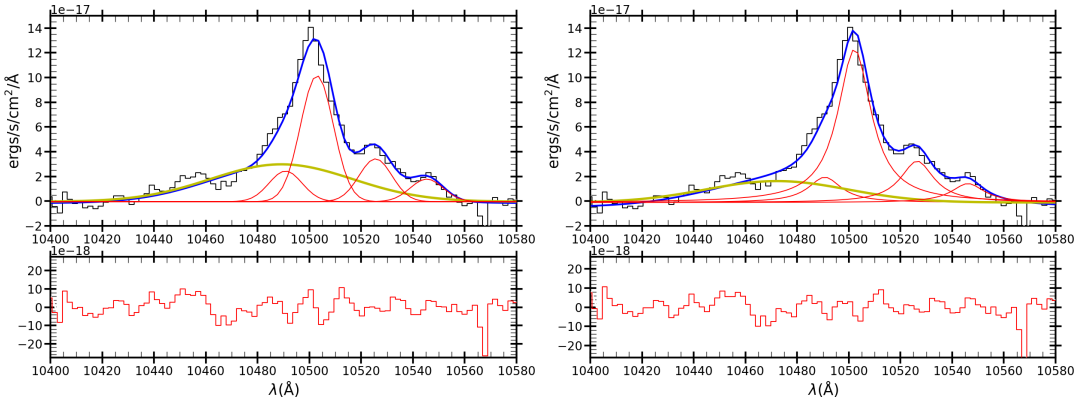

Deblending procedure applied to the FeII λ10501 line. The left panel shows the modelling assuming Gaussian components, while the right panel shows the results considering a Lorentzian profile for the part emitted by the classical BLR. The black histogram is the observed profile and the blue line is the fit. Individual components corresponding to the classical BLR are in red while the outflow component is in yellow. The bottom panel is the residual after subtracting from the observations the best fit.

SOURCE: Rodríguez-Ardila et al. (2024).

As in the Paβ fit, the presence of an outflow component is strongly favoured. The fit with the classical BLR plus the outflow component (with the width, intensity and centroid position left unconstrained in the fit) results in smaller BIC values, with the ΔBIC being > 10 when compared to that of without outflow. Moreover, the Lorentzian profile to represent the classical BLR is also favoured as the BIC in the latter case is smaller than when a Gaussian profile is assumed. The ΔBIC between these two cases amounts to 18.

The fits shown in Figure 5.1.2 confirm the results already gathered from Paβ. We found a classical BLR component, which within errors is characterized by a Lorentzian profile with FWHM of 432 km s^{-1} and coincident with the systemic velocity. This agrees with the results of Leighly and Moore (2004) for Mg II and Fe II. Moreover, there is a broad blueshifted component that we associate with outflowing gas from the BLR. It has a FWHM of $\sim$1856 km s^{-1} and an outflow velocity between -341 and -826 km s^{-1}. To the best of our knowledge, this is the first time that such an outflow has been detected in low-ionization BLR emission in 1H 0707$-$495. It is important to notice here some additional findings. First, the Fe II component emitted by the classical BLR displays an FWHM that is smaller than its counterpart in Paβ. This is in agreement with previous results found by Rodríguez-Ardila et al. (2002), Marinello et al. (2016a), and Marinello et al. (2020c). The latter two works report that the BLR component of Fe II is, on average, 30% narrower than that of Paβ. Second, the FWHM of the Fe II lines is likely one of the smallest already reported in the literature. And third, the presence of a shoulder centred at $\sim$10492, coinciding with Fe IIλ10493 suggests that we resolved that line. Spectra with better S/N is necessary to confirm this result.

5.1.3 The O I emission line

We took advantage of the presence of the strong O I emission at λ11287 in our spectrum and modeled that line using the two approaches already employed and described above. The fit with a single component to represent the BLR is in Figure 5.1.3 and the one including the outflow is shown in Figure 5.1.3. The corresponding BIC values are in Table 5.1.1.

An inspection of Figure 5.1.3 reveals that a single Gaussian function does not reproduce satisfactorily the observed profile. Strong residuals are left in the blue and red wings of the emission line. However, when a single Lorentzian profile is employed, the residuals are considerably reduced. This is supported by the BIC, which is the smallest when that latter profile is employed.

Figure 5.5 - Line fit carried out to the Fe II λ10501 lines.

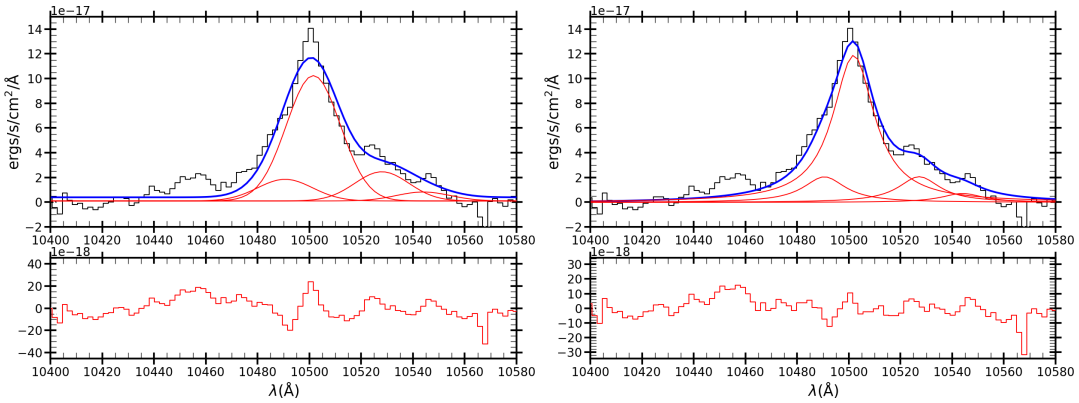

Line fit carried out to the Fe II λ10501 lines. The left panel shows the results after considering a BLR composed of a single Gaussian while the right panel the fit when a Lorentzian component is assumed. The BIC found from these fits are in Table 5.1.1. The observed profile is the black histogram, and the red curve is the BLR contribution. The blue line is the modeled profile. The bottom panel is the residual after subtracting the modeled emission line profile from the observations.

SOURCE: Rodríguez-Ardila et al. (2024).

Figure 5.6 - Line fit carried out to O I λ11287.

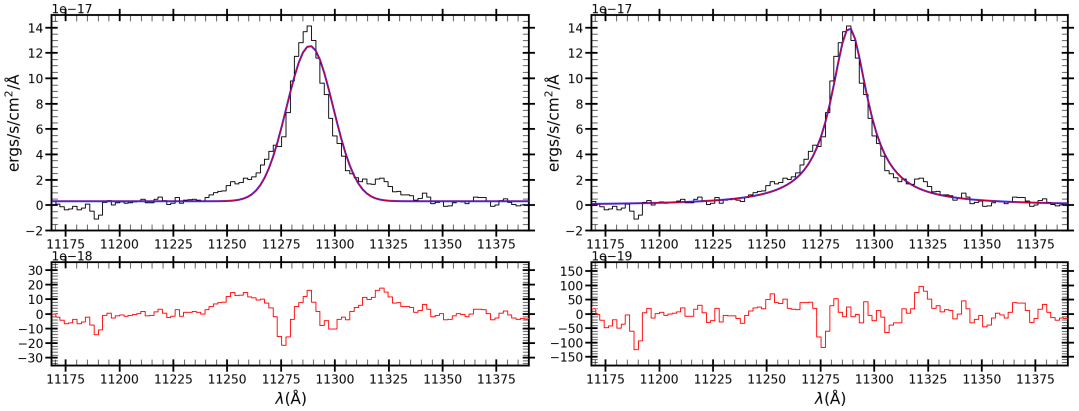

Line fit carried out to O I λ11287. The left panel shows the results after considering a BLR composed of a single Gaussian while the right panel the fit when a Lorentzian component is assumed. The BIC found from these fits are in Table 5.1.1. The observed profile is the black histogram, and the red curve is the BLR contribution. The blue line is the modeled profile. The bottom panel is the residual after subtracting the modeled emission line profile from the observations.

SOURCE: Rodríguez-Ardila et al. (2024).

We also tested the scenario where a blueshifted broad component is included in the fit. The results are displayed in Figure 5.1.3 and the corresponding BIC values are listed in Table 5.1.1. It can be seen that in a classical Gaussian BLR, the outflow component produces a smaller BIC, with a difference >10 relative to the case of no outflow. In the case of a classical Lorentzian BLR, though, the inclusion of an outflow component does not improve the modelling. Indeed, the BIC increases considerably. Therefore, for O I λ11287 an outflow component is acceptable under the assumption that the classical BLR is represented by a Gaussian profile. Nonetheless, it is important to highlight that the smallest BIC is obtained when that latter region is modelled using a Lorentzian function, making the outflow scenario uncertain for that line. It is possible that the outflow is present but it was not detected within our S/N because of the presence of a strong telluric absorption feature to the blue side of the line. Table 5.1.1 lists the parameters found for O I λ11287 using both the Gaussian and Lorentzian approaches.

Figure 5.7 - Deblending procedure applied to the O I λ11287.

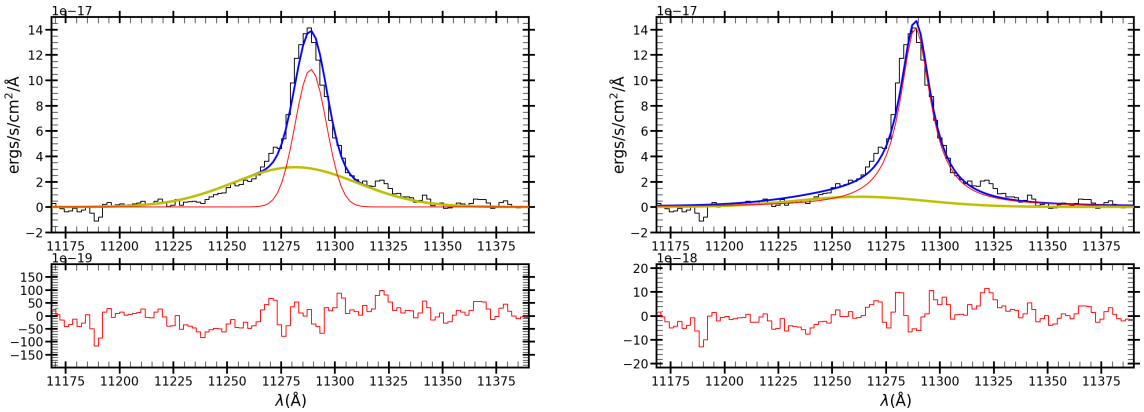

Deblending procedure applied to the O I λ11287. The left panel shows the modeling assuming Gaussian components, while the right panel shows the results considering a Lorentzian profile for the part emitted by the classical BLR. The observed profile is the black histogram, and the blue line is the best fit. Individual components corresponding to the classical BLR are in red while the outflow component is in yellow. The bottom panel is the residual after subtracting from the observations the best fit.

SOURCE: Rodríguez-Ardila et al. (2024)

5.1.4 Other line fittings

We next proceed to fit the blend formed by the Fe II lines at λ9997 and λ10172, the Paδ line and the He II line at λ10124. Figure 5.1.4 displays the fit when the BLR

Figure 5.8 - Deblending procedure applied to the FeII λ9997+Paδ blend without an outflow component.

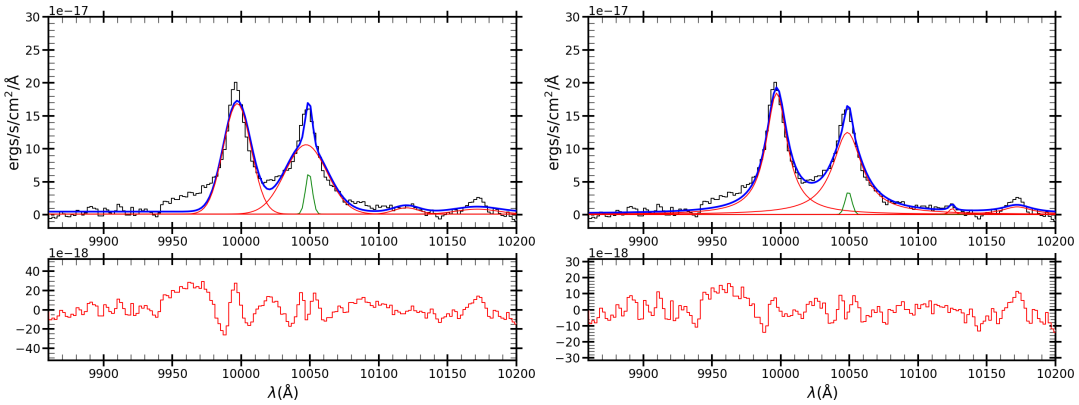

The left and right panels show the results assuming that the classical BLR is represented by a Gaussian and a Lorentzian profile, respectively. The observed profile is the black histogram, and the blue line is the best fit. Individual components corresponding to the classical BLR are in red. The green line is the component attributed to the NLR. The bottom panel is the residual after subtracting from the observations the best fit. .

SOURCE: Rodríguez-Ardila et al. (2024)

is modelled with a single component. The corresponding BIC is in Table 5.1.1. Figure 5.1.4 illustrates the scenario where a blueshifted Gaussian component is included in addition to a Gaussian profile (left panel) and a Lorentzian profile (right panel) for the classical BLR component. In this process, we tied the Paδ profile to have similar FWHM and centroid positions as that found for the Paβ line. BIC values are in Table 5.1.1 while Table 5.1.1 lists the best parameters of the different components found from the fit.

The BIC values supports the need for a blueshifted broad component in both Fe II and Paδ, in agreement with the results already found using Paβ and FeII λ10501. Moreover, the BIC is smaller for the Lorentzian approach, indicating that profile as the most suitable one to represent the classical BLR.

Finally, we fit the blend formed by the forbidden [S III] λ9531 line, the Pa 8 line at λ9547 and the FeII lines at $\lambda\lambda$9501,9571. This fit is very important because it involves the only forbidden line detected in the NIR spectrum of 1H 0707−495. Moreover, [S III] λ9531 is considered the NIR counterpart of [O III] λ5007 in the optical (FISCHER et al., 2017). Figure 5.11 pictures the result when the BLR is modelled with a single component while Figure 5.1.4 displays the profile fit after

Figure 5.9 - Deblending procedure applied to the FeII λ9997+Paδ blend.

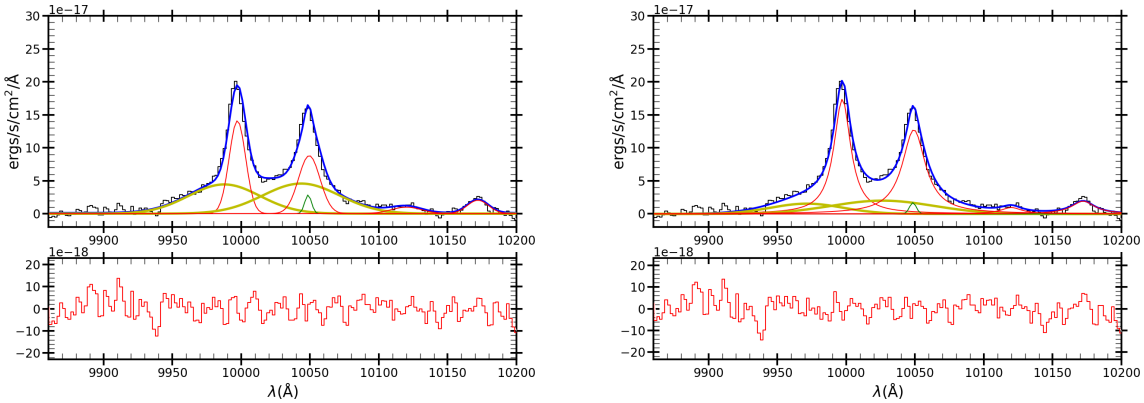

The left panel shows the modeling assuming Gaussian components, while the right panel shows the results considering a Lorentzian profile for the part emitted by the classical BLR. The observed profile is the black histogram, and the blue line is the best fit. Individual components corresponding to the classical BLR are in red while the outflow component is in yellow. The green line is the component attributed to the NLR. The bottom panel is the residual after subtracting from the observations the best fit.

SOURCE: Rodríguez-Ardila et al. (2024).

Figure 5.10 - Line fitting procedure applied to the [S III] λ9531 + Pa 8 blend.

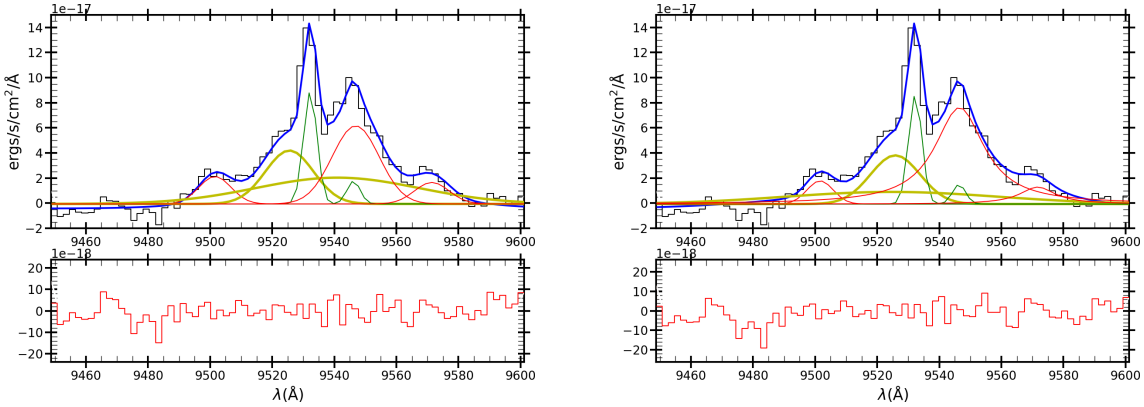

Line fitting procedure applied to the [S III] λ9531 + Pa 8 blend. The left panel shows the modeling assuming only Gaussian components, while the right panel shows the results considering a Lorentzian profile for the part emitted by the classical BLR. The observed profile is the black histogram, and the blue line is the modeled profile. Individual components are painted in different colors. The bottom panel is the residual after subtracting the modeled emission line profile.

SOURCE: Rodríguez-Ardila et al. (2024).

Figure 5.11 - Similar to Figure 5.1.4 for the [S III] λ9531+Pa 8 blend.

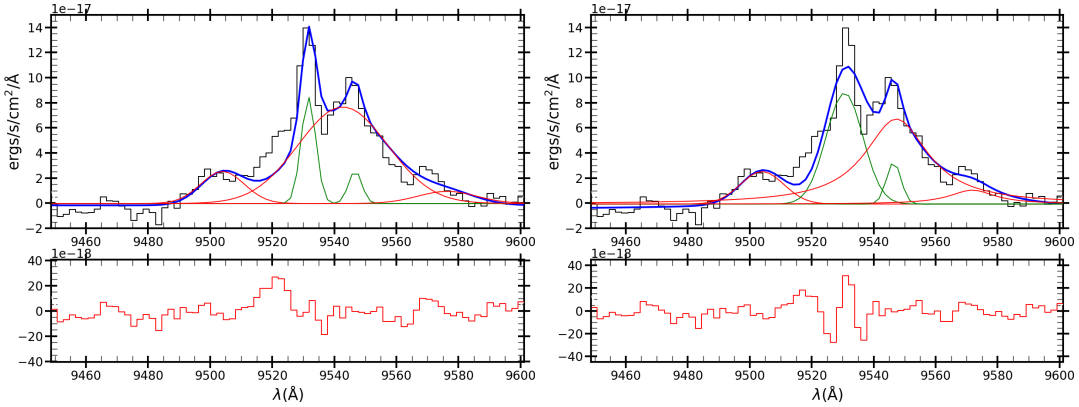

SOURCE: Rodríguez-Ardila et al. (2024).

adding a blueshifted Gaussian component to both [S III] and Pa 8. The corresponding BIC values are in Table 5.1.1.

It can be seen that, in addition to a narrow component due to the classical NLR, the [S III] λ9531 line displays a strong blue asymmetric wing, suitably fit with a broad component. The velocity derived from the peak centroid of the blueshifted line is -170 km s^{-1}, with a FWHM velocity of 570 km s^{-1} (see Table 5.1.1). Whether the blueshifted component represents the propagation of the BLR outflow into the NLR cannot be confirmed or discarded from the data. However, it is rather tempting to assume that it is, considering that the BLR lines thought to be produced in the outskirts of that region do display an outflow component. The BIC listed in Table 5.1.1 show that the smallest values are obtained when a blueshifted component is added to the blend, confirming the results discussed above. Moreover, the BIC$_{\rm min}$ criterion favours the Lorenztian profile for the classical BLR.

5.2 Discussion

Ultrafast outflows (UFOs) are the most extreme subset of AGN winds with velocities greater than 10000 km s^{-1}. They are believed to originate from the inner accretion disk within a few hundred gravitational radii from the black hole (TOMBESI et al., 2010; NARDINI et al., 2015). The existence of an UFO has been confirmed in 1H 0707−495 (DAUSER et al., 2012; HAGINO et al., 2016; KOSEC et al., 2018b) at a velocity of ∼0.13c with an ionisation parameter log(ξ/erg cm s^{-1}) ∼4.3. Blustin and Fabian (2009) detected Doppler-shifted emission lines, and Kosec et al. (2018b)

found that the velocities of the blueshifted emission increase in higher ionization species. This implies that the wind in 1H 0707−495 is likely stratified and is perhaps slowing down and cooling at larger distances from the SMBH.

The evidence gathered in this work using NIR spectroscopy and BIC analysis reveals the presence of a blueshifted emission in the low-ionization lines of H I (Paβ, Paδ, and Pa 8), Fe II $\lambda\lambda$9997,10501, and, and to a lower extend, in O I λ11287. Even the forbidden line of [S III] λ9531 displays clear evidence of such outflow. In all cases, the outflow component is modeled using a Gaussian function with a turbulent velocity between 1800 and 2600 km s^{-1}. The outflow velocity varies from -160 km s^{-1} to -820 km s^{-1} in the lines studied. The lowest velocity is derived when a Gaussian function is employed to model the classical BLR contribution, while the largest one is obtained when a Lorentzian profile is used to represent the classical BLR.

We suggest that the outflow that is detected in the BLR high-ionization lines reported in Leighly and Moore (2004) is also present in the low-ionization lines of H I and FeII. Previous observations of low-ionization lines such as Mg II in the UV and the Balmer lines in the optical by these authors had found that they appear to be rest-frame and of disc origin. Here, we confirm the detection of the disc component using BLR NIR lines, found at rest relative to the systemic velocity and with a turbulent velocity between 410 and 600 km s^{-1}. Moreover, the outflow component is unambiguous, regardless of the type of profile employed in the line fitting to represent the classical BLR although our study favours the Lorentzian representation. The outflow velocity can be as high as ∼826 km s^{-1}.

Kosec et al. (2018b) found a trend of increasing velocities with the increase of the ionization parameter of the ions. They also report possible similar kinetic powers of UV, soft X-ray emitters, and UFO absorbers. They suggest that we are witnessing the evolution of a stratified, kinetic energy-conserving wind. Our results suggest that the wind in 1H 0707−495 extends well into the outer boundary of the BLR, where the FeII and the O I lines are formed (MARINELLO et al., 2016a). Indeed, adding the FeII and O I measurements from this work to Figure 3 of Kosec et al. (2018b), which relates the strength of the outflows with the ionization parameter, gives further support to our results. They found a relationship of the form $V = b \times (\xi / \mathrm{erg\,cm\,s^{-1}})^a$, where V is the outflow velocity, ξ is the ionisation parameter, and a and b are constants, $a = 0.36 \pm 0.04$ and $b = (1800 \pm 300)$ km s^{-1}.

To derive the expected outflow velocity for Fe II we employed log U of ≈ -3.25. This value is calculated using CLOUDY and the observed SED for I Zw 1, super-solar

metal content (5-10 $Z_{\odot}$), and a microturbulence velocity of 20 km s^{-1} within the BLR cloud. The model further assumes a cloud column density of 10^{24} cm^{-2} (see for more details Panda (2021e)). From the above equation and employing the aforementioned value of U, an outflow velocity of -125 km s^{-1} is predicted. We note that Kosec et al. (2018b) choose arbitrary 500 km s^{-1} error bars on UV ion velocities due to a lack of uncertainties in Leighly and Moore (2004). Thus, assuming this uncertainty, the outflow velocity measured here in FeII and H I is less than a factor 2 than that predicted. Moreover, The detection of a blueshifted component in the forbidden line of [S III] indeed suggests that the outflow is coupled to the gas located in the NLR.

Another important result is that the disc component of the low-ionization lines displays a very low turbulent velocity, of ∼546 km s^{-1} in the FeII and the O I lines. These are likely some of the narrowest BLR lines already reported in the literature.

A full analysis of the NIR spectrum of 1H 0707−495 is out of the scope of this work. However, upon inspection of our spectrum, it is evident that IFU observations of this object, both in the optical and in the NIR, are necessary to fully assess the size and energetic properties of the outflow.

In conclusion, we have analyzed the NIR spectrum of the xA NLS1 galaxy 1H 0707−495, widely known for displaying a UFO from X-ray emission lines. The ultra-fast outflow is likely propagated to the inner portion of the BLR because UV high- and mid-ionization lines produced in that region are strongly blue asymmetric. In this work we provide convincing evidence that the outflow is observed farther out, reaching the outer portions of the BLR. Our results also suggest that at least part of the outflow is detected in the NLR because of the blue asymmetric line associated with [S III] λ9531.

The permitted emission lines studied in this work (i.e., H I, FeII, and O I) are thought to be formed in the mid and outer portions of the BLR. The analysis of the line profiles shows that overall, the classical BLR component is best represented using a Lorentzian profile plus and outflow component of up to ∼-730 km s^{-1} for H I and FeII. In this scenario, O I seems not to take part of the outflow. This result is supported by the use of Bayesian Information Criteria (BIC) to select the model that best represents each line. Previous observations have failed in detecting the outflow component in low-ionization lines in this AGN. Our results are also consistent, within the uncertainties, to models predicting outflow velocities down to -300 km s^{-1}, for lines formed in gas with $U < -3$, as is the case here.

Finally, the analysis made on the NIR continuum of 1H 0707−495 shows that it is well represented by the low-energy tail of the optical power-law, with a spectral index of α=1.95. Also, we found strong evidence of the presence of hot dust, with a temperature of $\sim$1300 K. This dust is likely located on the inner face of the torus.

6 CONCLUSION AND FUTURE WOKS

6.1 Conclusion

This thesis presents a comprehensive study of the BLR in three AGNs, focusing on the physical conditions, geometry, and kinematics of the low-ionization gas. Key results were obtained by carrying out photoionization modeling of the FeII emission using optical and NIR spectra, as well as a detailed analysis of double-peaked emission profiles and outflows in the FeII lines.

The first major contribution of this thesis is the first simultaneous modeling of optical and NIR FeII emission in the I Zw 1 galaxy. Using new FeII atomic datasets and the CLOUDY code, we derive physical conditions such as hydrogen density, metallicity, and column density, that can reproduce the observed R_{4570} and $R_{1\mu\,\mathrm{m}}$ ratios. We investigated how changes in micro-turbulence and metal content impact both optical and NIR FeII emissions. Using Verner et al. (1999) dataset, we find that the physical conditions that simultaneously reproduce optical and NIR FeII intensities are $n_{\mathrm{H}} = 10^{10.75}$–$10^{11.50}$ cm^{-3} and a metallicity range of $5\ Z_{\odot} \lesssim Z \lesssim 10\ Z_{\odot}$. Whereas for Smyth et al. (2018) and Tayal and Zatsarinny (2018) datasets, we obtain hydrogen densities between $10^{11.0}$ and $10^{12.0}$ cm^{-3} and solar metallicity. The introduction of micro-turbulence (10 km s^{-1}) in the models significantly improve the agreement between observed and simulated spectra, especially in the NIR, where Lyman-α fluorescence is particularly important. Our results also confirm that micro-turbulence acts as a metallicity controller in the gas. Moreover, our results suggest that the CaT and O I emissions can serve as analogs for the FeII emission study. Finally, we conclude that the new FeII atomic datasets − Smyth et al. (2019) and Tayal and Zatsarinny (2018) − successfully reproduce FeII emissions under less extreme physical conditions when compared to the Verner et al. (1999) dataset.

The second major contribution of this thesis was the first detection of a double-peaked profile in the O I λ11297 and Paα emission lines in the Seyfert 1 galaxy III Zw 002. This detection provides new insights into the geometry of the BLR, suggesting a disk-like structure with a low inclination angle of 18°. Using the inclination and four different values for κ: 0.3, 0.2, 0.1, and 0.0 (where κ=0 refers to a flat disk geometry) (COLLIN et al., 2006; GRIER et al., 2013; STORCHI-BERGMANN et al., 2017; PANDA et al., 2019), we obtained virial factors 5.39, 7.38, 9.47, and 10.47, respectively. These results are consistent with the inclinations measured for NGC 5273 (i=16°), NGC 3227 (i=17°), and NGC 5548 (i=19°), and with estimated virial factors of 12, 11.7, and 9.4, respectively (STORCHI-BERGMANN et al., 2017).

The application of the disk modeling allowed us to estimate the virial factor more accurately, addressing the common uncertainties in black hole mass estimates and BLR geometry. Using these parameters, we estimate BH masses of $4.86 \times 10^8 M_\odot$, $6.65 \times 10^8 M_\odot$, $8.55 \times 10^8 M_\odot$, and $9.44 \times 10^8 M_\odot$, which are in good agreement with the mass of BH estimated by RM, $1.84 \times 10^8 M_\odot$, using f=5.5 (GRIER et al., 2012). This result highlights the utility of double-peaked profiles in refining black hole mass measurement.

In the third major contribution, we investigate the kinematics of the low-ionization gas in the AGN 1H 0707-495. We report the first detection of an outflow gas component in the Paβ, FeII, and O I emission lines. We associate that component to the UFO previously observed in X-ray emission lines and HILs. We conclude that the UFO is likely propagated into the outer regions of the BLR. We provide convincing evidence for the first time that the outflow extends into the low-ionization region of the BLR, reaching velocities up to $\sim$-730 km s^{-1}. Furthermore, a blue asymmetric line associated with [S III] λ9531 also suggest that at least part of the outflow is detected in the NLR. Finally, from the NIR continuum fit of 1H 0707-495, we obtain that the optical power-law has a spectral index of $\alpha = 1.95$, while the hot dust emission, likely located on the inner face of the torus, was modeled with a temperature of $\sim$1300K.

In summary, the results of this thesis contribute to a deeper understanding of the physical conditions, geometry, and kinematics of the low ionization gas in AGN. We provide new insights for future studies on AGN evolution, the geometry of the BLR, and the connection between the accretion disk and outflows.

6.2 Future perspectives

As a continuation work of this thesis, we plan to expand our study of the FeII emission in both optical and NIR regimes by analyzing a sample of 105 Type-I AGNs, collected over the 4 years of this PhD. This investigation will allow us to further explore the line formation and gas physical conditions in sources with varying FeII emission strengths. We aim to utilize Principal Component Analysis (PCA) to establish correlations among the emission line properties and extend the Eigenvector 1 (EV1) parameter space by incorporating NIR lines, such as [S III], Paβ, and FeII at 1 μm. This expansion will increase our understanding of AGN populations and contribute to our knowledge of AGN evolution. All data have already been collected and reduced.

Additionally, we plan to continue our study of the NLSy1 galaxy 1H 0707-193 by applying the CLOUDY code to simulate the FeII emission, using the same setup as for 1ZwI. For instance, over 30% of the AGNs in our sample are classified as NLS1s, allowing us to compare the observations with our previous models. By fitting the FeII emission in these IZw 1-like NLS1s, we aim to establish a comprehensive comparison with theoretical predictions, which will enhance our understanding of the emission mechanisms in these extreme FeII emitters. Also, we plan to create an empirical template for FeII based on the NIR spectrum of the 1H 0707−495 galaxy. Although the traditional 1 Zw I template is widely used, it does not account for all variations in the iron spectrum of extreme FeII emitters. AGNs like 1H 0707−495 can help in creating new FeII templates, leading to more accurate modeling. In the optical region, progress has been made with an alternative template for Mrk 493, otherwise, any advance was made in the NIR. Thus, we aim to provide a new template that could improve the modeling of FeII emission in such xA AGNs.

In addition, we plan to extend our double-peaked study to a larger sample of AGNs selected from the SDSS catalog. Our current sample includes 25 AGNs, and we intend to analyze their optical and NIR spectra using the same modeling approach. Key objectives for future research include:

- **Advancing the understanding of the geometry and dynamics of accretion disks and the low-ionization region in AGNs:** Through multispectral analysis, we will characterize the O I and CaT emissions originating from the outer part of the BLR. By applying disk modeling to a diverse sample of AGNs, we aim at improving our understanding of the physical properties of accretion disks, including inclination, emissivity, and radial extent.

- **Contributing to the study of AGN evolution:** A systematic study of AGNs across the quasar main sequence will help investigating how the properties of accretion disks vary across different AGN populations, providing insights into their evolution over time.

- **Improving estimates of the virial factor (f) and black hole masses (SMBHs):** Fitting the disk model will enable us to derive the angle of inclination and estimate the virial factor, leading to more accurate black hole mass estimates. This will address the current bias in the SMBH mass estimates due to uncertainties in the virial factor and improve the precision of methods that depend on this parameter.

In summary, we expect with all of this work to contribute to a better understanding of the BLR in AGNs.

REFERENCES

ANTONUCCI, R. Unified models for active galactic nuclei and quasars. **Annual Review of Astronomy and Astrophysics**, v. 31, n. 1, p. 473–521, 1993. ISSN 00664146. Available from: <<https://ui.adsabs.harvard.edu/abs/1993ARA&A..31..473A/abstract>>. 5

ARNAUD, K. A.; BRANDUARDI-RAYMONT, G.; CULHANE, J. L.; FABIAN, A. C.; HAZARD, C.; MCGLYNN, T. A.; SHAFER, R. A.; TENNANT, A. F.; WARD, M. J. EXOSAT observations of a strong soft X-ray excess in MKN 841. **Monthly Notices of the Royal Astronomical Society**, v. 217, n. 1, p. 105–113, 11 1985. ISSN 0035-8711. Available from: <<https://academic.oup.com/mnras/article/217/1/105/994940>>. 3

BAO, D.-W.; BROTHERTON, M. S.; DU, P.; MCLANE, J. N.; ZASTROCKY, T. E.; OLSON, K. A.; FANG, F.-N.; ZHAI, S.; HUANG, Z.-P.; WANG, K.; ZHAO, B.-X.; LI, S.-S.; YANG, S.; CHEN, Y.-J.; LIU, J.-R.; YAO, Z.-H.; PENG, Y.-C.; GUO, W.-J.; SONGSHENG, Y.-Y.; LI, Y.-R.; JIANG, B.-W.; KASPER, D. H.; CHICK, W. T.; NGUYEN, M. L.; MAITHIL, J.; KOBULNICKY, H. A.; DALE, D. A.; HAND, D.; ADELMAN, C.; CARTER, Z.; MURPHREE, A. M.; OEUR, M.; SCHONSBERG, S.; ROTH, T.; WINKLER, H.; MARZIANI, P.; D'ONOFRIO, M.; HU, C.; XIAO, M.; XUE, S.; CZERNY, B.; ACEITUNO, J.; HO, L. C.; BAI, J.-M.; WANG, J.-M.; COLLABORATION, M. Monitoring AGNs with Hβ asymmetry. III. Long-term reverberation mapping results of 15 Palomar-Green quasars. **The Astrophysical Journal Supplement**, v. 262, n. 1, p. 14, 2022. ISSN 1538-4365. Available from: <<https://ui.adsabs.harvard.edu/abs/2022ApJS..262...14B>>. 79

BARGER, A. **Supermassive black holes in the distant universe**. Dordrecht: Springer Netherlands, 2004. 0–298 p. (Astrophysics and Space Science Library, v. 308). ISBN 978-90-481-6662-6. Available from: <<http://link.springer.com/10.1007/978-1-4020-2471-9>>. 2

BARTH, A. J.; PANCOAST, A.; BENNERT, V. N.; BREWER, B. J.; CANALIZO, G.; FILIPPENKO, A. V.; GATES, E. L.; GREENE, J. E.; LI, W.; MALKAN, M. A.; SAND, D. J.; STERN, D.; TREU, T.; WOO, J.-H.; ASSEF, R. J.; BAE, H.-J.; BUEHLER, T.; CENKO, S. B.; CLUBB, K. I.; COOPER, M. C.; DIAMOND-STANIC, A. M.; HÖNIG, S. F.; JONER, M. D.; LANEY, C. D.; LAZAROVA, M. S.; NIERENBERG, A. M.; SILVERMAN, J. M.; TOLLERUD, E. J.; WALSH, J. L. The lick AGN monitoring project 2011: Fe II reverberation from the outer broad-line region. **The Astrophysical Journal**, v. 769, n. 2, p. 128, 2013. ISSN 0004-637X. 7

BARVAINIS, R. Hot dust and the near-infrared bump in the continuum spectra of quasars and active galactic nuclei. **The Astrophysical Journal**, v. 320, p. 537, 9 1987. ISSN 0004-637X. 10, 39

BAUTISTA, M. A.; FIVET, V.; BALLANCE, C.; QUINET, P.; FERLAND, G.; MENDOZA, C.; KALLMAN, T. R. Atomic data and spectral model for Fe II. **The Astrophysical Journal**, v. 808, n. 2, p. 174, jul 2015. Available from: <<https://doi.org/10.1088/0004-637x/808/2/174>>. xv, 32, 44, 45, 46

BEGELMAN, M. C.; BLANDFORD, R. D.; REES, M. J. Massive black hole binaries in active galactic nuclei. **Nature**, v. 287, n. 5780, p. 307–309, 1980. 19

BENTZ, M. C.; PETERSON, B. M.; NETZER, H.; POGGE, R. W.; VESTERGAARD, M. The radius-luminosity relationship for active galactic nuclei: The effect of host-galaxy starlight on luminosity measurements. II. The full sample of reverberation-mapped AGNs. **The Astrophysical Journal**, v. 697, p. 160–181, 2009. Available from: <<http://ganymede.nmsu.edu/holtz/xvista.>>. 9, 85

BERGERON, J.; KUNTH, D. Inferences from a study of Fe II emission in radio-loud and radio-quiet quasars. **Monthly Notices of the Royal Astronomical Society**, v. 207, p. 263–286, 1984. 13

BLANDFORD, R. D.; EMMERING, R. T.; SHLOSMAN, I. A non-starburst model for agn broad emission lines. In: FILIPPENKO, A. V. (Ed.). **Relationships between active galactic nuclei and starburst galaxies.** [S.l.: s.n.], 1992. v. 31, p. 443–447. 18

BLANDFORD, R. D.; MCKEE, C. F. Reverberation mapping of the emission line regions of Seyfert galaxies and quasars. **The Astrophysical Journal**, v. 255, p. 419–439, 1982. 9

BLUSTIN, A. J.; FABIAN, A. C. An accretion disc origin for the 'X-ray broad-line region' in 1H0707-495. **Monthly Notices of the Royal Astronomical Society**, v. 399, n. 1, p. L169–L173, oct. 2009. 104

BOCHKAREV, N. G.; GASKELL, C. M. The accuracy of supermassive black hole masses determined by the single-epoch spectrum (Dibai) method. **Astronomicheski͡ı Zhurnal**, v. 35, n. 5, p. 322–329, 2009. 9

BOLLER, T.; FABIAN, A. C.; SUNYAEV, R.; TRÜMPER, J.; VAUGHAN, S.; BALLANTYNE, D. R.; BRANDT, W. N.; KEIL, R.; IWASAWA, K. XMM-Newton discovery of a sharp spectral feature at ∼7 keV in the narrow-line Seyfert 1 galaxy 1H 0707 - 49. **Monthly Notices of the Royal Astronomical Society**, v. 329, n. 1, p. L1–L5, jan. 2002. 32

BOLLER, T.; LIU, T.; WEBER, P.; ARCODIA, R.; DAUSER, T.; WILMS, J.; NANDRA, K.; BUCHNER, J.; MERLONI, A.; FREYBERG, M. J.; KRUMPE, M.; WADDELL, S. G. H. Extreme ultra-soft X-ray variability in an eROSITA observation of the narrow-line Seyfert 1 galaxy 1H 0707-495. **Astronomy and Astrophysics**, v. 647, p. A6, mar. 2021. 32

BONTÀ, E. D.; PETERSON, B. M. Black hole masses from emission-line widths. **Astronomische Nachrichten**, v. 343, n. 1-2, p. e210070, jan. 2022. 85

BOROSON, T. A.; GREEN, R. F. The emission-line properties of low-redshift quasi-stellar objects. **The Astrophysical Journal Supplement**, v. 80, p. 109, may 1992. 13, 15, 30, 31, 40, 68

BOROSON, T. A.; OKE, J. B. Detection of the underlying galaxy in the QSO 3C48. **Nature**, v. 296, n. 5856, p. 397–399, 1982. ISSN 00280836. 2

BOTTORFF, M. C.; FERLAND, G. J. Magnetic confinement, magnetohydrodynamic waves and smooth line profiles in active galactic nuclei. **Monthly Notices of the Royal Astronomical Society**, v. 316, n. 1, p. 103–106, 07 2000. ISSN 0035-8711. Available from: <<https://doi.org/10.1046/j.1365-8711.2000.03465.x>>. 47

BRUHWEILER, F.; VERNER, E. Modeling Fe ii emission and revised Fe ii (UV) empirical templates for the seyfert 1 galaxy I Zw 1. **The Astrophysical Journal**, v. 675, n. 1, p. 83–95, 3 2008. ISSN 0004-637X. 47, 56, 58, 61

BRUNTHALER, A.; FALCKE, H.; BOWER, G. C.; ALLER, M. F.; ALLER, H. D.; TERÄSRANTA, H.; LOBANOV, A. P.; KRICHBAUM, T. P.; PATNAIK, A. R. III Zw 2, the first superluminal jet in a Seyfert galaxy. **Astronomy and Astrophysics**, v. 357, p. L45–L48, may 2000. Available from: <<https://ui.adsabs.harvard.edu/abs/2000A&A...357L..45B>>. 29

BRUNTHALER, A.; FALCKE, H.; BOWER, G. C.; ALLER, M. F.; ALLER, H. D.; TERÄSRANTA, H. The extreme flare in III Zw 2:. **Astronomy & Astrophysics**, v. 435, n. 2, p. 497–506, 5 2005. ISSN 0004-6361. Available from: <<http://www.aanda.org/10.1051/0004-6361:20042427>>. 29

BURBIDGE, G. R.; BURBIDGE, E. M.; SANDAGE, A. R. Evidence for the occurrence of violent events in the nuclei of galaxies. **Reviews of Modern Physics**, v. 35, n. 4, p. 947–972, 1963. ISSN 00346861. 1

CAPETTI, A.; AXON, D.; MACCHETTO, F. Radio outflows and the origin of the narrow-line region in seyfert galaxies. **The Astrophysical Journal**, v. 469, p. 554, 1996. 5

CAPPI, M. Relativistic blue-and red-shifted absorption lines in agns. **Astronomische Nachrichten: Astronomical Notes**, v. 327, n. 10, p. 1012–1019, 2006. 24

CARDELLI, J. A.; CLAYTON, G. C.; MATHIS, J. S. The relationship between infrared, optical, and ultraviolet extinction. **The Astrophysical Journal**, v. 345, p. 245, oct. 1989. Available from: <<https://ui.adsabs.harvard.edu/abs/1989ApJ...345..245C>>. 36, 37

CHARTAS, G.; BRANDT, W.; GALLAGHER, S.; GARMIRE, G. Chandra detects relativistic broad absorption lines from apm 08279+ 5255. **The Astrophysical Journal**, v. 579, n. 1, p. 169, 2002. 24

CHEN, K.; HALPERN, J. P. Structure of line-emitting accretion disks in active galactic nuclei: ARP 102B. **The Astrophysical Journal**, v. 344, p. 115, sep. 1989. 18, 19, 48, 49, 50, 79, 85

CHEN, K.; HALPERN, J. P.; FILIPPENKO, A. V. Kinematic evidence for a relativistic Keplerian disk: ARP 102B. **The Astrophysical Journal**, v. 339, p. 742, apr. 1989. 18, 19, 48, 79

CHIANG, J.; MURRAY, N. Reverberation mapping and the disk wind model of the broad line region. **arXiv preprint astro-ph/9511006**, 1995. 19, 20

COLLIN, S. Quasars and galactic nuclei, a half-century agitated story. **AIP Conference Proceedings**, v. 861, n. 1, p. 587–595, 11 2006. 18

COLLIN, S.; HURÉ, J.-M. Size-mass-luminosity relations in agn and the role of the accretion disc. **Astronomy & Astrophysics**, v. 372, n. 1, p. 50–58, 2001. 17, 18

COLLIN, S.; KAWAGUCHI, T.; PETERSON, B. M.; VESTERGAARD, M. **Systematic effects in measurement of black hole masses by emission-line reverberation of active galactic nuclei: eddington ratio and inclination**. [S.l.], 2006. 8, 85, 86, 109

COLLIN-SOUFFRIN, S. On the origin of the optical and uv continuum in active galactic nuclei. **Astronomy and Astrophysics**, v. 249, p. 344–350, 1991. 18

COLLIN-SOUFFRIN, S.; DUMNONT, S.; JOLY, M.; PEQUIGNOT, D. The emission spectrum of active galactic nuclei. II. high column density photoionization models and low ionization lines. **Astronomy and Astrophysics**, v. 166, p. 27–35, 1986. Available from: <<https://ui.adsabs.harvard.edu/abs/1986A&A...166...27C/abstract>>. 13

COLLIN-SOUFFRIN, S.; DUMONT, A. Line and continuum emission from the outer regions of accretion discs in active galactic nuclei. ii-radial structure of the disc. **Astronomy and Astrophysics**, v. 229, p. 292–328, 1990. 18, 19

COLLIN-SOUFFRIN, S.; DUMONT, S.; HEIDMANN, N.; JOLY, M. Formation of permitted lines in the spectrum of type 1 seyfert galaxies and quasars. ii-fe ii lines and the low excitation region. **Astronomy and Astrophysics**, v. 83, p. 190–198, 1980. 13

COLLIN-SOUFFRIN, S.; LASOTA, J.-P. The broad-line region of active galactic nuclei revisited. **Publications of the Astronomical Society of the Pacific**, v. 100, n. 631, p. 1041, 1988. 18

CUSHING, M. C.; VACCA, W. D.; RAYNER, J. T. Spextool: a spectral extraction package for spex, a 0.8-5.5 micron cross-dispersed spectrograph. **Publications of the Astronomical Society of the Pacific**, v. 116, n. 818, p. 362–376, apr. 2004. 36

CZERNY, B.; ELVIS, M. Constraints on quasar accretion disks from the optical/ultraviolet/soft X-ray big bump. **The Astrophysical Journal**, v. 321, p. 305–320, 1987. 3

CZERNY, B.; HRYNIEWICZ, K. The origin of the broad line region in active galactic nuclei. **Astronomy & Astrophysics**, v. 525, p. 8, 10 2011. 10

CZERNY, B.; MODZELEWSKA, J.; PETROGALLI, F.; PYCH, W.; ADHIKARI, T. P.; ZYCKI, P. T.; HRYNIEWICZ, K.; KRUPA, M.; KURCZ, A.; NIKOLAJUK, M. The dust origin of the Broad Line Region and the model consequences for AGN unification scheme. **Advances in Space Research**, v. 55, n. 7, p. 1806–1815, 9 2014. 7

CZERNY, B.; WANG, J.; DU, P.; HRYNIEWICZ K.; KARAS, V. L. L. R. P. S.; SNIEGOWSKA, M.; WILDY, C.; YUAN, Y. F. Interpretation of departure from the broad-line region scaling in active galactic nuclei. **The Astrophysical Journal**, v. 870, p. 84, 2019. 10

DAUSER, T.; SVOBODA, J.; SCHARTEL, N.; WILMS, J.; DOV, M.; EHLE, M.; KARAS, V.; SANTOS-LLEÓ, M.; MARSHALL, H. L. Spectral analysis of 1H 0707-495 with XMM-Newton. **Monthly Notices of the Royal Astronomical Society**, v. 422, n. 3, p. 1914–1921, may 2012. 32, 104

DIAS DOS SANTOS, D. **Propriedades do contínuo e do gás emissor de linhas largas em AGNS emissores de Fe II**. 0–217 p. Master Thesis (Mestrado) — Instituto Nacional de Pesquisas Espaciais, São José dos Campos, 2021. Available from: <<http://www.inpe.br/posgraduacao/ast/arquivos/dissertacoes/dissertacao_denimara_dias_dos_santos.pdf>>. 37

DIBAI, A.; PRONIK, V. I.; DIBAI, A.; PRONIK, V. I. A spectrophotometric study of Seyfert-galaxy nuclei. **Astronomicheskii Zhurnal**, v. 44, p. 952, 1967. ISSN 0004-6299. Available from: <<https://ui.adsabs.harvard.edu/abs/1967AZh....44..952D/abstract>>. 11

DIPOMPEO, M.; HICKOX, R.; CARROLL, C. The profiles of infrared-selected active galactic nuclei: more powerful outflows in the obscured population. **The Astrophysical Journal**, 2018. 6

DONG, X.-B.; HO, L. C.; WANG, J.-G.; WANG, T.-G.; WANG, H.; FAN, X.; ZHOU, H. The prevalence of narrow optical fe ii emission lines in type 1 active galactic nuclei. **The Astrophysical Journal Letters**, v. 721, n. 2, p. L143, 2010. 21, 39

_____. The prevalence of narrow optical Fe ii emission lines in type 1 active galactic nuclei. **The Astrophysical Journal Letters**, v. 721, p. 143–147, 2010. Available from: <<http://staff.ustc.edu.cn/>>. 31

DU, P.; BROTHERTON, M. S.; WANG, K.; HUANG, Z.-P.; HU, C.; KASPER, D. H.; CHICK, W. T.; NGUYEN, M. L.; MAITHIL, J.; HAND, D.; LI, Y.-R.; HO, L. C.; BAI, J.-M.; BIAN, W.-H.; WANG, J.-M. Monitoring AGNs with H β

asymmetry. I. first results: velocity-resolved reverberation mapping . **The Astrophysical Journal**, v. 869, n. 2, p. 142, 12 2018. ISSN 15384357. 79

DU, P.; HU, C.; LU, K.-X.; HUANG, Y.-K.; CHENG, C.; QIU, J.; LI, Y.-R.; ZHANG, Y.-W.; FAN, X.-L.; BAI, J.-M.; BIAN, W.-H.; YUAN, Y.-F.; KASPI, S.; HO, L. C.; NETZER, H.; WANG, J.-M. Supermassive black holes with high accretion rates in active galactic nuclei. iv. Hβ time lags and implications for super-eddington accretion. **The Astrophysical Journal**, 2015. 21, 23, 27, 85

DU, P.; WANG, J.-M. The radius–luminosity relationship depends on optical spectra in active galactic nuclei. **The Astrophysical Journal**, v. 886, n. 1, p. 42, 11 2019. ISSN 0004-637X. Available from: <<https://iopscience.iop.org/article/10.3847/1538-4357/ab4908https://iopscience.iop.org/article/10.3847/1538-4357/ab4908/meta>>. 9, 21, 85

DUMONT, A.; COLLIN-SOUFFRIN, S. Line and continuum emission from the outer regions of accretion discs in active galactic nuclei-part iv-line emission. **Astronomy and Astrophysics**, v. 229, p. 313, 1990. 19

_____. Line and continuum emission from the outer regions of accretion discs in active galactic nuclei. v-detailed computational results. **Astronomy and Astrophysics Supplement Series**, v. 83, p. 71–89, 1990. 19

DURRÉ, M.; MOULD, J. **The southern hemisphere narrow-line Seyfert 1 infrared survey**. [S.l.], 2021. v. 000, 1–16 p. Available from: <<http://cdsarc.u-strasbg.fr/viz-bin/qcat?J/A+A/587/A138>>. 21

DURRÉ, M.; MOULD, J. The southern hemisphere narrow-line Seyfert 1 infrared survey. **Monthly Notices of the Royal Astronomical Society**, v. 509, n. 2, p. 2377–2389, jan. 2022. 33

D'ONOFRIO, M.; MARZIANI, P.; SULENTIC, J. W. **Fifty years of quasars** . [S.l.: s.n.], 2012. 0–583 p. 6, 12, 13, 21

ERACLEOUS, M.; HALPERN, J. P. Doubled-peaked emission lines in active galactic nuclei. **Astrophysical Journal Supplement Series**, v. 90, p. 1–30, 1994. 19

_____. Completion of a survey and detailed study of double-peaked emission lines in radio-loud active galactic nuclei. **The Astrophysical Journal**, v. 599, n. 2, p. 886–908, 12 2003. ISSN 0004-637X. 19, 79, 84

ERACLEOUS, M.; LEWIS, K. T.; BOGDANOVIĆ, T.; GEZARI, S.; HALPERN, J. P. Models and ideas for the interpretation of the variability of double-peaked emission lines. In: GASKELL, C. M.; MCHARDY, I. M.; PETERSON, B. M.; SERGEEV, S. G. (Ed.). **AGN variability from X-rays to radio waves**. [S.l.: s.n.], 2006. v. 360, p. 227. 19

ERACLEOUS, M.; LEWIS, K. T.; FLOHIC, H. M. **Double-peaked emission lines as a probe of the broad-line regions of active galactic nuclei**. [S.l.]: North-Holland, 7 2009. 133–139 p. 19, 79

ERACLEOUS, M.; LIVIO, M.; HALPERN, J. P.; STORCHI-BERGMANN, T. Elliptical accretion disks in active galactic nuclei. **The Astrophysical Journal**, v. 438, p. 610, 1 1995. ISSN 0004-637X. 19, 20, 79

EVENT HORIZON TELESCOPE COLLABORATION; AKIYAMA, K.; ALBERDI, A.; ALEF, W.; ALGABA, J. C.; ANANTUA, R.; ASADA, K.; AZULAY, R.; BACH, U.; BACZKO, A.-K.; BALL, D.; BALOKOVIĆ, M.; BARRETT, J.; BAUBÖCK, M.; BENSON, B. A.; BINTLEY, D.; BLACKBURN, L.; BLUNDELL, R.; BOUMAN, K. L.; BOWER, G. C.; BOYCE, H.; BREMER, M.; BRINKERINK, C. D.; BRISSENDEN, R.; BRITZEN, S.; BRODERICK, A. E.; BROGUIERE, D.; BRONZWAER, T.; BUSTAMANTE, S.; BYUN, D.-Y.; CARLSTROM, J. E.; CECCOBELLO, C.; CHAEL, A.; CHAN, C.-k.; CHATTERJEE, K.; CHATTERJEE, S.; CHEN, M.-T.; CHEN, Y.; CHENG, X.; CHO, I.; CHRISTIAN, P.; CONROY, N. S.; CONWAY, J. E.; CORDES, J. M.; CRAWFORD, T. M.; CREW, G. B.; CRUZ-OSORIO, A.; CUI, Y.; DAVELAAR, J.; LAURENTIS, M. D.; DEANE, R.; DEMPSEY, J.; DESVIGNES, G.; DEXTER, J.; DHRUV, V.; DOELEMAN, S. S.; DOUGAL, S.; DZIB, S. A.; EATOUGH, R. P.; EMAMI, R.; FALCKE, H.; FARAH, J.; FISH, V. L.; FOMALONT, E.; FORD, H. A.; FRAGA-ENCINAS, R.; FREEMAN, W. T.; FRIBERG, P.; FROMM, C. M.; FUENTES, A.; GALISON, P.; GAMMIE, C. F.; GARCÍA, R.; GENTAZ, O.; GEORGIEV, B.; GODDI, C.; GOLD, R.; GÓMEZ-RUIZ, A. I.; GÓMEZ, J. L.; GU, M.; GURWELL, M.; HADA, K.; HAGGARD, D.; HAWORTH, K.; HECHT, M. H.; HESPER, R.; HEUMANN, D.; HO, L. C.; HO, P.; HONMA, M.; HUANG, C.-W. L.; HUANG, L.; HUGHES, D. H.; IKEDA, S.; IMPELLIZZERI, C. M. V.; INOUE, M.; ISSAOUN, S.; JAMES, D. J.; JANNUZI, B. T.; JANSSEN, M.; JETER, B.; JIANG, W.; JIMÉNEZ-ROSALES, A.; JOHNSON, M. D.; JORSTAD, S.; JOSHI, A. V.; JUNG, T.; KARAMI, M.; KARUPPUSAMY, R.; KAWASHIMA, T.; KEATING, G. K.; KETTENIS, M.; KIM, D.-J.; KIM, J.-Y.; KIM, J.; KIM, J.; KINO, M.; KOAY, J. Y.; KOCHERLAKOTA, P.; KOFUJI, Y.; KOCH, P. M.; KOYAMA, S.; KRAMER, C.; KRAMER, M.; KRICHBAUM, T. P.; KUO, C.-Y.; BELLA, N. L.; LAUER, T. R.; LEE, D.; LEE, S.-S.; LEUNG, P. K.; LEVIS, A.; LI, Z.; LICO, R.; LINDAHL, G.; LINDQVIST, M.; LISAKOV, M.; LIU, J.; LIU, K.; LIUZZO, E.; LO, W.-P.; LOBANOV, A. P.; LOINARD, L.; LONSDALE, C. J.; LU, R.-S.; MAO, J.; MARCHILI, N.; MARKOFF, S.; MARRONE, D. P.; MARSCHER, A. P.; MARTÍ-VIDAL, I.; MATSUSHITA, S.; MATTHEWS, L. D.; MEDEIROS, L.; MENTEN, K. M.; MICHALIK, D.; MIZUNO, I.; MIZUNO, Y.; MORAN, J. M.; MORIYAMA, K.; MOSCIBRODZKA, M.; MÜLLER, C.; MUS, A.; MUSOKE, G.; MYSERLIS, I.; NADOLSKI, A.; NAGAI, H.; NAGAR, N. M.; NAKAMURA, M.; NARAYAN, R.; NARAYANAN, G.; NATARAJAN, I.; NATHANAIL, A.; FUENTES, S. N.; NEILSEN, J.; NERI, R.; NI, C.; NOUTSOS, A.; NOWAK, M. A.; OH, J.; OKINO, H.; OLIVARES, H.; ORTIZ-LEÓN, G. N.; OYAMA, T.; ÖZEL, F.; PALUMBO, D. C. M.; PARASCHOS, G. F.; PARK, J.; PARSONS, H.; PATEL, N.; PEN, U.-L.; PESCE, D. W.; PIÉTU, V.; PLAMBECK, R.; POPSTEFANIJA, A.; PORTH, O.; PÖTZL, F. M.; PRATHER, B.; PRECIADO-LÓPEZ, J. A.; PSALTIS, D.; PU, H.-Y.; RAMAKRISHNAN, V.; RAO, R.; RAWLINGS, M. G.; RAYMOND, A. W.; REZZOLLA, L.; RICARTE,

A.; RIPPERDA, B.; ROELOFS, F.; ROGERS, A.; ROS, E.; ROMERO-CAÑIZALES, C.; ROSHANINESHAT, A.; ROTTMANN, H.; ROY, A. L.; RUIZ, I.; RUSZCZYK, C.; RYGL, K. L. J.; SÁNCHEZ, S.; SÁNCHEZ-ARGÜELLES, D.; SÁNCHEZ-PORTAL, M.; SASADA, M.; SATAPATHY, K.; SAVOLAINEN, T.; SCHLOERB, F. P.; SCHONFELD, J.; SCHUSTER, K.-F.; SHAO, L.; SHEN, Z.; SMALL, D.; SOHN, B. W.; SOOHOO, J.; SOUCCAR, K.; SUN, H.; TAZAKI, F.; TETARENKO, A. J.; TIEDE, P.; TILANUS, R. P. J.; TITUS, M.; TORNE, P.; TRAIANOU, E.; TRENT, T.; TRIPPE, S.; TURK, M.; BEMMEL, I. van; LANGEVELDE, H. J. van; ROSSUM, D. R. van; VOS, J.; WAGNER, J.; WARD-THOMPSON, D.; WARDLE, J.; WEINTROUB, J.; WEX, N.; WHARTON, R.; WIELGUS, M.; WIIK, K.; WITZEL, G.; WONDRAK, M. F.; WONG, G. N.; WU, Q.; YAMAGUCHI, P.; YOON, D.; YOUNG, A.; YOUNG, K.; YOUNSI, Z.; YUAN, F.; YUAN, Y.-F.; ZENSUS, J. A.; ZHANG, S.; ZHAO, G.-Y.; ZHAO, S.-S.; AGURTO, C.; ALLARDI, A.; AMESTICA, R.; ARANEDA, J. P.; ARRIAGADA, O.; BERGHUIS, J. L.; BERTARINI, A.; BERTHOLD, R.; BLANCHARD, J.; BROWN, K.; CÁRDENAS, M.; CANTZLER, M.; CARO, P.; CASTILLO-DOMÍNGUEZ, E.; CHAN, T. L.; CHANG, C.-C.; CHANG, D. O.; CHANG, S.-H.; CHANG, S.-C.; CHEN, C.-C.; CHILSON, R.; CHUTER, T. C.; CIECHANOWICZ, M.; COLIN-BELTRAN, E.; COULSON, I. M.; CROWLEY, J.; DEGENAAR, N.; DORNBUSCH, S.; DURÁN, C. A.; EVERETT, W. B.; FABER, A.; FORSTER, K.; FUCHS, M. M.; GALE, D. M.; GEERTSEMA, G.; GONZÁLEZ, E.; GRAHAM, D.; GUETH, F.; HALVERSON, N. W.; HAN, C.-C.; HAN, K.-C.; HASEGAWA, Y.; HERNÁNDEZ-REBOLLAR, J. L.; HERRERA, C.; HERRERO-ILLANA, R.; HEYMINCK, S.; HIROTA, A.; HOGE, J.; SCHIMPF, S. R. H.; HOWIE, R. E.; HUANG, Y.-D.; JIANG, H.; JINCHI, H.; JOHN, D.; KIMURA, K.; KLEIN, T.; KUBO, D.; KURODA, J.; KWON, C.; LACASSE, R.; LAING, R.; LEITCH, E. M.; LI, C.-T.; LIU, C.-T.; LIU, K.-Y.; LIN, L. C.-C.; LU, L.-M.; MAC-AULIFFE, F.; MARTIN-COCHER, P.; MATULONIS, C.; MAUTE, J. K.; MESSIAS, H.; MEYER-ZHAO, Z.; MONTAÑA, A.; MONTENEGRO-MONTES, F.; MONTGOMERIE, W.; NOLASCO, M. E. M.; MUDERS, D.; NISHIOKA, H.; NORTON, T. J.; NYSTROM, G.; OGAWA, H.; OLIVARES, R.; OSHIRO, P.; PÉREZ-BEAUPUITS, J. P.; PARRA, R.; PHILLIPS, N. M.; POIRIER, M.; PRADEL, N.; QIU, R.; RAFFIN, P. A.; RAHLIN, A. S.; RAMÍREZ, J.; RESSLER, S.; REYNOLDS, M.; RODRÍGUEZ-MONTOYA, I.; SAEZ-MADAIN, A. F.; SANTANA, J.; SHAW, P.; SHIRKEY, L. E.; SILVA, K. M.; SNOW, W.; SOUSA, D.; SRIDHARAN, T. K.; STAHM, W.; STARK, A. A.; TEST, J.; TORSTENSSON, K.; VENEGAS, P.; WALTHER, C.; WEI, T.-S.; WHITE, C.; WIECHING, G.; WIJNANDS, R.; WOUTERLOOT, J. G. A.; YU, C.-Y.; (), W. Y.; ZEBALLOS, M. First Sagittarius A* event horizon telescope results. I. the shadow of the supermassive black hole in the center of the Milky Way. **The Astrophysical Journal Letters**, v. 930, n. 2, p. L12, 5 2022. ISSN 2041-8205. 2

FABIAN, A.; VAUGHAN, S.; NANDRA, K.; IWASAWA, K.; BALLANTYNE, D.; LEE, J.; ROSA, A. D.; TURNER, A.; YOUNG, A. A long hard look at

mcg–6-30-15 with xmm-newton. **Monthly Notices of the Royal Astronomical Society**, v. 335, n. 1, p. L1–L5, 2002. 24

FABIAN, A. C.; GUILBERT, P. W.; ARNAUD, K. A.; SHAFER, R. A.; TENNANT, A. F.; WARD, M. J. Some implications of excess soft X-ray emission from Seyfert 1 galaxies. **Monthly Notices of the Royal Astronomical Society**, v. 218, n. 3, p. 457–464, 2 1986. ISSN 0035-8711. Available from: <<https://academic.oup.com/mnras/article/218/3/457/1053341>>. 3

FABIAN, A. C.; MINIUTTI, G.; GALLO, L.; BOLLER, T.; TANAKA, Y.; VAUGHAN, S.; ROSS, R. R. X-ray reflection in the narrow-line Seyfert 1 galaxy 1H 0707-495. **Monthly Notices of the Royal Astronomical Society**, v. 353, n. 4, p. 1071–1077, 10 2004. ISSN 00358711. Available from: <<https://academic.oup.com/mnras/article/353/4/1071/976837>>. 3, 23

FABIAN, A. C.; ROSS, R. R. X-ray Reflection. **Space Science Reviews**, v. 157, n. 1, p. 167–176, 11 2010. ISSN 1572-9672. Available from: <<https://link.springer.com/article/10.1007/s11214-010-9699-y>>. 3

FABIAN, A. C.; ZOGHBI, A.; ROSS, R. R.; UTTLEY, P.; GALLO, L. C.; BRANDT, W. N.; BLUSTIN, A. J.; BOLLER, T.; CABALLERO-GARCIA, M. D.; LARSSON, J.; MILLER, J. M.; MINIUTTI, G.; PONTI, G.; REIS, R. C.; REYNOLDS, C. S.; TANAKA, Y.; YOUNG, A. J. Broad line emission from iron K- and L-shell transitions in the active galaxy 1H0707-495. **Nature**, v. 459, n. 7246, p. 540–542, may 2009. 32, 89

FERLAND, G. J.; CHATZIKOS, M.; GUZMÁN, F.; LYKINS, M. L.; HOOF, P. A. M. van; WILLIAMS, R. J. R.; ABEL, N. P.; BADNELL, N. R.; KEENAN, F. P.; PORTER, R. L.; STANCIL, P. C. The 2017 release Cloudy. **Revista Mexicana de Astronomía y Astrofísica**, v. 53, p. 385–438, oct. 2017. 12, 42, 46

FERLAND, G. J.; DONE, C.; JIN, C.; LANDT, H.; WARD, M. J. State-of-the-art AGN SEDs for photoionization models: BLR predictions confront the observations. **Monthly Notices of the Royal Astronomical Society**, v. 494, n. 4, p. 5917–5922, 6 2020. ISSN 0035-8711. 32, 42, 53

FERLAND, G. J.; KORISTA, K. T.; VERNER, D. A.; FERGUSON, J. W.; KINGDON, J. B.; VERNER, E. M. CLOUDY 90: numerical simulation of plasmas and their spectra. **Publications of the Astronomical Society of the Pacific**, v. 110, n. 749, p. 761–778, 7 1998. ISSN 0004-6280. 12

FISCHER, T. C.; MACHUCA, C.; DINIZ, M. R.; CRENSHAW, D. M.; KRAEMER, S. B.; RIFFEL, R. A.; SCHMITT, H. R.; BARON, F.; STORCHI-BERGMANN, T.; STRAUGHN, A. N.; REVALSKI, M.; POPE, C. L. Gemini near infrared field spectrograph observations of the Seyfert 2 galaxy Mrk 573: in situ acceleration of ionized and molecular gas off fueling flows. **The Astrophysical Journal**, v. 834, n. 1, p. 30, jan. 2017. 102

GALLAGHER, S. C.; EVERETT, J. E. Stratified quasar winds: integrating x-ray and infrared views of broad absorption line quasars. 2007. Available from: <<https://arxiv.org/abs/astro-ph/0701076>>. 18

GALLO, L. C. Investigating the nature of narrow-line Seyfert 1 galaxies with high-energy spectral complexity. **Monthly Notices of the Royal Astronomical Society**, v. 368, n. 1, p. 479–486, 2006. ISSN 13652966. 23

_____. _____. **Monthly Notices of the Royal Astronomical Society**, v. 368, n. 1, p. 479–486, may 2006. 28

GARCIA-RISSMANN, A.; RODRÍGUEZ-ARDILA, A.; SIGUT, T. A. A.; PRADHAN, A. K. A near-infrared template derived from I Zw 1 for the Fe II emission in active galaxies. **The Astrophysical Journal**, v. 751, n. 1, p. 7, may 2012. 27, 31, 36, 40, 41, 45, 46, 54, 68

GLIKMAN, E.; HELFAND, D. J.; WHITE, R. L. A near-infrared spectral template for quasars. **The Astrophysical Journal**, v. 640, n. 2, p. 579–591, apr. 2006. 91

GOAD, M.; WANDERS, I. The effect of a variable anisotropic continuum source upon the broad emission line profiles and responses. **Astrophysical Journal v. 469, p. 113**, v. 469, p. 113, 1996. 19

GONZALEZ, A. G.; WADDELL, S. G. H.; GALLO, L. C. The changing source of X-ray reflection in the radio-intermediate Seyfert 1 galaxy III Zw 2. 12 2017. Available from: <<http://arxiv.org/abs/1712.01116>>. 29

GONZÁLEZ-MARTÍN, O.; RODRÍGUEZ-ESPINOSA, J. M.; DÍAZ-SANTOS, T.; PACKHAM, C.; ALONSO-HERRERO, A.; ESQUEJ, P.; ALMEIDA, C. R.; MASON, R.; TELESCO, C. Dust in active galactic nuclei mid-infrared T-ReCS/Gemini spectra using the new RedCan pipeline. **Astronomy and Astrophysics**, v. 553, 3 2009. ISSN 14320746. 34

GOODMAN, J.; TAN, J. C. Supermassive stars in quasar disks. **The Astrophysical Journal**, v. 608, n. 1, p. 108, 2004. 18

GOODRICH, R. W. Spectropolarimetry of 'narrow-line' Seyfert 1 galaxies. **The Astrophysical Journal**, v. 342, p. 224, 7 1989. ISSN 0004-637X. 21

GREVESSE, N.; ASPLUND, M.; SAUVAL, A.; SCOTT, P. The chemical composition of the sun. **Canadian Journal of Physics**, v. 89, n. 4, p. 327–331, 2011. 47

GRIER, C. J.; PANCOAST, A.; BARTH, A. J.; FAUSNAUGH, M. M.; BREWER, B. J.; TREU, T.; PETERSON, B. M. The structure of the broad-line region in active galactic nuclei. II. Dynamical modeling of data from the AGN10 reverberation mapping campaign. **The Astrophysical Journal**, v. 849, n. 2, p. 146, 11 2017. ISSN 15384357. 9, 49, 84, 85

GRIER, C. J.; PETERSON, B. M.; HORNE, K.; BENTZ, M. C.; POGGE, R. W.; DENNEY, K. D.; ROSA, G. D.; MARTINI, P.; KOCHANEK, C. S.; ZU, Y.; SHAPPEE, B.; SIVERD, R.; BEATTY, T. G.; SERGEEV, S. G.; KASPI, S.; SALVO, C. A.; BIRD, J. C.; BORD, D. J.; BORMAN, G. A.; CHE, X.; CHEN, C.; COHEN, S. A.; DIETRICH, M.; DOROSHENKO, V. T.; EFIMOV, Y. S.; FREE, N.; GINSBURG, I.; HENDERSON, C. B.; KING, A. L.; MOGREN, K.; MOLINA, M.; MOSQUERA, A. M.; NAZAROV, S. V.; OKHMAT, D. N.; PEJCHA, O.; RAFTER, S.; SHIELDS, J. C.; SKOWRON, J.; SZCZYGIEL, D. M.; VALLURI, M.; SADERS, J. L. V. The structure of the broad-line region in active galactic nuclei. I. Reconstructed velocity-delay maps. **Astrophysical Journal**, v. 764, n. 1, p. 47, 2 2013. ISSN 15384357. 9, 49, 84, 85, 109

GRIER, C. J.; PETERSON, B. M.; POGGE, R. W.; DENNEY, K. D.; BENTZ, M. C.; MARTINI, P.; SERGEEV, S. G.; KASPI, S.; MINEZAKI, T.; ZU, Y.; KOCHANEK, C. S.; SIVERD, R.; SHAPPEE, B.; STANEK, K. Z.; SALVO, C. A.; BEATTY, T. G.; BIRD, J. C.; BORD, D. J.; BORMAN, G. A.; CHE, X.; CHEN, C.; COHEN, S. A.; DIETRICH, M.; DOROSHENKO, V. T.; DRAKE, T.; EFIMOV, Y. S.; FREE, N.; GINSBURG, I.; HENDERSON, C. B.; KING, A. L.; KOSHIDA, S.; MOGREN, K.; MOLINA, M.; MOSQUERA, A. M.; NAZAROV, S. V.; OKHMAT, D. N.; PEJCHA, O.; RAFTER, S.; SHIELDS, J. C.; SKOWRON, J.; SZCZYGIEL, D. M.; VALLURI, M.; SADERS, J. L. V. Reverberation mapping results for five Seyfert 1 galaxies. **Astrophysical Journal**, v. 755, n. 1, p. 60, 8 2012. ISSN 15384357. 30, 49, 82, 84, 85, 86, 110

HAARDT, F.; MARASCHI, L. A two-phase model for the x-ray emission from seyfert galaxies. **Astrophysical Journal, Letters**, v. 380, p. L51–L54, 1991. 3

HAGINO, K.; ODAKA, H.; DONE, C.; TOMARU, R.; WATANABE, S.; TAKAHASHI, T. A disc wind interpretation of the strong Fe Kα features in 1H 0707-495. **Monthly Notices of the Royal Astronomical Society**, v. 461, n. 4, p. 3954–3963, oct. 2016. 32, 104

HAMANN, F.; BARLOW, T.; COHEN, R.; JUNKKARINEN, V.; BURBIDGE, E. Ionization and abundances in intrinsic qso absorption-line systems. **arXiv preprint astro-ph/9704235**, 1997. 18

HICKOX, R. C.; ALEXANDER, D. M. Obscured active galactic nuclei. **Annual Review of Astronomy and Astrophysics**, v. 56, n. 1, p. 625–671, 9 2018. ISSN 0066-4146. 4, 5, 6

HU, C.; DU, P.; LU, K. X.; LI, Y. R.; WANG, F.; QIU, J.; BAI, J. M.; KASPI, S.; HO, L. C.; NETZER, H.; WANG, J. M. Supermassive black holes with bigh accretion rates in active galactic nuclei. III. Detection of Fe II reverberation in nine narrow-line Seyfert 1 galaxies. **Astrophysical Journal**, v. 804, n. 2, 5 2015. ISSN 15384357. 21, 23

HUANG, Y.-K.; HU, C.; ZHAO, Y.-L.; ZHANG, Z.-X.; LU, K.-X.; WANG, K.; ZHANG, Y.; DU, P.; LI, Y.-R.; BAI, J.-M.; HO, L. C.; BIAN, W.-H.; YUAN, Y.-F.; WANG, J.-M. Reverberation mapping of the narrow-line Seyfert 1 galaxy I

Zwicky 1: black hole mass. **The Astrophysical Journal**, v. 876, n. 2, p. 102, may 2019. 30, 32, 47

HUBBLE, E. The distribution of extra-galactic nebulae. **The Astrophysical Journal**, v. 79, p. 8, 1 1934. ISSN 0004-637X. 1

HUNG, T.; FOLEY, R. J.; RAMIREZ-RUIZ, E.; DAI, J. L.; AUCHETTL, K.; KILPATRICK, C. D.; MOCKLER, B.; BROWN, J. S.; COULTER, D. A.; DIMITRIADIS, G.; HOLOIEN, T. W.-S.; LAW-SMITH, J. A. P.; PIRO, A. L.; REST, A.; ROJAS-BRAVO, C.; SIEBERT, M. R. Double-peaked Balmer emission indicating prompt accretion disk formation in an X-Ray faint tidal disruption event. **The Astrophysical Journal**, v. 903, n. 1, p. 31, 10 2020. ISSN 0004-637X. Available from: <<https://iopscience.iop.org/article/10.3847/1538-4357/abb606https://iopscience.iop.org/article/10.3847/1538-4357/abb606/meta>>. 51

HUNTER, J. D. Matplotlib: A 2D graphics environment. **Computing in Science and Engineering**, v. 9, n. 3, p. 90–95, may 2007. 92

HURÉ, J.-M.; COLLIN-SOUFFRIN, S.; BOURLOT, J. L.; FORETS, G. Structure of the outer regions of accretion discs in active galactic nuclei. **Astronomy and Astrophysics**, v. 290, p. 19–33, 1994. 18

JACKSON, N.; PENSTON, M.; PÉREZ, E. Quasar hβ profiles and discs. **Monthly Notices of the Royal Astronomical Society**, v. 249, n. 4, p. 577–583, 1991. 19, 20

JIANG, J.; WALTON, D. J.; PARKER, M. L.; FABIAN, A. C. The ultrafast outflow of wkk 4438: suzaku and nustar x-ray spectral analysis. **Monthly Notices of the Royal Astronomical Society**, v. 481, n. 1, p. 639–644, 2018. 24

JIANG, L.; SHEN, Y.; MCGREER, I. D.; FAN, X.; MORGANSON, E.; WINDHORST, R. A. Reverberation mapping with intermediate-band photometry: detection of broad-line Hα time lags for quasars at $0.2 < z < 0.4$. **The Astrophysical Journal**, v. 818, n. 2, p. 137, 2 2016. ISSN 0004-637X. Available from: <<https://iopscience.iop.org/article/10.3847/0004-637X/818/2/137https://iopscience.iop.org/article/10.3847/0004-637X/818/2/137/meta>>. 6

JIN, C.; DONE, C.; WARD, M.; GARDNER, E. Super-Eddington QSO RX J0439.6-5311-II. Multiwavelength constraints on the global structure of the accretion flow. **Monthly Notices of the Royal Astronomical Society**, v. 471, n. 1, p. 706–721, 10 2017. ISSN 13652966. 23, 27

JOLY, M. The fe ii spectrum of seyfert 1 galaxies and quasars. **Astronomy and Astrophysics**, v. 102, p. 321–330, 1981. 16

_____. Formation of low ionization lines in active galactic nuclei. **Astronomy & Astrophysics**, v. 184, p. 33–42, 1987. ISSN 0004-6361. Available from: <<https://ui.adsabs.harvard.edu/abs/1987A&A...184...33J/abstract>>. 13, 17, 74

_____. Formation of CA II lines in active galactic nuclei. **Astronomy and Astrophysics**, v. 208, p. 47–51, jan. 1989. 16

_____. Relationship between Fe II and radio emission in active galactic nuclei. **Astronomy and Astrophysics**, Vol. 242, p. 49, 1991. 12, 13, 14, 17, 30, 74

_____. An unsolved problem in the spectrum of quasars: the FeII emission lines. **Annales de Physique**, p. 241–267, 1993. 13, 14

KASPI, S.; MAOZ, D.; NETZER, H.; PETERSON, B. M.; VESTERGAARD, M.; JANNUZI, B. T. The relationship between luminosity and broad-line region size in active galactic nuclei. 4 2005. Available from: <<http://arxiv.org/abs/astro-ph/0504484http://dx.doi.org/10.1086/431275>>. 9

KASPI, S.; SMITH, P. S.; NETZER, H.; MAOZ, D.; JANNUZI, B. T.; GIVEON, U. Reverberation measurements for 17 quasars and the size-mass-luminosity relations in active galactic nuclei. **The Astrophysical Journal**, v. 533, n. 2, p. 631–649, apr. 2000. 6, 7, 46, 47

KOLLATSCHNY, W.; ZETZL, M. The shape of broad-line profiles in active galactic nuclei. **Astronomy & Astrophysics**, v. 549, p. A100, 2013. 47

KOMOSSA, S. Narrow-line Seyfert 1 galaxies. **Revista Mexicana de Astronomia y Astrofisica: Serie de Conferencias**, v. 32, p. 86–92, 10 2007. 21, 24

KORATKAR, A.; BLAES, O. The ultraviolet and optical continuum emission in active galactic nuclei: the status of accretion disks. **Publications of the Astronomical Society**, v. 111, p. 755, 1999. 3

KORATKAR, A. P.; GASKELL, C. M. Radius-luminosity and mass-luminosity relationships for active galactic nuclei. **Astrophysical Journal**, v. 370, p. 61–64, 1991. 9

KOSEC, P.; BUISSON, D.; PARKER, M.; PINTO, C.; FABIAN, A.; WALTON, D. A stratified ultrafast outflow in 1h0707- 495? **Monthly Notices of the Royal Astronomical Society**, v. 481, n. 1, p. 947–953, 2018. 24

KOSEC, P.; BUISSON, D. J. K.; PARKER, M. L.; PINTO, C.; FABIAN, A. C.; WALTON, D. J. A stratified ultrafast outflow in 1H0707-495? **Monthly Notices of the Royal Astronomical Society**, v. 481, n. 1, p. 947–953, nov. 2018. 32, 104, 105, 106

KOVACEVIĆ-DOJCINOVIĆ, J.; POPOVIĆ, L. The connections between the UV and optical Fe II emission lines in type 1 AGNs. **Astrophysical Journal, Supplement Series**, 2015. ISSN 00670049. 31

KOVAČEVIĆ, J.; POPOVIĆ, L. v.; DIMITRIJEVIĆ, M. S. Analysis of optical Fe II emission in a sample of active galactic nucleus spectra. **The Astrophysical Journal Supplement Series**, v. 189, n. 1, p. 15, 2010. ISSN 0067-0049. 31, 39, 59

KRAMIDA, A.; RALCHENKO, Y.; READER, J. N. A. T. **NIST Atomic Spectra Database**. 2024. Acess on 7 Apr. 2025. Available from: <<https://physics.nist.gov/asd>>. 70

KRISS, G. A.; LEE, J. C.; DANEHKAR, A.; NOWAK, M. A.; FANG, T.; HARDCASTLE, M. J.; NEILSEN, J.; YOUNG, A. Discovery of an ultraviolet counterpart to an ultrafast x-ray outflow in the quasar pg 1211+ 143. **The Astrophysical Journal**, v. 853, n. 2, p. 166, 2018. 24

KUEHN, C. A.; BALDWIN, J. A.; PETERSON, B. M.; KORISTA, K. T. On the size of the Fe ii –emitting region in the AGN Arakelian 120. **The Astrophysical Journal**, v. 673, n. 1, p. 69–77, 1 2008. ISSN 0004-637X. 7

LAKIĆEVIĆ, M.; POPOVIĆ, L.; KOVAČEVIĆ-DOJČINOVIĆ, J. Kinematic differences between nls1 and blagn sources. **arXiv preprint arXiv:1808.02314**, 2018. 21

LANDT, H.; ELVIS, M.; WARD, M. J.; BENTZ, M. C.; KORISTA, K. T.; KAROVSKA, M. The near-infrared broad emission line region of active galactic nuclei - II. The 1-μm continuum. **Monthly Notices of the Royal Astronomical Society**, v. 414, n. 1, p. 218–240, 6 2011. ISSN 00358711. Available from: <<https://academic.oup.com/mnras/article-lookup/doi/10.1111/j.1365-2966.2011.18383.x>>. 81, 91

LAOR, A. On quasar masses and quasar host galaxies. **The Astrophysical Journal**, v. 505, n. 2, p. L83, 1998. 9

LAOR, A.; FIORE, F.; ELVIS, M.; WILKES, B. J.; MCDOWELL, J. C. The soft x-ray properties of a complete sample of optically selected quasars. II. Final results. **The Astrophysical Journal**, v. 477, n. 1, p. 93–113, 3 1997. ISSN 0004-637X. Available from: <<https://iopscience.iop.org/article/10.1086/303696https://iopscience.iop.org/article/10.1086/303696/meta>>. 30

LAWRENCE, A.; SAUNDERS, W. Extreme Fe II emission from an IRAS quasar. **Monthly Notices of the Royal Astronomical Society**, v. 235, p. 261–268, 1988. 13

LEAVITT, H. S.; PICKERING, E. C. 25 new variable stars, principally in Harvard maps 39 and 45. **Harvard College Observatory Circular**, v. 179, p. 1–4, 1913. Available from: <<https://ui.adsabs.harvard.edu/abs/1913HarCi.179....1L/abstract>>. 1

LEIGHLY, K. M. A comprehensive spectral and variability study of narrow-line Seyfert 1 galaxies observed by ASCA. I. Observations and time series analysis. **The Astrophysical Journal Supplement**, v. 125, n. 2, p. 297–316, dec. 1999. 32

LEIGHLY, K. M.; MOORE, J. R. Hubble space telescope STIS ultraviolet spectral evidence of outflow in extreme narrow-line Seyfert 1 galaxies. I. Data and analysis. **The Astrophysical Journal**, v. 611, n. 1, p. 107–124, aug. 2004. 32, 36, 91, 93, 94, 95, 99, 105, 106

LEIGHLY, K. M.; MUSHOTZKY, R. F.; NANDRA, K.; FORSTER, K. Evidence for relativistic outflows in narrow-line Seyfert 1 galaxies. **The Astrophysical Journal Letters**, v. 489, n. 1, p. L25–L28, nov. 1997. 36

LEWIS, K. T.; ERACLEOUS, M.; STORCHI-BERGMANN, T. Long-term profile variability in active galactic nucleus with double-peaked balmer emission lines. **The Astrophysical Journal Supplement Series**, v. 187, n. 2, p. 416, 2010. 19, 20

LIAO, N.-H.; XIN, Y.-L.; FAN, X.-L.; WENG, S.-S.; LI, S.-K.; CHEN, L.; FAN, Y.-Z. Discovery of γ-ray emission from the radio-intermediate quasar III Zw 2: violent jet activity with intraday γ-ray variability. **The Astrophysical Journal Supplement Series**, v. 226, n. 2, p. 17, 5 2016. Available from: <<http://arxiv.org/abs/1605.00276http://dx.doi.org/10.3847/0067-0049/226/2/17>>. 29

Liddle, A. R. Information criteria for astrophysical model selection. **Monthly Notices of the Royal Astronomical Society**, v. 377, n. 1, p. L74–L78, may 2007. 94

LIRA, P.; KASPI, S.; NETZER, H.; BOTTI, I.; MORRELL, N.; MEJÍA-RESTREPO, J.; SÁNCHEZ-SÁEZ, P.; MARTÍNEZ-PALOMERA, J.; LÓPEZ, P. Reverberation mapping of luminous quasars at high z. **The Astrophysical Journal**, 2018. Available from: <<https://iopscience.iop.org/article/10.3847/1538-4357/aada45/meta>>. 6

LONGINOTTI, A.; VEGA, O.; KRONGOLD, Y.; ARETXAGA, I.; YUN, M.; CHAVUSHYAN, V.; FERUGLIO, C.; GÓMEZ-RUIZ, A.; MONTAÑA, A.; LEÓN-TAVARES, J. Early science with the large millimeter telescope: an energy-driven wind revealed by massive molecular and fast x-ray outflows in the seyfert galaxy iras 17020+ 4544. **The Astrophysical Journal Letters**, v. 867, n. 1, p. L11, 2018. 24, 25

LOSKA, Z.; CZERNY, B.; SZCZERBA, R. Irradiation of accretion discs in active galactic nuclei due to the presence of a warm absorber. **Monthly Notices of the Royal Astronomical Society**, v. 355, n. 4, p. 1080–1090, 2004. 18

LYNDEN-BELL, D. Galactic nuclei as collapsed old quasars. **Nature**, v. 223, n. 5207, p. 690–694, 1969. ISSN 00280836. 2

MALKAN, M. A.; SARGENT, W. L. The ultraviolet excess of seyfert 1 galaxies and quasars. **Astrophysical Journal, Part 1, vol. 254, Mar. 1, 1982, p. 22-37.**, v. 254, p. 22–37, 1982. 18

MAO, W.; HU, C.; WANG, J.; BIAN, W.; ZHANG, S.; ZHAO, G. Narrow line Seyfert 1 galaxies: Where are the broad line regions? **Science China: Physics, Mechanics and Astronomy**, v. 53, n. 12, p. 2307–2311, 12 2010. ISSN 16747348. 15

MARINELLO, M.; RODRÍGUEZ-ARDILA, A.; GARCIA-RISSMANN, A.; SIGUT, T. A. A.; PRADHAN, A. K. The fe ii emission in active galactic nuclei: excitation mechanisms and location of the emitting region. **The Astrophysical Journal**, v. 820, n. 2, p. 116, apr. 2016. 27, 89, 98, 99, 105

_____. The Fe II emission in active galactic nuclei: excitation mechanisms and location of the emitting region. **The Astrophysical Journal**, v. 820, n. 2, p. 116, apr. 2016. 15, 17, 21, 23, 31, 41, 54, 55, 59, 61, 62, 64, 67, 68, 69, 70, 72, 74, 77, 83, 84

MARINELLO, M.; RODRÍGUEZ-ARDILA, A.; MARZIANI, P.; SIGUT, A.; PRADHAN, A. Panchromatic properties of the extreme Fe II emitter PHL 1092. **Monthly Notices of the Royal Astronomical Society**, v. 494, n. 3, p. 4187–4202, may 2020. 14, 17, 23, 27, 31, 54, 62, 64, 67, 84

_____. _____. **Monthly Notices of the Royal Astronomical Society**, v. 494, n. 3, p. 4187–4202, may 2020. 27

_____. _____. **Monthly Notices of the Royal Astronomical Society**, v. 494, n. 3, p. 4187–4202, may 2020. 89, 97, 99

MARTÍNEZ-ALDAMA, M. L.; DULTZIN, D.; MARZIANI, P.; SULENTIC, J. W.; BRESSAN, A.; CHEN, Y.; STIRPE, G. M. O I and Ca II observations in intermediate redshift quasars. **The Astrophysical Journal Supplement**, v. 217, n. 1, p. 3, mar. 2015. 16, 17, 74, 83, 84

MARTÍNEZ-ALDAMA, M. L.; PANDA, S.; CZERNY, B.; MARINELLO, M.; MARZIANI, P.; DULTZIN, D. The CaFe project: optical Fe II and near-infrared Ca II triplet emission in active galaxies. II. The driver(s) of the Ca II and Fe II and its potential use as a chemical clock. **The Astrophysical Journal**, v. 918, n. 1, p. 29, sep. 2021. 16

_____. _____. **The Astrophysical Journal**, v. 918, n. 1, p. 29, sep. 2021. 17, 74

MARZIANI, P.; BERTON, M.; PANDA, S.; BON, E. Optical singly-ionized iron emission in radio-quiet and relativistically jetted active galactic nuclei. **Universe**, v. 7, n. 12, p. 484, 12 2021. ISSN 2218-1997. Available from: <<https://www.mdpi.com/2218-1997/7/12/484/htmhttps://www.mdpi.com/2218-1997/7/12/484>>. 14, 59

MARZIANI, P.; DULTZIN, D.; SULENTIC, J. W.; OLMO, A. D.; NEGRETE, C. A.; MARTÍNEZ-ALDAMA, M. L.; D'ONOFRIO, M.; BON, E.; BON, N.; STIRPE, G. M. A main sequence for quasars. **Frontiers in Astronomy and Space Sciences**, v. 5, p. 6, mar. 2018. 21, 22, 27

MARZIANI, P.; OLMO, A. d.; NEGRETE, C. A.; DULTZIN, D.; PICONCELLI, E.; VIETRI, G.; MARTÍNEZ-ALDAMA, M. L.; D'ONOFRIO, M.; BON, E.; BON, N.; MACHADO, A. D.; STIRPE, G. M.; RIOS, T. M. B. The intermediate-ionization lines as virial broadening estimators for population A

quasars. **The Astrophysical Journal Supplement**, v. 261, n. 2, p. 30, aug. 2022. 30

MARZIANI, P.; SULENTIC, J. Highly accreting quasars: sample definition and possible cosmological implications. **Monthly Notices of the Royal Astronomical Society**, v. 442, p. 1211–1229, 2014. 27, 28

MARZIANI, P.; SULENTIC, J.; CALVANI, M.; PEREZ, E.; MOLES, M.; PENSTON, M. The peculiar balmer line profiles of oq 208. **arXiv preprint astro-ph/9301001**, 1993. 19

MARZIANI, P.; SULENTIC, J. W.; ZAMANOV, R.; CALVANI, M.; DULTZIN-HACYAN, D.; BACHEV, R.; ZWITTER, T. An optical spectroscopic atlas of low-eedshift active galactic nuclei. **The Astrophysical Journal Supplement Series**, v. 145, n. 2, p. 199–211, 4 2003. ISSN 0067-0049. Available from: <<https://iopscience.iop.org/article/10.1086/346025https://iopscience.iop.org/article/10.1086/346025/meta>>. 21, 27, 81

MASON, R. E.; RODRÍGUEZ-ARDILA, A.; MARTINS, L.; RIFFEL, R.; MARTÍN, O. G.; ALMEIDA, C. R.; DUTRA, D. R.; HO, L. C.; THANJAVUR, K.; FLOHIC, H.; ALONSO-HERRERO, A.; LIRA, P.; MCDERMID, R.; RIFFEL, R. A.; SCHIAVON, R. P.; WINGE, C.; HOENIG, M. D.; PERLMAN, E. The nuclear near-infrared spectral properties of nearby galaxies. **The Astrophysical Journal Supplement**, v. 217, n. 1, p. 13, 3 2015. ISSN 0067-0049. Available from: <<https://iopscience.iop.org/article/10.1088/0067-0049/217/1/13https://iopscience.iop.org/article/10.1088/0067-0049/217/1/13/meta>>. 34

MATHUR, S. New insights into the narrow-line Seyfert 1 phenomenon. **New Astronomy Reviews**, v. 44, n. 7-9, p. 469–475, 9 2000. ISSN 13876473. 21

MATHUR, S.; KURASZKIEWICZ, J.; CZERNY, B. Evolution of active galaxies: black-hole mass-bulge relations for narrow line objects. **New Astronomy**, v. 6, n. 5, p. 321–329, 8 2001. ISSN 13841076. 21

MATSUOKA, Y.; KAWARA, K.; OYABU, S. Low-ionization emission regions in quasars: gas properties probed with broad O i and Ca ii lines. **The Astrophysical Journal**, v. 673, n. 1, p. 62–68, 1 2008. ISSN 0004-637X. 83

MATTEO, T. D.; KING, A.; CORNISH, N. J.; KING, A. Supermassive black hole accretion and feedback. **Black Hole Formation and Growth: Saas-Fee Advanced Course 48. Swiss Society for Astrophysics and Astronomy**, p. 95–157, 2019. 24

MATTEO, T. D.; SPRINGEL, V.; HERNQUIST, L. Energy input from quasars regulates the growth and activity of black holes and their host galaxies. **Nature**, v. 433, n. 7026, p. 604–607, 2005. 24

MEHDIPOUR, M.; KRISS, G. A.; KRONGOLD, Y.; LONGINOTTI, A. L.; COSTANTINI, E.; GUPTA, A.; MATHUR, S.; NICASTRO, F.; PANESSA, F.;

SOM, D. Uv counterpart of an x-ray ultrafast outflow in iras 17020+ 4544. **The Astrophysical Journal**, v. 930, n. 2, p. 166, 2022. 24

MIZUMOTO, M.; EBISAWA, K.; SAMESHIMA, H. Interpretation of the X-ray spectral variation of 1H 0707-495 with a variable double partial covering model. **Publications of the Astronomical Society of Japan**, v. 66, n. 6, p. 122, dec. 2014. 32

MURRAY, N.; CHIANG, J. Photoionized disk winds. v. 128, p. 246, 1997. 18, 19, 20

NADDAF, M.-H.; CZERNY, B.; SZCZERBA, R. The picture of BLR in 2.5D FRADO: dynamics and geometry. **The Astrophysical Journal**, v. 920, n. 1, p. 30, 10 2021. ISSN 0004-637X. Available from: <<https://iopscience.iop.org/article/10.3847/1538-4357/ac139d>>. 10

NAKAMURA, K.; OSAKI, Y. Self-consistent accretion disk-coronal model for active galactic nuclei. **Astronomical Society of Japan**, v. 45, p. 775–787, 1993. 3

NARDINI, E.; REEVES, J. N.; GOFFORD, J.; HARRISON, F. A.; RISALITI, G.; BRAITO, V.; COSTA, M. T.; MATZEU, G. A.; WALTON, D. J.; BEHAR, E.; BOGGS, S. E.; CHRISTENSEN, F. E.; CRAIG, W. W.; HAILEY, C. J.; MATT, G.; MILLER, J. M.; O'BRIEN, P. T.; STERN, D.; TURNER, T. J.; WARD, M. J. Black hole feedback in the luminous quasar PDS 456. **Science**, v. 347, n. 6224, p. 860–863, feb. 2015. 104

NEGRETE, C.; DULTZIN, D.; MARZIANI, P.; ESPARZA, D. Highly accreting quasars: the SDSS low-redshift catalog. **Astronomy & Astrophysics**, v. 620, p. A118, 2018. 21

NENKOVA, M.; SIROCKY, M. M.; NIKUTTA, R.; IVEZIĆ, ; ELITZUR, M. AGN dusty tori. II. Observational implications of clumpiness. **The Astrophysical Journal**, v. 685, n. 1, p. 160–180, 9 2008. ISSN 0004-637X. 10

NETZER, H. On the profiles of the broad lines in the spectra of qsos and seyfert galaxies. **Monthly Notices of the Royal Astronomical Society**, v. 181, n. 1, p. 89P–92P, 1977. 6

_____. **The physics and evolution of active galactic nuclei**. [S.l.: s.n.], 2011. 1–361 p. ISBN 9781139109291. 3

_____. Revisiting the unified model of active galactic nuclei. **Annual Review of Astronomy and Astrophysics**, v. 53, n. 1, p. 365–408, 5 2015. 3

NETZER, H.; WILLS, B. J. Broad emission features in qsos and active galactic nuclei. i. New calculations of fe n line strengths. **The Astrophysical Journal**, v. 275, p. 445–460, 1983. 13

NEWVILLE, M.; INGARGIOLA, A.; STENSITZKI, T.; ALLEN, D. B. LMFIT: Non-linear least-square minimization and curve-fitting for Python. **Zenodo**, p. –, 2014. 38, 51

OIO, G. A.; VEGA, L. R.; SCHMIDT, E. O.; FERREIRO, D. Characterisation of the continuum and kinematical properties of nearby NLS1. **Astronomy & Astrophysics**, v. 629, p. A50, 2019. ISSN 0004-6361. 21, 23

OSTERBROCK, D. E. Spectrophotometry of Seyfert 1 galaxies. **The Astrophysical Journal**, v. 215, p. 733–745, aug. 1977. 13, 30

OSTERBROCK, D. E.; FERLAND, G. J. **Astrophysics of gaseous nebulae and active galactic nuclei**. 2. ed. Sausalito, CA: University Science Books, 2006. 11

OSTERBROCK, D. E.; POGGE, R. W. The spectra of narrow-line Seyfert 1 galaxies. **The Astrophysical Journal**, v. 297, p. 166–176, 1985. 21, 30

PANCOAST, A.; BREWER, B. J.; TREU, T.; PARK, D.; BARTH, A. J.; BENTZ, M. C.; WOO, J.-H. Modelling reverberation mapping data – II. Dynamical modelling of the Lick AGN monitoring project 2008 data set. **Monthly Notices of the Royal Astronomical Society**, v. 445, n. 3, p. 3073–3091, 10 2014. ISSN 0035-8711. Available from: <<https://doi.org/10.1093/mnras/stu1419>>. 84

PANDA, S. Physical conditions in the low-ionization broad-line region in active galaxies. In: **Publications de l'Observatoire Astronomique de Beograd**. [s.n.], 2021. v. 100, p. 333–338. ISSN 0373-3742. Available from: <<https://ui.adsabs.harvard.edu/abs/2021POBeo.100..333P/abstract>>. 12

_____. _____. In: **XIX Serbian Astronomical Conference**. [S.l.: s.n.], 2021. v. 100, p. 333–338. 16

_____. _____. In: **XIX Serbian Astronomical Conference**. [S.l.: s.n.], 2021. v. 100, p. 333–338. 83, 84

_____. The CaFe project: Optical Fe II and near-infrared Ca II triplet emission in active galaxies: simulated EWs and the co-dependence of cloud size and metal content. **Astronomy and Astrophysics**, v. 650, p. A154, jun. 2021. 16, 17, 56, 58, 61, 63, 67, 74, 76

_____. _____. **Astronomy and Astrophysics**, v. 650, p. A154, jun. 2021. 106

PANDA, S.; CZERNY, B.; ADHIKARI, T. P.; HRYNIEWICZ, K.; WILDY, C.; KURASZKIEWICZ, J.; ŚNIEGOWSKA, M. Modeling of the quasar main sequence in the optical plane. **The Astrophysical Journal**, v. 866, n. 2, p. 115, oct. 2018. 9, 47

PANDA, S.; CZERNY, B.; WILDY, C. The physical driver of the optical eigenvector 1 in quasar main sequence. **Frontiers in Astronomy and Space Sciences**, v. 4, 11 2017. ISSN 2296987X. 28

PANDA, S.; MAŁEK, K.; ŚNIEGOWSKA, M.; CZERNY, B. Strong feii emission in nls1s: an unsolved mystery. **Proceedings of the International Astronomical Union**, v. 15, n. S341, p. 297–298, 2019. 10, 15, 23

PANDA, S.; MART´-ALDAMA, M. L.; MARINELLO, M.; CZERNY, B.; MARZIANI, P.; DULTZIN, D. The CaFe project: optical Fe II and near-infrared Ca II triplet emission in active galaxies. I. Photoionization modeling. **The Astrophysical Journal**, v. 902, n. 1, p. 76, oct. 2020. 9, 17, 46, 47, 48, 58, 74, 76, 77, 83, 84

PANDA, S.; MARZIANI, P. High eddington quasars as discovery tools: current state and challenges. **Frontiers in Astronomy and Space Sciences**, v. 10, p. 1130103, 2023. 27

PANDA, S.; MARZIANI, P.; CZERNY, B. The quasar main sequence explained by the combination of Eddington ratio, metallicity, and orientation. **The Astrophysical Journal**, v. 882, n. 2, p. 79, sep. 2019. 16, 28, 85, 86, 109

PANDA, S.; SANTOS, D. D. d. Revisiting the spectral energy distribution of I Zw 1 under the CaFe project. **Acta Astrophysica Taurica**, v. 3, n. 1, p. 27–34, 11 2021. Available from: <<https://arxiv.org/abs/2111.01521v2>>. 12, 47

PANDEY, A.; MARTÍNEZ-ALDAMA, M. L.; CZERNY, B.; PANDA, S.; ZAJAČEK, M. New theoretical fe ii templates for bright quasars. **arXiv preprint arXiv:2401.18052**, 2024. 53

PARK, D.; BARTH, A. J.; HO, L. C.; LAOR, A. A new iron emission template for active galactic nuclei. I. Optical template for the Hβ region*. **The Astrophysical Journal Supplement**, v. 258, n. 2, p. 38, 2 2022. ISSN 0067-0049. Available from: <<https://iopscience.iop.org/article/10.3847/1538-4365/ac3f3e>>. 30, 31

PARKER, M. L.; PINTO, C.; FABIAN, A. C.; LOHFINK, A.; BUISSON, D. J.; ALSTON, W. N.; KARA, E.; CACKETT, E. M.; CHIANG, C.-Y.; DAUSER, T. The response of relativistic outflowing gas to the inner accretion disk of a black hole. **Nature**, v. 543, n. 7643, p. 83–86, 2017. 24, 28

PAUL, B.; WINKLER, H.; POTTER, S. Analysis of optical Fe II emission with the X-ray properties of a selected sample of I Zw 1 type objects. In: **High Energy Astrophysics in Southern Africa**. [S.l.: s.n.], 2021. p. 31. 23, 89

PECAUT, M. J.; MAMAJEK, E. E. Intrinsic colors, temperatures, and bolometric corrections of pre-main-sequence stars. **The Astrophysical Journal Supplement**, v. 208, n. 1, p. 9, sep. 2013. 34

PERSSON, S. Calcium infrared triplet emission in active galactic nuclei. **The Astrophysical Journal**, v. 330, p. 751–765, 7 1988. Available from: <<http://adsabs.harvard.edu/full/1988ApJ...330..751P>>. 16, 73

PERSSON, S.; MCGREGOR, P. Ca ii emission in i zwicky 1. **Astrophysical Journal**, v. 290, p. 125–129, 1985. 16

PETERSON, B. M. Reverberation mapping of active galactic nuclei. **Publications of the Astronomical Society of the Pacific**, v. 105, n. 685, p. 247, 1993. 6

_____. Black hole masses from reverberation measurements. **Proceedings of the International Astronomical Union**, v. 2004, n. IAUS222, p. 15–20, 3 2004. ISSN 1743-9213. Available from: <<https://doi.org/10.1017/S1743921304001358>>. 9, 85

POPOVIC, L.; VINCE, I.; ATANACKOVIC-VUKMANOVIC, O.; KUBICELA, A. Contribution of gravitational redshift to spectral line profiles of seyfert galaxies and quasars. **Astronomy and Astrophysics, Vol. 293, p. 309-314 (1995)**, v. 293, p. 309–314, 1995. 7

POPOVIĆ, L. C. Broad spectral lines in AGNs and supermassive black hole mass measurements. **Open Astronomy**, v. 29, n. 1, p. 1–14, 1 2020. ISSN 25436376. Available from: <<https://www.degruyter.com/document/doi/10.1515/astro-2020-0003/html>>. 7, 8

POPOVIĆ, L. ; MEDIAVILLA, E. G.; BON, E.; STANIĆ, N.; KUBIČELA, A. The line emission region in III Zw 2: kinematics and variability. **The Astrophysical Journal**, v. 599, n. 1, p. 185–192, 12 2003. ISSN 0004-637X. 29, 30

PRADHAN, A. K.; NAHAR, S. N. **Atomic astrophysics and spectroscopy**. [S.l.]: Cambridge University Press, 2011. 10

PRIETO, M. A.; RODRÍGUEZ-ARDILA, A.; PANDA, S.; MARINELLO, M. A novel black-hole mass scaling relation based on coronal gas, and its dependence with the accretion disc. **Monthly Notices of the Royal Astronomical Society**, v. 000, p. 1–14, 2021. Available from: <<http://www.astronomy.ohio-state.edu/>>. 5

PROGA, D.; KALLMAN, T. R. Dynamics of line-driven disk winds in active galactic nuclei. ii. effects of disk radiation. **The Astrophysical Journal**, v. 616, n. 2, p. 688, 2004. 18, 19

RAKSHIT, S.; STALIN, C.; CHAND, H.; ZHANG, X. A catalog of narrow line Seyfert 1 galaxies from the Sloan digital sky survey data release 12. **The Astrophysical Journal Supplement Series**, v. 124, p. 3042, 2017. 13

REES, M. J. Magnetic confinement of broad-line clouds in active galactic nuclei. **Monthly Notices of the Royal Astronomical Society**, v. 228, n. 1, p. 47P–50P, 09 1987. ISSN 0035-8711. Available from: <<https://doi.org/10.1093/mnras/228.1.47P>>. 47

REUNANEN, J.; KOTILAINEN, J. K.; PRIETO, M. A. Near-infrared spectroscopy of nearby seyfert galaxies - I. First results. **Monthly Notices of the Royal Astronomical Society**, v. 331, n. 1, p. 154–168, mar. 2002. 79

RICHARDSON, C. T.; ALLEN, J. T.; BALDWIN, J. A.; HEWETT, P. C.; FERLAND, G. J. Interpreting the ionization sequence in AGN emission-line spectra. **Monthly Notices of the Royal Astronomical Society**, v. 437, n. 3, p. 2376–2403, jan. 2014. 40

RIFFEL, R.; PASTORIZA, M. G.; RODRÍGUEZ-ARDILA, A.; BONATTO, C. Probing the near-infrared stellar population of Seyfert galaxies. **Monthly Notices of the Royal Astronomical Society**, v. 400, n. 1, p. 273–290, nov. 2009. 91

RIFFEL, R.; RODRÍGUEZ-ARDILA, A.; PASTORIZA, M. G. A 0.8-2.4 μm spectral atlas of active galactic nuclei. **Astronomy and Astrophysics**, v. 457, n. 1, p. 61–70, oct. 2006. 23, 33, 38, 89, 90, 91

RODRÍGUEZ-ARDILA, A.; FONSECA-FARIA, M. A.; SANTOS, D. D. dos; PANDA, S.; MARINELLO, M. First detection of outflowing gas in the outskirts of the broad-line region in 1h 0707- 495. **The Astronomical Journal**, v. 167, n. 5, p. 244, 2024. 89, 90, 92, 96, 98, 100, 101, 102, 103, 104

RODRÍGUEZ-ARDILA, A.; MAZZALAY, X. The near-infrared spectrum of Mrk 1239: direct evidence of the dusty torus? **Monthly Notices of the Royal Astronomical Society: Letters**, v. 367, n. 1, p. 1–5, 2006. ISSN 17453933. 23, 38, 81

RODRÍGUEZ-ARDILA, A.; PASTORIZA, M. G.; DONZELLI, C. J. Visible and near-infrared spectroscopy of Seyfert 1 and narrow-line Seyfert 1 galaxies. **The Astrophysical Journal Supplement**, v. 126, n. 1, p. 63–78, jan. 2000. 83

RODRÍGUEZ-ARDILA, A.; VIEGAS, S. M.; PASTORIZA, M. G.; PRATO, L. Infrared Fe II Emission in narrow-line Seyfert 1 galaxies. **The Astrophysical Journal**, v. 565, n. 1, p. 140–154, jan. 2002. 14, 15, 17, 31, 33, 36, 54, 55, 59, 64, 67, 69, 72, 74, 89, 97, 99

ROKAKI, E.; BOISSON, C.; COLLIN-SOUFFRIN, S. Fitting the broad line spectrum and uv continuum by accretion discs in active galactic nuclei. **Astronomy and Astrophysics**, v. 253, p. 57–73, 1992. 19

RUDY, R. J.; MAZUK, S.; PUETTER, R. C.; HAMANN, F. The 1 micron Fe II lines of the Seyfert galaxy I Zw 1. **The Astrophysical Journal**, v. 539, n. 1, p. 166–171, aug. 2000. 15, 30, 33, 97

RYBICKI, G. B.; LIGHTMAN, A. P. **Radiative processes in astrophysics**. [S.l.]: John Wiley & Sons, 2024. 10

SALPETER, E. E. Accretion of Interstellar Matter by Massive Objects. **The Astrophysical Journal**, 1964. 2

_____. Formation and destruction of dust grains. **Annual Review of Astronomy and Astrophysics**, v. 15, n. 1, p. 267–293, 9 1977. ISSN 0066-4146. 10, 39

SANTOS, D.; PANDA, S.; RODRíGUEZ-ARDILA, A.; MARINELLO, M. Modelling the strong fe ii emission. **Boletim da Sociedade Astronômica Brasileira**, v. 34, n. 1, p. 295–299, 2023. 69

_____. Joint analysis of the iron emission in the optical and near-infrared spectrum of i zw 1. **Physics**, v. 6, n. 1, p. 177–193, 2024. ISSN 2624-8174. Available from: <<https://www.mdpi.com/2624-8174/6/1/13>>. 41, 53, 55, 57, 60, 69

SANTOS, D.; RODRíGUEZ-ARDILA, A.; PANDA, S.; MARINELLO, M. First observation of a double-peaked o i emission in the near-infrared. **The Astrophysical Journal Letters**, v. 953, n. 1, p. L3, aug 2023. Available from: <<https://dx.doi.org/10.3847/2041-8213/ace974>>. 35, 80, 83

SARKAR, A.; FERLAND, G. J.; CHATZIKOS, M.; GUZMÁN, F.; HOOF, P. A. M. van; SMYTH, R. T.; RAMSBOTTOM, C. A.; KEENAN, F. P.; BALLANCE, C. P. Improved Fe ii emission-line models for AGNs using new atomic data sets. **The Astrophysical Journal**, v. 907, n. 1, p. 12, 1 2021. ISSN 0004-637X. Available from: <<https://iopscience.iop.org/article/10.3847/1538-4357/abcaa6https://iopscience.iop.org/article/10.3847/1538-4357/abcaa6/meta>>. 44

SCHIMOIA, J. S.; STORCHI-BERGMANN, T.; GRUPE, D.; ERACLEOUS, M.; PETERSON, B. M.; BALDWIN, J. A.; NEMMEN, R. S.; WINGE, C. Short-timescale monitoring of the x-ray, uv, and broad double-peak emission line of the nucleus of ngc 1097. **The Astrophysical Journal**, The American Astronomical Society, v. 800, n. 1, p. 63, feb 2015. Available from: <<https://dx.doi.org/10.1088/0004-637X/800/1/63>>. 49

SCHIMOIA, J. S.; STORCHI-BERGMANN, T.; NEMMEN, R. S.; WINGE, C.; ERACLEOUS, M. SHORT TIMESCALE VARIATIONS OF THE Hα Double-peaked PROFILE OF THE NUCLEUS OF NGC 1097. **The Astrophysical Journal**, v. 748, n. 12pp, p. 145, 4 2012. Available from: <<https://iopscience.iop.org/article/10.1088/0004-637X/748/2/145/meta>>. 19

_____. Short timescale variations of the h double-peaked profile of the nucleus of ngc 1097. **The Astrophysical Journal**, The American Astronomical Society, v. 748, n. 2, p. 145, mar 2012. Available from: <<https://dx.doi.org/10.1088/0004-637X/748/2/145>>. 49

SCHIMOIA, J. S.; STORCHI-BERGMANN, T.; WINGE, C.; NEMMEN, R. S.; ERACLEOUS, M.; SCHIMOIA, J. S.; STORCHI-BERGMANN, T.; WINGE, C.; NEMMEN, R. S.; ERACLEOUS, M. Evolution of the accretion disc around the supermassive black hole of NGC 7213. **Monthly Notices of the Royal Astronomical Society**, v. 472, n. 2, p. 2170–2180, 12 2017. ISSN 0035-8711. Available from: <<https://ui.adsabs.harvard.edu/abs/2017MNRAS.472.2170S/abstract>>. 19, 79, 84

SCHLAFLY, E. F.; FINKBEINER, D. P. Measuring reddening with Sloan digital sky survey stellar spectra and recalibrating SFD. **The Astrophysical Journal**, v. 737, n. 2, p. 103, aug. 2011. 36, 37

SCHLAWIN, E.; HERTER, T. L.; HENDERSON, C.; WILSON, J. C.; PROBST, R.; SPRAYBERRY, D.; BONATI, M.; SCHURTER, P.; JAMES, D.; WARNER, M.; TIGHE, R.; ADAMS, J. D.; MARTÍNEZ, M. Design updates and status of the fourth generation TripleSpec spectrograph. In: RAMSAY, S. K.; MCLEAN, I. S.; TAKAMI, H. (Ed.). **Ground-based and Airborne Instrumentation for Astronomy V**. SPIE, 2014. v. 9147, p. 91472H. Available from: <<https://doi.org/10.1117/12.2055233>>. 35

SCHMIDT, M. 3C 273: A star-like object with large red-shift. **Nature**, v. 197, n. 4872, p. 1040, 1963. ISSN 00280836. 1

SCHWARZ, G. Estimating the dimension of a model. **The Annals of Statistics**, p. 461–464, 1978. 93

SERGEEV, S. G. Spectral variability of the 3C390.3 nucleus for more than 20years – II. Variability of the broad emission-line profiles and HeIIλ4686 Å emission-line fluxes. **Monthly Notices of the Royal Astronomical Society**, v. 495, n. 1, p. 971–980, 05 2020. ISSN 0035-8711. Available from: <<https://doi.org/10.1093/mnras/staa1210>>. 84

SEYFERT, C. K. Nuclear emission in spiral nebulae. **The Astrophysical Journal**, vol. 97, p. p.28, 1943. 1

SHAKURA, N.; SUNYAEV, R. Black holes in binary systems. Observational appearance. **Astronomy and Astrophysics**, v. 24, p. 337–335, 1973. 3, 18

SHAPLEY, H.; CURTIS, H. D. The scale of the Universe. **BuNRC**, v. 2, n. 11, p. 171–217, 1921. 1

SHAPOVALOVA, A. I.; POPOVIĆ, L. C.; BURENKOV, A. N.; CHAVUSHYAN, V. H.; ILIĆ, D.; KOVAČEVIĆ, A.; BOCHKAREV, N. G.; LEÓN-TAVARES, J. Long-term variability of the optical spectra of NGC4151 - II. Evolution of the broad Hα and Hβ emission-line profiles. **Astronomy and Astrophysics**, v. 509, n. 1, p. A106, 1 2010. ISSN 0004-6361. Available from: <<https://www.aanda.org/articles/aa/abs/2010/01/aa12311-09/aa12311-09.html>>. 9, 49, 85

SHAPOVALOVA, A. I.; POPOVIĆ, L. C.; COLLIN, S.; BURENKOV, A.; CHAVUSHYAN, V. H.; BOCHKAREV, N. G.; BENÍTEZ, E.; DULTZIN, D.; KOVAČEVIĆ, A.; BORISOV, N.; CARRASCO, L.; LEÓN-TAVARES, J.; MERCADO, A.; VALDES, J. R.; VLASUYK, V. V.; ZHDANOVA, V. E. Long-term variability of the optical spectra of NGC4151 - I. Light curves and flux correlations. **Astronomy & Astrophysics**, v. 486, n. 1, p. 99–111, 7 2008. ISSN 0004-6361. Available from: <<https://www.aanda.org/articles/aa/abs/2008/28/aa9111-07/aa9111-07.html>>. 9, 49, 85

SHAPOVALOVA, A. I.; POPOVIĆ, L. ; BURENKOV, A. N.; CHAVUSHYAN, V. H.; ILIĆ, D.; KOVAČEVIĆ, A.; KOLLATSCHNY, W.; KOVAČEVIĆ, J.; BOCHKAREV, N. G.; VALDES, J. R.; TORREALBA, J.; LEÓN-TAVARES, J.; MERCADO, A.; BENÍTEZ, E.; CARRASCO, L.; DULTZIN, D.; FUENTE, E. d. l. Spectral optical monitoring of the narrow line Seyfert 1 galaxy Ark 564. **The Astrophysical Journal Supplement Series**, v. 202, n. 1, p. 10, 2012. ISSN 0067-0049. 49, 85

SHEN, Y.; HO, L. C. The diversity of quasars unified by accretion and orientation. **Nature**, v. 513, n. 7517, p. 210–213, 9 2014. 28

SHEN, Y.; RICHARDS, G. T.; STRAUSS, M. A.; HALL, P. B.; SCHNEIDER, D. P.; SNEDDEN, S.; BIZYAEV, D.; BREWINGTON, H.; MALANUSHENKO, V.; MALANUSHENKO, E.; ORAVETZ, D.; PAN, K.; SIMMONS, A. A catalog of quasar properties from SDSS DR7. **The Astrophysical Journal Supplement Series**, v. 194, n. 2, p. 45, 2011. ISSN 0067-0049. 29

SIGUT, T. A. A.; PRADHAN, A. K. Lyα fluorescent excitation of Fe II in active galactic nuclei. **The Astrophysical Journal Letters**, v. 499, n. 2, p. L139–L142, jun. 1998. 14, 15, 31, 69, 72

_____. Predicted Fe II emission-line strengths from active galactic nuclei. **The Astrophysical Journal Supplement**, v. 145, n. 1, p. 15–37, mar. 2003. 14, 15, 31, 40, 72

SIGUT, T. A. A.; PRADHAN, A. K.; NAHAR, S. N. Theoretical Fe i – iii emission-line strengths from active galactic nuclei with broad-line regions. **The Astrophysical Journal**, v. 611, n. 1, p. 81–92, 8 2004. ISSN 0004-637X. Available from: <<http://physics.nist.gov/PhysRef>>. 31, 40

SKRUTSKIE, M. F.; CUTRI, R. M.; STIENING, R.; WEINBERG, M. D.; SCHNEIDER, S.; CARPENTER, J. M.; BEICHMAN, C.; CAPPS, R.; CHESTER, T.; ELIAS, J.; HUCHRA, J.; LIEBERT, J.; LONSDALE, C.; MONET, D. G.; PRICE, S.; SEITZER, P.; JARRETT, T.; KIRKPATRICK, J. D.; GIZIS, J. E.; HOWARD, E.; EVANS, T.; FOWLER, J.; FULLMER, L.; HURT, R.; LIGHT, R.; KOPAN, E. L.; MARSH, K. A.; MCCALLON, H. L.; TAM, R.; DYK, S. V.; WHEELOCK, S. The Two Micron All Sky Survey (2MASS). **The Astronomical Journal**, v. 131, n. 2, p. 1163–1183, 2 2006. ISSN 0004-6256. 34

SMYTH, R. T.; RAMSBOTTOM, C. A.; KEENAN, F. P.; FERLAND, G. J.; BALLANCE, C. P. Towards converged electron-impact excitation calculations of low-lying transitions in Feii. **Monthly Notices of the Royal Astronomical Society**, v. 483, n. 1, p. 654–663, 11 2018. ISSN 0035-8711. Available from: <<https://doi.org/10.1093/mnras/sty3198>>. xv, 32, 44, 45, 46, 54, 56, 62, 63, 64, 66, 68, 73, 75, 76, 109

_____. _____. **Monthly Notices of the Royal Astronomical Society**, v. 483, n. 1, p. 654–663, 2 2019. ISSN 0035-8711. Available from: <<https://academic.oup.com/mnras/article/483/1/654/5211099>>. 77, 109

ŚNIEGOWSKA, M.; CZERNY, B.; YOU, B.; PANDA, S. Properties of active galaxies at the extreme of Eigenvector 1. **Astronomy and Astrophysics**, v. 613, n. Astronomy and Astrophysics, p. 12, 2018. 23, 27, 28

STORCHI-BERGMANN, T.; BALDWIN, J. A.; WILSON, A. S. Double-peaked broad line emission from the liner nucleus of ngc 1097. **Astrophysical Journal, Letters**, v. 410, p. L11–L14, 1993. 79

STORCHI-BERGMANN, T.; ERACLEOUS, M.; RUIZ, M. T.; LIVIO, M.; WILSON, A. S.; FILIPPENKO, A. V. Evidence for a precessing accretion disk in the nucleus of ngc 1097. **The Astrophysical Journal**, v. 489, n. 1, p. 87, 1997. 20, 79

STORCHI-BERGMANN, T.; LIVIO, M.; WILSON, A. S.; FILIPPENKO, A. V.; HALPEN, J. P. The variability of the double-peaked balmer lines in the active nucleus of ngc 1097. **The Astrophysical Journal**, v. 443, p. 617, apr. 1995. 19, 79

STORCHI-BERGMANN, T.; SCHIMOIA, J. S.; PETERSON, B. M.; ELVIS, M.; DENNEY, K. D.; ERACLEOUS, M.; NEMMEN, R. S. Double-peaked profiles: ubiquitous signatures of disks in the broad emission lines of active galactic nuclei. **The Astrophysical Journal**, v. 835, n. 2, p. 236, 1 2017. ISSN 15384357. 19, 79, 84, 85, 86, 109

STRATEVA, I. V.; STRAUSS, M. A.; HAO, L.; SCHLEGEL, D. J.; HALL, P. B.; GUNN, J. E.; LI, L.-X.; IVEZI, e.; RICHARDS, G. T.; ZAKAMSKA, N. L.; VOGES, W.; ANDERSON, S. F.; LUPTON, R. H.; SCHNEIDER, D. P.; BRINKMANN, J.; NICHOL, R. C. Double-peaked low-ionization emission lines in active galactic nuclei. **The Astronomical Journal**, v. 126, n. 4, p. 1720–1749, 10 2003. ISSN 0004-6256. 19, 20, 49, 79, 84

STURM, E.; DEXTER, J.; PFUHL, O.; STOCK, M. R.; DAVIES, R. I.; LUTZ, D.; CLÉNET, Y.; ECKART, A.; EISENHAUER, F.; GENZEL, R.; GRATADOUR, D.; HÖNIG, S. F.; KISHIMOTO, M.; LACOUR, S.; MILLOUR, F.; NETZER, H.; PERRIN, G.; PETERSON, B. M.; PETRUCCI, P. O.; ROUAN, D.; WAISBERG, I.; WOILLEZ, J.; AMORIM, A.; BRANDNER, W.; SCHREIBER, N. M. F.; GARCIA, P. J. V.; GILLESSEN, S.; OTT, T.; PAUMARD, T.; PERRAUT, K.; SCHEITHAUER, S.; STRAUBMEIER, C.; TACCONI, L. J.; WIDMANN, F. Spatially resolved rotation of the broad-line region of a quasar at sub-parsec scale. **Nature**, v. 563, n. 7733, p. 657–660, 11 2018. 9

SULENTIC, J.; MARZIANI, P.; ZAMFIR, S. The case for two quasar populations. **Baltic Astronomy**, v. 20, p. 427–434, 2011. 10, 21, 27

SULENTIC, J. W.; MARZIANI, P.; ZWITTER, T.; DULTZIN-HACYAN, D.; CALVANI, M. Double-peaked the demise of the classical broad-line region in the luminous quasar PG1416-129. **The Astrophysical Journal**, v. 545, p. 15–18, 2000. 27, 31, 53

SUN, J.; SHEN, Y. Dissecting the quasar main sequence: insight from host galaxy properties. **The Astrophysical Journal Letters**, v. 804, n. 1, p. L15, 4 2015. ISSN 2041-8205. Available from: <<https://iopscience.iop.org/article/10.1088/2041-8205/804/1/L15>>. 28

TAYAL, S. S.; ZATSARINNY, O. Electron-impact excitation of forbidden and allowed transitions in fe ii. **Physical Review A**, v. 98, p. 012706, Jul 2018. Available from: <<https://link.aps.org/doi/10.1103/PhysRevA.98.012706>>. xv, 32, 44, 45, 46, 54, 56, 62, 63, 64, 66, 77, 109

THE EVENT HORIZON TELESCOPE COLLABORATION. First M87 Event Horizon telescope results. I. The shadow of the supermassive black hole. **The Astrophysical Journal**, v. 875, n. 1, p. L1, 6 2019. Available from: <<http://arxiv.org/abs/1906.11238http://dx.doi.org/10.3847/2041-8213/ab0ec7>>. 2

TOMBESI, F.; CAPPI, M.; REEVES, J. N.; PALUMBO, G. G. C.; YAQOOB, T.; BRAITO, V.; DADINA, M. Evidence for ultra-fast outflows in radio-quiet AGNs. I. Detection and statistical incidence of Fe K-shell absorption lines. **Astronomy and Astrophysics**, v. 521, p. A57, oct. 2010. 24, 25, 28, 104

TSUZUKI, Y.; KAWARA, K.; YOSHII, Y.; OYABU, S.; TANABÉ, T.; MATSUOKA, Y. Fe ii emission in 14 low-redshift quasars. i. observations. **The Astrophysical Journal**, v. 650, n. 1, p. 57, 2006. 31, 39

TURNER, T. J.; GEORGE, I. M.; NANDRA, K.; TURCAN, D. On x-ray variability in Seyfert galaxies. **The Astrophysical Journal**, v. 524, n. 2, p. 667–673, oct. 1999. 32, 89

VACCA, W. D.; CUSHING, M. C.; RAYNER, J. T. A method of correcting near-infrared spectra for telluric absorption. **Publications of the Astronomical Society of the Pacific**, v. 115, n. 805, p. 389–409, mar. 2003. 36

VERNER, E. M.; VERNER, D. A.; KORISTA, K. T.; FERGUSON, J. W.; HAMANN, F.; FERLAND, G. J. Numerical simulations of Fe II emission spectra. **The Astrophysical Journal Supplement**, v. 120, n. 1, p. 101–112, jan. 1999. xv, 44, 45, 46, 53, 54, 55, 62, 63, 64, 66, 69, 109

VÉRON-CETTY, M.-P.; JOLY, M.; VÉRON, P. The unusual emission line spectrum of I Zw 1. **Astronomy and Astrophysics**, v. 417, p. 515–525, 2004. Available from: <<http://dx.doi.org/10.1051/0004-6361:20035714>>. 30, 56, 68

VESTERGAARD, M.; WILKES, B. J. An empirical ultraviolet template for iron emission in quasars as derived from I Zwicky 1. **The Astrophysical Journal Supplement**, v. 134, n. 1, p. 1–33, 5 2001. ISSN 0067-0049. 30, 31, 39

VIRTANEN, P.; GOMMERS, R.; OLIPHANT, T. E.; HABERLAND, M.; REDDY, T.; COURNAPEAU, D.; BUROVSKI, E.; PETERSON, P.; WECKESSER, W.; BRIGHT, J.; WALT, S. J. van der; BRETT, M.; WILSON, J.; MILLMAN, K. J.; MAYOROV, N.; NELSON, A. R. J.; JONES, E.; KERN, R.; LARSON, E.; CAREY, C. J.; POLAT, I.; FENG, Y.; MOORE, E. W.;

VANDERPLAS, J.; LAXALDE, D.; PERKTOLD, J.; CIMRMAN, R.; HENRIKSEN, I.; QUINTERO, E. A.; HARRIS, C. R.; ARCHIBALD, A. M.; RIBEIRO, A. H.; PEDREGOSA, F.; MULBREGT, P. van; SciPy 1. 0 Contributors. SciPy 1.0: fundamental algorithms for scientific computing in Python. **Nature Methods**, v. 17, p. 261–272, feb. 2020. 92

WALT, S.; COLBERT, S. C.; VAROQUAUX, G. The NumPy Array: a structure for efficient numerical computation. **Computing in Science and Engineering**, v. 13, n. 2, p. 22–30, mar. 2011. 92

WAMPLER, E. J.; WILSON, J. B. O. M.; OBSERVATORIES, P. The emission-line spectrum of 3C 273*. **The Astrophysical Journal**, v. 148, p. 19–67, 1967. 13

WANG, J. M.; DU, P.; HU, C.; NETZER, H.; BAI, J. M.; LU, K. X.; KASPI, S.; QIU, J.; LI, Y. R.; WANG; FANG. Supermassive black holes with high accretion rates in active galactic nuclei. II. The most luminous standard candles in the Universe. **The Astrophysical Journal**, v. 793, n. 2, p. 108, 9 2014. ISSN 0004-637X. Available from: <<https://iopscience.iop.org/article/10.1088/0004-637X/793/2/108https://iopscience.iop.org/article/10.1088/0004-637X/793/2/108/meta>>. 23

WANG, J.-M.; DU, P.; SONGSHENG, Y.-Y.; LI, Y.-R. Spiral arms in broad-line regions of active galactic nuclei. I. Reverberation and differential interferometric signals of tightly wound cases. **Astronomy and Astrophysics**, v. 666, p. A86, oct. 2022. 49

WANG, J.-M.; QIU, J.; DU, P.; HO, L. C. Self-shadowing effects of slim accretion disks in active galactic nuclei: the diverse appearance of the broad-line region. **The Astrophysical Journal**, v. 797, p. 65, dec. 2014. 27

WILL, B. J.; NETZER, H.; WILLS, D. Broad emission features in QSOs and active galactic nuclei. II. New observations and theory of Fe II and HI emission. **The Astrophysical Journal**, v. 288, p. 94–116, jan. 1985. 13, 14, 30

YANG, G.; BOQUIEN, M.; BUAT, V.; BURGARELLA, D.; CIESLA, L.; DURAS, F.; STALEVSKI, M.; BRANDT, W. N.; PAPOVICH, C. X-CIGALE: fitting AGN/galaxy SEDs from X-ray to infrared. **Monthly Notices of the Royal Astronomical Society**, v. 491, p. 740–757, 2020. Available from: <<https://academic.oup.com/mnras/article/491/1/740/5606820>>. 4

YUSEF-ZADEH, F.; BUSHOUSE, H.; ARENDT, R.; WARDLE, M.; MICHAIL, J.; CHANDLER, C. Nonstop variability of sgr a* using jwst at 2.1 and 4.8 μm wavelengths: evidence for distinct populations of faint and bright variable emission. **The Astrophysical Journal Letters**, v. 980, n. 2, p. L35, 2025. 2

ZEL'DOVICH, Y. B.; NOVIKOV, I. D. Relativistic astrophysics. **Soviet Physics Uspekhi**, v. 7, n. 6, p. 763–788, 6 1965. ISSN 0038-5670. 2

ZHANG, S.; ZHOU, H.; SHI, X.; JI, T.; JIANG, P.; PAN, X.; SHENG, Z.; SUN, L.; ZHONG, Z. SDSS J153636.22+044127.0 and its analogs: shocked outflows, not active binary black holes. **The Astrophysical Journal**, v. 877, n. 1, p. 33, may 2019. 79

ZHENG, W.; BINETTE, L.; SULENTIC, J. W. A double-stream model for line profiles. **Astrophysical Journal**, v. 365, p. 115–118, 1990. 19

ZHOU, X.-L.; WANG, J.-M. Narrow iron K α lines in active galactic nuclei: evolving populations? **The Astrophysical Journal**, v. 618, n. 2, p. L83–L86, 12 2004. Available from: <<http://arxiv.org/abs/astro-ph/0412075http://dx.doi.org/10.1086/427871>>. 15

ZOGHBI, A.; FABIAN, A. C.; UTTLEY, P.; MINIUTTI, G.; GALLO, L. C.; REYNOLDS, C. S.; MILLER, J. M.; PONTI, G. Broad iron L line and X-ray reverberation in 1H0707-495. **Monthly Notices of the Royal Astronomical Society**, v. 401, n. 4, p. 2419–2432, feb. 2010. 32

APPENDIX A - CODES FLUXOGRAM

A.1 Code for Continuum Fitting

A.2 Fe II Template Fitting in the Optical

A.3 Code for Building and Fitting the Fe II Template in the NIR

Figure A.1 - Schematic representation of the steps involved in the code that fits the continuum.

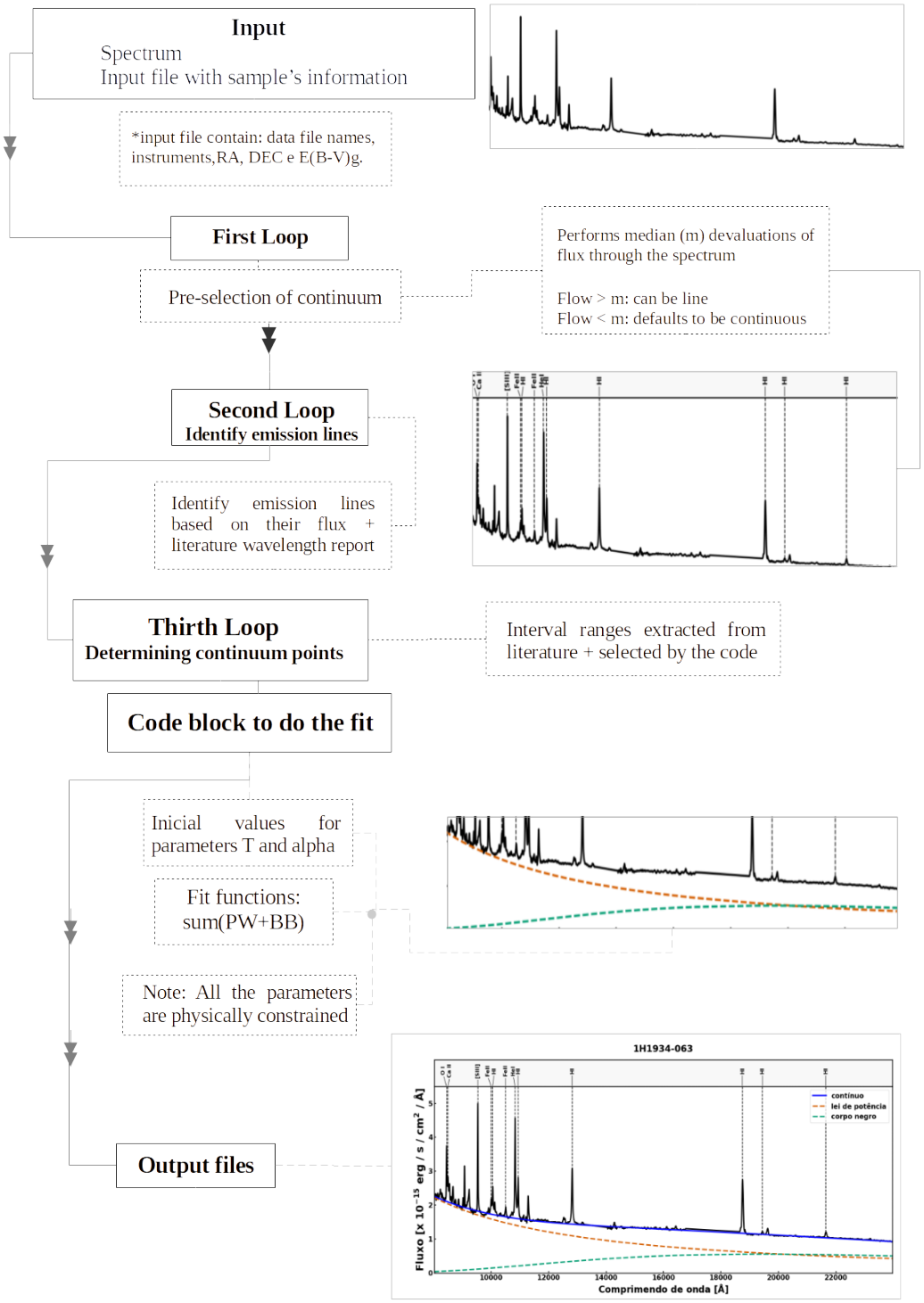

Figure A.2 - Schematic representation of the steps involved in the code for fitting the Fe,II template to the 4560 Å bump.

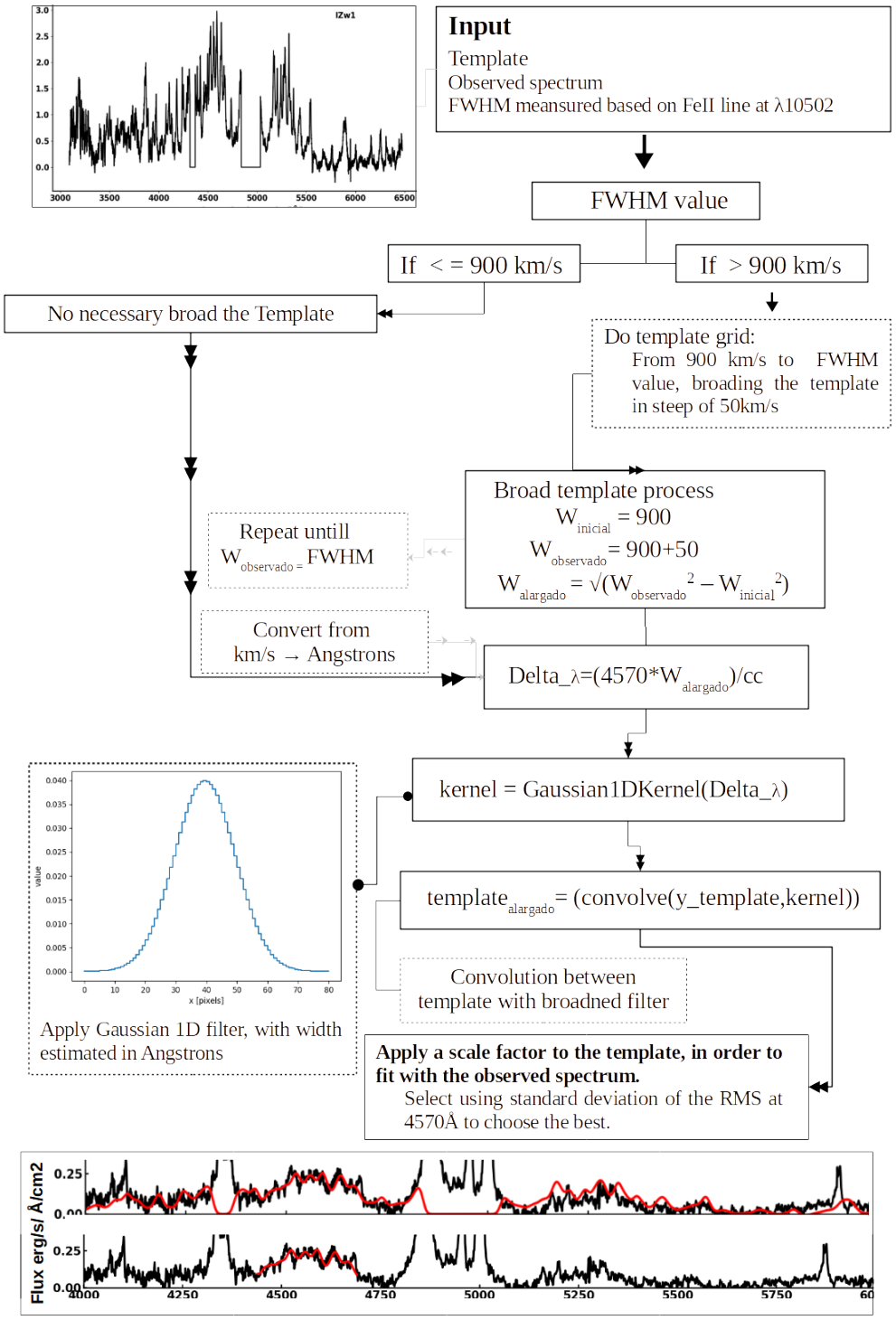

Figure A.3 - Schematic representation of the steps involved in the code for building the Fe,II template in the NIR.

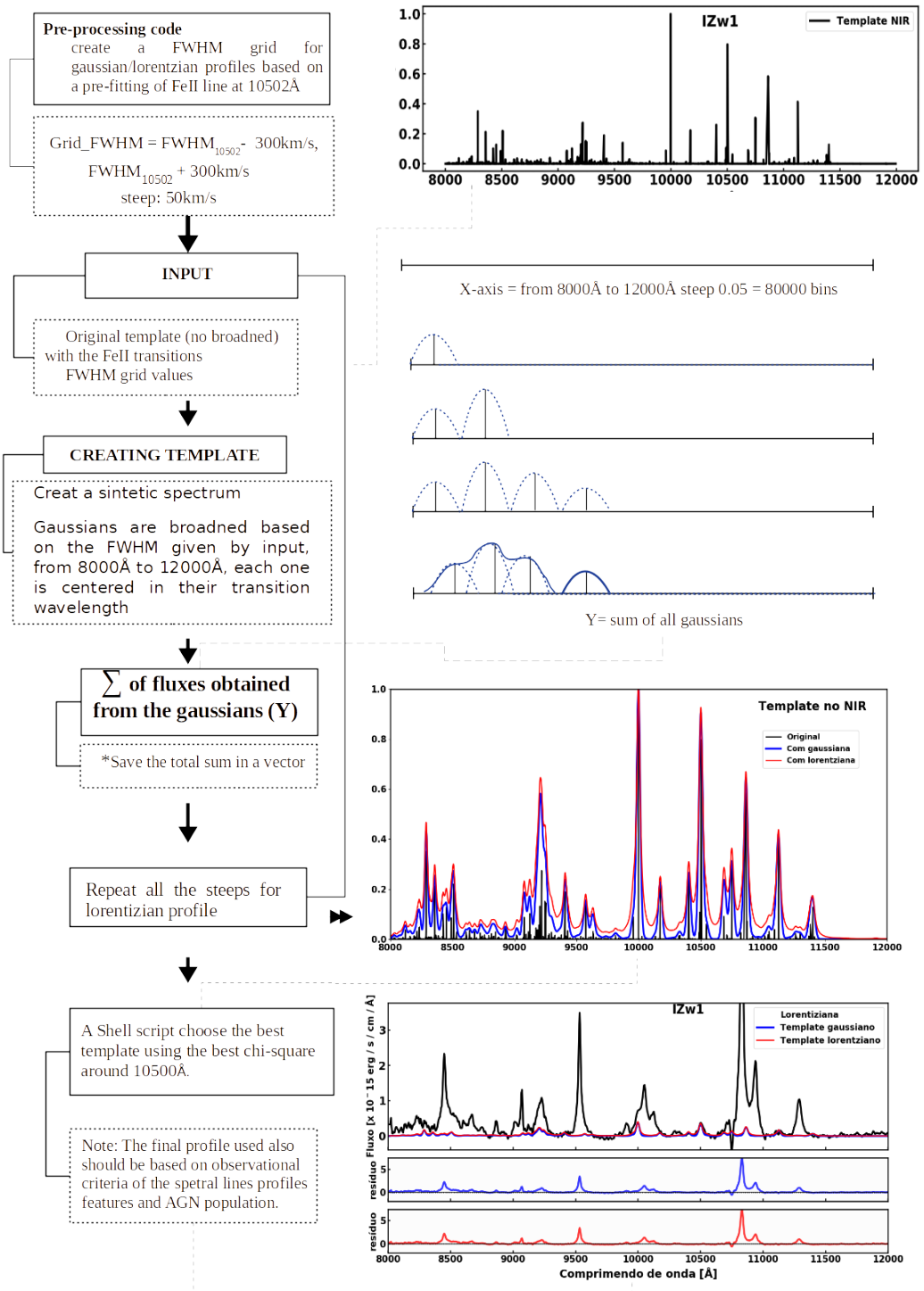

PUBLICAÇÕES TÉCNICO-CIENTÍFICAS EDITADAS PELO INPE

Teses e Dissertações (TDI)

Teses e Dissertações apresentadas nos Cursos de Pós-Graduação do INPE.

Notas Técnico-Científicas (NTC)

Incluem resultados preliminares de pesquisa, descrição de equipamentos, descrição e ou documentação de programas de computador, descrição de sistemas e experimentos, apresentação de testes, dados, atlas, e documentação de projetos de engenharia.

Propostas e Relatórios de Projetos (PRP)

São propostas de projetos técnico-científicos e relatórios de acompanhamento de projetos, atividades e convênios.

Publicações Seriadas

São os seriados técnico-científicos: boletins, periódicos, anuários e anais de eventos (simpósios e congressos). Constam destas publicações o Internacional Standard Serial Number (ISSN), que é um código único e definitivo para identificação de títulos de seriados.

Pré-publicações (PRE)

Todos os artigos publicados em periódicos, anais e como capítulos de livros.

Manuais Técnicos (MAN)

São publicações de caráter técnico que incluem normas, procedimentos, instruções e orientações.

Relatórios de Pesquisa (RPQ)

Reportam resultados ou progressos de pesquisas tanto de natureza técnica quanto científica, cujo nível seja compatível com o de uma publicação em periódico nacional ou internacional.

Publicações Didáticas (PUD)

Incluem apostilas, notas de aula e manuais didáticos.

Programas de Computador (PDC)

São a seqüência de instruções ou códigos, expressos em uma linguagem de programação compilada ou interpretada, a ser executada por um computador para alcançar um determinado objetivo. Aceitam-se tanto programas fonte quanto os executáveis.